ABSTRACT

Title of dissertation: Search for Pair Production of First-Generation Scalar Leptoquarks in Proton-Proton Collisions at $\sqrt{s} = 7$ TeV

Dinko Ferenček, Doctor of Philosophy, 2011

Dissertation directed by: Professor Sarah C. Eno
Department of Physics

A search for pair production of first-generation scalar leptoquarks in a final state containing an electron, a neutrino, and at least two jets is performed using proton-proton collision data at $\sqrt{s} = 7$ TeV. The data corresponding to an integrated luminosity of 36 pb^{-1} were collected by the CMS detector at the CERN LHC. The number of observed events is in good agreement with the predicted yield for Standard Model processes. Prior results from CMS in the dielectron channel are combined with this electron+neutrino search. A combined 95%-confidence-level lower limit of 339 GeV is set on the mass of a first-generation scalar leptoquark for β of 0.5, where β is the branching ratio for the leptoquark to decay to an electron and a quark. These results represent the most stringent direct limits to date for values of β greater than 0.35.

Search for Pair Production of First-Generation Scalar Leptoquarks in Proton-Proton Collisions at $\sqrt{s} = 7$ TeV

by

Dinko Ferenček

Dissertation submitted to the Faculty of the Graduate School of the
University of Maryland, College Park in partial fulfillment
of the requirements for the degree of
Doctor of Philosophy
2011

Advisory Committee:
Professor Sarah C. Eno, Chair/Advisor
Assistant Professor Zackaria Chacko
Professor Abolhassan Jawahery
Professor Andris Skuja
Professor Alice Mignerey, Dean's Representative

Dedication

To my parents, Josip and Marica

Acknowledgments

This dissertation marks the end of one "chapter" of my professional life, and its completion would not be possible without the selfless support and guidance from my advisor, Prof. Sarah Eno, to whom I owe my deepest gratitude. Sarah has always been available to answer all of my questions, and every new challenge that she put in front of me, no matter how difficult it seemed, was always for my own good and helped me to grow as a scientist.

I would also like to thank other members of the University of Maryland's High Energy Physics Group working on the CMS experiment: Prof. Andrew Baden, Prof. Nicholas Hadley, and Prof. Andris Skuja on their support and guidance; postdocs Dr. Paolo Rumerio, Dr. Francesco Santanastasio, and Dr. Jeffrey Temple from whom I learned a great deal and with whom it was a pleasure to work; and my fellow graduate students Malina Kirn, Dr. Kenneth Rossato, and Dr. Elizabeth Twedt on their friendship and support. A large portion of my knowledge of the HCAL subdetector I owe to Dr. Shuichi Kunori and Dr. Richard Kellogg, and I would like to thank them for the time they spent explaining to me all the details.

Ellie, Francesco, and Paolo provided crucial contributions to the analysis presented in this dissertation. I would like to thank them for all the hard work they did related to leptoquark searches at CMS. Sarah's knowledge and experience were essential for the successful completion of these analysis efforts. I would also like to thank Prof. Greg Landsberg (Brown University) for providing the limit setting code, and Prof. Michael Krämer (RWTH Aachen University, Germany) for providing a NLO leptoquark pair-production cross section at 7 TeV.

I would like to thank all the committee members for their willingness to serve on my doctoral dissertation committee. I would also like to thank Sarah and Jeff for spending time reading the dissertation. I greatly appreciate all the valuable comments they provided to help clarify the dissertation.

I was lucky enough to spend my time at CERN during the restart of the LHC operation after the 2008 incident and to witness the first proton-proton collisions at a center-of-mass energy of 7 TeV. Although stressful at times, taking part in the detector operations in these early stages of data taking was a rewarding experience. The most important lesson I learned was the importance of collecting good-quality data, a necessary ingredient for all physics analyses, and how much care and attention it requires. I would like to thank all the members of the CMS collaboration, especially those with whom I worked closely, and the CERN accelerator departments for their dedication and hard work that resulted in excellent performance of both the CMS detector and the LHC. I would also like to thank the administrative staff at the University of Maryland and at CERN. Their help was essential in making my navigation through the necessary paperwork as smoothly as possible.

I would like to express my gratitude to my housemates at "IHoP"[1]: Prateek Agrawal, Jupiter Bagaipo, Kaushik Mitra, Kevin Schoeffler, Yigit Subasi, and Juraj Radić for their friendship and support. With them, my graduate school experience has been the one I will cherish forever.

And last but not least, I would like to thank my beloved wife Zrinka, my parents Josip and Marica, my sister Lidija, and the rest of my family for their

[1]International House of Physicists

unconditional support throughout my studies.

Contents

Table of Contents vi

List of Tables viii

List of Figures xii

List of Abbreviations xvii

1 Introduction 1
1.1 Brief Overview of the Standard Model . . . 3
1.1.1 Limitations of the Standard Model . . . 8
1.2 Dissertation Outline . . . 10

2 Leptoquark Phenomenology 12
2.1 Buchmüller-Rückl-Wyler Effective Leptoquark Model . . . 13
2.2 Leptoquark Production in Proton-Proton Collisions . . . 17
2.3 Leptoquark Decays . . . 21
2.4 Current Limits from Experiments Other than CMS . . . 24

3 Experimental Apparatus 29
3.1 The Large Hadron Collider . . . 29
3.2 The Compact Muon Solenoid Detector . . . 38
3.2.1 Superconducting Magnet . . . 41
3.2.2 Inner Tracking System . . . 43
3.2.3 Electromagnetic Calorimeter . . . 48
3.2.4 Hadron Calorimeter . . . 53
3.2.5 Muon System . . . 61
3.2.6 Trigger System . . . 65

4 Event Reconstruction 68
4.1 Track and Vertex Reconstruction . . . 70
4.2 Electron Reconstruction . . . 73
4.3 Muon Reconstruction . . . 74
4.4 Particle-Flow Event Reconstruction . . . 76
4.5 Jet and MET Reconstruction . . . 77
4.6 Event and Detector Simulation . . . 79
4.6.1 Event Generation . . . 80
4.6.2 Detector Simulation . . . 83

5 Data Analysis 85
5.1 Search Strategy . . . 85
5.2 Data Samples . . . 89
5.3 Monte Carlo Samples . . . 90
5.4 Event Selection . . . 95

5.4.1 Electron Selection . . . 95
5.4.2 Muon Selection . . . 98
5.4.3 Jet Selection . . . 99
5.4.4 Event Preselection . . . 99
5.4.5 Event Selection Optimization and Final Event Selection . . . 107
5.5 Background Estimation . . . 114
5.5.1 $t\bar{t}$ Background . . . 116
5.5.2 QCD Multijet Background . . . 116
5.5.2.1 Fake Rate Method . . . 117
5.5.2.2 Fake Rate Calculation . . . 120
5.5.2.3 QCD Multijet Background Estimation . . . 124
5.5.3 W+jets Background . . . 125
5.6 Systematic Uncertainties . . . 126

6 Results 133

7 Conclusions and Prospects 138

A Trigger Tables for Primary Datasets 140

B Monte Carlo Datasets 160

C HEEP Electron Identification and Isolation 165

D Event Displays for Three Highest-S_{T} Events 170

E Background Shape Uncertainty 173
E.1 W+jets Background Shape Uncertainty . . . 173
E.2 $t\bar{t}$ Background Shape Uncertainty . . . 175

F Bayesian Method for Calculating Upper Limits 178
F.1 Upper Limit Calculation . . . 178
F.2 Combination with the $eejj$ Channel . . . 182

G The CMS Collaboration 185

Bibliography 204

List of Tables

1.1 Fermionic states of the Standard Model and their quantum numbers. T, T_3, Y, and Q denote the weak isospin, the third component of the weak isospin, the weak hypercharge, and the electric charge, respectively. 6

2.1 Leptoquark types, and their quantum numbers and decay modes, in the minimal Buchmüller-Rückl-Wyler model. 16

3.1 The design LHC beam parameters. 36
3.2 Main parameters of the CMS magnet. 42
3.3 Sizes of the HCAL readout towers in η and ϕ as well as the segmentation in depth. The HF has a non-pointing geometry, and the tower η ranges provided here correspond to $|z| = 11.2$ m. *The HE towers 28 and 29 shares the same third depth segment whose energy is artificially divided in two equal portions and shared between these two towers. †The HF tower 29 is located behind the HE and because of the non-projective HF geometry, its energy is added to the HF tower 30. 58

5.1 Electron primary datasets: dataset name, version of the CMS software (CMSSW) used for the event reconstruction, run range considered and corresponding integrated luminosity $\mathcal{L}_{\text{int}}$ after removing data-taking periods with known detector problems. 91
5.2 Photon primary datasets: dataset name, version of the CMS software (CMSSW) used for the event reconstruction, run range considered and corresponding integrated luminosity $\mathcal{L}_{\text{int}}$ after removing data-taking periods with known detector problems. 91
5.3 Generated LQ signal samples used in the analysis. For each sample, the number of generated $e\nu jj$ events, the equivalent integrated luminosity, and the corresponding NLO cross section at $\sqrt{s} = 7$ TeV [34] with the associated theoretical uncertainties, are reported. 93
5.4 Final, optimized event selection criteria. The first seven cuts from the left are already included in the event preselection. 110
5.5 Expected LQ (for $M_{\text{LQ}} = 300$ GeV assuming $\beta = 0.5$) and SM background yields, and the number of observed events in data for the integrated luminosity of 36 pb^{-1} after different stages of the event selection. "Other bkgs" includes Z/γ^*+jets, diboson, single top, b+jets, and γ+jets. A rescaling factor of 1.18 described in Section 5.5.3 is applied to the W+jets MC prediction. The reported uncertainties are statistical. Systematic uncertainties are discussed in Section 5.6. The product of signal acceptance and efficiency is also reported (the statistical uncertainty is less than 1%). 112

5.6 Expected LQ (assuming $\beta = 0.5$) and SM background yields, and the numbers of observed events in data for the integrated luminosity of 36 pb^{-1} after the final, optimized event selection. "Other bkgs" includes Z/γ^*+jets, diboson, single top, b+jets, and γ+jets. A rescaling factor of 1.18 described in Section 5.5.3 is applied to the W+jets MC prediction, as described in Section 5.5.3. The reported uncertainties are statistical. Systematic uncertainties are discussed in Section 5.6. The product of signal acceptance and efficiency is also reported for different LQ masses (the statistical uncertainty is less than 1%). . . . 113
5.7 Isolation criteria for superclusters employed in the estimation of the QCD multijet background. This selection has to be looser than the one applied in the HEEP selection for electrons. However, in the barrel (endcaps) this is strictly true only for superclusters with $E_{\mathrm{T}} < 200$ GeV ($E_{\mathrm{T}} < 225$ GeV). Since the fake rate calculation is dominated by the lower-E_{T} superclusters, this inconsistency has a negligible effect on the final fake rate. 119
5.8 Single-photon triggers employed in the estimation of the QCD multijet background. The information on the trigger prescales is reported for different run ranges. Single-photon triggers with higher p_{T} thresholds were included in the HLT trigger menus for later runs with higher instantaneous luminosities. 120
5.9 MC-corrected fake rate functions, $P(e|c)$, for superclusters reconstructed in the ECAL barrel and endcaps for different jet multiplicity requirements (with jet $p_{\mathrm{T}} > 30$ GeV). Statistical uncertainties on the fit are shown. The last two columns show the estimate of the number of QCD multijet events (using Equation 5.6) in the $e\nu jj$ sample at the preselection stage (without the muon veto applied) and after the final selection (optimized for $M_{\mathrm{LQ}} = 300$ GeV) for different jet multiplicity requirements. 123
5.10 Summary of the systematic uncertainties on the number of signal and background events passing the final event selection for the signal hypothesis with a leptoquark mass of 300 GeV. 132

6.1 Observed and expected 95% CL upper limits on the LQ pair-production cross section times $2\beta(1-\beta)$ as a function of LQ mass. 135
6.2 Observed and expected 95% CL lower limits on the LQ mass for β values of 0.1, 0.5, and 1, obtained by combining the $eejj$ and $e\nu jj$ channels and using the nominal value of the signal cross section ($\mu = M_{\mathrm{LQ}}$). 136

A.1 Trigger table for EG primary dataset in run range 136035–137028. . 140
A.2 Trigger table for EG primary dataset in run range 138560–138747. . 141
A.3 Trigger table for EG primary dataset in run range 138749–139103. . 142
A.4 Trigger table for EG primary dataset in run range 139195–139980. . 143
A.5 Trigger table for EG primary dataset in run range 140058–140076. . 144

A.6 Trigger table for EG primary dataset in run range 140116–140401. . 145
A.7 Trigger table for EG primary dataset in run range 141956–142936. . 146
A.8 Trigger table for EG primary dataset in run range 143318–143962. . 147
A.9 Trigger table for EG primary dataset in run range 144010–144011. . 148
A.10 Trigger table for EG primary dataset in run range 144083–144114. . 149
A.11 Trigger table for Electron primary dataset in run range 146428–146644. 150
A.12 Trigger table for Electron primary dataset in run range 146698–147116. 150
A.13 Trigger table for Electron primary dataset in run range 147196–147284. 151
A.14 Trigger table for Electron primary dataset in run range 147390–148058. 152
A.15 Trigger table for Electron primary dataset in run range 148819–149064. 153
A.16 Trigger table for Electron primary dataset in run range 149181–149182. 154
A.17 Trigger table for Electron primary dataset in run range 149291–149294. 155
A.18 Trigger table for Photon primary dataset in run range 146428–146589. 156
A.19 Trigger table for Photon primary dataset in run range 146644–147116. 156
A.20 Trigger table for Photon primary dataset in run range 147196–147757. 157
A.21 Trigger table for Photon primary dataset in run range 147926–148058. 158
A.22 Trigger table for Photon primary dataset in run range 148819–149294. 159

B.1 Dataset names and corresponding theoretical cross sections, before any data-driven rescaling, for the signal and background MC samples used in the analysis. For the LQ signal samples, $\sigma_{\mathrm{NLO}} \times 2\beta(1-\beta)$, with $\beta = 0.5$, is reported. None of the samples listed below have pile-up simulated. GEN-SIM refers to the event generation and detector simulation stage of the sample production, while RECO refers to the event reconstruction stage of the sample production. 161

C.1 HEEP v3.0 selection cuts. 166

E.1 MC datasets and corresponding theoretical cross sections, before any data-driven rescaling, used in the estimation of the shape uncertainty for the W+jets background. The datasets are generated using MadGraph (v4.4.13), with matrix elements corresponding to up to four additional partons, and subsequently processed with pythia (v6.4.22), with tau decays handled by tauola [128] (v27.121.5). None of the datasets have pile-up simulated. GEN-SIM refers to the event generation and detector simulation stage of the sample production, while RECO refers to the event reconstruction stage of the sample production. 174

E.2 W+jets rescaling factors, the number of events passing the event preselection and the final $M_{\mathrm{T},e\nu}$ cut ($M_{\mathrm{T},e\nu} > 125$ GeV), and the number of events passing the event preselection and the final S_{T} cut for $M_{\mathrm{LQ}} = 300$ GeV ($S_{\mathrm{T}} > 490$ GeV) for datasets listed in Table E.1. For reference, the corresponding values for the ALPGEN samples used in the main analysis are also included. 175
E.3 MC datasets and corresponding theoretical cross sections used in the estimation of the shape uncertainty for the $t\bar{t}$ background. The datasets are generated using the MADGRAPH (v4.4.12) event generator, with matrix elements corresponding to up to three additional partons, and subsequently processed with PYTHIA (v6.4.22), with tau decays handled by TAUOLA [128] (v27.121.5); and using the MC@NLO [124, 129] (v3.4) event generator and subsequently processed with HERWIG [107, 130] (v6.510.3). None of the datasets have pile-up simulated. GEN-SIM refers to the event generation and detector simulation stage of the sample production, while RECO refers to the event reconstruction stage of the sample production. 176
E.4 The number of events passing the event preselection and the final $M_{\mathrm{T},e\nu}$ cut ($M_{\mathrm{T},e\nu} > 125$ GeV), and the number of events passing the event preselection and the final S_{T} cut for $M_{\mathrm{LQ}} = 300$ GeV ($S_{\mathrm{T}} > 490$ GeV) for datasets listed in Table E.3. For reference, the corresponding values for the "Spring10" MADGRAPH sample used in the main analysis are also included. 177

List of Figures

2.1 LO Feynman diagrams for single leptoquark production in association with a lepton in pp collisions. 19
2.2 LO Feynman diagrams for leptoquark pair production in pp collisions. 19
2.3 Total cross section for $pp \to \mathrm{LQ}\overline{\mathrm{LQ}} + X$ at $\sqrt{s} = 7$ TeV including next-to-leading order (NLO) QCD corrections [34] as a function of the leptoquark mass M_{LQ}. The CTEQ6L1 [35] LO and CTEQ6.6 [36] NLO parton distribution functions (PDFs) were used to calculate the LO and NLO cross section, respectively. The variation in the NLO cross section when varying the renormalization/factorization scale between $\mu = M_{\mathrm{LQ}}/2$ and $\mu = 2M_{\mathrm{LQ}}$ is indicated by the shaded band around the nominal value obtained using $\mu = M_{\mathrm{LQ}}$. 20
2.4 Possible final states for a decay of a pair of first-generation scalar leptoquarks. q (q') denotes either u or d quark. 23
2.5 Observed (red solid line) and expected (red dot-dashed line) D0 mass limits at 95% CL in the β versus M_{LQ} plane for the pair production of first-generation scalar leptoquarks and the nominal hypothesis for the signal cross section ($\mu = M_{\mathrm{LQ}}$) using 1 fb^{-1} of $p\bar{p}$ collision data [53]. The regions to the left of the curves are excluded. The observed limits found individually using each of the three final states are shown for the nominal cross-section hypothesis ($\mu = M_{\mathrm{LQ}}$), and the hatched area indicates the part of the plane previously excluded by the D0 collaboration with a lower integrated luminosity of 250 pb^{-1} and for the minimal cross-section hypothesis ($\mu = 2M_{\mathrm{LQ}}$). 26
2.6 ATLAS 95% CL exclusion region in the β versus M_{LQ} plane obtained from the combination of the $eejj$ and $e\nu jj$ channels using 35 pb^{-1} of pp collision data [54]. The gray area indicates the D0 exclusion limit with 1 fb^{-1} of $p\bar{p}$ collision data [53], and the thick dotted line indicates the CMS exclusion in the $eejj$ channel only using 33 pb^{-1} of pp collision data [56]. The dotted and dot-dashed lines show the individual limits for the $eejj$ and $e\nu jj$ channels, respectively. The combined expected limit is indicated by the thick dashed line. The combined observed limit is indicated by the solid line. 27
2.7 95% CL observed limit for $\mu = M_{\mathrm{LQ}}$ on the leptoquark mass as a function of β obtained in the $e\nu jj$ channel using 5.4 fb^{-1} of $p\bar{p}$ collision data [55]. The limit is compared with the previous D0 result [53], and CMS [56, 57] and ATLAS [54] results. 28

3.1 LHC cryodipole magnet and its main components (from [63]). The LHC ring accommodates 1232 such dipole magnets all of which have to be cooled down to 1.9 K for normal operation. 30
3.2 Schematic layout of the LHC ring (from [63]). In this view, Beam 1 revolves clockwise and Beam 2 anticlockwise. 31
3.3 LHC injector complex (from [63]). 33

3.4 PSB-PS transfer with two-batch filling scheme for the LHC. 33
3.5 Generation of the nominal 25-ns bunch train in the PS complex. . . 34
3.6 Nominal PS-SPS-LHC filling sequence and the final 25-ns bunch structure of the LHC beam. 34
3.7 The maximum instantaneous luminosity per day (left panel) and the total integrated luminosity per day (right panel) for the 2010 run. . 38
3.8 A perspective view of the CMS detector. 40
3.9 Artistic view of the CMS solenoid composed of five modules placed inside the cryostat. Details of the supporting system (vertical, radial and longitudinal tie rods) can also be seen. 43
3.10 Schematic r-z cross section through the CMS tracker. Each line represents a detector module. Double lines indicate back-to-back modules which deliver stereo hits. 45
3.11 Layout of the CMS pixel detector. 46
3.12 Transverse section through the CMS electromagnetic calorimeter. . . 50
3.13 Layout of the CMS electromagnetic calorimeter showing the arrangement of crystal modules, supermodules and endcaps, with the preshower in front. 51
3.14 Longitudinal view of the CMS detector showing the locations of the HCAL barrel (HB), endcap (HE), outer (HO) and forward (HF) calorimeters. 55
3.15 Isometric view of an HB wedge showing the slots the end of the wedge into which the scintillator trays are inserted. 56
3.16 The HCAL tower segmentation in the r-z plane for one-fourth of the HB, HE, and HO subdetectors. 56
3.17 Material thickness in radiation lengths after the ECAL, HCAL, and at the depth of each muon station as a function of pseudorapidity. The thickness of the HF is approximately constant over the range $3 < |\eta| < 5$ (not shown). 62
3.18 Material thickness in interaction lengths after the ECAL, HCAL, and at the depth of each muon station as a function of pseudorapidity. The thickness of the HF is approximately constant over the range $3 < |\eta| < 5$ (not shown). 63
3.19 Layout of one quarter of the CMS muon system for the LHC startup. 63
3.20 Architecture of the Level-1 Trigger. 67

4.1 Transverse slice through the CMS detector depicting typical detection patterns for muons, electrons, photons, and charged and neutral hadrons. 69
4.2 Schematic view of a proton-proton collision, with a $2 \to 2$ hard scattering event (from [105]). 81
4.3 Diagrammatic structure of a generic hard scattering process (from [105]). 82

5.1 Examples of LO Feynman diagrams for (a) $t\bar{t}$ and (b) W+jets production, the two dominant SM backgrounds in the $e\nu jj$ channel. . . 87
5.2 Luminosity profile and total integrated luminosity for delivered, recorded, and certified collision data for the entire 2010 run at 7 TeV. 90
5.3 Examples of LO Feynman diagrams for single top production in s, t, and tW channels. 96
5.4 The p_{T} (left panel) and η (right panel) distributions of the selected electron for events passing the event preselection. The distribution for the signal with $M_{\mathrm{LQ}} = 300$ GeV and the contributing backgrounds are shown. The distribution labeled "Other backgrounds" includes Z/γ^*+jets, diboson, single top, b+jets, and γ+jets. A rescaling factor of 1.18 described in Section 5.5.3 is applied to the W+jets MC prediction. The black dots indicate data, with error bars representing the Poisson uncertainty on the bin content. 103
5.5 The p_{T} (left panel) and η (right panel) distributions of the leading jet in p_{T} for events passing the event preselection. The distribution for the signal with $M_{\mathrm{LQ}} = 300$ GeV and the contributing backgrounds are shown. The distribution labeled "Other backgrounds" includes Z/γ^*+jets, diboson, single top, b+jets, and γ+jets. A rescaling factor of 1.18 described in Section 5.5.3 is applied to the W+jets MC prediction. The black dots indicate data, with error bars representing the Poisson uncertainty on the bin content. The rightmost bin in the p_{T} distribution includes the overflow. 103
5.6 The p_{T} (left panel) and η (right panel) distributions of the second leading jet in p_{T} for events passing the event preselection. The distribution for the signal with $M_{\mathrm{LQ}} = 300$ GeV and the contributing backgrounds are shown. The distribution labeled "Other backgrounds" includes Z/γ^*+jets, diboson, single top, b+jets, and γ+jets. A rescaling factor of 1.18 described in Section 5.5.3 is applied to the W+jets MC prediction. The black dots indicate data, with error bars representing the Poisson uncertainty on the bin content. The rightmost bin in the p_{T} distribution includes the overflow. 104
5.7 The $\not\!\!E_{\mathrm{T}}$ (left panel) and $\min(p_{\mathrm{T},e}, \not\!\!E_{\mathrm{T}})$ (right panel) distributions of the second leading jet in p_{T} for events passing the event preselection. The distribution for the signal with $M_{\mathrm{LQ}} = 300$ GeV and the contributing backgrounds are shown. The distribution labeled "Other backgrounds" includes Z/γ^*+jets, diboson, single top, b+jets, and γ+jets. A rescaling factor of 1.18 described in Section 5.5.3 is applied to the W+jets MC prediction. The black dots indicate data, with error bars representing the Poisson uncertainty on the bin content. The rightmost bin includes the overflow. 104

5.8 The $\min \Delta R(e,j)$ distribution (top) for events passing the electron, jet, and $\not\!\!E_{\mathrm{T}}$ preselection cuts (other preselection cuts not applied); and the distributions of $\left|\Delta\phi(e,\not\!\!E_{\mathrm{T}})\right|$ (bottom left) and $\left|\Delta\phi(j1,\not\!\!E_{\mathrm{T}})\right|$ (bottom right) for events passing the electron, jet, $\not\!\!E_{\mathrm{T}}$, and $\min \Delta R(e,j)$ preselection cuts (other preselection cuts not applied). The distribution for the signal with $M_{\mathrm{LQ}} = 300$ GeV and the contributing backgrounds are shown. The distribution labeled "Other backgrounds" includes Z/γ^*+jets, diboson, single top, b+jets, and γ+jets. A rescaling factor of 1.18 described in Section 5.5.3 is applied to the W+jets MC prediction. The black dots indicate data, with error bars representing the Poisson uncertainty on the bin content. 105

5.9 The distribution of $\left|\Delta\phi(j2,\not\!\!E_{\mathrm{T}})\right|$ for events passing the electron, jet, $\not\!\!E_{\mathrm{T}}$, and $\min \Delta R(e,j)$ preselection cuts (other preselection cuts not applied) (left panel) and for events passing all preselection cuts except for the muon veto and the S_{T} cut (right panel). The distribution for the signal with $M_{\mathrm{LQ}} = 300$ GeV and the contributing backgrounds are shown. The distribution labeled "Other backgrounds" includes Z/γ^*+jets, diboson, single top, b+jets, and γ+jets. A rescaling factor of 1.18 described in Section 5.5.3 is applied to the W+jets MC prediction. The black dots indicate data, with error bars representing the Poisson uncertainty on the bin content. This observable is not used in the final event selection but it is included in the event selection optimization described in Section 5.4.5. 106

5.10 The $M_{\mathrm{T},e\nu}$ distribution in linear (left panel) and logarithmic (right panel) scale for events passing the event preselection. The distribution for the signal with $M_{\mathrm{LQ}} = 300$ GeV and the contributing backgrounds are shown. The distribution labeled "Other backgrounds" includes Z/γ^*+jets, diboson, single top, b+jets, and γ+jets. A rescaling factor of 1.18 described in Section 5.5.3 is applied to the W+jets MC prediction. The black dots indicate data, with error bars representing the Poisson uncertainty on the bin content. The rightmost bin includes the overflow. 106

5.11 The distribution of the number of selected muons (left panel) for events passing all preselection cuts except for the muon veto, and the S_{T} distribution (right panel) for events passing the event preselection. The distribution for the signal with $M_{\mathrm{LQ}} = 300$ GeV and the contributing backgrounds are shown. The distribution labeled "Other backgrounds" includes Z/γ^*+jets, diboson, single top, b+jets, and γ+jets. A rescaling factor of 1.18 described in Section 5.5.3 is applied to the W+jets MC prediction. The black dots indicate data, with error bars representing the Poisson uncertainty on the bin content. 107

5.12 Optimized S_{T} cut employed in the final event selection as a function of the LQ mass. 111

5.13 The S_{T} distribution (top) for events passing the final selection excluding the optimized S_{T} cut itself (the preselection $S_{\mathrm{T}} > 250$ GeV cut is applied), and the distributions of M_{ej} (bottom left) and $M_{\mathrm{T},\nu j}$ (bottom right) for events passing the final selection optimized for $M_{\mathrm{LQ}} = 300$ GeV ($S_{\mathrm{T}} > 490$ GeV). The distribution for the signal with $M_{\mathrm{LQ}} = 300$ GeV and the contributing backgrounds are shown. The distribution labeled "Other backgrounds" includes Z/γ^*+jets, diboson, single top, b+jets, and γ+jets. A rescaling factor of 1.18 described in Section 5.5.3 is applied to the W+jets MC prediction. The black dots indicate data, with error bars representing the Poisson uncertainty on the bin content. The rightmost bin includes the overflow. 115
5.14 Probability $P(e|c)$ for an isolated supercluster c to be reconstructed as a HEEP electron e as a function of the supercluster E_{T} in the ECAL barrel (top) and two endcap regions, $|\eta| < 2.2$ (bottom left) and $|\eta| > 2.2$ (bottom right), calculated from data events with exactly one supercluster, at least one jet with $p_{\mathrm{T}} > 30$ GeV, and passing the other selection criteria described in Section 5.5.2.2. A MC-based p_{T}-dependent correction to remove the contribution from real electrons in the numerator of the fake rate is applied. The black line is the result of the zero-degree (first-degree) polynomial fit to the barrel (endcap) fake rate. 122

6.1 Observed and expected 95% CL upper limits on the LQ pair-production cross section times $2\beta(1-\beta)$ as a function of LQ mass. A NLO prediction of the LQ pair-production cross section times $2\beta(1-\beta)$ as a function of LQ mass, assuming $\beta = 0.5$, is also shown. The theoretical uncertainties on σ_{NLO} due to the definition of the renormalization/factorization scale and the choice of PDFs are represented as a band around the central value. 134
6.2 Observed and expected 95% CL lower limits on the LQ mass as a function of β for the $e\nu jj$ channel. The region to the left of the observed limit curve is excluded. The band around the observed limit corresponds to the uncertainty band for the theoretical cross section shown in Figure 6.1. 136
6.3 Observed 95% CL lower limits on the LQ mass as a function of β, obtained using the nominal value of the signal cross section ($\mu = M_{\mathrm{LQ}}$), for the individual $eejj$ and $e\nu jj$ channels, and their combination. The combined expected limit is also shown. The regions to the left of the observed limit curves are excluded. For comparison, D0 [53, 55] and ATLAS [54] limits are also shown. 137

List of Abbreviations

ALICE	A Large Ion Collider Experiment
APD	Avalanche Photodiode
APV	Atomic Parity Violation
ATLAS	A Toroidal LHC ApparatuS
BPTX	Beam Pick-up Timing for the eXperiments
BRW	Buchmüller-Rückl-Wyler
BSM	Beyond Standard Model
CERN	European Organization for Nuclear Research
CL	Confidence Level
CMS	Compact Muon Solenoid
CMSSW	CMS Software
CP	Charge-Parity
CPU	Central Processing Unit
CSC	Cathode Strip Chamber
CTF	Combinatorial Track Finder
DAQ	Data Acquisition
DT	Drift Tube
EB	ECAL Barrel
ECAL	Electromagnetic Calorimeter
EE	ECAL Endcap
EM	Electromagnetic
FCNC	Flavor-Changing Neutral Current
FSR	Final-State Radiation
GSF	Gaussian Sum Filter
GUT	Grand Unified Theory
HB	HCAL Barrel
HCAL	Hadron Calorimeter
HE	HCAL Endcap
HEEP	High Energy Electron Pairs
HERA	Hadron-Electron Ring Accelerator
HF	HCAL Forward
HO	HCAL Outer
HPD	Hybrid Photodiode
HLT	High-Level Trigger
IP	Interaction Point
ISR	Initial-State Radiation
L1	Level 1
L1A	Level-1 Accept
LEP	Large Electron-Positron Collider
LHC	Large Hadron Collider
LQ	Leptoquark
LO	Leading Order

mBRW	minimal Buchmüller-Rückl-Wyler
MB	Muon Barrel
MC	Monte Carlo
ME	Muon Endcap
MET	Missing Transverse Energy
NLO	Next-to-Leading Order
NNLO	Next-to-Next-to-Leading Order
PD	Primary Dataset
PF	Particle Flow
PDF	Parton Distribution Function
PMT	Photomultiplier Tube
PS	Proton Synchrotron, Preshower
PSB	Proton Synchrotron Booster
QED	Quantum Electrodynamics
QCD	Quantum Chromodynamics
RBX	Readout BoX
RF	Radio Frequency
RMS	Root Mean Square
RPC	Resistive Plate Chamber
SLHA	SUSY Les Houches Accord
SM	Standard Model
SPS	Super Proton Synchrotron
TCS	Trigger Control System
TEC	Tracker End Cap
TIB	Tracker Inner Barrel
TID	Tracker Inner Disks
TOB	Tracker Outer Barrel
TPG	Trigger Primitive Generator
TTC	Timing, Trigger and Control
VPT	Vacuum Phototriode
WLS	Wavelength-Shifting

Chapter 1

Introduction

Several decades of experimental and theoretical research in the field of elementary particle physics lead to the formulation of the Standard Model, a theoretical framework representing our current understanding of elementary particles and their interactions. One of the cornerstones of the Standard Model is the hypothesized Higgs boson particle, responsible for the electroweak symmetry breaking and generation of particle masses. The Higgs boson in the only remaining particle predicted by the Standard Model which has yet to be observed.

Just outside Geneva, Switzerland, some 100 m underground, one of the greatest scientific endeavors is taking place. It is the Large Hadron Collider (LHC), a machine which accelerates proton beams to the highest energies ever achieved in a laboratory, and collides them inside several detectors located along the LHC ring. It is the hope of thousands of physicists, gathered in large international collaborations, that studying these collisions will improve our understanding of the basic building blocks of the Universe and help us unravel some its mysteries. The quest for an understanding what the Universe is made of and how it all works started with the ancient Greeks and has continued to this day, with the LHC being the latest and the biggest scientific effort towards that goal. One of the main objectives of the LHC physics program is to discover the Standard Model Higgs boson, or any new

physics Beyond the Standard Model (BSM) that could serve as a substitute for the Standard Model Higgs boson. Apart from the purely scientific goal of expanding the boundaries of human knowledge, this type of fundamental research can also lead to practical benefits for society at large. The most prominent example is the invention of the World Wide Web, without which it would be hard to imagine modern society.

Paradoxical as it may seem, some of the largest pieces of scientific instrumentation are needed to study the smallest building blocks of the Universe. The reason for this is two-fold. First, to study the Universe at very short length scales, it is necessary to accelerate particles to very high energies. However, while being accelerated, particles can receive only a limited amount of energy over a given acceleration distance, and thus a long accelerator complex is needed. In addition, to reduce the amount of synchrotron radiation, which leads to energy loss and deceleration, produced by particles experiencing radial acceleration in a circular accelerator, such as the LHC, a large ring radius is needed. Secondly, since the colliding particles have high energy, the collision debris will also have high energy. To fully contain these particles inside the detector (except for muons and neutrinos), a large detector is needed. Since energy can be converted into mass (according to the famous formula $E = mc^2$), new heavy particle, that have not been around since the Big Bang, could be produced in collisions. Leptoquarks, the main subject of this dissertation, are just one type of hypothesized heavy particles that could be produced in proton-proton collisions at the LHC.

The detectors built around collision points can be viewed as giant digital cameras taking snapshots of the collision debris. By analyzing these snapshots, physicists

can reconstruct the type and energy of stable (over a time scale of a few ns) particles produced in the collision, and based on this information, decide if a given collision is interesting enough to be stored for a more detailed analysis. What constitutes an interesting collision depends on the type of analysis being performed. Typically, interesting collisions are those in which new heavy particles are potentially produced. It is important to realize that most hypothesized heavy particles have a very short lifetime; immediately after their production they decay to well-known stable particles. Other types of new particles are expected to interact weakly with the detector and have a lifetime long enough to escape undetected; a typical signature of the production of such particles is the momentum imbalance of the collision debris. Therefore, based on the detection of well-known stable particles, possibly in configurations that apparently violate the momentum conservation, it is possible to infer a production of new particles. Due to the nature of proton-proton collisions, only a small fraction of all collisions is interesting enough to be permanently stored.

1.1 Brief Overview of the Standard Model

The Standard Model (SM) is a theoretical framework describing all known elementary particles and their interactions in the context of relativistic quantum field theory. In this section, only a brief overview of the most important aspects of the Standard Model is given. For a more detailed description of the Standard Model, including a historical overview, the reader is referred to [1–3].

In the Standard Model, particles of matter are represented as spin-1/2 fermions,

which respect the Fermi-Dirac statistics, whereas spin-1 bosons, which respect the Bose-Einstein statistics, serve as force carrier particles mediating interactions between the particles. Three of the four known force are described within the SM framework: the strong force, which holds together protons and neutrons inside atomic nucleus; the weak force, which is responsible for the radioactive decay; and the electromagnetic force, which holds atoms and molecules together. The fourth know force, gravitational, is not part of the SM framework. All known subatomic particles are either directly contained in the Standard Model or are bound states of the Standard Model particles.

Photons are electrically neutral spin-1 bosons that mediate the electromagnetic interaction between electrically charged particles, and the theory of electromagnetic interaction is called Quantum Electrodynamics (QED). Since photons are massless, the range of the electromagnetic force is infinite. The weak force is mediated when the W^+, W^-, and Z spin-1 gauge bosons are exchanged between particles carrying weak isospin, which includes the gauge bosons themselves. Since the gauge bosons are massive ($\sim$ 100 GeV), the weak force is short ranged ($R \sim 10^{-18}$ m). The $W^\pm$ bosons only interact with fermions of *left-handed chirality* and antifermions of *right-handed chirality*, whereas the neutral Z boson interacts with both chiralities of fermions and antifermions. The eight gluons mediate the strong interaction between color-charged particles, and the theory of strong interaction is called Quantum Chromodynamics (QCD). Gluons are massless electrically neutral spin-1 bosons that carry the color charge, and because of this, they can interact with one another. Contrary to what would be naively expected based on the gluon mass, the nature

of the strong interaction is such that the resulting range of the strong force is short ($R \sim 10^{-15}$ m).

The Standard Model fermions are grouped according to the charges they carry, and include six *flavors* of leptons and six *flavors* of quarks. Each fermion has a corresponding antiparticle. The six leptons are electron (e), electron neutrino (ν_e), muon (μ), muon neutrino (ν_μ), tau (τ), and tau neutrino (ν_τ). Electrons, muons, and taus carry one unit of electric charge, and thus interact electromagnetically, whereas all neutrinos are electrically neutral. However, all leptons carry weak isospin and therefore interact via weak force. The second group of fermions, quarks, are called up (u), down (d), charm (c), strange (s), top (t), and bottom (b). All quarks carry weak isospin, fractional electric, and color charge, and therefore interact via all three forces described by the Standard Model. Due to the nature of the strong force, gluons contribute more energy to the gluon field as the interaction distance increases. It is therefore energetically favorable to create a quark-antiquark pair from the vacuum than to have isolated quarks interact over long distances. Due to this phenomenon, called *confinement*, quarks are never observed as free particles; they are bound into *mesons*, color-neutral bound states of a quark and antiquark, and *baryons*, color-neutral bound states of three quarks. The proton and the neutron are the two most well-known baryons. Mesons and baryons are collectively called *hadrons*. Another interesting property of the strong force is the phenomenon called *asymptotic freedom*. It is the property of the strong interaction that it becomes weaker as the amount of energy exchanged between the two interacting particles increases, or, equivalently, as they get closer to each other. All SM fermions can

be grouped into three *families* or *generations*. Each generation consist of a pair of leptons, one charged lepton and one neutrino, and a pair of quarks. Corresponding particles from different generations have the same quantum numbers except for flavor, and by convention particles from higher generations have greater mass than their lower generation counterparts. Fermionic states of the Standard Model and their quantum numbers are shown in Table 1.1. Table 1.1 can be viewed as a sort of "periodic table" for the Standard Model fermions. All stable matter is made of the first-generation charged fermions, since all other charged fermions have a finite lifetime.

Table 1.1: Fermionic states of the Standard Model and their quantum numbers. T, T_3, Y, and Q denote the weak isospin, the third component of the weak isospin, the weak hypercharge, and the electric charge, respectively.

	T	T_3	Y	Q	Generation		
					1^{st}	2^{nd}	3^{rd}
Leptons	$\frac{1}{2}$	$\begin{pmatrix} \frac{1}{2} \\ -\frac{1}{2} \end{pmatrix}$	-1	$\begin{pmatrix} 0 \\ -1 \end{pmatrix}$	$\begin{pmatrix} \nu_e \\ e \end{pmatrix}_L$	$\begin{pmatrix} \nu_\mu \\ \mu \end{pmatrix}_L$	$\begin{pmatrix} \nu_\tau \\ \tau \end{pmatrix}_L$
	0	0	-2	-1	e_R	μ_R	τ_R
Quarks	$\frac{1}{2}$	$\begin{pmatrix} \frac{1}{2} \\ -\frac{1}{2} \end{pmatrix}$	$\frac{1}{3}$	$\begin{pmatrix} \frac{2}{3} \\ -\frac{1}{3} \end{pmatrix}$	$\begin{pmatrix} u \\ d \end{pmatrix}_L$	$\begin{pmatrix} c \\ s \end{pmatrix}_L$	$\begin{pmatrix} t \\ b \end{pmatrix}_L$
	0	0	$\frac{4}{3}$	$\frac{2}{3}$	u_R	c_R	t_R
	0	0	$-\frac{2}{3}$	$-\frac{1}{3}$	d_R	s_R	b_R

At the heart of the Standard Model is the concept of local gauge invariance, where all interactions between fermions appear as a natural consequence of a requirement that the Standard Model Lagrangian has to be invariant under local gauge transformations of fermionic and bosonic fields. Fermionic and bosonic fields can transform under different symmetry groups, leading to different types of in-

teractions, i.e., different forces are associated with different symmetry groups and different particles belong to different representations of these symmetry group. The strong force is associated with the SU(3) group, while the electromagnetic and weak force are together associated with the direct product of SU(2) and U(1) groups. Therefore, the combined symmetry group of the Standard Model is the direct product of these three symmetry groups, i.e., $\mathrm{SU}(3)_C \times \mathrm{SU}(2)_L \times \mathrm{U}(1)_Y$, where C, L, and Y denote *color*, *left-handed chirality*, and *weak hypercharge*, respectively. There is one problem, however; local gauge invariance requires all fermions and gauge bosons to be massless, which clearly does not agree with experimental observations. For example, if fermions were massless, no atoms would be formed. To overcome this problem, a fundamental spin-0 (scalar) field, which permeates all of space, is introduced. This field is called the Higgs field, and a quantum of this field is the Higgs boson. The Higgs field interacts with SM fermions and electroweak gauge bosons associated with the $\mathrm{SU}(2)_L \times \mathrm{U}(1)_Y$ symmetry. However, by acquiring a *vacuum expectation value*, the Higgs field *spontaneously breaks* the $\mathrm{SU}(2)_L \times \mathrm{U}(1)_Y$ electroweak symmetry group to the $\mathrm{U}(1)_{\mathrm{em}}$ of the electromagnetic interaction, and provides mass to the $W^{\pm}$ and Z gauge bosons and charged fermions, and leaves the photon and neutrinos massless. The Higgs boson is therefore an essential building block of the Standard Model.

1.1.1 Limitations of the Standard Model

The Standard Model is certainly one of the most successful scientific theories in the history of physics. It has been tested to an extreme level of precision, and its predictions are in excellent agreement with most experimental data [4]. Nevertheless, the Standard Model has its own problems and limitations.

One obvious limitation of the Standard Model is the absence of the gravitation force from the description of elementary particle interactions. At an esthetic level, the Standard Model has about 20 free parameters that have to determined from experimental data, rather than being fixed by some underlying principle. It is also a mystery why there are three generations of fermions, and what is the reason for an apparent symmetry between quarks and leptons. This symmetry between the SM quarks and leptons is the prime motivation for a search for leptoquarks presented in this dissertation.

There are other problems with the Standard Model of a more technical nature. It is widely believed that the three fundamental forces described by the Standard Model are just different manifestations of a single underlying force, and their wildly differing strengths at the electroweak scale ($\sim$ 250 GeV) would eventually unify to a common value at some higher energy scale. However, it is known that this unification does not occur within the Standard Model itself. Another technical problem is known as the *hierarchy problem*, and refers to the large gap between the electroweak scale and the Planck scale ($\sim 10^{19}$ GeV), which is the scale at which the effects of quantum gravity become important. The hierarchy problem is closely

related to the problem related to the Higgs boson mass, known as the *fine-tuning problem*. The Higgs boson mass is one of the free parameters of the Standard Model and has to be determined from experimental data. For the Standard Model theory to be consistent, the mass of the Higgs boson has to be of the order of the electroweak scale. At the same time, it is known that the radiative corrections from fermion loops to the Higgs mass are negative and quadratically divergent in energy. Since there is no symmetry within the Standard Model that would protect the Higgs boson mass from uncontrollably running[1] with energy, then if there is no new physics between the electroweak scale and the Planck scale, quantum corrections to the Higgs boson mass will be of the order of the Planck scale. Therefore, the bare Higgs boson mass also has to be of the order of the Planck scale, and an extraordinary level of fine-tuning (1 part in $\sim 10^{16}$) is needed for the bare mass and quantum correction to add up to the expected physical mass of the Higgs boson.

Although in excellent agreement with most experimental data, there are a few noticeable examples of SM predictions disagreeing with experimental observations. In its basic form, the Standard Model predicts massless neutrinos. However, the experimental observation of neutrino oscillations confirms that neutrinos have a small but non-zero mass. Another problem for the Standard Model is the experimental observation that about one quarter of the energy density of the Universe is accounted for by an invisible *dark matter*, and almost three quarter by *dark energy*, both revealing their presence through large-scale gravitational effects. The Stan-

[1]Since it can be shown that the values of measurable parameters, such as couplings and masses, depend on the amount of energy exchanged between the interacting particles, these parameters are often said to "run" with energy.

dard Model does not contain any viable dark matter particle candidates, and at the same time gives contributions to the dark energy that are far too large. The experimentally observed matter/antimatter asymmetry in the Universe presents yet another problem for the Standard Model, since the amount of CP violation present in the Standard Model is far too small to explain the observed asymmetry.

Because of the above-mentioned problems and limitations of the Standard Model, it is widely believed that the Standard Model is an effective low-energy remnant of a more fundamental theory at higher energies. Such theories that go beyond the Standard Model are a subject of an intense theoretical research. Since many BSM theories predict the scale of new physics to be $\mathcal{O}(1)$ TeV, it is believed that the LHC has a potential to open a window to a wide variety of new phenomena at the TeV scale. This is why the LHC is often called a *discovery machine*.

1.2 Dissertation Outline

This dissertation is organized as follows. The motivation for the leptoquark search as well as a brief overview of leptoquark phenomenology at hadron colliders is presented in Chapter 2. In Chapter 3, the LHC and the Compact Muon Solenoid (CMS) detector are described. A brief overview of the event reconstruction and the types of reconstructed objects employed in this search is given in Chapter 4. Chapter 5 is the main chapter describing the search strategy, the data samples used, the event selection employed, and the methods used to estimate the Standard Model backgrounds for this search. Chapter 5 also includes a discussion of systematic

uncertainties considered in the evaluation of the final results presented in Chapter 6. The dissertation is concluded in Chapter 7 with a short discussion of the final results and future prospects for this search.

Chapter 2

Leptoquark Phenomenology

One of the striking features of the Standard Model is the apparent symmetry between quarks and leptons. This symmetry manifests itself in the arrangement of quarks and leptons in weak isospin multiplets and in the fact that these multiplets are replicated for three different generations of fermions. It turns out that this symmetry is essential for achieving an exact cancellation of chiral (triangle) anomalies in each generation of fermions and preserving the renormalizability of the theory [5]. This cancellation also requires that quarks have exactly three color states. Therefore, the symmetry between quarks and leptons in the Standard Model could be a hint of a more fundamental theory in which quarks and leptons are related in some way. It is natural to expect that in such a theory there would exist new exotic particles called leptoquarks (LQs), coupling to lepton-quark pairs and mediating lepton-quark transitions.

Leptoquarks arise in many theories beyond the Standard Model. They are, however, not meant to be solutions to any of the specific limitations of the Standard Model mentioned in Chapter 1; they are simply a natural outcome of the BSM theories. A non-exhaustive list of such theories includes Grand Unified Theories (GUTs) based on the gauge groups SU(5) [6, 7], SO(10) [8, 9] with Pati-Salam SU(4) color symmetry [10, 11], and SU(15) [12, 13]); superstring-inspired E_6 models [14]; ex-

tended Technicolor models [15–17]; composite models [18, 19]; horizontal symmetry theories [20]; strongly coupled weak-interaction models [21]; and R-parity violating supersymmetric models [22, 23].

In all the models listed above, the leptoquarks are color triplets under $SU(3)_C$, appearing as scalar (spin-0) or vector (spin-1) bosons carrying both baryon (B) and lepton (L) number and fractional electric charge. Their exact properties, such as spin, weak isospin, electric charge, chirality of the fermion couplings, and fermion number ($F = 3B + L$), depend on the structure of each specific model. Because different models contain leptoquarks of many differing properties, direct searches for leptoquarks at collider experiments are typically carried out in the context of effective leptoquark models.

2.1 Buchmüller-Rückl-Wyler Effective Leptoquark Model

A general effective Lagrangian describing interactions of leptoquarks with Standard Model fermions was proposed by Buchmüller, Rückl, and Wyler [24]. In this effective Lagrangian, (a) leptoquarks are required to have dimensionless couplings to Standard Model lepton-quark pairs in order for their interactions to be renormalizable, (b) leptoquark interactions are required to be invariant under the Standard Model $SU(3)_C \times SU(2)_L \times U(1)_Y$ gauge groups, and (c) leptoquarks are allowed to couple only to Standard Model fermions and gauge bosons. Furthermore, to avoid inducing rapid proton decay, (d) leptoquark interactions with lepton-quark pairs are required to preserve baryon and lepton number separately. Such lepto-

quarks have a fermion number F of either $|F| = 0$ or 2. This effective Lagrangian in the so-called Aachen notation [25] has the following form [24]:

$$\mathcal{L} = \mathcal{L}_{|F|=2} + \mathcal{L}_{F=0}, \tag{2.1}$$

where

$$\begin{aligned}\mathcal{L}_{|F|=2} =&(g_{1L}\bar{q}_L^c i\tau_2 l_L + g_{1R}\bar{u}_R^c e_R)S_0 + \tilde{g}_{1R}\bar{d}_R^c e_R \tilde{S}_0 + g_{3L}\bar{q}_L^c i\tau_2 \vec{\tau} l_L \vec{S}_1 \\ &+ (g_{2L}\bar{d}_R^c \gamma^\mu l_L + g_{2R}\bar{q}_L^c \gamma^\mu e_R)V_{\frac{1}{2}\mu} + \tilde{g}_{2L}\bar{u}_R^c \gamma^\mu l_L \tilde{V}_{\frac{1}{2}\mu} + \text{h.c.},\end{aligned} \tag{2.1a}$$

and

$$\begin{aligned}\mathcal{L}_{F=0} =&(h_{2L}\bar{u}_R l_L + h_{2R}\bar{q}_L i\tau_2 e_R)S_{\frac{1}{2}} + \tilde{h}_{2L}\bar{d}_R l_L \tilde{S}_{\frac{1}{2}} \\ &+ (h_{1L}\bar{q}_L \gamma^\mu l_L + h_{1R}\bar{d}_R \gamma^\mu e_R)V_{0\mu} + \tilde{h}_{1R}\bar{u}_R \gamma^\mu e_R \tilde{V}_{0\mu} + h_{3L}\bar{q}_L \vec{\tau}\gamma^\mu l_L V_{1\mu} + \text{h.c.}\end{aligned} \tag{2.1b}$$

Here, S and V denote scalar and vector leptoquarks, respectively; q_L and l_L denote $\mathrm{SU}(2)_L$ left-handed quark and lepton doublets; e_R, u_R, and d_R denote the corresponding right-handed singlets for leptons, u- and d-type quarks; and τ_i are the Pauli matrices. The ψ^c represent the charge conjugate of the fermion fields and are defined as $\psi^c = C\bar{\psi}^T$, where C is the charge conjugation operator. The subscripts L and R of the coupling constants refer to the chirality of the coupled lepton. It is customary to use $\lambda_{L,R}$ to generically represent the Yukawa coupling constants $g_{iL,R}$ and $h_{iL,R}$. The indices of the leptoquark fields indicate their $\mathrm{SU}(2)_L$ isospin. For

simplicity, color, weak isospin, and generation (flavor) indices have been suppressed.

In general, the coupling constants in the effective Lagrangian in Equation 2.1 can be intergenerational and lead to possibly large tree-level flavor-changing neutral currents (FCNCs) and lepton flavor violation. Furthermore, S_0 and $S_{\frac{1}{2}}$ leptoquarks can mediate helicity-unsuppressed leptonic two-body pion decays, such as $\pi \rightarrow e\nu_e$. To evade the existing low-energy constraints from such processes [26, 27], two additional requirements on the original Buchmüller-Rückl-Wyler (BRW) effective model have to be imposed: (e) leptoquarks can only couple to a single lepton-quark generation i with $i = 1$, 2 or 3, i.e., $\lambda^i \times \lambda^j \simeq 0$ for $i \neq j$, resulting in the standard nomenclature of first-, second-, and third-generation leptoquarks; and (f) leptoquarks are required to have purely chiral couplings to lepton-quark pairs, i.e., $\lambda_L \times \lambda_R \simeq 0$. The BRW model with these two additional requirements will be referred to as the minimal Buchmüller-Rückl-Wyler (mBRW) model. It should be noted, however, that leptoquarks are not required to couple to the same generation of leptons and quarks, as is traditionally assumed by the requirement (e); what is required is that leptoquarks do not couple to more than one generation of leptons and quarks (e.g., a given leptoquark could in principle couple to the first-generation leptons and second-generation quarks). In total, the mBRW model defines fourteen different types of leptoquarks; seven scalar leptoquarks with $|F| = 2$ ($S_{0,L}$, $S_{0,R}$, $\tilde{S}_{0,R}$, $S_{1,L}$) or $F = 0$ ($S_{\frac{1}{2},L}$, $S_{\frac{1}{2},R}$, $\tilde{S}_{\frac{1}{2},L}$), and seven vector leptoquarks with $|F| = 2$ ($V_{\frac{1}{2},L}$, $V_{\frac{1}{2},R}$, $\tilde{V}_{\frac{1}{2},L}$) or $F = 0$ ($V_{0,L}$, $V_{0,R}$, $\tilde{V}_{0,R}$, $V_{1,L}$). By convention, leptoquarks are distinguished by the chirality (L, R index) of the coupled lepton. A tilde is used to differentiate between leptoquarks that differ by two units of the weak hypercharge.

All fourteen leptoquarks along with their quantum numbers and possible decay modes are listed in Table 2.1. Leptoquarks with $F = 2$ decay to lepton-quarks pairs and those with $F = 0$ decay to lepton-antiquark pairs. In experimental searches, mass degeneracy within each isospin family is generally assumed [27, 28]. Therefore, the same symbol represents any of the leptoquark states within a family, regardless of their electric charge (e.g., the $S_{\frac{1}{2},L}$ represents scalar leptoquark states with electric charge of either $-5/3$ or $-2/3$ coupling to left-handed leptons).

Table 2.1: Leptoquark types, and their quantum numbers and decay modes, in the minimal Buchmüller-Rückl-Wyler model.

Scalar (spin-0) leptoquarks					Vector (spin-1) leptoquarks				
LQ type	Q	T_3	F	Decay mode	LQ type	Q	T_3	F	Decay mode
$S_{0,L}$	$-1/3$	0	2	$e_L u_L$, $\nu_L d_L$	$V_{0,L}$	$-2/3$	0	0	$e_L \bar{d}_R$, $\nu_L \bar{u}_L$
$S_{0,R}$	$-1/3$	0	2	$e_R u_R$	$V_{0,R}$	$-2/3$	0	0	$e_R \bar{d}_L$
$\tilde{S}_{0,R}$	$-4/3$	0	2	$e_R d_R$	$\tilde{V}_{0,R}$	$-5/3$	0	0	$e_R \bar{u}_L$
$S_{\frac{1}{2},L}$	$-5/3$	$-1/2$	0	$e_L \bar{u}_L$	$V_{\frac{1}{2},L}$	$-4/3$	$-1/2$	2	$e_L d_R$
	$-2/3$	$+1/2$	0	$\nu_L \bar{u}_L$		$-1/3$	$+1/2$	2	$\nu_L d_R$
$S_{\frac{1}{2},R}$	$-5/3$	$-1/2$	0	$e_R \bar{u}_R$	$V_{\frac{1}{2},R}$	$-4/3$	$-1/2$	2	$e_R d_L$
	$-2/3$	$+1/2$	0	$e_R \bar{d}_R$		$-1/3$	$+1/2$	2	$e_R u_L$
$\tilde{S}_{\frac{1}{2},L}$	$-2/3$	$-1/2$	0	$e_L \bar{d}_L$	$\tilde{V}_{\frac{1}{2},L}$	$-1/3$	$-1/2$	2	$e_L u_R$
	$+1/3$	$+1/2$	0	$\nu_L \bar{d}_L$		$+2/3$	$+1/2$	2	$\nu_L u_R$
$S_{1,L}$	$-4/3$	-1	2	$e_L d_L$	$V_{1,L}$	$-5/3$	-1	0	$e_L \bar{u}_R$
	$-1/3$	0	2	$e_L u_L$, $\nu_L d_L$		$-2/3$	0	0	$e_L, \bar{d}_R$, $\nu_L \bar{u}_R$
	$+2/3$	$+1$	2	$\nu_L u_L$		$+1/3$	$+1$	0	$\nu_L, \bar{d}_R$

A particular BSM model containing leptoquarks, typically only contains a

subset of the leptoquark types in the mBRW model. For example, a weak isospin singlet scalar leptoquark $S_{1,L(R)}$ appears in superstring-inspired E_6 models [14], a weak isospin doublet of scalar leptoquarks anti-$\tilde{S}_{\frac{1}{2},L}$ appears in a refined SU(5) model [7], and a weak isospin singlet vector leptoquark $V_{0,L(R)}$ appears in the Pati-Salam GUT model [10, 11]. However, all fourteen leptoquark types of the mBRW model appear in the GUT theory based on the SU(15) gauge group [12, 13].

2.2 Leptoquark Production in Proton-Proton Collisions

The scalar leptoquarks described by the effective Lagrangian in Equation 2.1 have their representations under the Standard Model gauge groups, and hence their couplings to the gauge bosons, fully specified. However, vector leptoquarks could be a low-energy manifestation of a more fundamental theory at higher energy scales, and so their couplings to gauge bosons can be supplemented by anomalous couplings specified by two parameters κ_A and λ_A, where $A = \gamma$, g, $W^{\pm}$, or Z [29–31]. The anomalous coupling parameters κ_A and λ_A are assumed to be real and independent, and are related to anomalous trilinear $A\mathrm{LQ}\overline{\mathrm{LQ}}$ and quartic $AA\mathrm{LQ}\overline{\mathrm{LQ}}$ couplings.

In pp collisions, leptoquarks can be directly produced either singly or in pairs. At leading order (LO) in α_s, single leptoquark production in association with a lepton proceeds through quark-gluon scattering and depends on the unknown Yukawa coupling λ. The LO Feynman diagrams for the single leptoquark production in pp collisions are shown in Figure 2.1. Since leptoquarks are SU(3) color triplets, pair production occurs mostly via the strong interaction, via $q\bar{q}$ annihilation and

gg fusion processes. A general effective Lagrangian describing the interaction of leptoquarks with gluons can be found in Reference [31]. The LO Feynman diagrams for pair production of leptoquarks in pp collisions are shown in Figure 2.2. Stringent bounds from low-energy precision experiments require the Yukawa coupling λ to be smaller than the electromagnetic coupling $\lambda_{\mathrm{em}} = \sqrt{4\pi\alpha_{\mathrm{em}}} \approx 0.3$ for leptoquark masses $M_{\mathrm{LQ}} \lesssim 1$ TeV for most leptoquark types [28, 32]. Hence, for leptoquark masses accessible at the LHC ($M_{\mathrm{LQ}} \lesssim 1.2$–$1.5$ TeV) [33], pair production is the dominant direct production mechanism and is essentially independent of the Yukawa coupling λ. This also implies that the pair-production cross section for scalar leptoquarks depends only on the leptoquark mass. The production cross section is generally larger for vector leptoquarks, but can vary by one or two orders of magnitude depending on the specific choice of the anomalus coupling parameters κ_g and λ_g [31, 33]. The relative contributions of $q\bar{q}$ annihilation and gg fusion processes depend on the leptoquark mass. For leptoquark masses accessible at the LHC, the gg fusion process is the dominant contribution. Due to the fact that pair production proceeds via the strong interaction, leptoquarks of all three generations can be produced. Furthermore, the pair-production cross section for scalar leptoquarks is essentially model independent.

The total cross section for the pair production of first- or second-generation scalar leptoquarks in pp collisions at $\sqrt{s} = 7$ TeV as a function of the leptoquark mass, including next-to-leading order (NLO) QCD corrections [34], is shown in Figure 2.3. The relatively large cross section lead to the expectation that light leptoquarks, if they exist, could be discovered in the early LHC data.

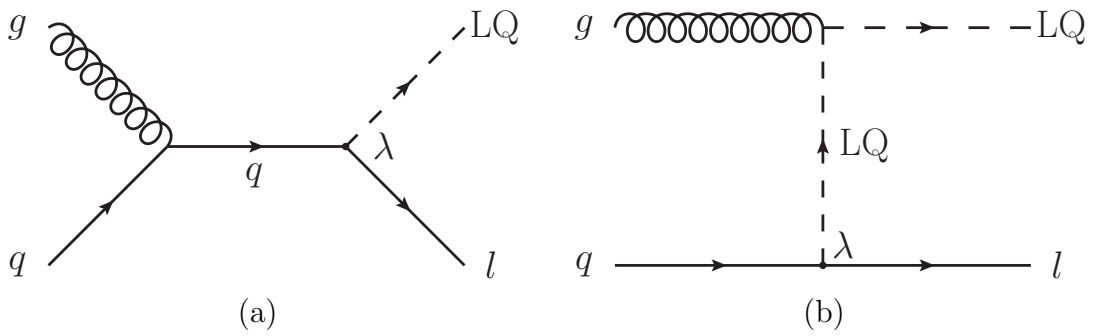

Figure 2.1: LO Feynman diagrams for single leptoquark production in association with a lepton in pp collisions.

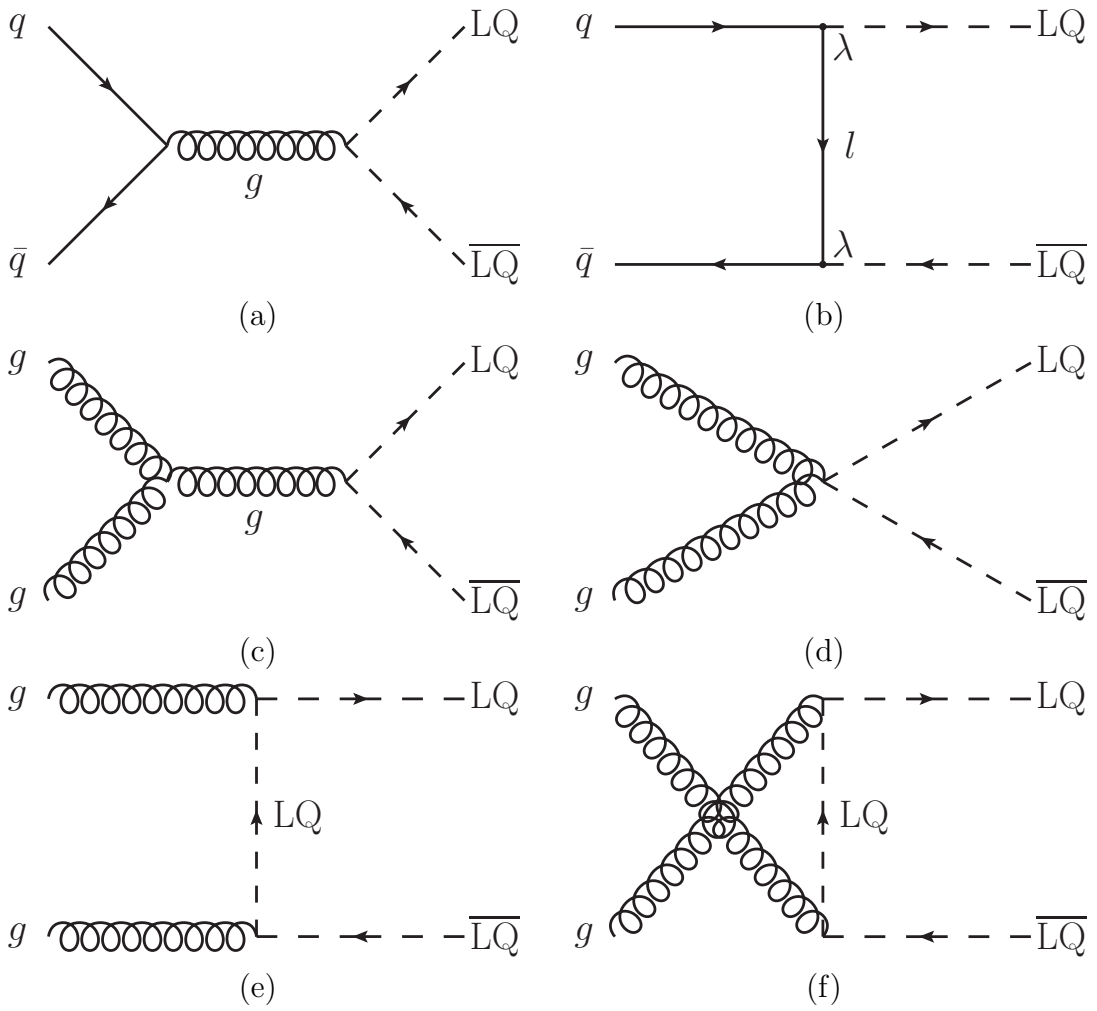

Figure 2.2: LO Feynman diagrams for leptoquark pair production in pp collisions.

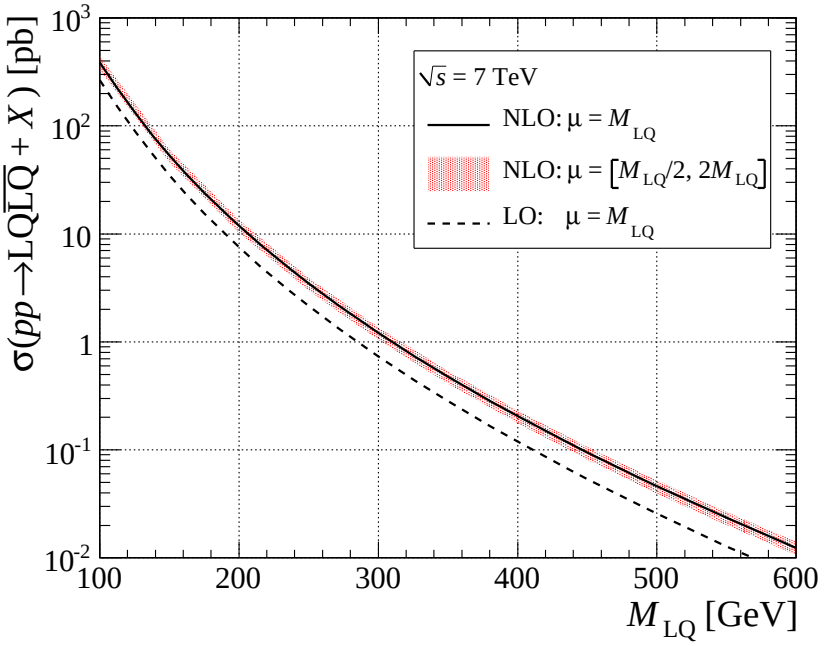

Figure 2.3: Total cross section for $pp \to \mathrm{LQ}\overline{\mathrm{LQ}} + X$ at $\sqrt{s} = 7$ TeV including next-to-leading order (NLO) QCD corrections [34] as a function of the leptoquark mass M_{LQ}. The CTEQ6L1 [35] LO and CTEQ6.6 [36] NLO parton distribution functions (PDFs) were used to calculate the LO and NLO cross section, respectively. The variation in the NLO cross section when varying the renormalization/factorization scale between $\mu = M_{\mathrm{LQ}}/2$ and $\mu = 2M_{\mathrm{LQ}}$ is indicated by the shaded band around the nominal value obtained using $\mu = M_{\mathrm{LQ}}$.

2.3 Leptoquark Decays

Leptoquarks decay to a lepton-quark pair with total decay widths [24, 33]

$$\Gamma_{J=0} = \sum_i \frac{\lambda_i^2}{16\pi} M_{\mathrm{LQ}}, \tag{2.2}$$

and

$$\Gamma_{J=1} = \sum_i \frac{\lambda_i^2}{24\pi} M_{\mathrm{LQ}}, \tag{2.3}$$

where J denotes the leptoquark spin, and the sums extend over all possible leptoquark decay modes. QCD corrections to these widths are very small [37]. For a scalar (vector) leptoquark with a mass of 1 TeV and a single decay mode with $\lambda = 0.3$, Equation 2.2 (2.3) results in a total decay width of approximately 1.8 (1.2) GeV. Hence, leptoquark states are expected to have a fairly narrow width, well below experimental resolutions.

Depending on the type, leptoquarks can decay either to a charged lepton and a quark or to a neutrino and a quark. It is customary to denote the branching ratio to a charged lepton and a quark, $\mathrm{BR}(\mathrm{LQ} \to l^{\pm} q)$, as β. In the mBRW model, β is required to be either 0, 1/2, or 1, as can be seen from Table 2.1. In more general approaches, typically employed in experimental collider searches, β is treated as a free parameter. Having β as a free parameter is possible if some of the assumptions of the mBRW model are relaxed [38–40] and leptoquarks are, for example, allowed to couple to fields other than the SM gauge bosons and fermions. Nevertheless, in experimental collider searches, it is generally assumed that the branching ratio to a

neutrino and a quark, BR(LQ $\rightarrow \nu q$), equals $(1-\beta)$.

In this search, we focus on the pair production of first-generation scalar leptoquarks. Three different final states are possible: (1) two electrons[1] and two quarks in the final state, with a branching ratio of β^2; (2) an electron, a neutrino, and two quarks in the final state, with a branching ratio of $2\beta(1-\beta)$; and (3) two neutrinos and two quarks in the final state, with a branching ratio of $(1-\beta)^2$. All three possible final states and their corresponding branching ratios are shown in Figure 2.4. From the point of view of an experimentalist, these final states result in three distinct experimental signatures: (1) two electrons and two jets ($eejj$ channel); (2) one electron, two jets, and missing transverse energy ($e\nu jj$ channel); and (3) two jets and missing transverse energy ($\nu\nu jj$ channel).

In this dissertation, we consider pair production of leptoquarks where λ is large enough that the leptoquarks decay promptly. From Equations 2.2 and 2.3, if the Yukawa coupling λ is very small, leptoquark states become very narrow (long-lived), and so the above signatures are only valid when the Yukawa coupling λ is large enough to allow leptoquarks to decay inside the detector volume (for a scalar leptoquark with $M_{\mathrm{LQ}} = 300$ GeV and 7 TeV of total energy, λ has to be $\gtrsim 3 \times 10^{-8}$ for the decay length to be $\lesssim 1$ m). Proton-proton collisions are therefore well suited for a model- and generation-independent search for the pair production of leptoquarks in a wide range of possible values of the Yukawa coupling λ.

[1]Unless stated otherwise, the term "electron" refers generically to both electrons and positrons

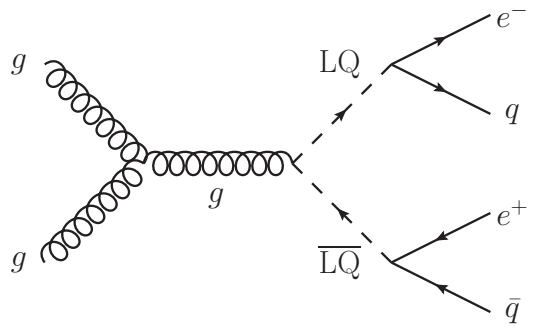

$\text{BR}(\text{LQ}\overline{\text{LQ}} \to e^- q e^+ \bar{q}) = \beta^2$

(1) $eejj$ channel

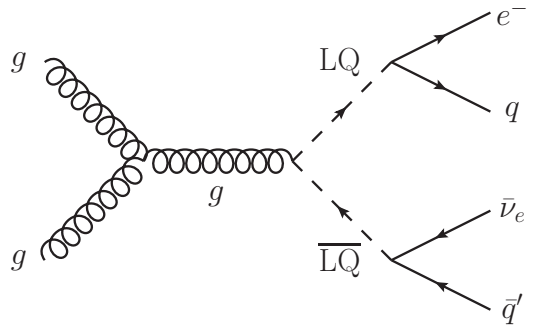

$\text{BR}(\text{LQ}\overline{\text{LQ}} \to e^- q \bar{\nu}_e \bar{q}', \nu_e q' e^+ \bar{q}) = 2\beta(1-\beta)$

(2) $e\nu jj$ channel

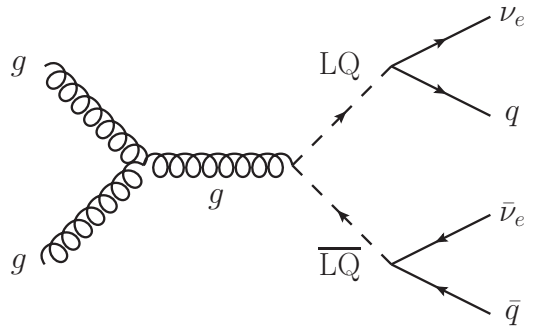

$\text{BR}(\text{LQ}\overline{\text{LQ}} \to \nu_e q \bar{\nu}_e \bar{q}) = (1-\beta)^2$

(3) $\nu\nu jj$ channel

Figure 2.4: Possible final states for a decay of a pair of first-generation scalar leptoquarks. q (q') denotes either u or d quark.

2.4 Current Limits from Experiments Other than CMS

Experimental limits on the leptoquark states can be grouped into two categories: (i) indirect limits, coming from bounds on leptoquark-induced four-fermion interactions in low-energy precision experiments or in collider experiments below the direct production threshold; and (ii) direct limits, coming from the direct production in collider experiments.

Indirect limits on the leptoquark states are typically expressed in terms of a lower bound on the M_{LQ}/λ ratio. The most stringent indirect limits on M_{LQ}/λ come from measurements of atomic parity violation (APV) and from the universality of leptonic π decays, and are in the TeV range for all first-generation leptoquark types [28]. For a detailed review of indirect limits on the leptoquark states, the reader is referred to [4, 26, 27, 41–43]. In the remainder of this section, a brief overview of the most recent direct limits on the production of first-generation scalar leptoquarks is given.

Direct searches for single and pair production of leptoquarks are performed at collider experiments. Searches for single and pair production of first-generation scalar leptoquarks have been performed at the e^+e^- LEP collider [44–49], but result in model-dependent limits (and in the case of single production, λ-dependent limits as well), since the production cross section depends on the leptoquark $\mathrm{SU}(2)_L \times \mathrm{U}(1)_Y$ quantum numbers. Searches for single production of first-generation scalar leptoquarks have also been performed at the $e^{\pm}p$ HERA collider [50–52], yielding model- and λ-dependent limits, since in these experiments the production cross section di-

rectly depends on the Yukawa coupling λ. Before the start of LHC operation, the most stringent direct limit on the mass of a first-generation scalar leptoquark was set by the D0 collaboration at the $p\bar{p}$ Tevatron collider. Figure 2.5 shows the D0 mass limits in the β versus M_{LQ} plane using 1 fb^{-1} of $p\bar{p}$ collision data [53]. The observed D0 limits on the leptoquark mass at 95% confidence level (CL) are 235, 284, and 299 GeV for β values of 0.1, 0.5, and 1, respectively. Recently, the ATLAS collaboration at the LHC and the D0 collaboration have obtained mass limits on the first-generation scalar leptoquarks which exceed the previous D0 limits. Figure 2.6 shows the ATLAS mass limits in the β versus M_{LQ} plane using 35 pb^{-1} of pp collision data [54]. The observed ATLAS limits on the leptoquark mass at 95% CL are 319 and 376 GeV for β values of 0.5 and 1, respectively. Figure 2.7 shows the most recent D0 mass limits in the β versus M_{LQ} plane using 5.4 fb^{-1} of $p\bar{p}$ collision data [55]. The observed D0 limit on the leptoquark mass at 95% CL is 326 GeV for β of 0.5.

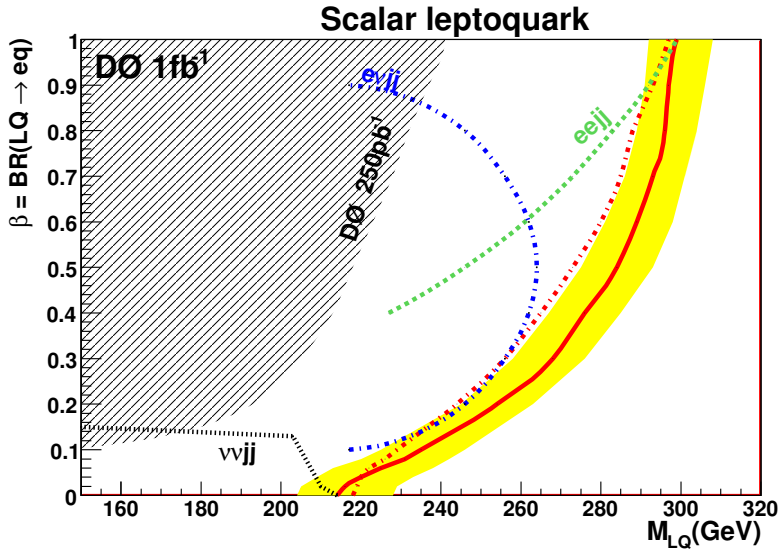

Figure 2.5: Observed (red solid line) and expected (red dot-dashed line) D0 mass limits at 95% CL in the β versus $M_{\rm LQ}$ plane for the pair production of first-generation scalar leptoquarks and the nominal hypothesis for the signal cross section ($\mu = M_{\rm LQ}$) using 1 fb^{-1} of $p\bar{p}$ collision data [53]. The regions to the left of the curves are excluded. The observed limits found individually using each of the three final states are shown for the nominal cross-section hypothesis ($\mu = M_{\rm LQ}$), and the hatched area indicates the part of the plane previously excluded by the D0 collaboration with a lower integrated luminosity of 250 pb^{-1} and for the minimal cross-section hypothesis ($\mu = 2M_{\rm LQ}$).

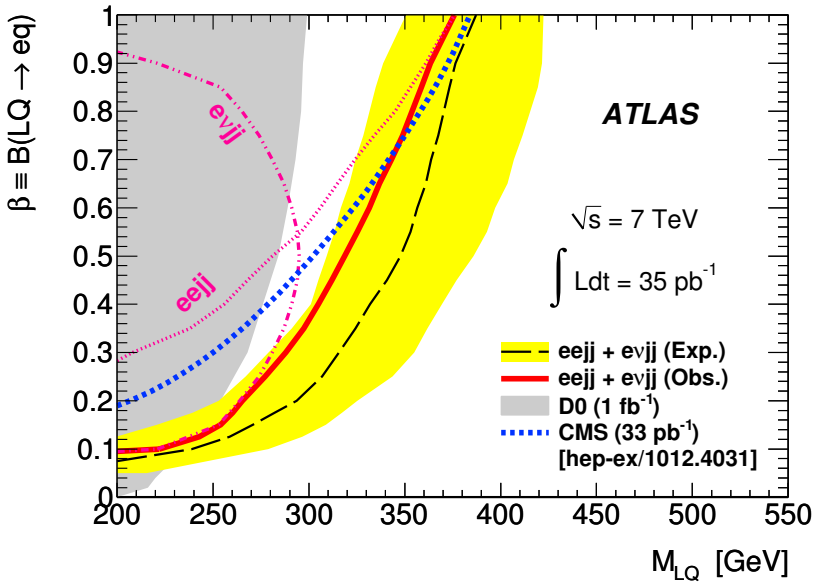

Figure 2.6: ATLAS 95% CL exclusion region in the β versus M_{LQ} plane obtained from the combination of the $eejj$ and $e\nu jj$ channels using 35 pb^{-1} of pp collision data [54]. The gray area indicates the D0 exclusion limit with 1 fb^{-1} of $p\bar{p}$ collision data [53], and the thick dotted line indicates the CMS exclusion in the $eejj$ channel only using 33 pb^{-1} of pp collision data [56]. The dotted and dot-dashed lines show the individual limits for the $eejj$ and $e\nu jj$ channels, respectively. The combined expected limit is indicated by the thick dashed line. The combined observed limit is indicated by the solid line.

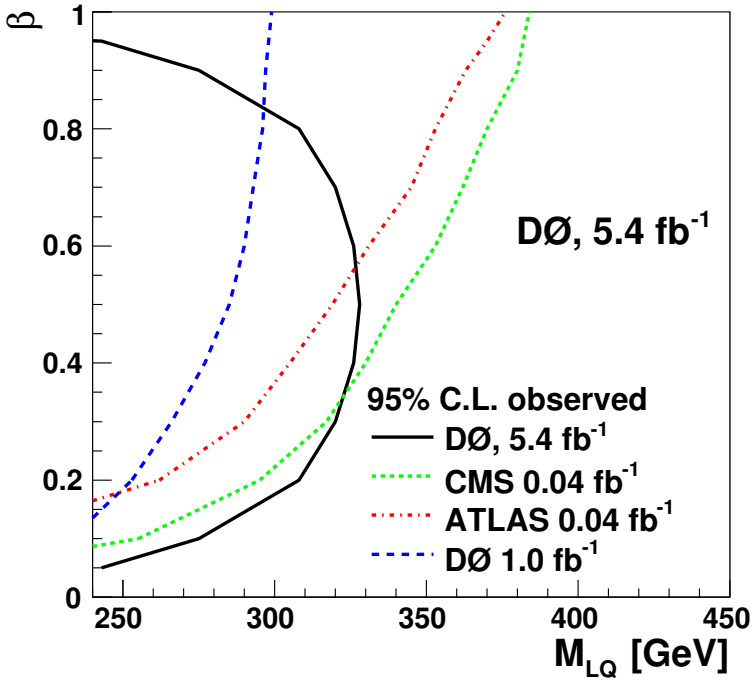

Figure 2.7: 95% CL observed limit for $\mu = M_{\mathrm{LQ}}$ on the leptoquark mass as a function of β obtained in the $e\nu jj$ channel using 5.4 fb^{-1} of $p\bar{p}$ collision data [55]. The limit is compared with the previous D0 result [53], and CMS [56, 57] and ATLAS [54] results.

Chapter 3

Experimental Apparatus

3.1 The Large Hadron Collider

The Large Hadron Collider is the world's highest-energy particle accelerator. It was installed inside the existing 26.7 km tunnel constructed between 1984 and 1989 for the CERN LEP collider [58]. The tunnel itself lies between 45 and 170 m underground just outside Geneva, Switzerland. The LHC is a two-ring superconducting synchrotron designed to accelerate and collide proton beams at a center-of-mass energy of 14 TeV and instantaneous luminosity of 10^{34} $\mathrm{cm}^{-2}\mathrm{s}^{-1}$. It is also capable of colliding heavy-ion (in this case lead nuclei) beams at an energy of 2.76 TeV per nucleon and peak instantaneous luminosity of 10^{27} $\mathrm{cm}^{-2}\mathrm{s}^{-1}$. Unless stated otherwise, the information presented in this section is taken from References [59–62].

The high instantaneous luminosity mandated by the LHC design excludes the use of antiproton beams and consequently excludes the proton-antiproton collider configuration. Hence, the LHC had to be designed as a proton-proton collider, with two counter-rotating proton beams requiring separate and opposite magnetic dipole fields to steer the beams around the accelerator ring. Due to the limited space available, it is not possible to install two completely separate proton rings in the existing LHC/LEP tunnel. This limitation lead to the adoption of a twin-bore magnet design. The peak beam energy is limited by the strength of the magnetic

dipole field. The LHC superconducting cryodipole magnets, shown in Figure 3.1, were designed to provide a magnetic field of 0.54 to 8.33 T, corresponding to proton energies from 450 GeV to 7 TeV.

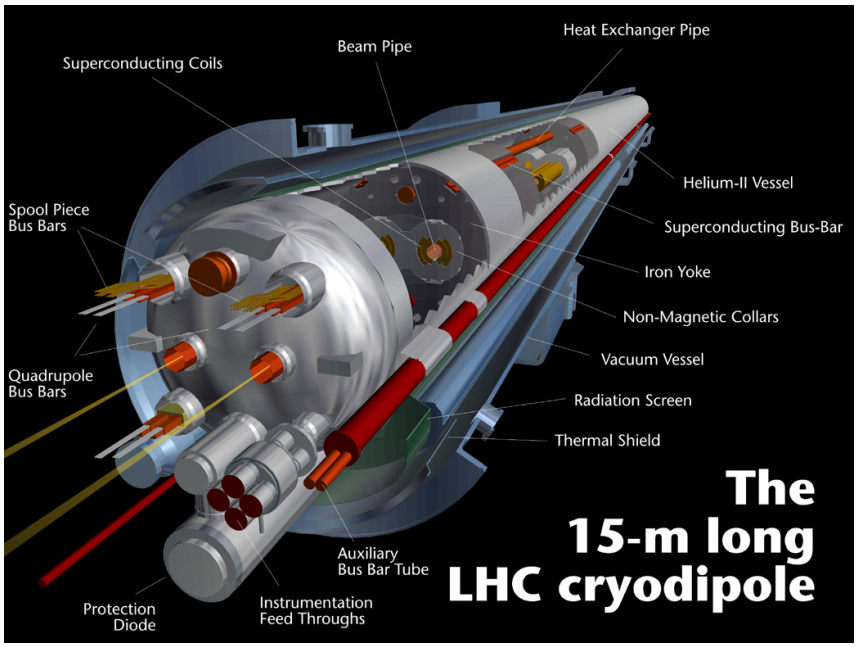

Figure 3.1: LHC cryodipole magnet and its main components (from [63]). The LHC ring accommodates 1232 such dipole magnets all of which have to be cooled down to 1.9 K for normal operation.

The LHC ring consists of eight straight sections and eight arcs. The straight sections are each approximately 528 m long and can serve as experimental or utility insertions. Figure 3.2 depicts a schematic layout of the LHC ring. Experimental insertions at Points 2 and 8 include the beam injection system for Beam 1 and Beam 2, respectively. Two high-luminosity general purpose detectors are located within two diametrically-opposite straight sections; ATLAS [64] at Point 1 and CMS [65] at Point 5. Two lower-luminosity experiments are located in experimental insertions at Point 2 and 8: ALICE [66], a dedicated heavy ion detector, at Point 2; and LHCb [67], a dedicated B-physics detector, at Point 8. At the locations of the four

detectors, the beams cross from one magnet bore to the other. In the remaining four straight sections, the beams do not cross. Insertions at Points 3 and 7 each contain two collimation systems, and the insertion at Point 4 contains two radio frequency (RF) systems, one for each LHC beam. The insertion at Point 6 contains the beam dump system. Each beam features an independent abort system. The LHC beams are steered by separate magnetic fields and are confined in separate vacuum chambers in the main arcs, and share an approximately 130 m long common section in the experimental detector regions. The LHC is divided into eight independent sectors, each having the arc between two consecutive straight sections at its center.

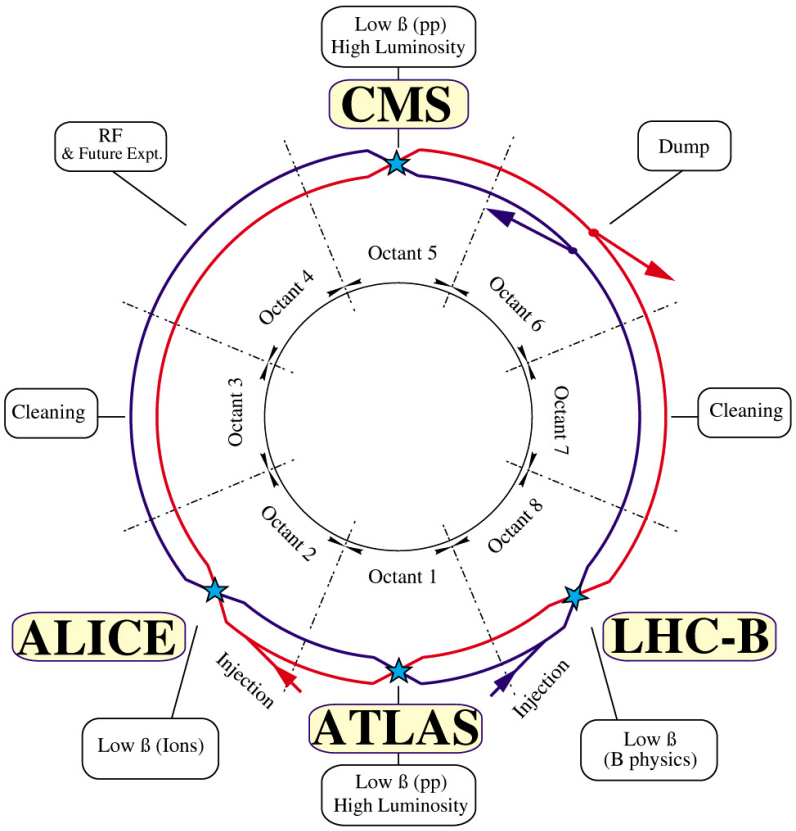

Figure 3.2: Schematic layout of the LHC ring (from [63]). In this view, Beam 1 revolves clockwise and Beam 2 anticlockwise.

The existing CERN accelerator complex serves as the LHC injector, as shown

in Figure 3.3. The role of the accelerator chain shown in Figure 3.3 is to form proton bunches, accelerate them in stages to 450 GeV, and finally inject them into the main LHC ring. Protons are produced in a duoplasmatron source, injected into a linear accelerator (Linac2), and accelerated to 50 MeV. Protons are then injected into the Proton Synchrotron Booster (PSB), where they are accelerated to 1.4 GeV. The PSB consists of four independent synchrotron rings, 1/4 of the Proton Synchrotron (PS) circumference each, which operate on the first harmonic of the natural wavelength of the radio-frequency (RF) acceleration system (harmonic $h = 1$). For the generation of the 25-ns bunch trains, a multiple splitting scheme is used. Six PSB bunches (two batches of $3 + 3$ or $4 + 2$ bunches) are captured on harmonic $h = 7$ in the PS, as shown in Figure 3.4. The bunches are then split into three smaller bunches and accelerated on harmonic $h = 21$ to 25 MeV. Each of the smaller bunches is further split into four, as illustrated in Figure 3.5. Hence, each of the initial six bunches has been split into 12 bunches, resulting in a final bunch train containing 72 filled and 12 empty bunches on RF harmonic $h = 84$. The twelve empty bunches provide a gap for the rise-time of the ejection kicker.

In the next stage, proton bunches are injected into the Super Proton Synchrotron (SPS) and accelerated to 450 GeV, the injection energy for the main LHC ring. Finally, proton bunches are injected into the main LHC ring through two transfer lines, one per LHC beam, which connect the main LHC ring with the rest of the CERN accelerator complex. The nominal PS-SPS-LHC filling sequence and the final 25-ns bunch structure of the LHC beam are shown in Figure 3.6. Gaps in the bunch structure of the LHC beam are necessary to accommodate the rise time

of the injection and ejection kickers. These gaps are also used for synchronization, acquiring calibration data, and providing resets to front-end electronics, as well as for searches for exotic new physics.

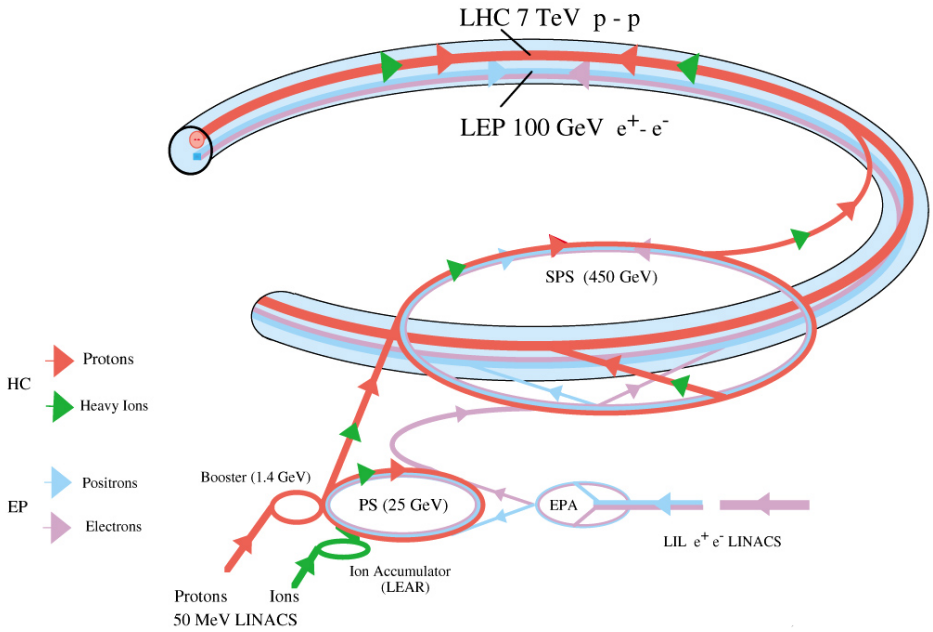

Figure 3.3: LHC injector complex (from [63]).

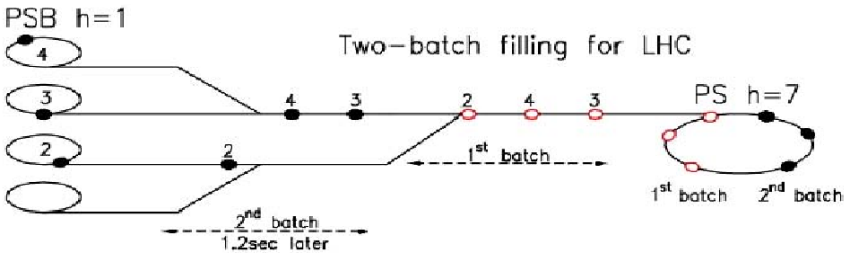

Figure 3.4: PSB-PS transfer with two-batch filling scheme for the LHC.

One of the primary goals of the LHC is to search for new physics beyond the Standard Model. This typically implies detecting events with very small production cross sections. The relation between the number of events produced in particle

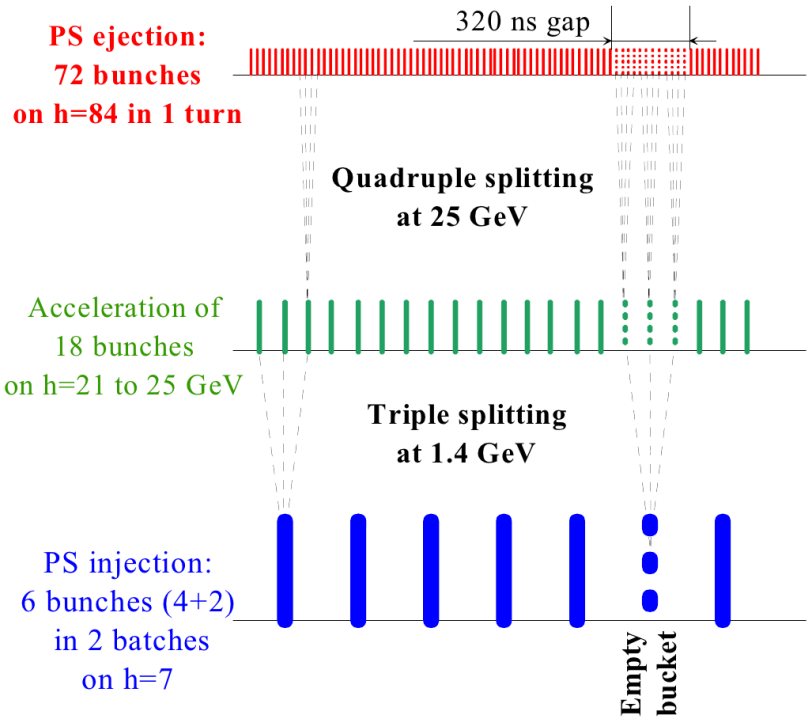

Figure 3.5: Generation of the nominal 25-ns bunch train in the PS complex.

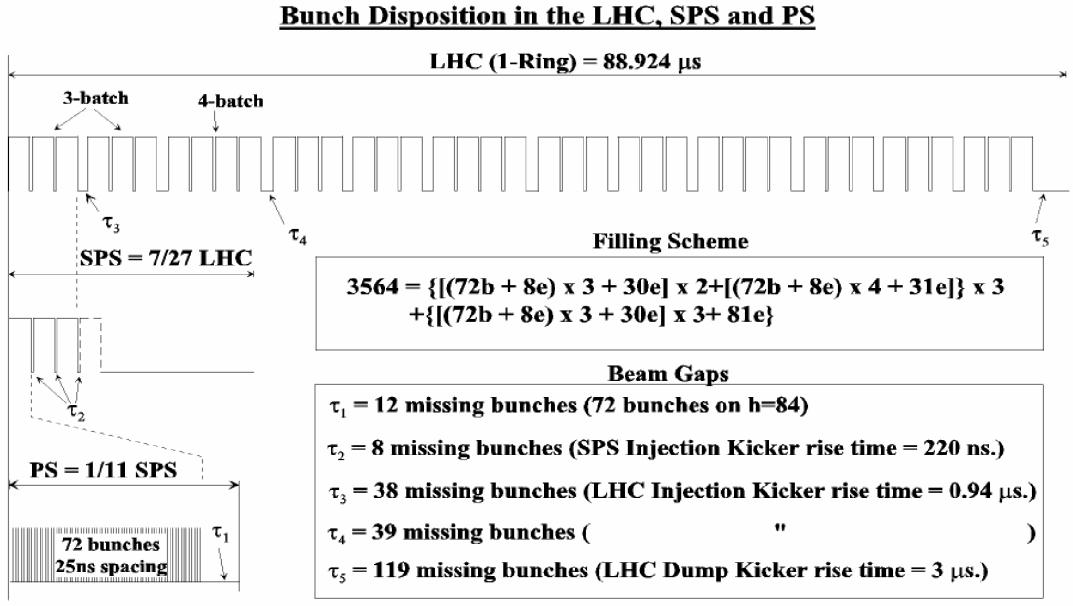

Figure 3.6: Nominal PS-SPS-LHC filling sequence and the final 25-ns bunch structure of the LHC beam.

collisions and the production cross section is:

$$N_{\text{event}} = \int \sigma_{\text{event}} \mathcal{L} dt, \tag{3.1}$$

where N_{event} is the number of produced events, σ_{event} is the production cross section for the events under study, and $\mathcal{L}$ is the instantaneous luminosity of the two colliding beams. The instantaneous luminosity depends only on the beam parameters. For a Gaussian beam distribution this dependence can be written as:

$$\mathcal{L} = \frac{N_b^2 n_b f_{\text{rev}} \gamma_r}{4\pi \varepsilon_n \beta^*} F, \tag{3.2}$$

where N_b is the number of particles per bunch, n_b the number of bunches per beam, f_{rev} the revolution frequency, γ_r the relativistic gamma factor, ε_n the normalized transverse beam emittance, β^* the beta function at the interaction point (IP). The parameter F represents the geometric luminosity reduction factor due to the crossing angle at the interaction point:

$$F = \left(1 + \frac{\theta_c \sigma_z}{2\sigma^*}\right)^{-\frac{1}{2}}, \tag{3.3}$$

where θ_c is the full crossing angle at the interaction point, σ_z is the RMS bunch length, and σ^* is the transverse RMS beam size at the interaction point. The above expression assumes round transverse beam profiles, with $\sigma_z \ll \beta$, and with equal beam parameters for both beams.

Since production cross sections typically increasing with energy, for an efficient

search for new physics, the LHC beams are required to have both high energy and high intensity. Table 3.1 lists the design LHC beam parameters. With a design beam current of 0.582 A, the total energy stored per LHC beam is approximately 362 MJ. If the electromagnetic energy stored in the LHC magnet systems, corresponding to approximately 600 MJ, is included, the total energy stored in the LHC ring exceeds 1 GJ. All of this energy has to be absorbed safely at the end of each fill or in the case of a malfunction or emergency. The beam dump system and the magnet system therefore impose an upper limit on the maximum attainable beam energies and intensities.

Table 3.1: The design LHC beam parameters.

Parameter	Unit	Nominal design value
Proton energy	GeV	7000
γ_r		7461
N_b		1.15×10^{11}
n_b		2808
ε_n	μm rad	3.75
β	m	0.55
f_{rev}	kHz	11.245
Circulating beam current	A	0.582
Stored energy per beam	MJ	362
σ_z	cm	7.55
σ^*	μm	16.7
θ_c	μrad	285
F		0.836
$\mathcal{L}$	$\text{cm}^{-2}\text{s}^{-1}$	1.0×10^{34}

The LHC project was approved by the CERN Council in December 1994. In 2000, the LEP was closed to liberate the tunnel for the LHC. In June 2007, an

announcement was made for delayed LHC start-up, scheduled for May 2008 [68]. On September 10 2008, the first proton beam was successfully steered around the entire LHC ring [69]. Nine days after the first circulating beams, an incident occurred due to a faulty electrical connection between two of the accelerator's magnets, resulting in a large helium leak and serious mechanical damage of the LHC systems [70, 71]. In August 2009, while the LHC was still being repaired, it was announced that the LHC operations would restart with proton beams at half of the nominal energy, 3.5 TeV, to gain experience of running the machine safely and minimize the risk of a repeated incident [72]. In November 2009, proton beams were back in the LHC [73] and the first collisions at the injection energy of 450 GeV were achieved [74]. On March 19, 2010 beams were successfully accelerated to 3.5 TeV [75] and on March 30, 2010 the first proton-proton collisions at the center-of-mass energy of 7 TeV were delivered [76], marking the start of the LHC physics program. Proton-proton collisions at 7 TeV continued, with a gradual increase in the number of bunches and instantaneous luminosity, until November 2010, when the LHC switched to heavy-ion collisions [77]. By the end of the 2010 proton run, 368 bunches per beam, with a bunch spacing of 150 ns, and an instantaneous luminosity of 2.07×10^{32} $\mathrm{cm}^{-2}\mathrm{s}^{-1}$ were reached, and a total of close to 50 pb^{-1} of collision data were delivered. Figure 3.7 shows the maximum instantaneous luminosity per day and the total integrated luminosity per day for the 2010 run. The current plan is to use the next long maintenance shutdown, scheduled to start at the end of 2012 and expected to finish in the first half of 2014, to complete the repairs and consolidation work needed to reach a design energy of 14 TeV [78].

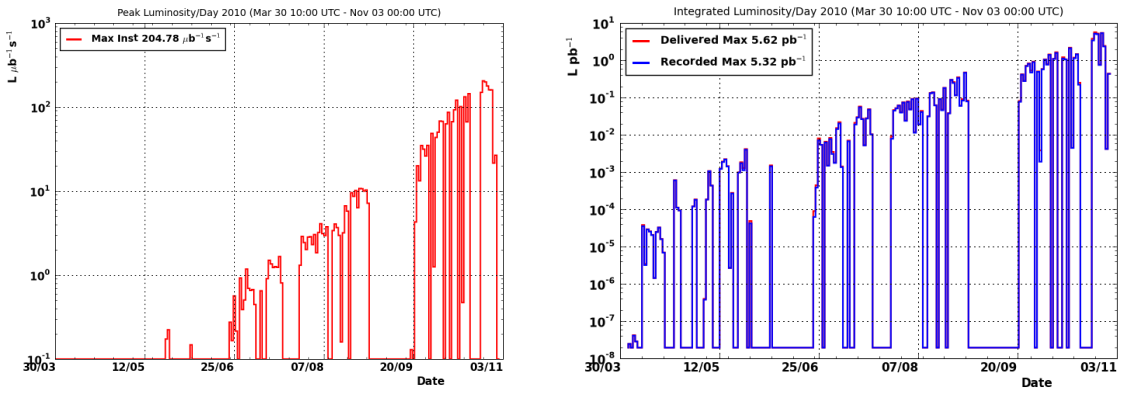

Figure 3.7: The maximum instantaneous luminosity per day (left panel) and the total integrated luminosity per day (right panel) for the 2010 run.

3.2 The Compact Muon Solenoid Detector

The Compact Muon Solenoid detector is a high-luminosity general purpose detector installed inside an experimental cavern located about 100 m underground at Point 5 of the main LHC ring. The total inelastic proton-proton cross section at $\sqrt{s} = 14$ TeV is expected to be roughly 100 mb (1 b $= 10^{-28}$ m^2 $= 10^{-24}$ cm^2), resulting in a rate of approximately 10^9 inelastic collisions/s at the LHC design luminosity. With the 25-ns bunch spacing, this corresponds to a mean of about 20 inelastic collisions per crossing leading to roughly 1000 particles emerging from the interaction point every 25 ns. These conditions have important implications on the design of the CMS detector and its trigger and readout systems, requiring high granularity, fast response time, and radiation-hard detector components and electronics.

CMS uses a right-handed coordinate system, with the origin at the nominal interaction point in the center of the CMS detector, the x-axis pointing radially

inward toward the centre of the LHC, the y-axis pointing vertically upward (perpendicular to the LHC plane), and the z-axis pointing along the anticlockwise-beam direction (Beam 2 direction). The azimuthal angle ϕ is measured from the x-axis in the x-y plane and the radial coordinate in this plane is denoted by r. The polar angle θ is measured from the positive z-axis. Pseudorapidity is defined as $\eta = -\ln[\tan(\theta/2)]$. The momentum transverse to the beam direction, denoted by p_{T}, is therefore computed from the x and y components. The vector momentum imbalance in the transverse plane is known as the missing transverse momentum, and is denoted by $\vec{\not{E}}_{\mathrm{T}}$. Its magnitude is called missing transverse energy (MET), and is denoted by $\not{E}_{\mathrm{T}}$.

The overall layout of the CMS detector is shown in Figure 3.8. The central feature of the CMS detector in a 13 m long, 6 m inner diameter superconducting solenoid magnet providing a 3.8-T axial magnetic field. The bore of the magnet coil is big enough to accommodate the inner tracker, electromagnetic, and hadron calorimeters. Muon detectors are embedded inside the iron return yoke. CMS also features an extensive forward calorimeter system. The CMS detector has an overall length of 22 m, a diameter of 15 m, and weighs 12 500 metric tons. An unusual feature of the CMS detector is that it was first built on the surface, unlike most detectors of this kind that are typically built *in situ*, and then lowered underground in multiple sections and reassembled inside the experimental cavern.

In order to meet the goals of the LHC physics program, the CMS detector has to meet the following requirements:

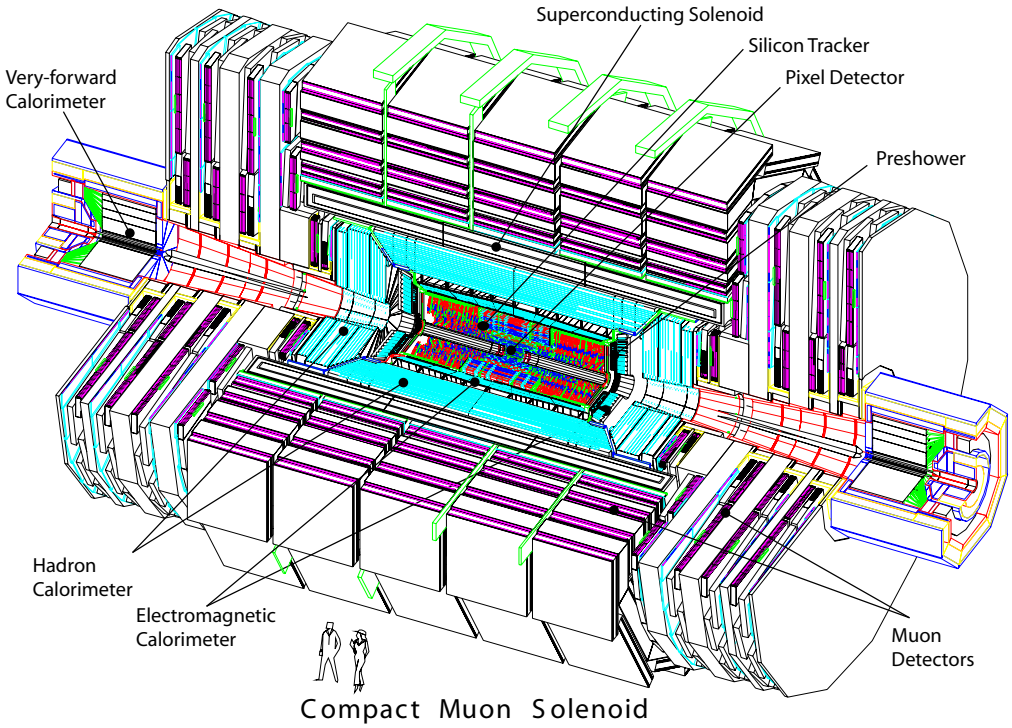

Figure 3.8: A perspective view of the CMS detector.

- Good muon identification and momentum resolution over a wide range of momenta and angles, good dimuon mass resolution ($\approx 1\%$ at 100 GeV), and the ability to determine unambiguously the charge of muons with $p < 1$ TeV (this requires a momentum resolution of $\Delta p/p \approx 10\%$ at $p = 1$ TeV);

- Good charged-particle momentum resolution and reconstruction efficiency in the inner tracker. Efficient triggering and offline tagging of τ's and b-jets, requiring pixel detectors close to the interaction region;

- Good electromagnetic energy resolution, good diphoton and dielectron mass resolution ($\approx 1\%$ at 100 GeV), wide geometric coverage, good π^0 rejection, and efficient photon and lepton isolation at high luminosities;

- Good $\not\!\!E_{\mathrm{T}}$ and dijet mass resolution, requiring a hadron calorimeter with a large hermetic geometric coverage ($|\eta| < 5$) and with fine lateral segmentation ($\Delta\eta \times \Delta\phi < 0.1 \times 0.1$).

The design of the CMS detector, detailed in the following sections, meets all these requirements. In the following sections, a brief overview of the main CMS detector subsystems is given. Unless stated otherwise, the information presented in this section is taken from References [65] and [79].

3.2.1 Superconducting Magnet

The purpose of the CMS magnet is to provide the magnetic field necessary for the momentum measurement of charged particles. For good momentum resolution at high track momenta, a large bending power is needed. The CMS solenoid uses superconducting technology that can carry a high enough current through the solenoid coil to produce a sufficiently strong magnetic field. A favorable length/radius ratio is also needed to ensure good track momentum resolution in the forward region. With a diameter of 6.3 m and length of 12.9 m, the CMS magnet provides a 3.8-T axial magnetic field inside its volume with a stored energy of 2.35 GJ at full current. The solenoid is composed of five separate modules that are mechanically and electrically coupled with a total cold mass of 220 metric tons. The ratio between the stored energy and cold mass is 10.48 kJ/kg, well beyond the values of previous solenoidal detector magnets, which causes a considerable mechanical deformation (0.15%) during the magnet ramp-up. The parameters of the CMS magnet are listed

in Table 3.2.

Table 3.2: Main parameters of the CMS magnet.

General parameters	
Magnetic length	12.5 m
Cold bore diameter	6.3 m
Central magnetic induction	3.8 T
Total Ampere-turns	39.6 MA-turns
Nominal current	18.18 kA
Inductance	14.2 H
Stored energy	2.35 GJ
Cold mass	
Layout	Five modules mechanically and electrically coupled
Radial thickness of cold mass	312 mm
Radiation thickness of cold mass	3.9 X_0
Weight of cold mass	200 metric tons
Maximum induction on conductor	4.4 T
Temperature margin wrt operating temperature	1.8 K
Stored energy/unit cold mass	10.48 kJ/kg
Iron yoke	
Outer diameter of the iron flats	14 m
Length of barrel	13 m
Thickness of iron layers in barrel	300, 630, and 630 mm
Mass of iron in barrel	6000 metric tons
Thickness of iron disks in endcaps	250, 600, and 600 mm
Mass of iron in each endcap	2000 metric tons
Total mass of iron in return yoke	10 000 metric tons

Another distinctive feature of the CMS magnet is its four-layer winding made from NbTi conductor stabilized with pure aluminum and mechanically reinforced with an aluminum alloy in order to withstand the mechanical stresses generated during operation. The solenoid cold mass is placed inside the cryostat, as shown in Figure 3.9, and cooled down to 4.5 K during normal operation. The magnetic flux

is returned through an iron yoke consisting of five barrel wheels and two endcaps, with each endcap composed of three disks.

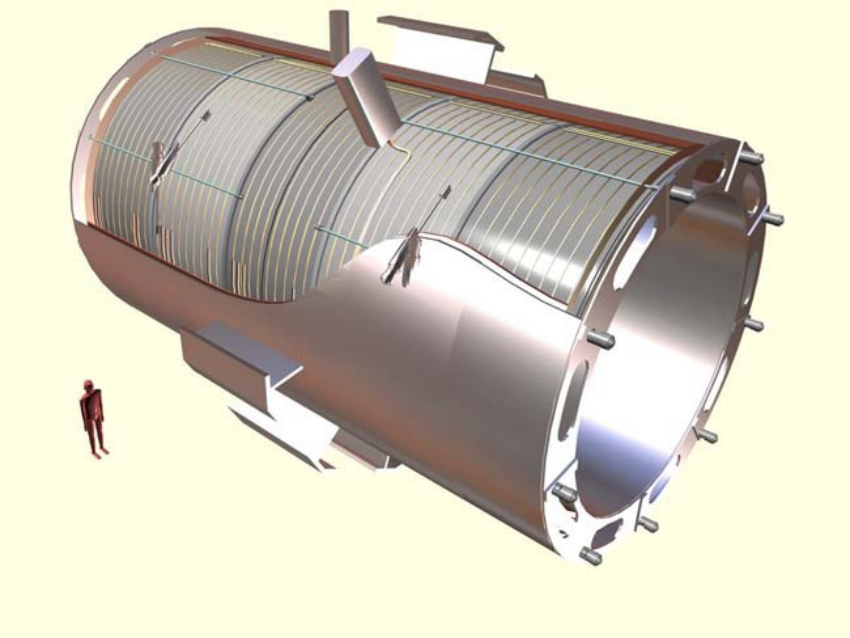

Figure 3.9: Artistic view of the CMS solenoid composed of five modules placed inside the cryostat. Details of the supporting system (vertical, radial and longitudinal tie rods) can also be seen.

3.2.2 Inner Tracking System

The primary purpose of the CMS inner tracking system, which is the subdetector system closest to the interaction region, is to provide a precise and efficient measurement of the trajectories of charged particles produced in the LHC collisions. It is also used for precise measurement of displaced secondary vertices and track impact parameters[1] necessary for efficient heavy flavor identification. It is also instrumental in tau lepton identification and, together with the electromagnetic

[1]Track impact parameter is defined as the distance of closest approach of a track with respect to some reference point, usually a primary vertex.

calorimeter and the muon system, is used to identify electrons and muons, respectively. The tracker also plays an important role in event triggering by providing the tracking information to the CMS trigger system.

The CMS tracker has a length of 5.8 m and a diameter of 2.5 m. With about 1000 particles emerging from the interaction region and traversing the tracker every 25 ns at the LHC design energy and instantaneous luminosity, a tracker that is radiation hard and features high granularity and fast response is required in order to reliably measure the charge particle trajectories and associate them with the correct bunch crossing. However, a high granularity implies a high power density for the on-detector electronics, and thus efficient cooling, while maintaining the amount of material in front of the electromagnetic calorimeter to a minimum in order to limit multiple scattering, bremsstrahlung, photon conversion and nuclear interactions. All these requirements lead to an all-silicon tracker design.

The CMS tracker consists of an inner silicon pixel and outer silicon microstrip detectors. A schematic cross section of the CMS tracker is shown in Figure 3.10. The pixel detector covers a pseudorapidity range $|\eta| < 2.5$ and consists of three barrel layers (BPix) and two endcap disks on each side (FPix). The layout of the pixel detector is shown in Figure 3.11. The three BPix layers are located at mean radii of 4.4, 7.3, and 10.2 cm, and each have a length of 53 cm. The two FPix disks extend from 6 to 15 cm in radius and are located at $|z| = 34.5$ and 46.5 cm. The BPix contains 48 million pixels covering a total area of 0.78 m^2, with a total of 768 pixel modules. The FPix contains 18 million pixels covering a total area of 0.28 m^2, with a total of 672 pixel modules. Due to a pixel size of 100×150 μm^2, a similar

track resolution in both r-ϕ and z directions is achieved (about 10 μm for the r-ϕ measurement and about 20 μm for the z measurement), and the occupancy is of the order 10^{-4} per pixel per LHC bunch crossing at design energy and instantaneous luminosity. In the BPix, the drift of the electrons in a pixel is perpendicular to the magnetic field, and the resulting Lorentz drift facilitates charge sharing among pixels and consequently improves the r-ϕ resolution. The FPix disks are assembled in a turbine-like geometry with blades rotated by 20° to induce charge-sharing. The charge sharing is due to the geometric effect of particles entering the detector at an angle away from the normal incidence, and is further enhanced by the Lorentz drift. The arrangement of the BPix layers and FPix disks on each side is such that three points are measured on tracks over almost the full η-range of the pixel detector ($|\eta| < 2.5$).

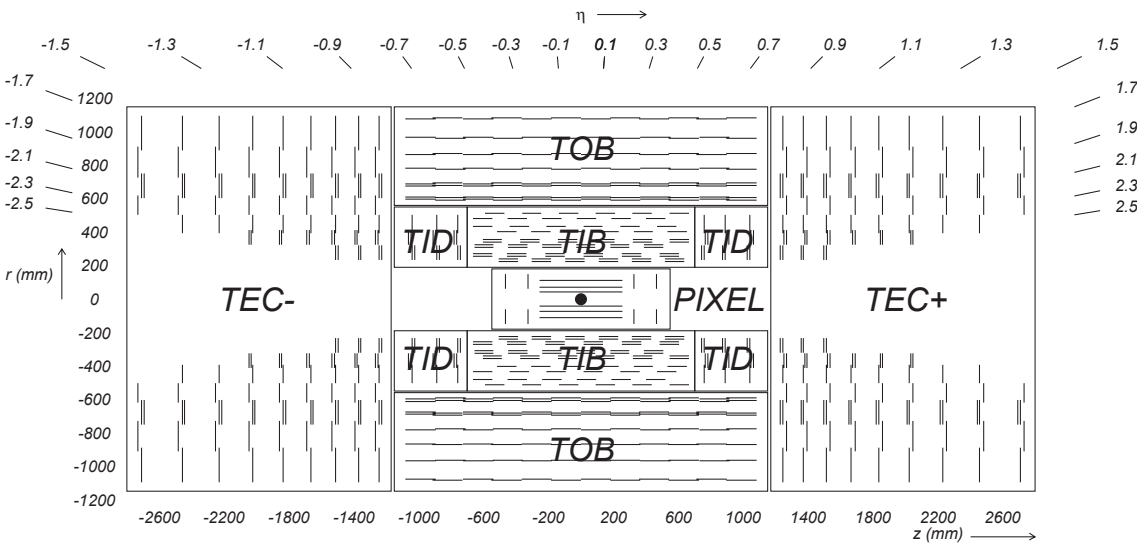

Figure 3.10: Schematic r-z cross section through the CMS tracker. Each line represents a detector module. Double lines indicate back-to-back modules which deliver stereo hits.

The silicon strip tracker occupies the radial region between 20 and 116 cm.

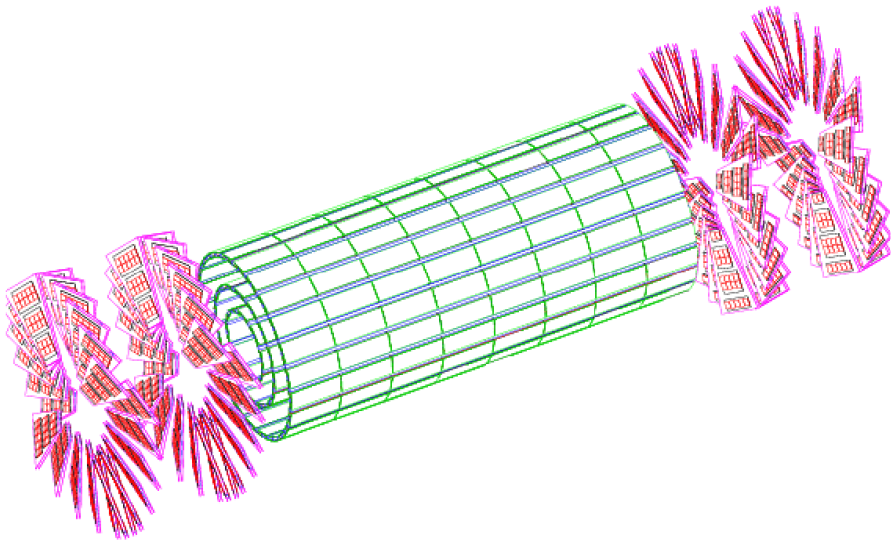

Figure 3.11: Layout of the CMS pixel detector.

It has the same pseudorapidity coverage as the pixel detector, $|\eta| < 2.5$, and is composed of four different subsystems. The Tracker Inner Barrel (TIB) extends in radius from 20 cm up to 55 cm and covers up to $|z| < 65$ cm. It consists of four layers and is made of silicon sensors with a thickness of 320 μm and a strip pitch which varies from 80 to 120 μm. The Tracker Outer Barrel (TOB) has an inner radius of 55 cm, an outer radius of 116 cm, and consists of six layers covering up to $|z| < 118$ cm. Because of smaller radiation levels in the outer tracker, it has thicker silicon sensors (500 μm) and a strip pitch which varies from 120 to 180 μm. The first two layers in both the TIB and the TOB are made with stereo modules (with a stereo angle of 100 mrad) in order to provide measurements in both r-ϕ and r-z coordinates. In the TIB (TOB), this results in a single-point resolution of between 23–35 μm (35–53 μm) in r-ϕ and 230 μm (530 μm) in z. Each Tracker End Cap (TEC) consists of nine disks in the region $124 < |z| < 282$ cm. The Tracker Inner Disks (TID) consist of three disks that fill the gap between the TIB

and the TEC. The TEC and TID modules are arranged in rings centered on the beam line and have variable pitch strips that point towards the beam line. The first two rings of the TID and rings 1, 2, and 5 of the TEC have stereo modules. The thickness of the silicon sensors is 320 μm for the TID and the three innermost rings of the TEC. It is 500 μm for the rest of the TEC. In the intermediate region ($20 < r < 55$ cm), the particle flux is low enough that the resulting occupancy is $\approx$ 2–3% per strip per LHC bunch crossing at design energy and instantaneous luminosity. In the outermost region ($r > 55$ cm), the occupancy is $\approx$ 1% per strip per LHC bunch crossing. The layout of the CMS tracker ensures at least ≈ 9 hits in the silicon strip tracker in the range $|\eta| < 2.4$, with at least ≈ 4 two-dimensional measurements. The silicon strip tracker has a total of 9.3 million strips, with 198 m^2 of active silicon area, and has a total of 15 148 detector modules distributed among the four different subsystems (TIB, TID, TOB, TEC). The material budget of the CMS tracker in units of radiation length increases from 0.4 X_0 at $\eta \approx 0$ to about 1.8 X_0 at $|\eta| \approx 1.4$. It falls to about 1 X_0 at $|\eta| \approx 2.5$.

The CMS tracker will have to operate in a harsh environment with high fluxes of particles coming from the interaction region. These particles can cause radiation damage to both the front-end electronics and the silicon sensors. They can also cause transient phenomena in which the charge produced by an ionizing particle traversing the electronic circuitry changes the state of a memory cell or in general disturbs the normal operation of the read-out system. In order to minimize the radiation damage accumulated over the course of detector operation and to ensure robust hit detection with an acceptable fake hit rate, it is necessary to operate the

CMS tracker with the whole tracker volume at or slightly below $-10°$C. With the total power dissipated inside the tracker volume expected to be close to 60 kW, a robust and efficient cooling system is required. This is complicated by the fact that the outer surface of the tracker faces the electromagnetic calorimeter which has to be operated at room temperature and requires good temperature stability. The tracker cooling system therefore has to be capable of maintaining this thermal gradient over a very limited radial thickness.

During the 2010 run, 98.2% of all channels in the pixel detector and 98.1% of all channels in the silicon strip tracker were fully operational. The live time during stable beam conditions was 97.57% for the pixel detector, and 98.83% for the silicon strip tracker.

3.2.3 Electromagnetic Calorimeter

The CMS electromagnetic calorimeter (ECAL) is the subdetector system surrounding the inner tracking system. Its primary purpose is to measure the energy of particles that primarily interact and lose their energy via electromagnetic interactions. It is a homogeneous hermetic calorimeter made of lead tungstate ($PbWO_4$) crystals, and consists of a barrel (EB) closed on either side by endcaps (EE). Preshower (PS) detector is placed in front of the two endcaps. The configuration of the magnetic field and the expected level of radiation led to the choice of avalanche photodiodes (APDs) and vacuum phototriodes (VPTs) as photodetectors in the EB and EE, respectively.

Lead tungstate crystals are optically clear and characterized by their high density (8.28 g/cm^3), short radiation length (0.89 cm), small Molière radius (2.2 cm), and radiation hardness making them a suitable choice for a compact electomagnetic calorimeter with fine granularity. The crystals emit blue-green scintillation light (the maximum is at 420–430 nm) and have a scintillation decay time comparable to the LHC bunch spacing, with 80% of the light emitted in 25 ns. However, the light output is relatively low (about 4.5 photoelectrons per MeV are collected in either APDs or VPTs at 18°C) and has a strong temperature dependence ($-2.1\%/°$C at 18°C).

The ECAL barrel has an inner radius of 129 cm and extends to $|\eta| = 1.479$. It has a (2×85)-fold granularity in η and 360-fold granularity in ϕ, resulting in an approximate $\Delta\eta \times \Delta\phi$ granularity of 0.0174×0.0174 and a total of 61 200 crystals. The crystals have a tapered shape, with a cross section of 22×22 mm^2 at the front face and 26×26 mm^2 at the rear face and a total length of 230 mm, corresponding to 25.8 X_0. To detect the scintillation light, a pair of APDs is attached to the rear face of each EB crystal. The EB is structurally divided into 36 supermodules, each covering half the barrel length and containing 4 modules. The crystals are mounted in a quasi-projective geometry (the crystal axes are tilted at 3° in both η and ϕ with respect to the line from the nominal interaction point) in order to avoid cracks in detector coverage aligned with particle trajectories. The barrel crystal volume is 8.14 m^3 and its weight is 67.4 metric tons. A transverse section through the CMS electromagnetic calorimeter is shown in Figure 3.12.

The ECAL endcaps, located at 315.4 cm from the nominal interaction point

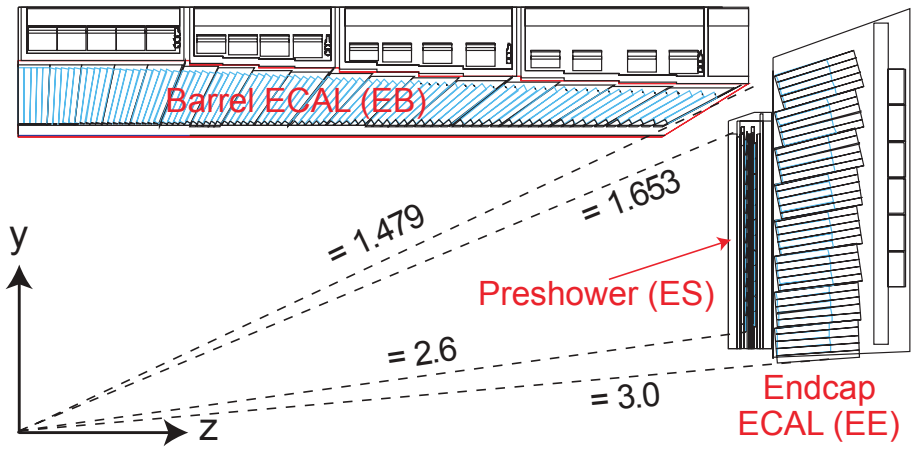

Figure 3.12: Transverse section through the CMS electromagnetic calorimeter.

and covering the pseudorapidity range $1.479 < |\eta| < 3.0$, are each structurally divided in two halves, called "Dees". Each Dee holds 3662 identically shaped crystals grouped in mechanical units of 5×5 crystals called "supercrystals". Each Dee consists of 138 standard supercrystals and 18 special supercrystals on the inner and outer circumference. Because they are mounted on the inner and outer circumference, special supercrystals contain less than 25 crystals arranged in what is not necessarily a rectangular unit. The endcap crystals are arranged in a rectangular x-y grid with the crystals pointing at a focal point 130 cm beyond the nominal interaction point, giving off-pointing angles ranging from 2° to 8°. The crystals have a cross section of 28.62×28.62 mm^2 at the front face and 30×30 mm^2 at the rear face and a total length of 220 mm, corresponding to 24.7 X_0. To detect the scintillation light, a single VPT is attached to the rear face of each EE crystal. The EE crystal volume is 2.9 m^3 and the weight is 24.0 metric tons. The overall layout of the CMS electromagnetic calorimeter is shown in Figure 3.13.

The CMS preshower (PS) detector is placed in front of the endcap crystal

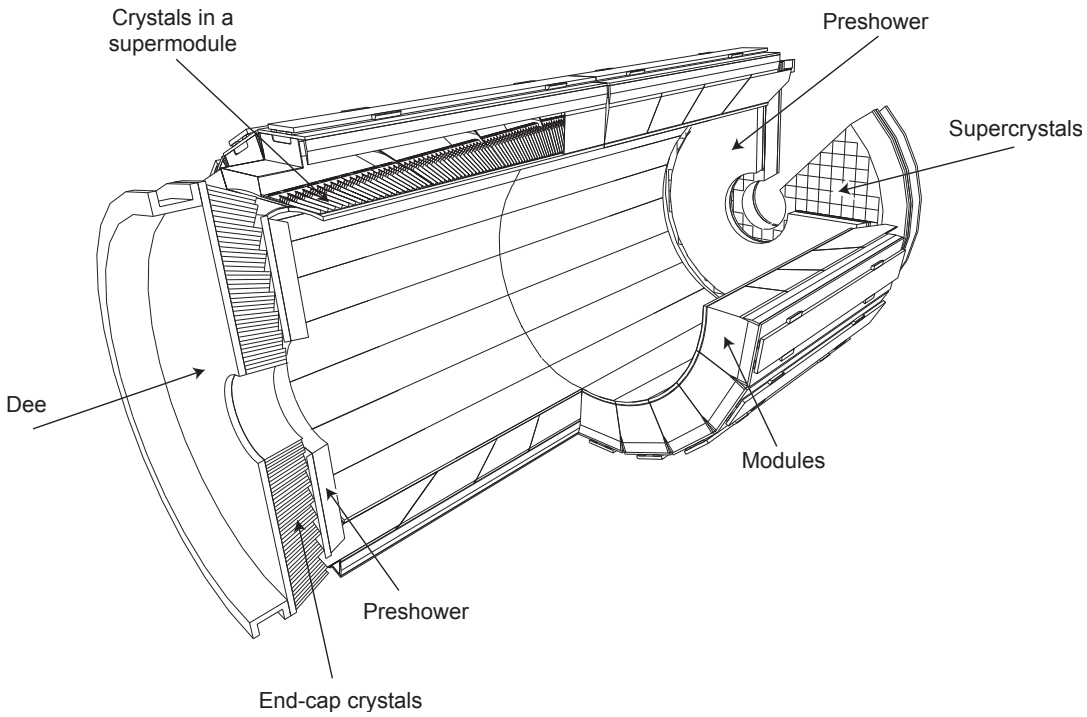

Figure 3.13: Layout of the CMS electromagnetic calorimeter showing the arrangement of crystal modules, supermodules and endcaps, with the preshower in front.

calorimeter within a fiducial region $1.653 < |\eta| < 2.6$. Its main purpose is to identify neutral pions through the detection of two closely-spaced photons. It consists of two lead radiators, about two and one radiation lengths thick, respectively. Each radiator is followed by a plane of silicon strip sensors used to measure the deposited energy and the transverse shower profiles. The silicon strip sensors have a pitch of 1.9 mm, and their orientation in the two planes is orthogonal. The CMS preshower detector has a total thickness of 20 cm and is separated into two Dees with the same orientation as the crystal Dees. The granularity of the ECAL endcaps is not sufficient to identify two closely-spaced photons and, in the absence of the transverse shower profile information from the preshower detector, many neutral pions directed toward the endcaps of CMS would be reconstructed as single photons. The preshower

detector also helps the discrimination of electrons from minimum ionizing particles, and improves the position determination of electrons and photons.

The light output of the crystals and the amplification of the APD both decrease with increasing temperature. The overall change in the response with temperature has been measured in test beam to be $(-3.8 \pm 0.4)\%/^{\circ}\mathrm{C}$. It is therefore important to keep the temperature constant to high precison ($\pm 0.05^{\circ}\mathrm{C}$) in order to preserve the energy resolution. The nominal operating temperature of the CMS ECAL is $18^{\circ}\mathrm{C}$.

The energy resolution of the electromagnetic calorimeter can be parametrized by the following function

$$\frac{\sigma(E)}{E} = \frac{S}{\sqrt{E}} \oplus \frac{N}{E} \oplus C, \tag{3.4}$$

where S is the stochastic term, N the noise term, and C the constant term. The ECAL energy resolution measured with an electron test beam by summing the energy measured in a grid of 3×3 crystals was found to be

$$\frac{\sigma(E)}{E} = \frac{2.8\%}{\sqrt{E}} \oplus \frac{12\%}{E} \oplus 0.3\%, \tag{3.5}$$

where E is the measured energy in units of GeV. This result is in good agreement with the design-goal performance expected for a perfectly calibrated detector [80]. For energies in the range of interest for most physics analyses ($E \gtrsim 100$ GeV), the energy resolution will be dominated by the constant term, sensitive to inter-calibration errors. Therefore, the performance of the electromagnetic calorimeter

will critically depend on the quality of the calibration. Using the first 250 nb^{-1} of collision data at the center-of-mass energy of 7 TeV, the energy scale of the electromagnetic calorimeter was found to agree with the expectation to within about 1% in the barrel and 3% in the endcaps, and a channel-to-channel *in situ* calibration precision of about 0.6% has been achieved in the central barrel ($|\eta| < 0.8$), and between 0.6% and about 1.5% in the rest of the barrel [80].

The CMS ECAL was found to occasionally record anomalous signals that correspond to particles hitting and directly ionizing the APD sensitive volume [81, 82]. Such anomalous signals are characterized by a high energy deposit in a single crystal and very little or no energy in the surrounding crystal, atypical of energy deposits from real electrons and positrons. Algorithms have been developed to identify and address such anomalous energy deposits in data [81, 82].

During the 2010 run, 99.3% of all channels in the ECAL barrel, 98.9% of all channels in the ECAL endcaps, and 99.8% of all channels in the preshower detector were fully operational. The live time during stable beam conditions was 99.46% for the ECAL barrel and endcaps, and 99.91% for the preshower detector.

3.2.4 Hadron Calorimeter

The CMS hadron calorimeter (HCAL), in conjunction with the ECAL subdetector, forms a complete calorimeter system necessary for the measurement of hadronic jets and missing transverse energy ($\not\!\!E_{\text{T}}$). An important requirement on the HCAL performance is to minimize the non-Gaussian tails in the energy resolution

and to provide good containment and hermeticity for the $\not\!\!E_{\mathrm{T}}$ measurement. This requires an HCAL design that maximizes material inside the magnet coil in terms of interaction lengths. The HCAL barrel (HB) and endcap (HE) subdetectors completely surround the ECAL subdetector and are fully contained inside the solenoid volume. The HB is located between the outer radius of the ECAL ($r = 177$ cm) and the inner radius of the solenoid magnet ($r = 295$ cm). This constrains the total amount of material that can absorb hadronic showers and therefore an additional HCAL outer (HO) detector is placed outside the solenoid volume to complement the barrel calorimeter and serve as a tail catcher. To further extend the pseudorapidity coverage and improve the overall hermeticity of the CMS calorimeter, the HCAL forward (HF) detector is placed outside the solenoid volume at 11.2 m from the interaction point. The location of the HCAL subdetectors inside the CMS detector is shown in Figure 3.14.

The HB covers the pseudorapidity range $|\eta| < 1.4$ and is divided into two half-barrels each consisting of 18 identical azimuthal wedges. Each wedge is segmented into 16 projective towers in η and 4 projective towers in ϕ, resulting in a tower segmentation $\Delta\eta \times \Delta\phi = 0.087 \times 0.087$ and a total of 2304 towers in HB. Each HB wedge, shown in Figure 3.15, is a sampling calorimeter constructed out of flat brass-alloy absorber plates bolted together and machined so as to leave slots between them for the plastic scintillator tiles. This configuration leaves essentially no uninstrumented cracks or dead regions in ϕ over the full radial extent of a wedge. The innermost and outermost absorber plates are made of stainless steel for structural strength. The front steel plate is 40 mm thick, followed by eight 50.5-mm-thick

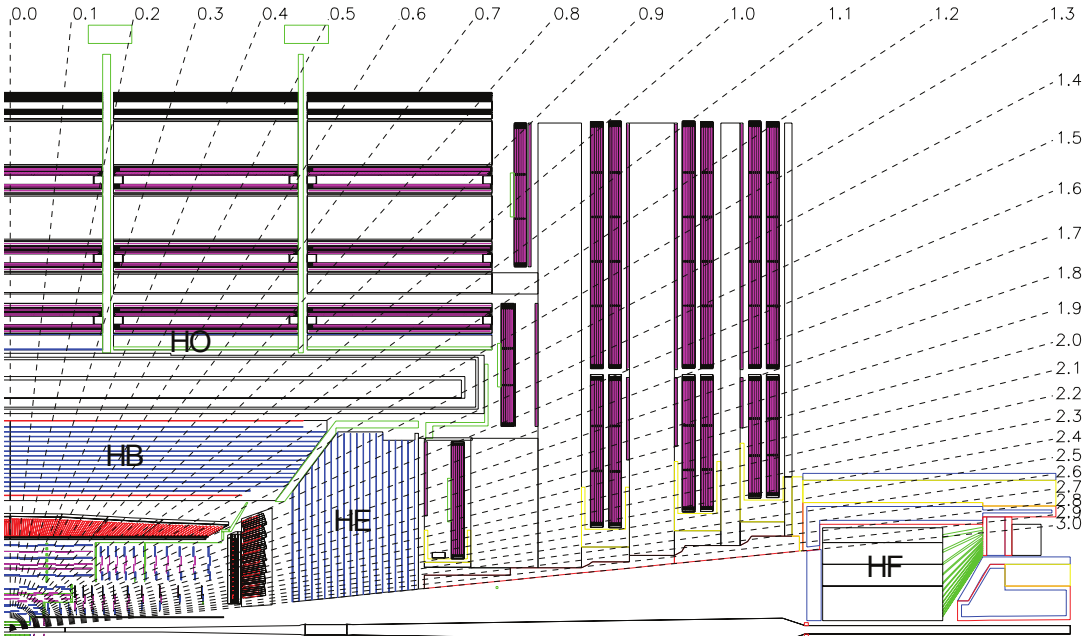

Figure 3.14: Longitudinal view of the CMS detector showing the locations of the HCAL barrel (HB), endcap (HE), outer (HO) and forward (HF) calorimeters.

brass plates, six 56.5-mm-thick brass plates, and a 75-mm-thick steel back plate. The scintillator tiles are 3.7 mm thick and are grouped into mechanical scintillator tray units. The two exceptions are the layer 0 tiles, which are 9 mm thick and are placed in front of the innermost absorber steel plate to sample hadronic showers developing in the inert material between EB and HB; and layer 16 tiles, which are also 9 mm thick and serve to correct for late developing showers leaking out the back of HB. The individual scintillator tiles are instrumented with a single wavelength-shifting (WLS) fiber which is spliced to a clear fiber. The clear fiber goes to an optical connector at the end of the tray from where an optical cable takes the light signal to an optical decoding unit. The optical decoding unit arranges the fibers into read-out towers and brings the light to a pixelated hybrid photodiode (HPD). There are 4 HPDs, one per ϕ-slice, mounted inside a Readout BoX (RBX) located

at the outward edge of each HB wedge. The 17 scintillator layers are combined into a single longitudinal readout, with the exception of towers 15 and 16 at the edge of the HB half-barrel, which are segmented into two depths. The detailed HB tower segmentation is shown in Figure 3.16.

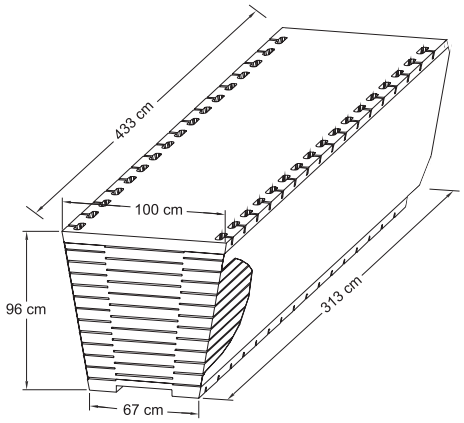

Figure 3.15: Isometric view of an HB wedge showing the slots the end of the wedge into which the scintillator trays are inserted.

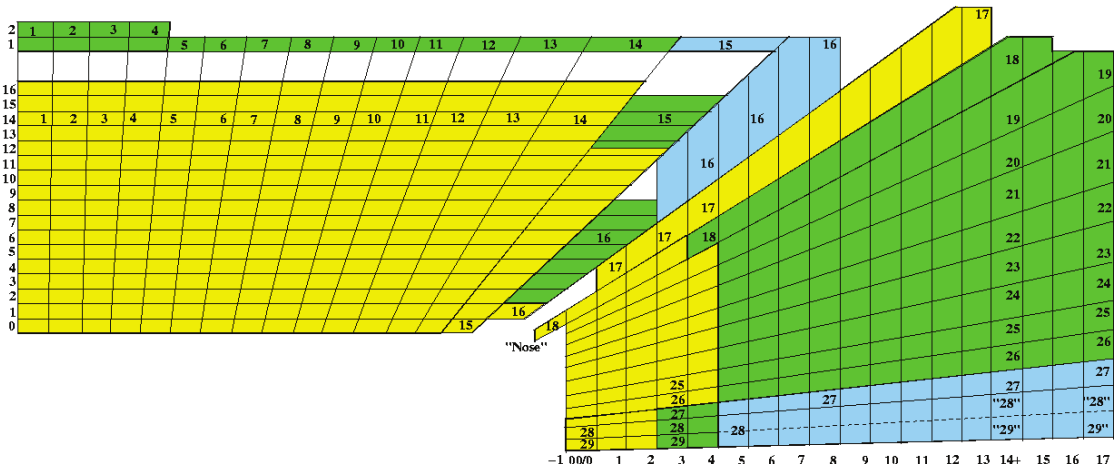

Figure 3.16: The HCAL tower segmentation in the r-z plane for one-fourth of the HB, HE, and HO subdetectors.

The HE covers the pseudorapidity range $1.3 < |\eta| < 3.0$ and has a tapered geometry in order to interlock with the HB. The HE is very similar to the HB. It is also a sampling calorimeter, entirely composed of 78-mm-thick brass absorber plates

interleaved with active layers of 3.7-mm-thick plastic scintillator tiles. A special scintillator layer installed in front of the absorber (layer 0) is 9 mm thick. As with HB, the individual scintillator tiles are instrumented with a single WLS fiber, and HPDs are used as photodetectors. In the range $1.3 < |\eta| < 1.74$, the $\Delta\eta \times \Delta\phi$ segmentation of the towers matches that of the HB, while for $1.74 < |\eta| < 3.0$, it increases as shown in Table 3.3. The total number of HE towers, including towers in η-ring 16 that overlap with the HB towers, is 1368. Starting with tower 18, the first tower beyond the η coverage of the EB, HE towers have 2 depth segments with the exception of the three towers closest to the beam line, that have 3 depth segments each. The detailed HE tower segmentation is shown in Figure 3.16.

The HO covers the pseudorapidity range $|\eta| < 1.26$ and is located outside the solenoid volume but inside of the barrel muon system, and is therefore constrained by the geometry and construction of that system. The entire assembly is divided into 5 sections, called "rings", along η, labelled -2, -1, 0, 1, and 2. Each ring is divided into 12 identical ϕ sectors, and each sector has 6 slices in ϕ. The ring 0 has two 10-mm-thick scintillator layers on either side of a 19.5-cm-thick iron absorber (the tail catcher iron) at radial distances of 382 cm and 407 cm. The other rings have single 10-mm-thick scintillator layers at a radial distance of 407 cm. Each ring covers 2.54 m along the z-axis. The HO scintillator tiles approximately follow the HB tower geometry in η and ϕ. As in HB and HE, the scintillation light is collected by WLS fibers, and HPDs are used as photodetectors. The inclusion of the HO layers extends the total depth of the calorimeter system to a minimum of $\approx 11\ \lambda_{\mathrm{I}}$ except at the barrel-endcap boundary region, as shown in Figure 3.18.

Table 3.3: Sizes of the HCAL readout towers in η and ϕ as well as the segmentation in depth. The HF has a non-pointing geometry, and the tower η ranges provided here correspond to $|z| = 11.2$ m. *The HE towers 28 and 29 shares the same third depth segment whose energy is artificially divided in two equal portions and shared between these two towers. †The HF tower 29 is located behind the HE and because of the non-projective HF geometry, its energy is added to the HF tower 30.

Tower	η range		Detector	Size		Depth
index	Low	High		η	ϕ	segments
1	0.000	0.087	HB, HO	0.087	5°	HB=1, HO=1
2	0.087	0.174	HB, HO	0.087	5°	HB=1, HO=1
3	0.174	0.261	HB, HO	0.087	5°	HB=1, HO=1
4	0.261	0.348	HB, HO	0.087	5°	HB=1, HO=1
5	0.348	0.435	HB, HO	0.087	5°	HB=1, HO=1
6	0.435	0.522	HB, HO	0.087	5°	HB=1, HO=1
7	0.522	0.609	HB, HO	0.087	5°	HB=1, HO=1
8	0.609	0.696	HB, HO	0.087	5°	HB=1, HO=1
9	0.696	0.783	HB, HO	0.087	5°	HB=1, HO=1
10	0.783	0.870	HB, HO	0.087	5°	HB=1, HO=1
11	0.879	0.957	HB, HO	0.087	5°	HB=1, HO=1
12	0.957	1.044	HB, HO	0.087	5°	HB=1, HO=1
13	1.044	1.131	HB, HO	0.087	5°	HB=1, HO=1
14	1.131	1.218	HB, HO	0.087	5°	HB=1, HO=1
15	1.218	1.305	HB, HO	0.087	5°	HB=2, HO=1
16	1.305	1.392	HB, HE	0.087	5°	HB=2, HE=1
17	1.392	1.479	HE	0.087	5°	HE=1
18	1.479	1.566	HE	0.087	5°	HE=2
19	1.566	1.653	HE	0.087	5°	HE=2
20	1.653	1.740	HE	0.087	5°	HE=2
21	1.740	1.830	HE	0.090	10°	HE=2
22	1.830	1.930	HE	0.100	10°	HE=2
23	1.930	2.043	HE	0.113	10°	HE=2
24	2.043	2.172	HE	0.129	10°	HE=2
25	2.172	2.322	HE	0.150	10°	HE=2
26	2.322	2.500	HE	0.178	10°	HE=2
27	2.500	2.650	HE	0.150	10°	HE=3
28	2.650	2.868	HE	0.218	10°	HE=3
*29	2.868	3.000	HE	0.132	10°	HE=3
†29	2.853	2.964	HF	0.111	10°	HF=2
30	2.964	3.139	HF	0.175	10°	HF=2
31	3.139	3.314	HF	0.175	10°	HF=2
32	3.314	3.489	HF	0.175	10°	HF=2
33	3.489	3.664	HF	0.175	10°	HF=2
34	3.664	3.839	HF	0.175	10°	HF=2
35	3.839	4.013	HF	0.174	10°	HF=2
36	4.013	4.191	HF	0.178	10°	HF=2
37	4.191	4.363	HF	0.172	10°	HF=2
38	4.363	4.538	HF	0.175	10°	HF=2
39	4.538	4.716	HF	0.178	10°	HF=2
40	4.716	4.889	HF	0.173	20°	HF=2
41	4.889	5.191	HF	0.302	20°	HF=2

The HF covers the pseudorapidity range $2.85 < |\eta| < 5.2$ and is located outside the solenoid volume, with its front faces at $|z| = 11.2$ m. It consists of a steel absorber and embedded radiation-hard quartz fibers arranged in a square grid with a separation of 5 mm. The depth of the absorber is 165 cm and the quartz fibers have a diameter of 0.6 mm. The HF is essentially a cylindrical steel structure with an outer radius of 130 cm and an inner radius of 12.5 cm. This structure is divided into 18 azimuthal wedges arranged in a non-projective geometry, with the quartz fibers running parallel to the beam axis along the length of the steel absorber. The HF signal originates from Cerenkov light produced by relativistic charged shower particles in the quartz fibers, resulting in a very fast response time. The fibers are bundled at the back of the detector and are read out by photomultiplier tubes (PMTs). The HF detector is functionally divided into two longitudinal segments, with half of the fibers extending the full length of the absorber and the other half starting at a depth of 22 cm from the front face of the detector. This arrangement makes it possible to distinguish photon and electron showers, which deposit a large fraction of their energy in the first 22 cm, from those initiated by hadrons, which deposit nearly equal amounts of energy in both absorber segments on average. Long and short fibers are arranged alternately in the square grid and are read out separately. There are 13 towers in η and 36 towers in ϕ, except for the two η-rings closest to the beam line that have 18 towers in ϕ. The total number of HF towers is 864. The detailed description of the HF tower sizes can be found in Table 3.3.

The HCAL, when combined with the ECAL, measures pions with an energy

resolution

$$\frac{\sigma(E)}{E} \approx \frac{100\%}{\sqrt{E}} \oplus 5\%, \tag{3.6}$$

where E is the pion energy measured in units of GeV. Therefore, only for very high energy pions ($E \gtrsim 400$ GeV), the energy resolution will be dominated by the constant term.

The CMS HCAL was found to occasionally record anomalous signals associated with particles hitting the transducers or with rare random discharges of the readout detectors [82]. Some of these effects had already been observed during past test beam and cosmic data taking [83]. In the HB and HE, electronics noise from the HPD and/or RBX occurs, and can affect from one up to all 72 channels in an RBX. This noise is not related to interactions with particles from *pp* interactions but instead occurs at a low rate and at random times, so the overlap with *pp* interactions is very low at the bunch spacings of the 2010 run. Three main types of noise have been identified in HF: scintillation light produced in the light guides that carry the light from the quartz fibers to the photomultipliers, Cherenkov light produced in the PMT window, and punch-through particles hitting the PMTs. While the scintillation and Cherenkov sources typically affect only a single channel, signals generated by the punch-through particles can affect clusters of channels. Algorithms have been developed to identify and address such anomalous energy deposits in data [82].

During the 2010 run, 99.9% of all channels in the HB, all channels in the HE, and 99.9% of all channels in the HF were fully operational, with a live time during stable beam conditions of 99.55% for all three HCAL subsystems.

3.2.5 Muon System

The CMS muon system has to be capable of reconstructing the momentum and the charge of muons over the entire kinematic range expected for muons produced in pp collisions at the LHC. Since muons are minimum ionizing particles and fly through the detector material mostly unaffected, the muon detector system is typically the outermost detector system. The material thickness in radiation and interaction lengths crossed by muons before reaching the muon system as a function of pseudorapidity is shown in Figures 3.17 and 3.18, respectively. The minimum transverse momentum threshold for muons to reach the muon system and be triggered drops from about 4 GeV at $\eta = 0$ to about 2 GeV at $|\eta| = 2.4$ [84]. At CMS, the muon system is embedded inside the iron return yoke. It is divided into the muon barrel (MB) section ($|\eta| < 1.2$) and the muon endcap (ME) section ($|\eta| < 2.4$). The choice of the detector technologies was driven by the very large surface to be covered, requiring an inexpensive design, and by the different radiation environments in which the system will be placed. In the barrel region, where the neutron-induced background is small, the muon rate is low, and the magnetic field uniform and mostly contained in the iron yoke, drift tube (DT) chambers with rectangular drift cells are used. In the endcap region, where the muon rates and background levels are higher and the magnetic field is large and non-uniform, cathode strip chambers (CSCs) are used. Because of the expected background rates and the uncertainty in the ability of the muon system to measure the correct beam-crossing time when the LHC reaches its design instantaneous luminosity, a complementary dedicated trigger system con-

sisting of resistive plate chambers (RPCs) was added in both the barrel and endcap regions. The RPCs are double-gap chambers operated in the avalanche mode to ensure good performance at high rates. They cover a large portion ($|\eta| < 1.6$) of the pseudorapidity range of the muon system ($|\eta| < 2.4$). The layout of the CMS muon system is shown in Figure 3.19. In total, the muon system consists of about 25 000 m^2 of active detection planes, and nearly 1 million electronic channels.

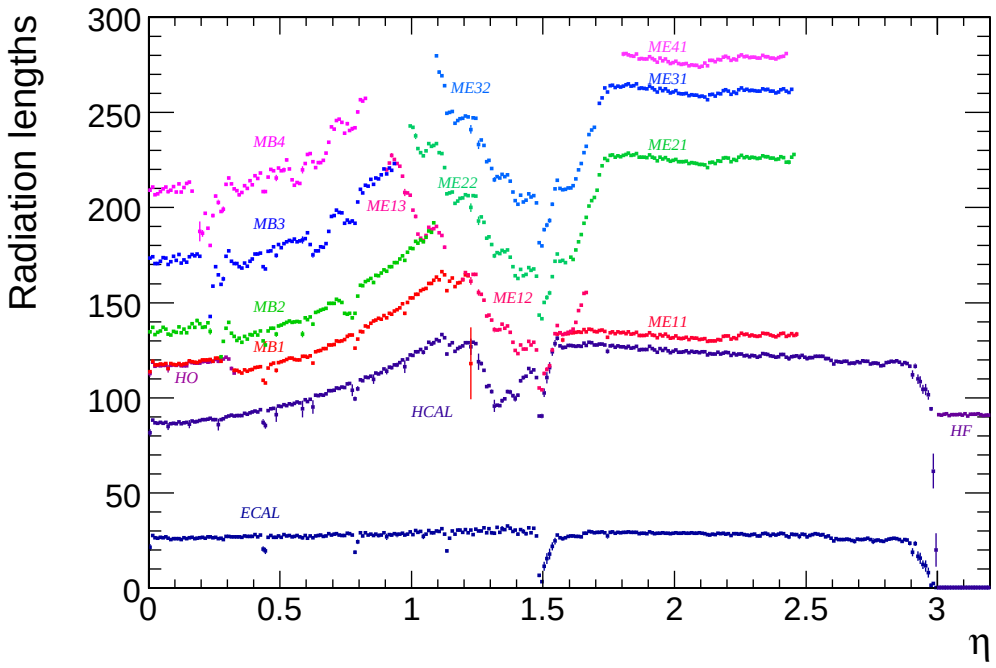

Figure 3.17: Material thickness in radiation lengths after the ECAL, HCAL, and at the depth of each muon station as a function of pseudorapidity. The thickness of the HF is approximately constant over the range $3 < |\eta| < 5$ (not shown).

The muon barrel section consist of four concentric stations divided into 5 wheels, from "YB−2" for the furthest wheel in $-z$ to "YB+2" for the furthest wheel in $+z$, and contains a total of 250 chambers. Each wheel is divided into 12 sections, each covering a 30° azimuthal angle. The two innermost stations, MB1 and MB2, consist of packages containing a DT chamber sandwiched between two

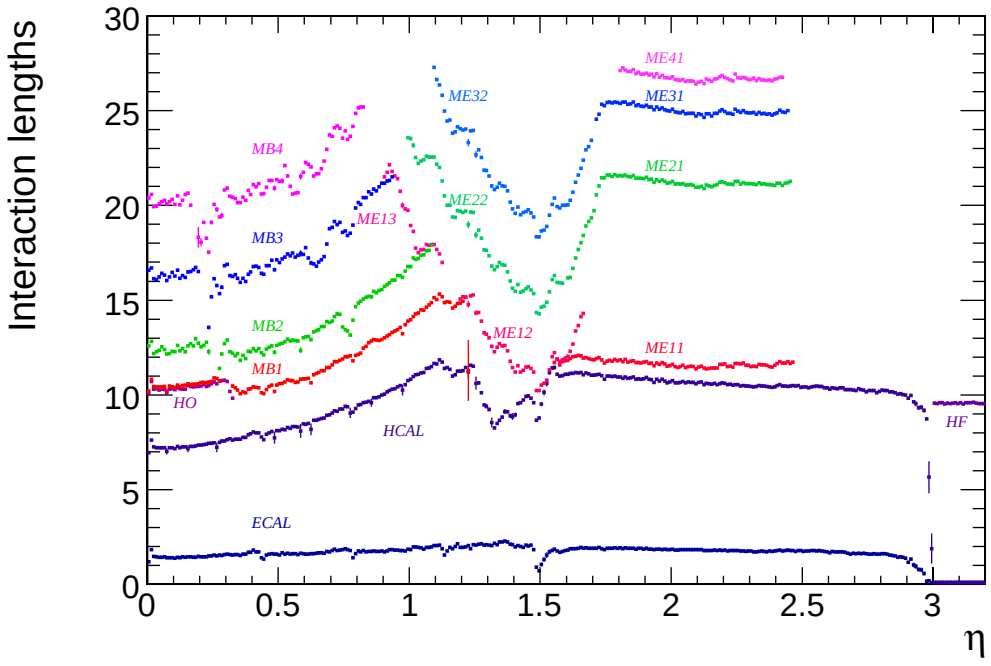

Figure 3.18: Material thickness in interaction lengths after the ECAL, HCAL, and at the depth of each muon station as a function of pseudorapidity. The thickness of the HF is approximately constant over the range $3 < |\eta| < 5$ (not shown).

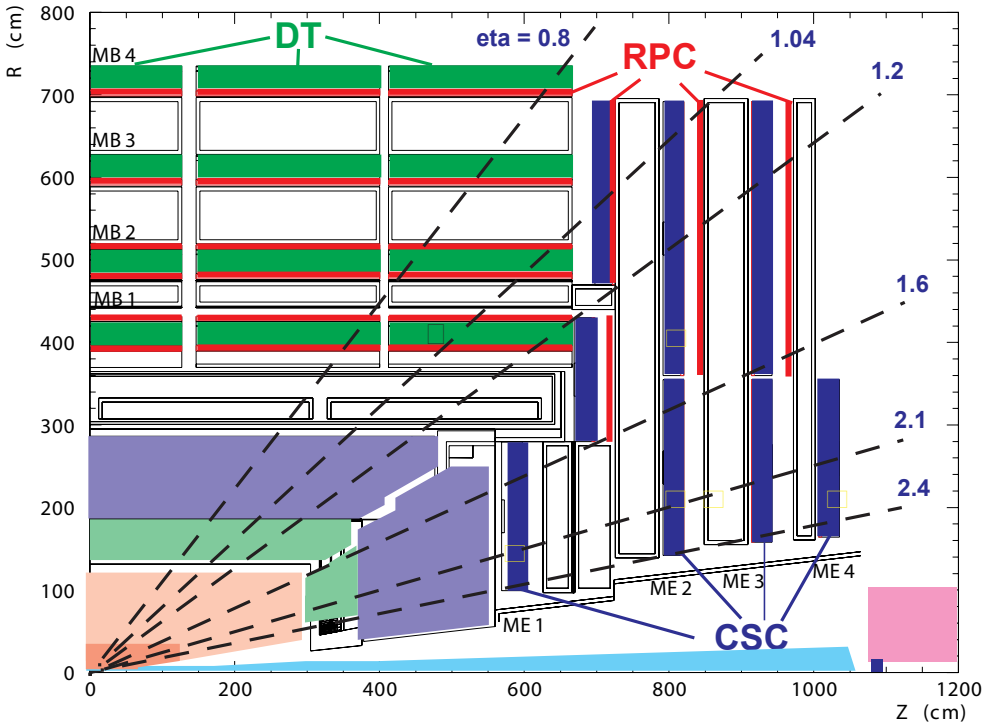

Figure 3.19: Layout of one quarter of the CMS muon system for the LHC startup.

RPCs. The two outermost stations, MB3 and MB4, consist of packages containing a DT chamber coupled to a layer composed of 1, 2, or 4 RPCs, depending on the sector and station, placed on the inner side of the station. The first three stations provide measurements of the muon coordinates in the r-ϕ bending plane as well as along the z-axis. The fourth station only provides measurements in the r-ϕ bending plane. Chambers in different stations are staggered to ensure that there are no uninstrumented regions aligned with particle trajectories.

The muon endcap section consists of four stations, labeled ME1 to ME4, in order of increasing distance from the nominal interaction point, that are mounted on the endcap disks perpendicular to the beam line and enclosing the CMS magnet. In station ME1, chambers are arranged in 3 concentric rings around the beam axis. In stations ME2 and ME3, chambers are arranged in 2 concentric rings. In station ME4, only the innermost ring has been fully deployed, while 5 spare CSCs have been installed in the outer ring (ME4/2) on the $+z$ side. There are a total of 468 CSCs in the two muon endcaps, excluding ME4/2. All CSCs, except those in the outermost ring of ME1 (ME1/3), overlap in ϕ in order to avoid gaps in the muon acceptance. There are 36 chambers in each ring of a muon station, except for the innermost rings of ME2 to ME4 (ME2/1, ME3/1, and ME4/1) which have 18 chambers. Each CSC measures all three spatial coordinates (r, ϕ, z) in each of its 6 layers. The RPCs are mounted only in the outer rings of the first three endcap stations.

During the 2010 run, 99.8% of all DT channels, 98.5% of all CSC channels, and 98.8% of all RPC channels were fully operational. The live time during stable beam conditions was 99.91% for the DT subsystem, 99.55% for the CSC subsystem,

and 99.91% for the RPC subsystem.

3.2.6 Trigger System

With a potential bunch crossing frequency of 40 MHz, corresponding to the LHC design bunch spacing of 25 ns, and with several inelastic pp collisions in each bunch crossing, a large amount of data is generated that is impossible to store. The rate of events that can be stored for further analysis is $\mathcal{O}(100)$ Hz. It is therefore necessary to reduce the rate of events by almost six orders of magnitude and keep only the most interesting events. This task is performed by the trigger system, which is the first step in the event selection process. It is important that the trigger system does not miss any interesting events that will be otherwise lost forever.

The CMS experiment utilizes a two-level trigger system. The first level, Level 1 (L1), of the trigger system consists of custom-designed, largely programmable fast electronics, and is designed to reduce the event rate down to 100 kHz. For this purpose the L1 Trigger uses coarsely segmented data from the calorimeters and the muon system. The L1 Trigger has local, regional, and global components. The local components consists of the Local Triggers, also called Trigger Primitive Generators (TPGs), which are based on energy deposit in calorimeter trigger towers and track segments or hit patterns in the muon system. Regional Triggers combine information from the Local Triggers and use pattern logic to form in limited spatial regions and rank trigger objects such as electron and muon candidates. The Global Calorimeter and Global Muon Triggers, using the information from the Regional

Triggers, determine the highest-ranked among the calorimeter and muon trigger objects and transfer them to the Global Trigger. The Global Trigger makes the decision to reject an event or to keep it for further evaluation. This decision is based on the algorithm calculations as well as the readiness of the subdetectors and Data Acquisition (DAQ) systems, which is determined by the Trigger Control System (TCS). Once issued, the Level-1 Accept (L1A) decision is communicated to the subdetector systems through the Timing, Trigger and Control (TTC) system. The architecture of the L1 Trigger is depicted in Figure 3.20. The allowed L1 Trigger latency, i.e., the time between a given bunch crossing and the distribution of the L1A decision to the detector front-end electronics, is 3.2 μs. During this time, the high-resolution data have to be temporarily stored in memory buffers in the front-end electronics. The L1 Trigger electronics is partly located on the detector itself and is partly housed in the underground control room located approximately 90 m from the underground experimental cavern.

The second level of the trigger system is the High-Level Trigger (HLT) consisting of a farm of commercially available CPUs running a version of the offline reconstruction software optimized for fast processing. The HLT has access to the high-resolution data and can therefore perform complex calculations similar to those made in offline analysis if required for specially interesting events. The HLT selects and sorts events in different datasets, called *primary datasets* (PDs), based on a list of triggers, called *trigger table* or *trigger menu*. The trigger table is organized so as to minimize the overlap between different primary datasets by putting events with similar event contents and topologies into the same primary dataset. The HLT

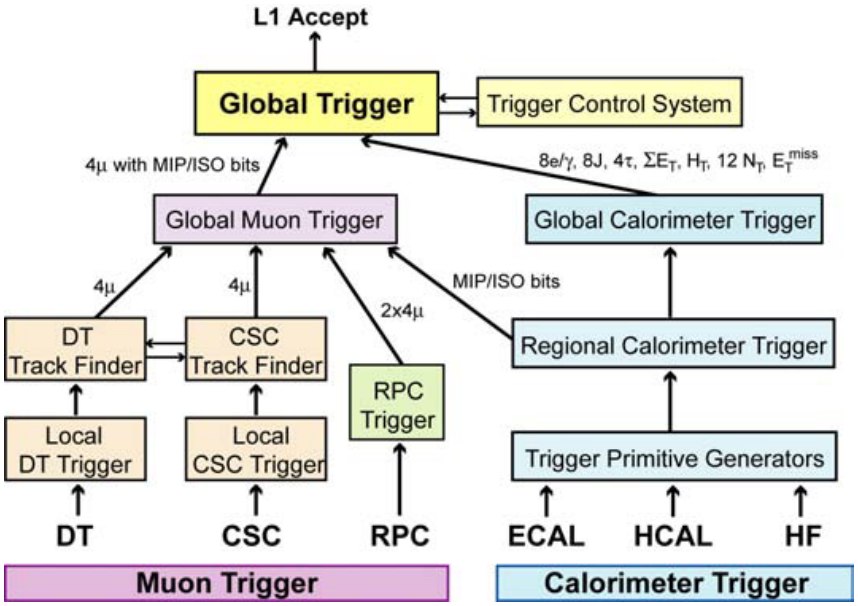

Figure 3.20: Architecture of the Level-1 Trigger.

software is designed to be flexible and to allow changes in the trigger table over time. The HLT reduces the event rate from the L1 Trigger output rate (100 kHz) down to an event rate of $\mathcal{O}(100)$ Hz that can be stored for further offline analysis. The combined L1 and HLT reduction in the event rate is therefore by a factor of $\sim 10^5$.

The maximum L1 and HLT event rates reached during stable beam conditions in the 2010 run were around 65 kHz and 350 Hz, respectively. The live time for the same period for the entire trigger system was 99.55%.

Chapter 4

Event Reconstruction

A necessary prerequisite for any type of physics analysis is the event reconstruction. Different types of particles produce different detection patterns in the CMS detector, as depicted in Figure 4.1. Muons produce hits in the inner tracking system and the outer muon system and deposit very little energy in the calorimeters. Electrons produce hits in the inner tracking system and deposit most of their energy in the ECAL, while photons do not produce hits in the inner tracking system and deposit most of their energy in the ECAL. Hadrons deposit most of their energy in the HCAL, with charged hadrons also producing hits in the inner tracking system. It is the goal of the event reconstruction algorithms to exploit these differences and to use a combination of information from different CMS subdetectors in an attempt to identify and measure particles and other higher-level objects present in the event.

The event reconstruction starts from raw data, containing digitized event information recorded by different subdetector systems, and applies to it a set of reconstruction and pattern recognition algorithms in order to produce various higher-level objects. At CMS, the event reconstruction process is divided into three steps: *local*, *global*, and *high-level* reconstruction. In the local reconstruction step, digitized raw data from individual subdetector modules are used to produce reconstructed hits, or "RecHits". The RecHits typically represent position measurements in the tracking-

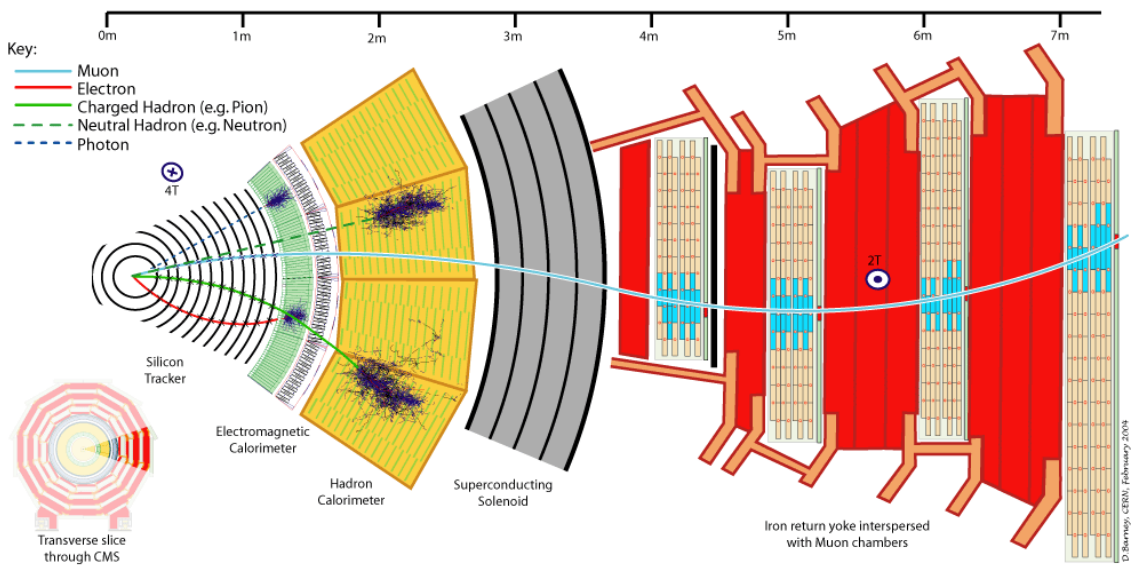

Figure 4.1: Transverse slice through the CMS detector depicting typical detection patterns for muons, electrons, photons, and charged and neutral hadrons.

type subdetectors, such as the tracker and muon systems, or energy depositions in the calorimetric subdetectors, such as the ECAL and HCAL. During the process of local reconstruction, detector calibration and alignment data are extensively used to assign the correct position or energy to a given RecHit. In the global reconstruction step, information from different modules within a given subdetector is combined. For example, charged particle tracks are reconstructed from tracker RecHits. In the final, high-level reconstruction step, information obtained across different subdetectors is combined to produce objects suitable for use in high-level triggering or for physics analysis. For example, electrons are reconstructed by combining information from the ECAL and tracker systems. Known dead or noisy channels in the CMS subdetectors are masked in the event reconstruction.

The event reconstruction is performed utilizing the CMS application framework based on the C++ and Python programming languages and the ROOT [85–87]

data analysis framework. For more information about the architecture, design and implementation of the CMS software framework, the reader is referred to [65] and [79]. An important design feature of the reconstruction code is that the same code is run both in the HLT and in the offline reconstruction. When used in the HLT, the code is run in a configuration that gives the most precise reconstruction possible within the allowed processing time. In order to additionally reduce the processing time, the reconstruction is performed only in those regions of the detector from which a Level-1 trigger was received. In this chapter, a brief overview of the reconstruction of higher-level objects used in this analysis is presented.

4.1 Track and Vertex Reconstruction

The track reconstruction relies on a good estimate of the location of the luminous region near the center of the CMS detector, where protons from both LHC beams collide, and referred to as the beam spot. Starting from the location of the beam spot, an initial round of track and vertex reconstruction is performed using only pixel hits. The pixel vertices found at this stage are used in the standard track reconstruction, which is performed in an iterative procedure making use of the Combinatorial Track Finder (CTF) [88–90]. Each iteration starts with the creation of *seeds* that serve as building blocks for the initial estimate of a charged particle trajectory. These initial trajectories are then propagated through the tracker volume in order to find additional compatible hits in other layers of the tracker system. As new compatible hits are found, track parameters and uncertainties are updated. This

procedure continues until the boundary of the tracker system is reached or until no compatible hits are found. At that point, the final collection of compatible hits is fitted to obtain the best estimate of the track parameters. There are six iterations in total. The main difference between different iterations is in the seeding step. In the first two iterations, triplets of pixel hits or pairs of pixel hits with an additional constraint from the beam spot or a pixel vertex are used as seeds to find prompt tracks with transverse momenta $p_{\mathrm{T}} > 0.9$ GeV. The third iteration removes the transverse momentum cut, while the fourth iteration includes hits from the strip tracker to reconstruct displaced tracks. The last two iterations use pairs of strip tracker hits as seeds for the reconstruction of tracks lacking pixel hits, such as tracks originating from photon conversions or nuclear interactions in the tracker material. Between each iteration, tracker hits that can be unambiguously assigned to tracks from the previous iteration are removed from the collection of tracker hits. This reduced collection of tracker hits is then used in the next iteration. At the end of each iteration, the reconstructed tracks are filtered to remove those that are likely fakes and to label the remaining tracks according to their quality. The filtering is performed based on the number of hits in a track, the normalized χ^2 of the track (χ^2/ndof[1]), the longitudinal and transverse impact parameters, and their significances[2]. The reconstructed tracks failing the loosest selection are rejected, while those that pass the tightest selection are labeled as *highPurity* [89]. The main advantage of this iterative track reconstruction approach is high track reconstruction efficiency and a

[1]Number of degrees of freedom

[2]Impact parameter significance, S_{IP}, is defined as the ratio of the impact parameter to its uncertainty, i.e., $S_{\mathrm{IP}} = \mathrm{IP}/\sigma_{\mathrm{IP}}$.

low fake rate.

The reconstruction of the primary interaction vertex starts from prompt tracks selected based on their transverse impact parameter significance with respect to the beam spot, number of strip and pixel hits, and the normalized track χ^2 [91, 92]. The selected tracks are then clustered based on their z coordinates at the point of closest approach to the beam spot by requiring tracks in each cluster to be separated in z by less than a distance $z_{\text{sep}} = 1$ cm from their nearest neighbor. This particular choice of the clustering distance represents a compromise between large values of z_{sep}, which result in merging of nearby vertices, and small values of z_{sep}, which produce false vertices from vertex splitting. Clusters containing at least two tracks are fitted with an adaptive vertex fit [93] to compute the best estimate of vertex parameters. If multiple primary vertices are reconstructed, they are stored in the collection of primary vertices and ordered in descending order of the sum of the p_{T}^2 of the associated tracks. If no primary vertices are found, a fake primary vertex with the same location as the beam spot is created. In the adaptive vertex fit, each track associated with a vertex is assigned a track weight between 0 and 1 based on its compatibility with the vertex. For a track consistent with the given vertex, its weight is close to 1. The number of degrees of freedom of a primary vertex is defined as

$$n_{\text{dof}} = 2 \sum_i w_i - 3, \tag{4.1}$$

where w_i is the weight of the i^{th} track. This parameter is therefore strongly correlated with the number of tracks compatible with the primary interaction vertex,

and can be used to select real pp collisions.

4.2 Electron Reconstruction

Electrons, being charged particles that deposit most of their energy in the electromagnetic calorimeter, are reconstructed using information from both the inner tracking system and the calorimeters. Electon and photon showers deposit their energy across several neighboring ECAL crystals, resulting in the reconstruction of a cluster of energy in the ECAL. However, the presence of the tracker material in front of the calorimeter leads to the production of electron brehmsstrahlung and photon conversions. Because of the strong solenoidal magnetic field, the energy reaching the calorimeter is spread in ϕ when the shower starts in the tracker. Hence, to include as much energy deposited by electrons and photons as possible, a cluster of clusters extending in ϕ, called *supercluster*, is built. A supercluster is therefore a group of one or more associated clusters of energy deposits in the ECAL characterized by a narrow width in η and its spread in ϕ. The electron reconstruction at CMS [94–96] is performed using two complementary algorithms with differing track seeding procedure: the first uses *tracker-driven* seeding and the second uses *ECAL-driven* seeding. The tracker-driven seeding is more suitable for low-p_{T} electrons and also performs better for electrons embedded inside jets. The ECAL-driven seeding starts from the reconstruction and selection of ECAL superclusters with transverse energy $E_{\mathrm{T}} > 4$ GeV and the ratio of the hadronic energy behind the supercluster over the supercluster energy $H/E < 0.15$, and is optimized for isolated electrons. In

the first filtering step, superclusters are matched to track seeds consisting of pairs or triplets of pixel hits from which electron tracks are built using a Gaussian Sum Filter (GSF) [97] algorithm. This algorithm is capable of modeling the electron energy loss through radiative interactions in the tracker material and is able to follow the change in curvature of the electron track, allowing an unbiased estimate of the track momentum at both track ends. The initial filtering obtained through the track-seeding procedure is complemented by an additional preselection. For tracker-driven electron candidates, the preselection is based on a multivariate analysis [98]. For ECAL-driven electron candidates, the preselection is based on the matching between the GSF track and the supercluster in η and ϕ. A small fraction of ECAL-driven electron candidates ($\sim$ 1% for isolated electrons) that are not accepted by this matching preselection but which pass the multivariate preselection are kept in the final collection of electron candidates. It is also possible for electron candidates to be both tracker- and ECAL-driven.

4.3 Muon Reconstruction

Muons are reconstructed using information from the inner tracking system and the muon system [99]. The CMS calorimeters provide supplementary information used in muon identification variables. Before a dedicated muon reconstruction can be performed, tracks are reconstructed independently in the inner tracking system and in the muon spectrometer, resulting in a collection of *tracker tracks* and *standalone-muon tracks*, respectively. In the *outside-in* reconstruction approach, a

standalone-muon track is used as a starting point and a search is performed for a matching tracker track. If a matching tracker track is found, a *global-muon track* is fitted, combining hits from the tracker track and standalone-muon track. This type of global track fit can improve the muon momentum resolution at large transverse momenta ($p_{\mathrm{T}} \gtrsim 200$ GeV). In the *inside-out* reconstruction approach, all tracker tracks with $p_{\mathrm{T}} > 0.5$ GeV and $p > 2.5$ GeV are considered as potential muon candidates and are extrapolated to the muon system taking into account the expected energy loss and the uncertainty arising from multiple scattering. If at least one matching muon segment, i.e., a short track stub formed from DT or CSC hits, is found at the expected location in the muon system, the corresponding tracker track qualifies as a *tracker-muon track*. At low muon momenta ($p \lesssim 5$ GeV), this approach is more efficient than the global muon reconstruction since it requires only one muon segment in the muon system.

The muon reconstruction therefore produces three non-exclusive categories of muon candidates: *standalone muons*, *global muons*, and *tracker muons*. The majority of muons from collisions are reconstructed as either global or tracker muons, and often as both. Only about 1% of muons from collisions are standalone muons only. This category of muons, however, is more susceptible to contamination from cosmic muons. Muon candidates from all three categories are merged into a single collection with each candidate containing information from all available fits. Tracker and global muon candidates that share the same tracker track are merged into a single muon candidate. Similarly, standalone muons having no corresponding global muon are merged with a tracker muon if they share a muon segment.

4.4 Particle-Flow Event Reconstruction

The particle-flow (PF) event reconstruction algorithm [100] provides an alternative particle identification. It starts from the following basic building *elements*: reconstructed charged-particle tracks, calorimeter clusters, and muon tracks. The clustering of the calorimeter energy deposits is performed separately in each subdetector: EB, EE, HB, HE, and the two layers of PS. In the HF, no clustering is performed, so each HF cell gives rise to one cluster.

In general, a given particle is expected to give rise to more than one PF element in different CMS subdetectors. It is therefore necessary to correctly link together different PF elements in order to fully reconstruct each particle and to avoid any possible double counting from different subdetectors caused by incorrect linking. It is the task of the link algorithm to tentatively match each pair of the PF elements and to define their "distance" as a measure of the link quality. For links between a tracker track and a calorimeter cluster, the link distance is defined as the distance in the η-ϕ plane between the track extrapolated to the calorimeter and the calorimeter cluster; for links between two calorimeter clusters, it is defined as their distance in the η-ϕ plane; and for links between a tracker track and a muon track, it is defined as the χ^2 of a global-muon track fit. The link algorithm finally produces *blocks* of PF elements that are linked together, either directly or indirectly, with a reasonable link distance.

PF blocks constitute input for the particle reconstruction and identification part of the particle-flow algorithm. The muon reconstruction and identification is

first performed for each PF block, followed by the electron reconstruction and identification. All PF elements used to build PF muons and electrons are then removed from PF blocks. In the next step, all the remaining PF blocks and their constituent elements give rise to charged hadrons, photons, or neutral hadrons, and less frequently additional muons. Depending on the particle type, a dedicated calibration of calorimeter clusters may be performed as part of the particle reconstruction and identification. All particles reconstructed and identified by the particle-flow algorithm are stored in a collection of PF *candidates* which represent a global description of each event. This collection of PF candidates is used as input for the subsequent reconstruction of higher-level objects used in physics analysis. The particle-flow event reconstruction has a built-in identification and removal of the anomalous noise signals in the calorimeters [98, 101], similar in performance to the calorimeter noise cleaning implemented in the rest of the event reconstruction.

4.5 Jet and MET Reconstruction

Jets [102] are collimated sprays of energetic hadrons arising from the fragmentation and hadronization of an underlying quark or gluon. At CMS, jets are reconstructed by clustering objects using the anti-k_{T} [103] jet clustering algorithm. In the standard event reconstruction at CMS, four different types of anti-k_{T} jets are reconstructed [104]: calorimeter jets (Calo jets), Jet-Plus-Track jets (JPT jets), particle-flow jets (PF jets), and track jets. Different jet types combine differently information from individual CMS subdetector in order to form the input for the

jet clustering algorithm. For PF jets, the PF candidates are used as input for the jet clustering algorithm. Since the particle-flow algorithm attempts to identify individual charged hadrons and photons inside jets, which constitute $\sim 90\%$ of the jets energy, PF jets are expected to have more precise momentum measurements with better energy and spatial resolutions than the other jet types. In this analysis, anti-k_{T} PF jets with a radius parameter [103] $R = 0.5$ are used.

Neutral weakly interacting particles, such as neutrinos, produced in pp collisions normally escape undetected, and their presence must be inferred from the imbalance of total momentum. As stated in Section 3.2, the vector momentum imbalance in the transverse plane is known as the missing transverse momentum, and is denoted by $\vec{\not{E}}_{\mathrm{T}}$. Its magnitude is called missing transverse energy (MET), and is denoted by $\not{E}_{\mathrm{T}}$. In the standard event reconstruction at CMS, three different types of $\not{E}_{\mathrm{T}}$ are reconstructed [82]: calorimeter $\not{E}_{\mathrm{T}}$ (Calo $\not{E}_{\mathrm{T}}$), track-corrected $\not{E}_{\mathrm{T}}$ (TC $\not{E}_{\mathrm{T}}$), and particle-flow $\not{E}_{\mathrm{T}}$ (PF $\not{E}_{\mathrm{T}}$). As with jets, different types of $\not{E}_{\mathrm{T}}$ combine differently information from individual CMS subdetector in order to calculate the missing transverse momentum. In the particle-flow event reconstruction, the missing transverse momentum $\vec{\not{E}}_{\mathrm{T}}$ is calculated as the negative of the vector sum of the transverse momenta of all PF candidates, i.e.,

$$\vec{\not{E}}_{\mathrm{T}} = -\sum_{i} \vec{p}_{\mathrm{T},i}, \tag{4.2}$$

where the sum is performed over all PF candidates. The missing transverse energy

$\not\!\!E_{\mathrm{T}}$ is therefore defined as

$$\not\!\!E_{\mathrm{T}} = \left|\vec{\not\!\!E}_{\mathrm{T}}\right|. \tag{4.3}$$

For similar reasons as for PF jets, PF $\not\!\!E_{\mathrm{T}}$ is expected to perform better than the other types of $\not\!\!E_{\mathrm{T}}$. Hence, the particle-flow $\not\!\!E_{\mathrm{T}}$ is used in this analysis.

4.6 Event and Detector Simulation

An important aspect of experimental research is the simulation of processes being measured in an experiment. In this way, it is possible to compare measured results with theoretical expectations and establish how well a given process is understood. Very often measured results lead to improvements in theoretical description. At the same time, simulated processes are used to optimize the design of future experiments and to develop and optimize analysis tools and techniques at existing experiments. In searches for new physics simulated events are especially important in establishing if measured results can be interpreted in the context of the Standard Model, or if the effects of new physics are being observed. For all these reasons, simulation tools have become indispensable in modern experimental research.

Simulation of collision events at particle colliders is divided in two steps. In the first step, the collision process is simulated using software programs, called *event generators*, that produce as their output a list of particles produced in the collision. In the second step, these particles are passed on as input to software programs that simulate the interaction of particles with the detector material. Both event generator and detector simulation tools make use of Monte Carlo (MC) methods to

simulate the probabilistic nature of particle collisions and interactions of particles with matter.

4.6.1 Event Generation

Protons are color-neutral bound states of three quarks and "sea" gluons and quark-antiquark pairs, collectively referred to as *partons*. Each of these partons carries a fraction x of the proton momentum. The probability that parton a inside proton A carries a fraction x_a of the proton momentum is described by a parton distribution function (PDF) $f_{a/A}(x_a, Q^2)$, where Q^2 is the square of the exchanged four-momentum during the interaction. PDFs at a given Q^2 have to be determined from experimental data, and their evolution with Q^2 is described by DGLAP equations [105]. When the two high-energy protons A and B inelastically collide, the exchanged energy is typically much higher than the proton mass, leading to the interaction time that is much shorter than a time scale on which partons inside a given proton interact with each other. Because of this, parton a from proton A has enough time to interact with only one parton, parton b, from proton B. Therefore, an inelastic collision of protons A and B can be viewed as consisting of a "hard scattering" of partons a and b and "soft interactions" among the remaining partons coming from broken-up protons, often referred to as *beam remnants*. In the high energy limit, the center-of-mass energy of the system of hard scattering partons is $\sqrt{\hat{s}} = \sqrt{x_a x_b s}$, where $\sqrt{s}$ is the center-of-mass energy of the proton-proton system. Depending on what charges they carry, partons will radiate photons and gluons which can split

into quark-antiquark pairs which then further radiate. Hence, the hard scattering will have associated with it initial- and final-state radiation (ISR/FSR radiation) produced by incoming and outgoing partons, respectively. Everything else in the event except the hard scattering and the associated ISR/FSR radiation is referred to as the *underlying event*. A schematic view of a proton-proton collision is shown in Figure 4.2.

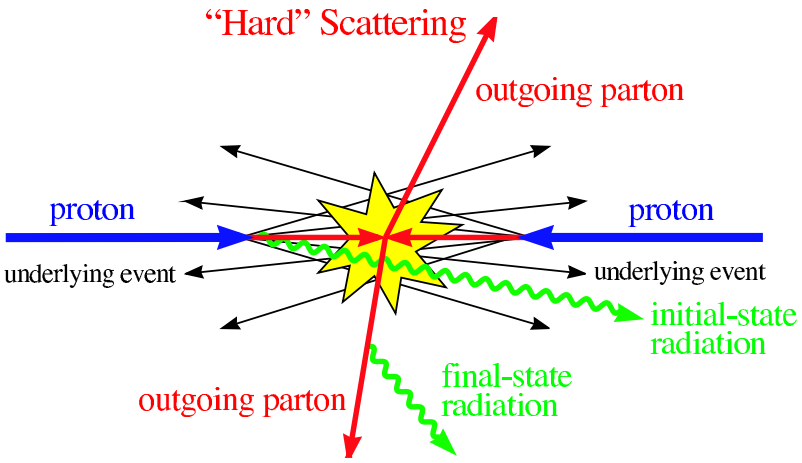

Figure 4.2: Schematic view of a proton-proton collision, with a $2 \to 2$ hard scattering event (from [105]).

The properties of the hard scattering component of proton-proton collisions can be predicted with good precision using perturbative QCD. The underlying event, on the other hand, involves non-perturbative QCD effects and therefore has to be described by various phenomenological model which have to be properly "tuned" to reproduce experimental observations. From the QCD factorization theorem [105], it follows that the total cross section for a $pp \to X$ process can be described as:

$$\sigma_{pp\to X}(s) = \sum_{a,b} \int dx_a dx_b f_{a/A}(x_a, \mu_F^2) f_{b/B}(x_b, \mu_F^2) \hat{\sigma}_{ab\to X}(x_a x_b s, \mu_R^2), \tag{4.4}$$

corresponding to the structure depicted in Figure 4.3. Here, μ_F is the *factorization scale*, which can be viewed as a scale that separates long- and short-distance physics, and μ_R is the *renormalization scale* for the QCD running coupling. The standard choice is $\mu_F = \mu_R = \mu$, with μ set to some characteristic scale of the hard scattering (e.g., the invariant mass of the system of hard scattering partons, the p_{T} of the hard scattering partons, etc.).

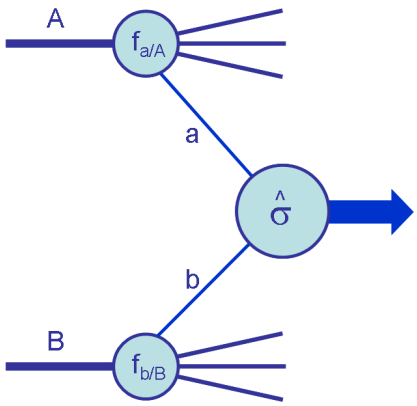

Figure 4.3: Diagrammatic structure of a generic hard scattering process (from [105]).

All of the above-described features of proton-proton collisions and hard scattering are employed in Monte Carlo event generators to simulate proton-proton collision events. In more traditional event generators, such as PYTHIA [106] and HERWIG [107], the hard scattering is typically described by a $2 \to 2$ matrix element, with the initial- and final-state radiation produced through the process called *parton showering* [105]. The parton shower, however, is an approximation that describes well soft and collinear radiation, but does not provide an accurate description of hard, large-angle radiation. This is particularly important at the LHC where large center-of-mass energy can give rise to events with multiple hard and well separated

jets. For this purpose, new generation of event generators has been developed that are capable of generating matrix elements with additional hard and well separated partons in the final state. Examples of such event generators are MadGraph [108] and alpgen [109]. They, however, do not generate soft and collinear radiation, and therefore have to be interfaced with traditional event generator which provide the showering of the partons coming from matrix elements. In this way, the phase space for parton radiation is divided into two regions, one dominated by matrix elements and another dominated by the parton showers. However, some care must be taken when combining these two approaches, since they can overlap at the boundary of these two phase space regions. To avoid any double-counting of such regions, algorithms for matching matrix elements with parton showers have been developed [105].

The final stage of the event generation is the process of transforming partons coming out of the parton shower to hadrons, which are observed experimentally. This process, called *hadronization*, is based on phenomenological models that try to capture main aspects of this otherwise non-perturbative process.

4.6.2 Detector Simulation

A detailed simulation of the CMS detector response is based on the Geant4 [110, 111] simulation toolkit, and is integrated in the CMS software framework [79]. Several different Monte Carlo event generators can be interfaced with the CMS application framework to provide the generated collision events as input for the detailed detector simulation, often referred to as the *full detector simulation*. Monte-Carlo-

generated collision events processed through the full detector simulation are reconstructed in the same manner as collision data. The detector geometry description used in the simulation and reconstruction of MC events can mimic ideal detector conditions, and can also include realistic misalignment and miscalibration scenarios as well as a map of dead and noisy channels found in the real detector. The position and width of the beam spot in the simulation can be adjusted to match what is observed in collision data.

Chapter 5

Data Analysis

5.1 Search Strategy

The pair production of first-generation scalar leptoquarks in pp collisions depends only on the leptoquark mass, as described in Section 2.2. From Figure 2.3, the total pair-production cross section for scalar leptoquarks with $M_{\mathrm{LQ}} \sim 300$ GeV is approximately 1 pb. This observation lead to the expectation that light leptoquarks could be discovered in the early LHC data, with less than 100 pb^{-1} of integrated luminosity. The search described in this dissertation is performed using the very first LHC collision data at $\sqrt{s} = 7$ TeV, and considering the limited amount of integrated luminosity available, a simple event counting approach, often called a "cut-and-count" approach, was adopted to analyze the data.

The basic strategy to search for pair production of first-generation scalar leptoquarks in the $e\nu jj$ channel is to look for events containing exactly one electron and at least two jets. The reason for not requiring exactly two high-p_{T} jets is that additional high-p_{T} jets can arise from the initial- and final-state gluon radiation (ISR/FSR jets). However, events with this signature can also arise from various Standard Model processes with much larger production cross sections, collectively referred to as *background*. Examples of such processes include the pair production of top quarks ($t\bar{t}$); associated production of a W boson with jets (W+jets); associ-

ated production of a Z boson with jets (Z/γ^*+jets); and single top, diboson (WW, WZ, ZZ), b+jets, and γ+jets production. There is also a non-negligible contribution from QCD multijet events in which a jet is misidentified as an electron. Since any leptoquarks expected to be discovered are heavier than any of the particles in background processes, most of the background events can be rejected by simply requiring the electron to have high p_{T}. Similarly, the presence of a high-p_{T} neutrino results in the reconstruction of a large $\not\!\!E_{\mathrm{T}}$. Hence, an additional requirement of large reconstructed $\not\!\!E_{\mathrm{T}}$ will further reduce the background and lead to a reasonable *signal-over-background ratio* (S/B). After the application of p_{T} and $\not\!\!E_{\mathrm{T}}$ cuts, the major sources of background events are the Standard Model processes with neutrinos in the final states ($t\bar{t}$, W+jets, single top, diboson, and b+jets) and events with spurious $\not\!\!E_{\mathrm{T}}$ due to mismeasurement of jets (Z/γ^*+jets, γ+jets, and QCD multijet events). The fact that all leptoquark decay products typically have high p_{T} can be exploited to further discriminate signal from the background by cutting on the S_{T} variable defined as:

$$S_{\mathrm{T}} = p_{\mathrm{T},e} + p_{\mathrm{T},j1} + p_{\mathrm{T},j2} + \not\!\!E_{\mathrm{T}}, \tag{5.1}$$

where $p_{\mathrm{T},e}$ is the electron p_{T}, and $p_{\mathrm{T},j1}$ and $p_{\mathrm{T},j2}$ are the p_{T} of the leading and second leading (in p_{T}) jet, respectively. A cut on S_{T} is a general event selection requirement suitable for the selection of a decay of a pair of massive particles, and it provides a strong *signal-to-background* discrimination power. At this stage of the selection, the two dominant SM background processes are the pair production of top quarks and associated production of a W boson with jets, examples of which are shown in

Figure 5.1.

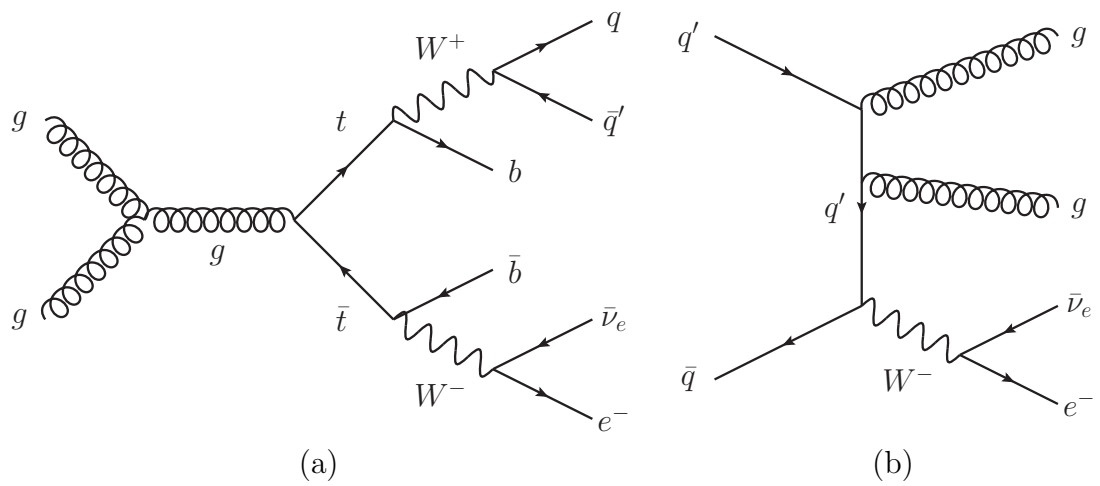

Figure 5.1: Examples of LO Feynman diagrams for (a) $t\bar{t}$ and (b) W+jets production, the two dominant SM backgrounds in the $e\nu jj$ channel.

Of all the SM background processes, W+jets production has the largest production cross section. These events can be further suppressed by rejecting all events in which the *transverse mass* of the electron and neutrino, $M_{\mathrm{T},e\nu}$, is consistent with the W boson mass. The transverse mass M_{T} is defined as the Lorentz-invariant two-particle mass using only the momentum components in the transverse plane [4, 112]:

$$M_{\mathrm{T}}^2 = (p_{\mathrm{T},1}^{\mu} + p_{\mathrm{T},2}^{\mu})(p_{\mathrm{T},1;\mu} + p_{\mathrm{T},2;\mu}), \tag{5.2}$$

where $p_{\mathrm{T},i}^{\mu} = (E_{\mathrm{T},i}, \vec{p}_{\mathrm{T},i})$ and $E_{\mathrm{T},i}^2 = E_i^2 - p_{z,i}^2$, resulting in

$$M_{\mathrm{T}}^2 = m_1^2 + m_2^2 + 2\left(E_{\mathrm{T},1}E_{\mathrm{T},2} - \vec{p}_{\mathrm{T},1} \cdot \vec{p}_{\mathrm{T},2}\right). \tag{5.3}$$

In the limit of zero-mass particles ($E_{\mathrm{T},i} = p_{\mathrm{T},i}$), which is an approximation justified

when $E_{\mathrm{T},i} \approx p_{\mathrm{T},i} \gg m_i$, Equation 5.3 reduces to

$$M_{\mathrm{T}}^2 = 2p_{\mathrm{T},1}p_{\mathrm{T},2}\left(1 - \cos\Delta\phi_{12}\right), \tag{5.4}$$

where $\Delta\phi_{12}$ is the opening angle between particles 1 and 2 in the transverse plane. For a W decaying to an electron and a neutrino, the transverse mass may thus be written:

$$M_{\mathrm{T},e\nu} = \sqrt{2p_{\mathrm{T},e}\not{E}_{\mathrm{T}}\left[1 - \cos\Delta\phi(e,\not{E}_{\mathrm{T}})\right]}, \tag{5.5}$$

where $\not{E}_{\mathrm{T}}$ is used as an estimator of the transverse momentum of the neutrino, and $\Delta\phi(e,\not{E}_{\mathrm{T}})$ is the azimuthal opening angle between the electron transverse momentum and $\vec{\not{E}}_{\mathrm{T}}$. The M_{T} distribution of the W exhibits a Jacobian peak at the W boson mass, so selected events with $M_{\mathrm{T},e\nu}$ less than some value greater the W boson mass are dominated by the W+jets background. A cut on $M_{\mathrm{T},e\nu}$ is thus useful for rejecting W+jets events, as well as other SM backgrounds containing W bosons.

The invariant mass of the electron-jet pairs can be used to additionally qualify the selected events and establish the presence of the leptoquark signal, since leptoquarks would produce a peak in the distribution of this observable. The same is true for the transverse mass of the neutrino-jet pairs. These types of resonant signatures in the lepton-jet spectra do not occur within the Standard Model.

5.2 Data Samples

The proton-proton collision data used in this analysis were collected in 2010 by the CMS detector at the CERN LHC and correspond to an integrated luminosity of 36 pb^{-1}. The number of additional inelastic pp collisions per bunch crossing (pile-up) in the entire data-taking period considered was relatively modest and corresponded to an average of approximately 2 pile-up interactions per bunch crossing. Only runs that were taken during periods with stable LHC beams and with all CMS subdetectors operating without problems have been used in the analysis (the lumi mask file that was used to select certified luminosity sections is `Cert_136033-149442_7TeV_Nov4ReReco_Collisions10_JSON.txt`[1]). The luminosity profile for delivered, recorded, and certified collision data for the entire 2010 run is shown in Figure 5.2. The collision data used in the analysis are stored in the primary datasets listed in Tables 5.1 and 5.2. The datasets include events collected by a mixture of electron and photon triggers, respectively, except for the EG dataset which contains both. The events used for the LQ search and for the determination of the main backgrounds in this analysis are collected by unprescaled triggers forming the datasets listed in Table 5.1. Prescaled single photon triggers from the datasets listed in Table 5.2 are used for a data-driven estimation of the QCD multijet background, which is described in Section 5.5.2. To adapt to the rapid increase in the instantaneous luminosity delivered by the LHC during the 2010 run, several versions of the HLT trigger menu were deployed, with each new version applying

[1] Can be found in
/afs/cern.ch/cms/CAF/CMSCOMM/COMM_DQM/certification/Collisions10/7TeV/Reprocessing/ or at
https://cms-service-dqm.web.cern.ch/cms-service-dqm/CAF/certification/Collisions10/7TeV/Reprocessing/

more stringent trigger requirements in order to keep the total HLT rate within the allowed limits ($\lesssim$ 350 Hz). The trigger tables used to form the primary datasets listed in Tables 5.1 and 5.2 are reported in Appendix A.

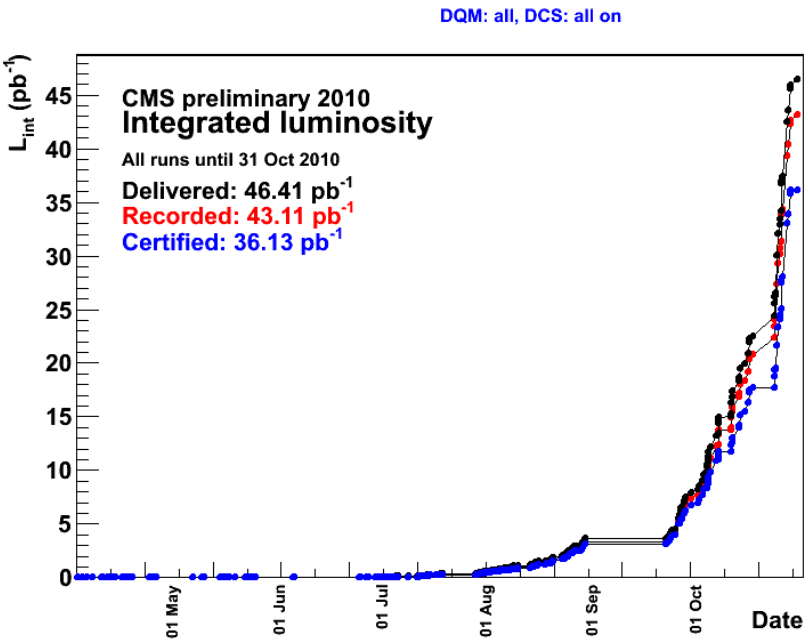

Figure 5.2: Luminosity profile and total integrated luminosity for delivered, recorded, and certified collision data for the entire 2010 run at 7 TeV.

5.3 Monte Carlo Samples

The collision data are compared to samples of Monte Carlo generated events. Different MC event generators were used to produce different MC samples, as detailed below. For the generation of all the MC samples used in this analysis, the CTEQ6L1 [35] parton distribution functions and the D6T [113] underlying event tune were used. The detector geometry description included realistic subsystem conditions such as dead and noisy channels, and the position and width of the beam spot have been adjusted to match the collision data.

Table 5.1: Electron primary datasets: dataset name, version of the CMS software (CMSSW) used for the event reconstruction, run range considered and corresponding integrated luminosity $\mathcal{L}_{\text{int}}$ after removing data-taking periods with known detector problems.

Primary dataset	CMSSW version	Run range (Data-taking era)	$\mathcal{L}_{\text{int}}$ [pb^{-1}]
/EG/Run2010A-Nov4ReReco_v1/RECO	CMSSW_3_8_6	136035–144114 (Run2010A)	3
/Electron/Run2010B-Nov4ReReco_v1/RECO	CMSSW_3_8_6	146428–149294 (Run2010B)	33
		Total integrated luminosity	36

Table 5.2: Photon primary datasets: dataset name, version of the CMS software (CMSSW) used for the event reconstruction, run range considered and corresponding integrated luminosity $\mathcal{L}_{\text{int}}$ after removing data-taking periods with known detector problems.

Primary dataset	CMSSW version	Run range (Data-taking era)	$\mathcal{L}_{\text{int}}$ [pb^{-1}]
/EG/Run2010A-Nov4ReReco_v1/RECO	CMSSW_3_8_6	136035–144114 (Run2010A)	3
/Photon/Run2010B-Nov4ReReco_v1/RECO	CMSSW_3_8_6	146428–149294 (Run2010B)	33
		Total integrated luminosity	36

LQ signal samples are generated using the PYTHIA [106] (v6.4.22) event generator and external SUSY Les Houches Accord (SLHA) decay files [114]. The external SLHA decay files specify the LQ decay products (in this case an electron and a u quark or an electron neutrino and a d quark) as well as the branching ratio β. The unknown Yukawa coupling λ is set to $\lambda = 0.3$. The LQ signal samples at 10 different LQ masses, ranging from 200 to 500 GeV, are generated with $\beta = 0.5$, and a generator-level filter selects only events in the $e\nu jj$ channel ($\mathrm{LQ}\overline{\mathrm{LQ}} \to e^- u\bar{\nu}_e\bar{d}, \nu_e d e^+\bar{u}$), with a filter efficiency of $2\beta(1-\beta) = 0.5$. The selected events are processed through the full detector simulation and event reconstruction. Although the charge $-1/3$ LQs are generated, the analysis itself is not sensitive to the LQ charge and therefore the model independence of the search is preserved. The full list of the LQ signal samples is reported in Table 5.3 along with the number of generated $e\nu jj$ events, the equivalent integrated luminosity (relative to the nominal cross section with $\mu = M_{\mathrm{LQ}}$ and assuming $\beta = 0.5$), and the corresponding NLO cross section at $\sqrt{s} = 7$ TeV [34] with the associated theoretical uncertainties for each of the LQ samples. A theoretical uncertainty due to the definition of the renormalization and factorization scales (both set to the same value μ) is estimated by varying the scales by a factor of two, up and down, from the nominal value $\mu = M_{\mathrm{LQ}}$. A theoretical uncertainty related to the choice of PDFs used to model the hard scattering of the pp collisions is estimated by varying PDFs within their 90% CL uncertainty using the CTEQ6.6 error PDF set [36].

In addition to the LQ signal samples, SM background samples have been produced. An inclusive $t\bar{t}$+jets sample is generated using the MADGRAPH [108, 115]

Table 5.3: Generated LQ signal samples used in the analysis. For each sample, the number of generated $e\nu jj$ events, the equivalent integrated luminosity, and the corresponding NLO cross section at $\sqrt{s} = 7$ TeV [34] with the associated theoretical uncertainties, are reported.

M_{LQ} [GeV]	Events generated ($e\nu jj$ only)	Equivalent luminosity $\beta = 0.5$ [pb^{-1}]	σ_{NLO} for $pp \to \mathrm{LQ}\overline{\mathrm{LQ}} + X$ [pb]			$\delta\sigma_{\mathrm{NLO}}$ due to PDF unc. [pb]
			$\mu = M_{\mathrm{LQ}}$	$\mu = M_{\mathrm{LQ}}/2$	$\mu = 2M_{\mathrm{LQ}}$	
200	109260	8.40×10^3	11.9	13.5 (+13%)	10.2 (−14%)	0.97 (±8.2%)
250	110189	6.35×10^4	3.47	3.93 (+13%)	2.99 (−14%)	0.37 (±11%)
280	109418	1.20×10^5	1.82	2.05 (+13%)	1.56 (−14%)	0.22 (±12%)
300	109629	1.81×10^5	1.21	1.37 (+13%)	1.04 (−14%)	0.16 (±13%)
320	110153	2.67×10^5	0.82	0.93 (+13%)	0.71 (−14%)	0.11 (±14%)
340	109711	3.85×10^5	0.57	0.64 (+13%)	0.49 (−14%)	0.084 (±15%)
370	110499	6.50×10^5	0.34	0.38 (+13%)	0.29 (−14%)	0.054 (±16%)
400	108796	1.09×10^6	0.20	0.23 (+13%)	0.175 (−14%)	0.036 (±17%)
450	110058	2.32×10^6	0.095	0.11 (+13%)	0.081 (−15%)	0.0185 (±19%)
500	108507	4.72×10^6	0.046	0.052 (+13%)	0.0395 (−15%)	0.010 (±22%)

(v4.4.12) event generator with inclusive top decays and matrix elements corresponding to up to three additional partons. Approximate next-to-next-to-leading-order (NNLO) calculations for the $t\bar{t}$ production cross section are available [116, 117], and events in this sample are normalized to an approximate NNLO cross section of 165 pb for a top quark mass of 173 GeV, as calculated in Reference [116]. W+jets and Z+jets samples, in bins of the boson p_{T} and additional parton multiplicity (from 0 to 5 additional partons), are generated using the ALPGEN [109] (v2.13) event generator with leptonic W and Z boson decays. Separately generating ALPGEN sample in bins of the boson p_{T} and additional parton multiplicity allows for a more efficient population of the regions of the phase space relevant for this analysis, i.e., regions with high boson p_{T} and high additional parton multiplicity. For the W+jets (Z/γ^*+jets) sample, the sum of the LO cross sections for all ALPGEN samples is scaled to the NNLO W (Z/γ^*) production cross section calculated using the FEWZ [118] cross-section calculator, keeping the relative contributions of different samples the same as at the LO and thus assuming a constant k-factor[2] for all bins of the boson p_{T} and additional parton multiplicity. Because of this assumption, the W+jets samples are finally normalized to data using a procedure described in Section 5.5.3.

The single top samples are produced for three separate production channels (s, t, and tW), and are generated using MADGRAPH (v4.2.11) with leptonic top decays in the s- and t-channel samples and inclusive t and W decays in the tW-channel sample. Examples of LO Feynman diagrams for the single top production in the s,

[2] k-factor is the ratio of a higher-order (e.g., NLO) to LO cross section for a given process.

t, and tW channels are shown in Figure 5.3. Events in the s-channel sample are normalized to an approximate NNLO cross section [119], while the t- and tW-channel samples are normalized to NLO cross sections calculated using the MCFM [120] (v5.8) cross-section calculator. The diboson samples (WW, WZ and ZZ) are generated using PYTHIA with inclusive W and Z boson decays and are normalized to NLO cross sections calculated using MCFM. The b+jets and γ+jets samples are generated using MADGRAPH (v4.4.33 and v4.4.30, respectively) in bins of H_{T}[3] with matrix elements corresponding to up to three and four additional partons, respectively. For the b+jets and γ+jets samples, the LO cross sections obtained from MADGRAPH are used. Events generated with MADGRAPH and ALPGEN are subsequently processed with PYTHIA (v6.4.22) to provide the showering of the partons, and to perform the matching of the soft radiation with the contributions from the matrix element. The full list of dataset names and corresponding theoretical cross sections, before any data-driven rescaling, for the signal and background MC samples used in the analysis is reported in Appendix B.

5.4 Event Selection

5.4.1 Electron Selection

Electron selection starts from the collection of GSF electron candidates, described in Section 4.2, to which the High Energy Electron Pairs (HEEP) v3.0 selection criteria for electron identification and isolation is applied in order to select

[3]Here, H_{T} is definedas the scalar sum of the p_{T} of all jets at the parton level where photons and leptons are excluded from the jet definition.

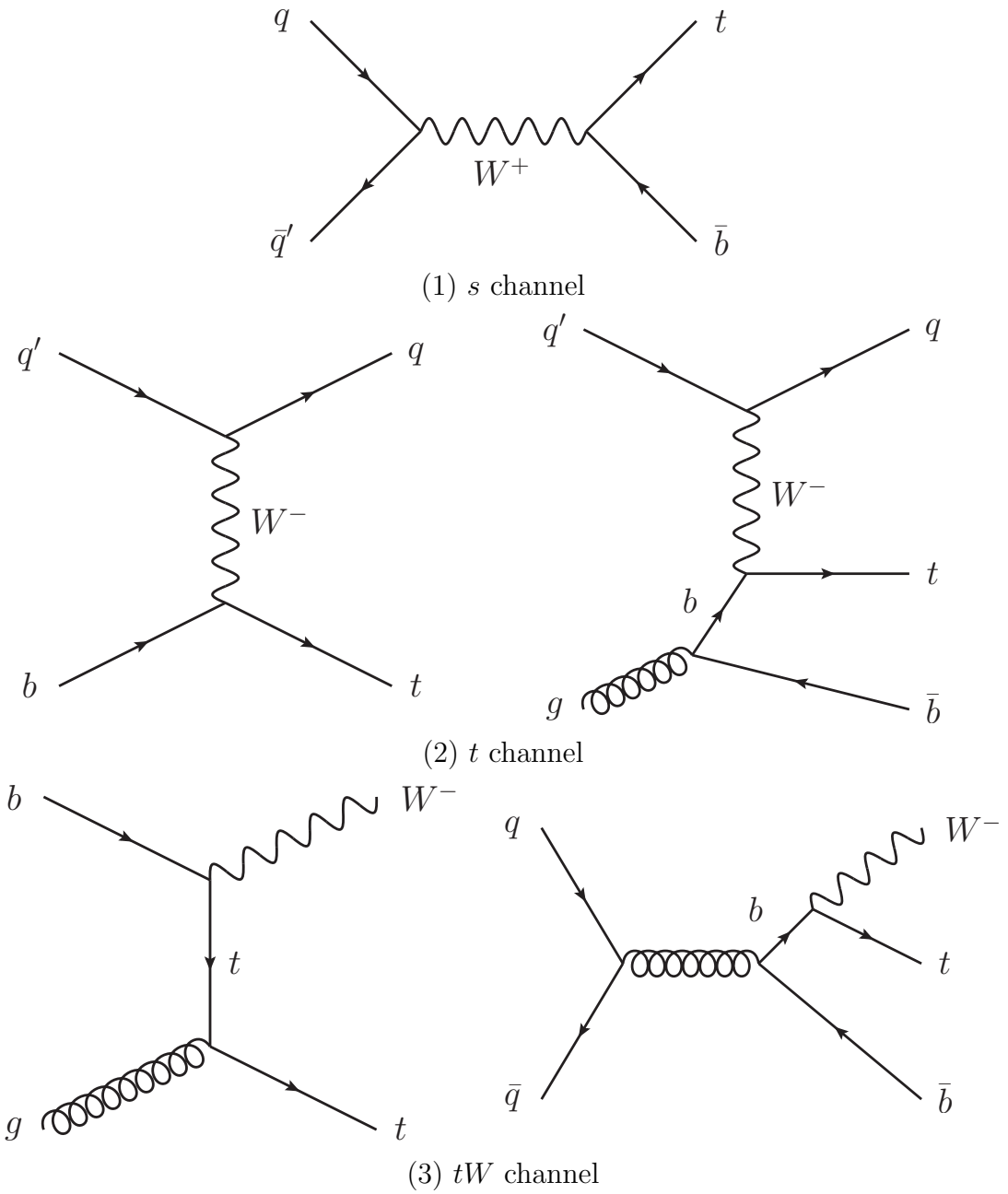

Figure 5.3: Examples of LO Feynman diagrams for single top production in s, t, and tW channels.

true electrons and reduce the contamination from fake electrons. The HEEP selection criteria were originally developed for a Z' search in a final state containing electons [121]. Since it is specifically optimized for high-p_{T} electrons, the HEEP selection was also adopted for the leptoquark searches at CMS. The HEEP selection requires electron candidates to have an electromagnetic cluster in ECAL that is spatially matched to a reconstructed track in the inner tracking system in both η and ϕ, to have a shower shape consistent with that of an electromagnetic shower, and to be isolated from additional energy deposits in the calorimeters and from additional reconstructed tracks, beyond the matched track, in the inner tracking system. A detailed description of the HEEP selection criteria is given in Appendix C. All electron candidates passing the HEEP selection criteria are further required to have a transverse momentum $p_{\mathrm{T}} > 35$ GeV and pseudorapidity $|\eta| < 2.2$. Events with more than one selected electron are rejected.

In addition, to remove possible fake electrons produced by an anomalous noise signal in the ECAL [81] overlapping with a track, a topological cut on the lateral shape of the ECAL supercluster associated with the electron is applied. The electron is rejected if the so-called "Swiss Cross" [81] variable $E4/E1$, where $E1$ is the energy of the highest energy crystal inside the supercluster and $E4$ is the sum of the energies in the four adjacent crystals in η and ϕ, is less than 5%, i.e., if $E4/E1 < 0.05$.

The product of single-electron selection efficiency and the LQ signal acceptance, requiring a minimum electron p_{T} of 35 GeV, is estimated from the MC signal samples and varies from $\sim 76\%$ to $\sim 83\%$ for LQ masses from 200 to 500 GeV.

5.4.2 Muon Selection

Reconstructed muon candidates are required to pass the muon identification criteria defined under the *GlobalMuonPromptTight* selection type. This selection type, designed to suppress hadronic punch-throughs and muons from decays in flight, consists of the following requirements: the reconstructed muon is identified as a global muon, the normalized χ^2 (χ^2/ndof) of the global-muon track fit is < 10, and at least one muon chamber hit is included in the final track fit. To ensure a precise measurement of the impact parameter, only muons with tracks containing at least 11 hits in the silicon tracker are considered. To reject cosmic muons, the transverse impact parameter of the tracker track with respect to the beam spot is required to be less than 2 mm. The relative isolation parameter is defined as the scalar sum of the p_{T} of all tracks in the tracker and the transverse energies of hits in the ECAL and HCAL in a cone of radius $R = \sqrt{(\Delta\eta)^2 + (\Delta\phi)^2} = 0.3$ around the muon track, excluding the contribution from the muon itself, divided by the muon p_{T}. Muons are required to have a relative isolation value less than 5%. Finally, in addition to all of the above requirements, muon candidates are required to have a transverse momentum $p_{\mathrm{T}} > 10$ GeV and pseudorapidity $|\eta| < 2.4$. A veto on the presence of isolated muons in the final state is used to reject $t\bar{t}$ background events, as described in Section 5.4.4.

5.4.3 Jet Selection

The reconstructed jets are first calibrated using jet energy corrections derived from Monte Carlo simulation and *in situ* measurements using dijet and photon+jet events [122]. Only jets with a transverse momentum $p_{\mathrm{T}} > 30$ GeV and pseudorapidity $|\eta| < 3$ are considered for further analysis. In order to reject any fake jets arising from calorimeter or readout electronics noise, jet are required to pass the following jet quality criteria, collectively referred to as *Loose PF Jet ID*: number of jet constituents[4] > 1, neutral hadron fraction < 0.99, neutral electromagnetic (photon) fraction < 0.99; and if within tracking fiducial region of $|\eta| < 2.4$, charged hadron fraction > 0, charged electromagnetic (electron) fraction < 0.99, and charged multiplicity > 0. Finally, to address the double counting of electrons also reconstructed as jets, the closest selected jet within distance $\Delta R = \sqrt{(\Delta\eta)^2 + (\Delta\phi)^2} = 0.3$ from the selected electron is removed from the jet collection.

5.4.4 Event Preselection

Events used in this analysis are collected by single-electron triggers without isolation requirements. The trigger p_{T} thresholds are dependent upon the running period because of the evolving beam conditions during the 2010 run. The bulk of the data were collected with a trigger requiring an electron with $p_{\mathrm{T}} > 22$ GeV. In order to reduce the size of the data and MC and the time to analyze them, skims were defined. For the MC samples, the skim requires every event to have at least

[4]Constituents of a PF jet are PF candidates

one GSF electron with $p_{\mathrm{T}} > 15$ GeV. For data, the skim requires every event to have at least one GSF electron with $p_{\mathrm{T}} > 20$ GeV.

As the first step in the selection of good collision candidate events, the coincidence of the signals from both BPTX[5] beam pick-up monitors [65], located around the beam pipe at a distance of ± 175 m from the interaction point on either side of the CMS detector, which indicate the crossing of the two proton bunches (one from each of the two LHC beams) at the interaction point, is required. This requirement is not applied to the MC samples. In the second step, at least one primary vertex reconstructed with the number of degrees of freedom > 4 (see Equation 4.1), the position along the beam line $|z| < 24$ cm, and position in the transverse plane $r < 2$ cm is required. In addition, the fraction of *highPurity* tracks is requested to be greater than 25% in events with more than 10 tracks. This last requirement removes rare beam-induced background, arising from collisions of the beam with residual gas in the LHC vacuum chambers and interactions of stray protons with limiting apertures upstream of the CMS detector, that produces high multiplicity of clusters in the pixel detector and therefore results in the reconstruction of a large number of fake tracks.

In order to verify the theoretical modeling of the SM background processes, a preliminary event selection, *preselection*, is defined. The event preselection consists of the following event selection requirements, where all the reconstructed objects are required to pass the selection criteria described earlier in this Chapter (in Sections 5.4.1, 5.4.2, and 5.4.3):

[5]Beam Pick-up Timing for the eXperiments

- exactly one electron with $p_{\mathrm{T}} > 35$ GeV and $|\eta| < 2.2$ present in the event;
- at least two jets with $p_{\mathrm{T}} > 30$ GeV and $|\eta| < 3$ present in the event;
- $\not\!\!E_{\mathrm{T}} > 45$ GeV;
- $\Delta R(e, j) > 0.7$, where $j = j1, j2$ are the two leading jets in p_{T};
- $\left|\Delta\phi(e, \not\!\!E_{\mathrm{T}})\right| > 0.8$ and $\left|\Delta\phi(j1, \not\!\!E_{\mathrm{T}})\right| > 0.5$;
- no selected muons with $p_{\mathrm{T}} > 10$ GeV and $|\eta| < 2.4$ ($N_{\mu} = 0$);
- $S_{\mathrm{T}} > 250$ GeV.

The electron p_{T} cut, the $\not\!\!E_{\mathrm{T}}$ cut, and the S_{T} cut are looser than the ones applied in the final selection. The jet $|\eta|$ cut rejects possible fake jets reconstructed in the forward region outside the tracker acceptance arising from the anomalous signals in HF; this cut has a negligible impact on the LQ signal efficiency. The electron $|\eta|$ cut is applied to reduce the contribution from QCD multijet events; the optimization of this cut is described in Section 5.4.5. The cut on selected muons is useful for rejecting dileptonic $t\bar{t}$ events with the $e\mu$ final state. The requirement on $\Delta R(e, j)$ is applied to reject events with fake electrons, while the $\left|\Delta\phi(e, \not\!\!E_{\mathrm{T}})\right|$ and $\left|\Delta\phi(j1, \not\!\!E_{\mathrm{T}})\right|$ cuts are applied to reduce the contribution from QCD multijet events and, in general, events with spurious $\not\!\!E_{\mathrm{T}}$ due to jet mismeasurement. The cut values for $\Delta R(e, j)$, $\left|\Delta\phi(e, \not\!\!E_{\mathrm{T}})\right|$, and $\left|\Delta\phi(j1, \not\!\!E_{\mathrm{T}})\right|$ have been optimized using a procedure described in Section 5.4.5.

In addition to the selection criteria already included in the event preselection, the final, optimized event selection adds selection requirements on the following two

observables: $M_{\mathrm{T},e\nu}$ and $\min(p_{\mathrm{T},e}, \not{E}_{\mathrm{T}})$. A cut on the transverse mass $M_{\mathrm{T},e\nu}$ is used to reject W+jets events since these typically have values for $M_{\mathrm{T},e\nu}$ close to the W Jacobian peak; the $\min(p_{\mathrm{T},e}, \not{E}_{\mathrm{T}})$ requirement exploits the fact that in LQ decays both the electron and the neutrino usually have large p_{T}, while this behavior is less pronounced for the SM backgrounds. The cut values for $M_{\mathrm{T},e\nu}$ and $\min(p_{\mathrm{T},e}, \not{E}_{\mathrm{T}})$ have been optimized using a procedure described in Section 5.4.5.

A sufficient number of data events survive the preselection to allow a comparison with the predicted background yield, as well as between the predicted and observed distributions for all the observables employed in the final event selection. The shapes of the distributions for the SM backgrounds are taken from the corresponding MC samples. The overall normalization of the MC samples is discussed in more detail in Section 5.5. The QCD multijet background is entirely estimated from data using a fake rate method described in Section 5.5.2. The p_{T} and η distributions of the electron and the two leading jets are shown in Figures 5.4, 5.5, and 5.6. The distribution of $\not{E}_{\mathrm{T}}$ and the minimum between the electron p_{T} and the $\not{E}_{\mathrm{T}}$, $\min(p_{\mathrm{T},e}, \not{E}_{\mathrm{T}})$, are shown in Figure 5.7. The distribution of the minimum between $\Delta R(e, j1)$ and $\Delta R(e, j2)$, $\min \Delta R(e, j)$; and the distributions of $\left|\Delta\phi(e, \not{E}_{\mathrm{T}})\right|$ and $\left|\Delta\phi(j1, \not{E}_{\mathrm{T}})\right|$ are shown in Figure 5.8. Figure 5.9 shows the distribution of $\left|\Delta\phi(j2, \not{E}_{\mathrm{T}})\right|$. The distribution of the transverse mass $M_{\mathrm{T},e\nu}$, as defined in Equation 5.5, is shown in Figure 5.10, in linear and logarithmic scale. The distributions of the number of selected muons and the S_{T} distribution are shown in Figure 5.11. The plot on the left in Figure 5.11 shows that events with at least one selected muon are indeed dominated by the $t\bar{t}$ background.

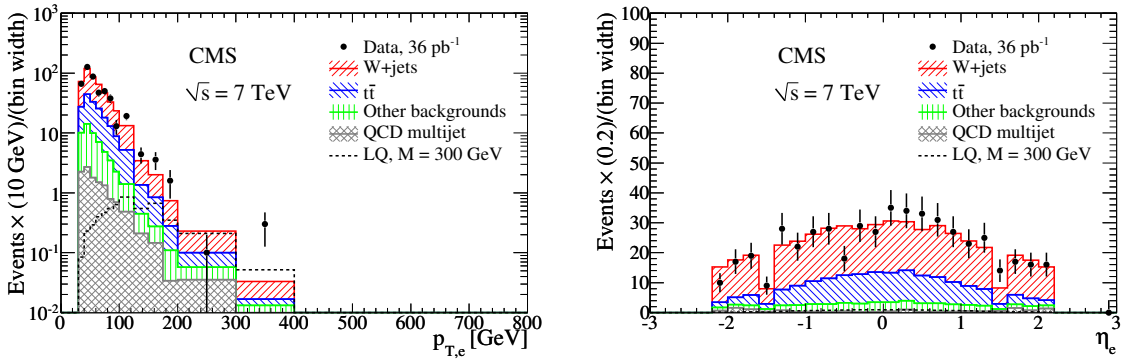

Figure 5.4: The p_{T} (left panel) and η (right panel) distributions of the selected electron for events passing the event preselection. The distribution for the signal with $M_{\mathrm{LQ}} = 300$ GeV and the contributing backgrounds are shown. The distribution labeled "Other backgrounds" includes Z/γ^*+jets, diboson, single top, b+jets, and γ+jets. A rescaling factor of 1.18 described in Section 5.5.3 is applied to the W+jets MC prediction. The black dots indicate data, with error bars representing the Poisson uncertainty on the bin content.

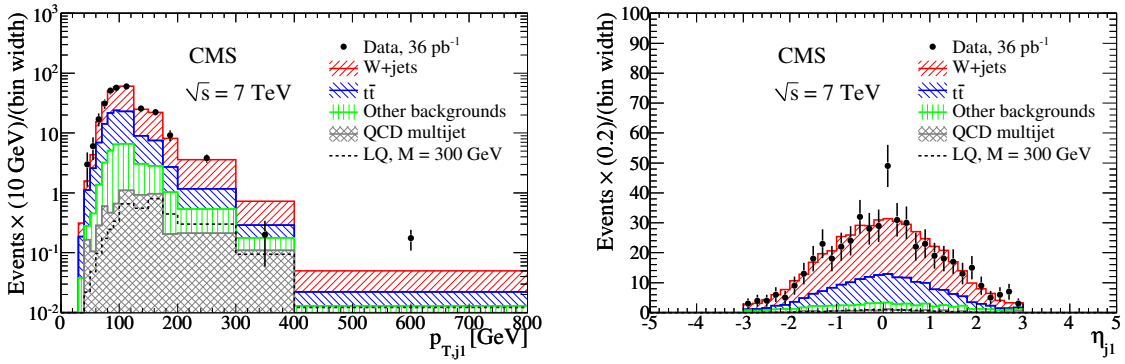

Figure 5.5: The p_{T} (left panel) and η (right panel) distributions of the leading jet in p_{T} for events passing the event preselection. The distribution for the signal with $M_{\mathrm{LQ}} = 300$ GeV and the contributing backgrounds are shown. The distribution labeled "Other backgrounds" includes Z/γ^*+jets, diboson, single top, b+jets, and γ+jets. A rescaling factor of 1.18 described in Section 5.5.3 is applied to the W+jets MC prediction. The black dots indicate data, with error bars representing the Poisson uncertainty on the bin content. The rightmost bin in the p_{T} distribution includes the overflow.

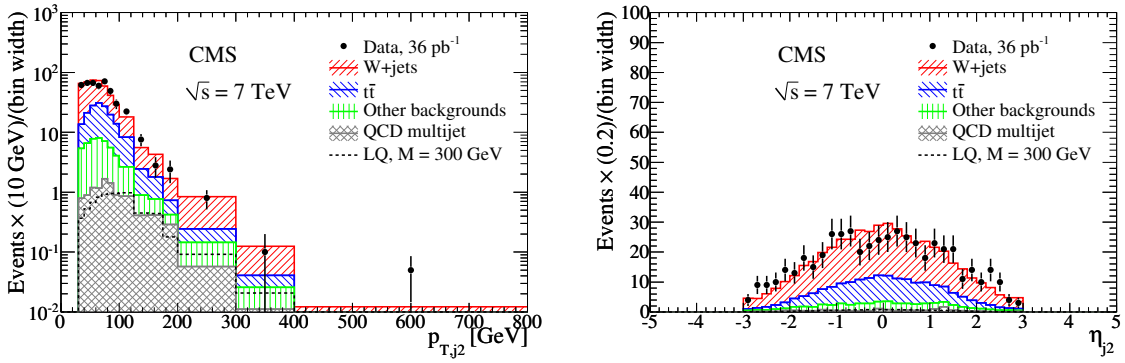

Figure 5.6: The p_{T} (left panel) and η (right panel) distributions of the second leading jet in p_{T} for events passing the event preselection. The distribution for the signal with $M_{\mathrm{LQ}} = 300$ GeV and the contributing backgrounds are shown. The distribution labeled "Other backgrounds" includes Z/γ^*+jets, diboson, single top, b+jets, and γ+jets. A rescaling factor of 1.18 described in Section 5.5.3 is applied to the W+jets MC prediction. The black dots indicate data, with error bars representing the Poisson uncertainty on the bin content. The rightmost bin in the p_{T} distribution includes the overflow.

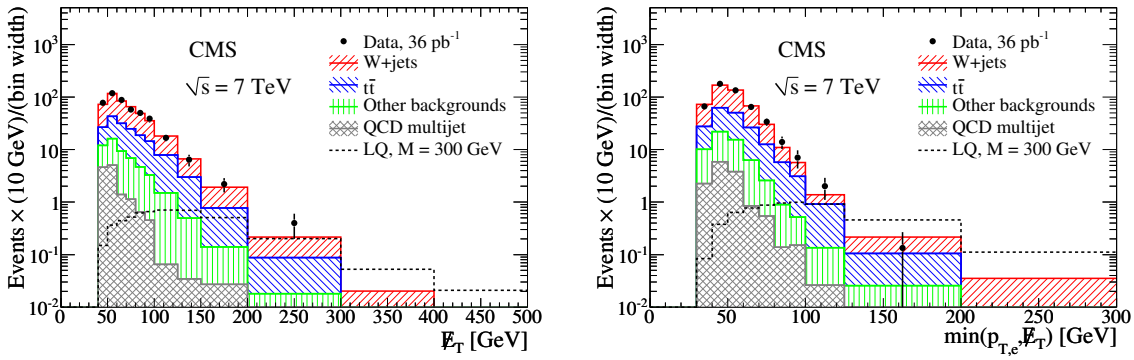

Figure 5.7: The $\not\!\!E_{\mathrm{T}}$ (left panel) and $\min(p_{\mathrm{T},e}, \not\!\!E_{\mathrm{T}})$ (right panel) distributions of the second leading jet in p_{T} for events passing the event preselection. The distribution for the signal with $M_{\mathrm{LQ}} = 300$ GeV and the contributing backgrounds are shown. The distribution labeled "Other backgrounds" includes Z/γ^*+jets, diboson, single top, b+jets, and γ+jets. A rescaling factor of 1.18 described in Section 5.5.3 is applied to the W+jets MC prediction. The black dots indicate data, with error bars representing the Poisson uncertainty on the bin content. The rightmost bin includes the overflow.

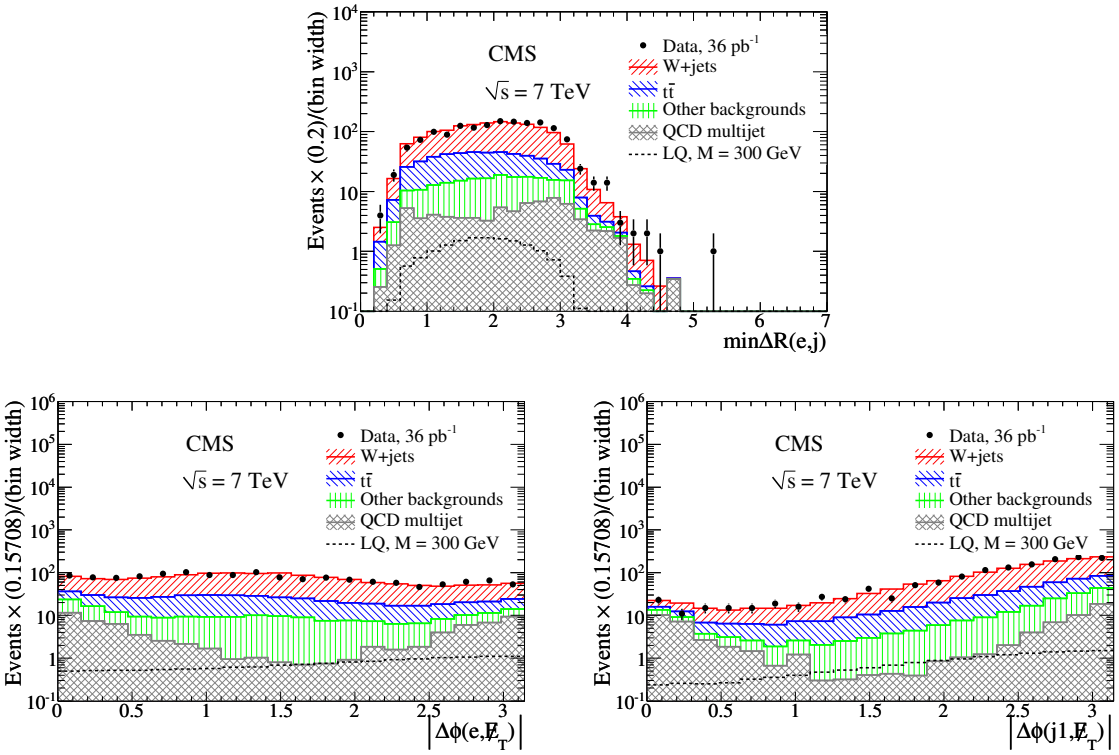

Figure 5.8: The $\min \Delta R(e, j)$ distribution (top) for events passing the electron, jet, and $\not\!\!E_{\mathrm{T}}$ preselection cuts (other preselection cuts not applied); and the distributions of $\left|\Delta\phi(e, \not\!\!E_{\mathrm{T}})\right|$ (bottom left) and $\left|\Delta\phi(j1, \not\!\!E_{\mathrm{T}})\right|$ (bottom right) for events passing the electron, jet, $\not\!\!E_{\mathrm{T}}$, and $\min \Delta R(e, j)$ preselection cuts (other preselection cuts not applied). The distribution for the signal with $M_{\mathrm{LQ}} = 300$ GeV and the contributing backgrounds are shown. The distribution labeled "Other backgrounds" includes Z/γ^*+jets, diboson, single top, b+jets, and γ+jets. A rescaling factor of 1.18 described in Section 5.5.3 is applied to the W+jets MC prediction. The black dots indicate data, with error bars representing the Poisson uncertainty on the bin content.

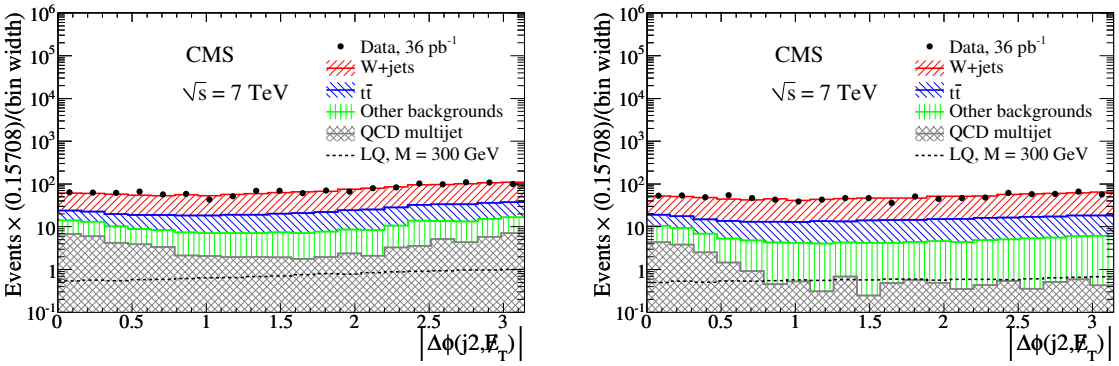

Figure 5.9: The distribution of $\left|\Delta\phi(j2,\not\!\!E_{\mathrm{T}})\right|$ for events passing the electron, jet, $\not\!\!E_{\mathrm{T}}$, and $\min\Delta R(e,j)$ preselection cuts (other preselection cuts not applied) (left panel) and for events passing all preselection cuts except for the muon veto and the S_{T} cut (right panel). The distribution for the signal with $M_{\mathrm{LQ}} = 300$ GeV and the contributing backgrounds are shown. The distribution labeled "Other backgrounds" includes Z/γ^*+jets, diboson, single top, b+jets, and γ+jets. A rescaling factor of 1.18 described in Section 5.5.3 is applied to the W+jets MC prediction. The black dots indicate data, with error bars representing the Poisson uncertainty on the bin content. This observable is not used in the final event selection but it is included in the event selection optimization described in Section 5.4.5.

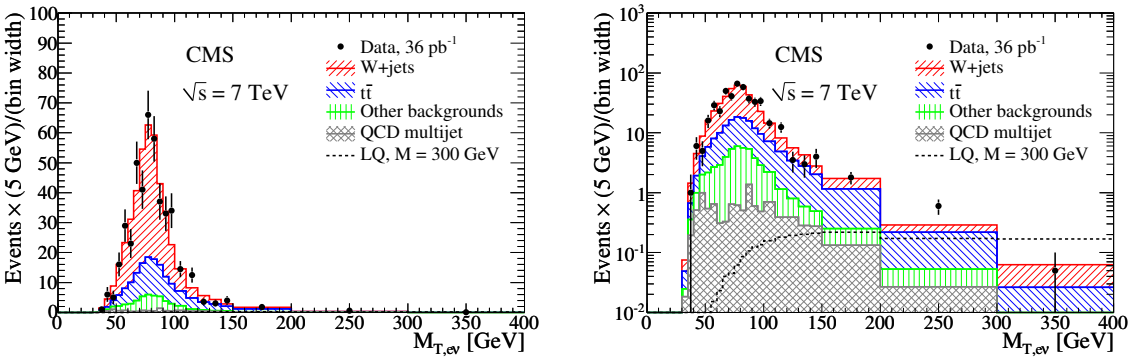

Figure 5.10: The $M_{\mathrm{T},e\nu}$ distribution in linear (left panel) and logarithmic (right panel) scale for events passing the event preselection. The distribution for the signal with $M_{\mathrm{LQ}} = 300$ GeV and the contributing backgrounds are shown. The distribution labeled "Other backgrounds" includes Z/γ^*+jets, diboson, single top, b+jets, and γ+jets. A rescaling factor of 1.18 described in Section 5.5.3 is applied to the W+jets MC prediction. The black dots indicate data, with error bars representing the Poisson uncertainty on the bin content. The rightmost bin includes the overflow.

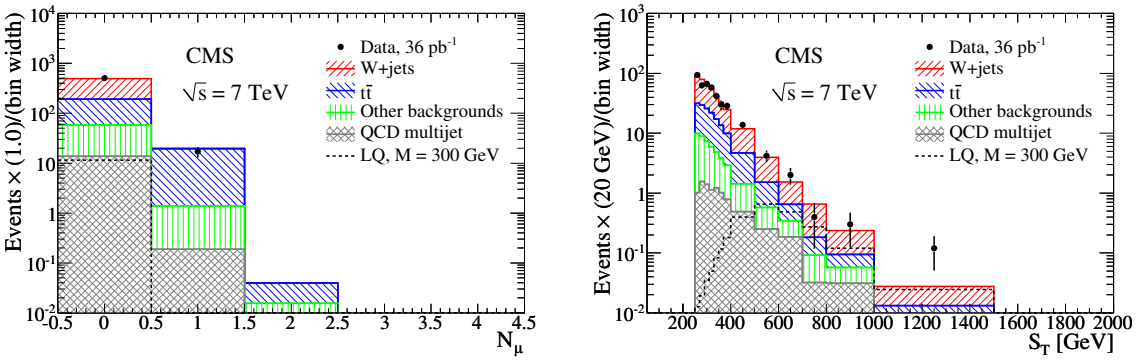

Figure 5.11: The distribution of the number of selected muons (left panel) for events passing all preselection cuts except for the muon veto, and the S_{T} distribution (right panel) for events passing the event preselection. The distribution for the signal with $M_{\mathrm{LQ}} = 300$ GeV and the contributing backgrounds are shown. The distribution labeled "Other backgrounds" includes Z/γ^*+jets, diboson, single top, b+jets, and γ+jets. A rescaling factor of 1.18 described in Section 5.5.3 is applied to the W+jets MC prediction. The black dots indicate data, with error bars representing the Poisson uncertainty on the bin content.

The number of expected LQ signal (for $M_{\mathrm{LQ}} = 300$ GeV assuming $\beta = 0.5$), SM background, and observed data events after the event preselection are reported in the first line of Table 5.5. Overall, a good agreement is observed at the preselection stage between data and background predictions in the shape and normalization of all the distributions employed in the final event selection.

5.4.5 Event Selection Optimization and Final Event Selection

The event selection optimization starts by optimizing cuts on the following reconstructed observables:

- $\min(p_{\mathrm{T},e}, \not{E}_{\mathrm{T}})$, the minimum between the p_{T} of the electron and the $\not{E}_{\mathrm{T}}$;
- $p_{\mathrm{T},j}^{\mathrm{min}}$, the minimum p_{T} for the two leading jets;
- $|\eta_e^{\mathrm{max}}|$, the maximum $|\eta|$ of the electron;

- $\left|\eta_j^{\max}\right|$, the maximum $|\eta|$ for the two leading jets;
- $\min \Delta R(e, j)$, the minimum between $\Delta R(e, j1)$ and $\Delta R(e, j2)$;
- $\left|\Delta\phi(e, \not\!\!E_{\mathrm{T}})\right|$, the absolute value of the azimuthal opening angle between the electron and the $\not\!\!E_{\mathrm{T}}$;
- $\left|\Delta\phi(j1, \not\!\!E_{\mathrm{T}})\right|$, the absolute value of the azimuthal opening angle between the leading jet and the $\not\!\!E_{\mathrm{T}}$;
- $\left|\Delta\phi(j2, \not\!\!E_{\mathrm{T}})\right|$, the absolute value of the azimuthal opening angle between the second leading jet and the $\not\!\!E_{\mathrm{T}}$;
- N_μ, the number of muons with $p_{\mathrm{T}} > 10$ GeV and $|\eta| < 2.4$;
- $M_{\mathrm{T},e\nu}$, the transverse mass of the electron and the $\not\!\!E_{\mathrm{T}}$ defined in Equation 5.5;
- S_{T}, the scalar sum of the p_{T} of the electron and two leading jets, and the $\not\!\!E_{\mathrm{T}}$.

The cut values on the above reconstructed observables are optimized by minimizing the expected upper limit on the product of the leptoquark pair-production cross section and the branching ratio $2\beta(1-\beta)$ in the absence of LQ signal in a scenario with 30 pb^{-1} of integrated luminosity using a Bayesian method for calculating upper limits described in Appendix F. The steps of the optimization are the following:

1. preliminary selection cuts are initialized as in the preselection defined in Section 5.4.4;
2. holding the values of the cuts defined in step 1 constant, an optimization is performed by scanning the 3-dimensional space ($\min(p_{\mathrm{T},e}, \not\!\!E_{\mathrm{T}})$, $M_{\mathrm{T},e\nu}$,S_{T});

3. holding the values of the optimized cuts from steps 2 constant, an optimization is performed by scanning the 3-dimensional space ($\left|\Delta\phi(e,\not\!\!E_{\rm T})\right|$, $\left|\Delta\phi(j1,\not\!\!E_{\rm T})\right|$, $\left|\Delta\phi(j2,\not\!\!E_{\rm T})\right|$);

4. holding the values of the optimized cuts from steps 2 and 3 constant, an optimization is performed by scanning the 3-dimensional space ($\min\Delta R(e,j)$, $|\eta_e^{\rm max}|$, $\left|\eta_j^{\rm max}\right|$), with $\left|\eta_j^{\rm max}\right|$ forced to be < 3 (to reject possible fake jets in HF).

The final, optimized event selection criteria are summarized in Table 5.4. An alternative discovery optimization that maximizes the significance estimator $S/\sqrt{S+B+\sigma_B^2}$, where S and B are the number of signal and background events, respectively, passing the final selection and σ_B is the systematic uncertainty on the background, gives similar results.

The optimized cut on $\left|\Delta\phi(j1,\not\!\!E_{\rm T})\right|$ is 0.5, consistent with the jet cone size. The optimized cut on $\left|\Delta\phi(e,\not\!\!E_{\rm T})\right|$ of 0.8 is tighter than the one on $\left|\Delta\phi(j1,\not\!\!E_{\rm T})\right|$. For LQ events, the region at low values of $\left|\Delta\phi(e,\not\!\!E_{\rm T})\right|$ is naturally depleted after the $M_{{\rm T},e\nu}$ cut, allowing a harder cut on $\left|\Delta\phi(e,\not\!\!E_{\rm T})\right|$ without affecting the signal efficiency. The optimization procedure suggests not to apply any $\left|\Delta\phi(j2,\not\!\!E_{\rm T})\right|$ requirement. The optimized lower cuts on $M_{{\rm T},e\nu}$ and $\min(p_{{\rm T},e},\not\!\!E_{\rm T})$ are found to be 125 GeV and 85 GeV, respectively, for all LQ masses, while that on $S_{\rm T}$ was found to vary with the assumed LQ mass, as indicated in Table 5.4 and Figure 5.12. Figure 5.12 shows the smooth dependence of the optimized $S_{\rm T}$ cut on the assumed LQ mass.

Table 5.5 shows the expected LQ (for $M_{\rm LQ} = 300$ GeV assuming $\beta = 0.5$) and SM background yields, and the number of observed events in data after dif-

Table 5.4: Final, optimized event selection criteria. The first seven cuts from the left are already included in the event preselection.

M_{LQ} [GeV]	$p_{\mathrm{T},j}^{\mathrm{min}}$	$\lvert\eta_e^{\mathrm{max}}\rvert$	$\lvert\eta_j^{\mathrm{max}}\rvert$	$\min \Delta R(e,j)$	$\lvert\Delta\phi(e,\not{E}_{\mathrm{T}})\rvert$	$\lvert\Delta\phi(j1,\not{E}_{\mathrm{T}})\rvert$	N_μ	$M_{\mathrm{T},e\nu}$	$\min(p_{\mathrm{T},e},\not{E}_{\mathrm{T}})$
All	> 30 GeV	< 2.2	< 3	> 0.7	> 0.8	> 0.5	$= 0$	> 125 GeV	> 85 GeV
200	$S_{\mathrm{T}} > 350$ GeV								
250	$S_{\mathrm{T}} > 410$ GeV								
280	$S_{\mathrm{T}} > 460$ GeV								
300	$S_{\mathrm{T}} > 490$ GeV								
320	$S_{\mathrm{T}} > 520$ GeV								
340	$S_{\mathrm{T}} > 540$ GeV								
370	$S_{\mathrm{T}} > 570$ GeV								
400	$S_{\mathrm{T}} > 600$ GeV								
450	$S_{\mathrm{T}} > 640$ GeV								
500	$S_{\mathrm{T}} > 670$ GeV								

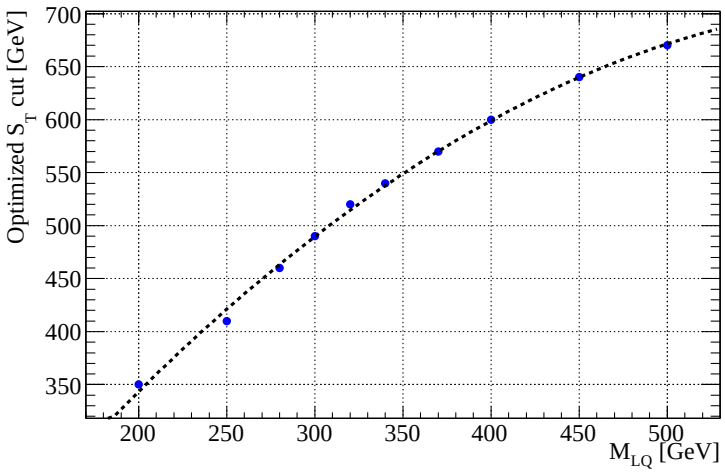

Figure 5.12: Optimized S_{T} cut employed in the final event selection as a function of the LQ mass.

ferent stages of the event selection. Table 5.6 shows the expected LQ (for all LQ masses considered assuming $\beta = 0.5$) and SM background yields, and the number of observed events in data after applying the final, optimized event selection summarized in Table 5.4. The dominant background contributions are from $t\bar{t}$ and W+jets events, while the contribution from the other backgrounds is below 25% of the total background for all the LQ masses considered in this analysis. The signal selection efficiencies reported in Tables 5.5 and 5.6 include the kinematic acceptance, and are estimated from the MC signal samples. The uncertainties reported in Tables 5.5 and 5.6 are statistical. Systematic uncertainties are discussed in Section 5.6. The expected yield for the SM background processes and the number of observed events in data are in agreement within statistical uncertainties at each stage of the selection.

Figure 5.13 shows the distribution of S_{T} after applying the final selection except for the optimized S_{T} cut. Figure 5.13 also shows the electron-jet invariant mass, M_{ej}, and the neutrino-jet transverse mass, $M_{\mathrm{T},\nu j}$, after applying the final selection

Table 5.5: Expected LQ (for $M_{\mathrm{LQ}} = 300$ GeV assuming $\beta = 0.5$) and SM background yields, and the number of observed events in data for the integrated luminosity of 36 pb^{-1} after different stages of the event selection. "Other bkgs" includes Z/γ^*+jets, diboson, single top, b+jets, and γ+jets. A rescaling factor of 1.18 described in Section 5.5.3 is applied to the W+jets MC prediction. The reported uncertainties are statistical. Systematic uncertainties are discussed in Section 5.6. The product of signal acceptance and efficiency is also reported (the statistical uncertainty is less than 1%).

Cut	Signal ($M_{\mathrm{LQ}} = 300$ GeV) Selected events	Signal ($M_{\mathrm{LQ}} = 300$ GeV) Acceptance ×efficiency	SM backgrounds Selected events in $t\bar{t}$	W+jets	Other bkgs	QCD multijet	Total	Events in Data
Preselection	11.52 ± 0.03	0.529	132.9 ± 0.7	306 ± 3	44.6 ± 0.6	13.7 ± 0.4	497 ± 4	505
$M_{\mathrm{T},e\nu} > 125$ GeV	10.01 ± 0.03	0.459	22.7 ± 0.3	14.2 ± 0.8	3.3 ± 0.2	3.5 ± 0.2	43.6 ± 0.9	46
$\min(p_{\mathrm{T},e}, \not{E}_{\mathrm{T}}) > 85$ GeV	7.89 ± 0.03	0.362	5.3 ± 0.2	3.0 ± 0.4	0.63 ± 0.06	0.27 ± 0.05	9.2 ± 0.4	7
$S_{\mathrm{T}} > 490$ GeV	6.89 ± 0.03	0.317	1.09 ± 0.07	1.0 ± 0.2	0.27 ± 0.05	0.14 ± 0.04	2.5 ± 0.2	2

Table 5.6: Expected LQ (assuming $\beta = 0.5$) and SM background yields, and the numbers of observed events in data for the integrated luminosity of 36 pb^{-1} after the final, optimized event selection. "Other bkgs" includes Z/γ^*+jets, diboson, single top, b+jets, and γ+jets. A rescaling factor of 1.18 described in Section 5.5.3 is applied to the W+jets MC prediction, as described in Section 5.5.3. The reported uncertainties are statistical. Systematic uncertainties are discussed in Section 5.6. The product of signal acceptance and efficiency is also reported for different LQ masses (the statistical uncertainty is less than 1%).

M_{LQ} (S_{T} cut) [GeV]	Signal		SM backgrounds					Events in
	Selected events	Acceptance ×efficiency	Selected events in $t\bar{t}$	W+jets	Other bkgs	QCD multijet	Total	Data
200 ($S_{\mathrm{T}} > 350$)	34.5 ± 0.2	0.161	3.6 ± 0.1	2.2 ± 0.3	0.48 ± 0.06	0.20 ± 0.04	6.5 ± 0.3	5
250 ($S_{\mathrm{T}} > 410$)	15.9 ± 0.1	0.255	2.24 ± 0.09	1.7 ± 0.3	0.35 ± 0.05	0.18 ± 0.05	4.4 ± 0.3	3
280 ($S_{\mathrm{T}} > 460$)	9.54 ± 0.05	0.291	1.43 ± 0.08	1.2 ± 0.2	0.29 ± 0.05	0.14 ± 0.04	3.1 ± 0.2	3
300 ($S_{\mathrm{T}} > 490$)	6.89 ± 0.03	0.317	1.09 ± 0.07	1.0 ± 0.2	0.27 ± 0.05	0.14 ± 0.04	2.5 ± 0.2	2
320 ($S_{\mathrm{T}} > 520$)	5.03 ± 0.02	0.339	0.75 ± 0.05	0.8 ± 0.2	0.22 ± 0.05	0.13 ± 0.04	1.9 ± 0.2	2
340 ($S_{\mathrm{T}} > 540$)	3.73 ± 0.02	0.364	0.65 ± 0.05	0.7 ± 0.2	0.20 ± 0.05	0.12 ± 0.04	1.6 ± 0.2	2
370 ($S_{\mathrm{T}} > 570$)	2.40 ± 0.01	0.396	0.50 ± 0.04	0.6 ± 0.1	0.18 ± 0.04	0.08 ± 0.03	1.3 ± 0.2	1
400 ($S_{\mathrm{T}} > 600$)	1.57 ± 0.01	0.426	0.34 ± 0.04	0.5 ± 0.1	0.17 ± 0.04	0.08 ± 0.03	1.1 ± 0.1	1
450 ($S_{\mathrm{T}} > 640$)	0.797 ± 0.003	0.467	0.26 ± 0.03	0.4 ± 0.1	0.13 ± 0.04	0.08 ± 0.04	0.9 ± 0.1	0
500 ($S_{\mathrm{T}} > 670$)	0.417 ± 0.001	0.500	0.18 ± 0.03	0.4 ± 0.1	0.12 ± 0.04	0.08 ± 0.04	0.8 ± 0.1	0

optimized for $M_{\mathrm{LQ}} = 300$ GeV ($S_{\mathrm{T}} > 490$ GeV). The M_{ej} ($M_{\mathrm{T},\nu j}$) distribution contains two entries per event since there are two electron-jet ($\not\!\!E_{\mathrm{T}}$-jet) pairs in each event. Only one of the two pairs corresponds to the LQ decay products; the other pair is combinatorial background. Despite this, the M_{ej} and $M_{\mathrm{T},\nu j}$ distribution both exhibit a peak at the mass of the leptoquark. Although they are not used in the event selection, both represent important control distributions that could be used to verify the presence of the LQ signal. All three distributions in Figure 5.13 show good agreement with SM predictions. Event displays for the three highest-S_{T} events are shown in Appendix D.

5.5 Background Estimation

An essential ingredient in any search for new physics is a sound understanding of the SM backgrounds. In order to be able to claim an observation or discovery of new physics, it is necessary to have a reliable estimation of various background processes. Very often the background estimation relies on MC simulation of the background processes. However, it is advantageous to reduce the dependence on the theoretical modeling of the background processes and detector response by supplementing MC-based predictions with information from data, and obtain a *data-driven* background prediction.

In this analysis, a combination of MC-based and data-driven techniques is used. The estimation of the SM backgrounds for this analysis is done in sequence as follows. The shapes of the kinematic distributions for $t\bar{t}$, single top, Z/γ^*+jets,

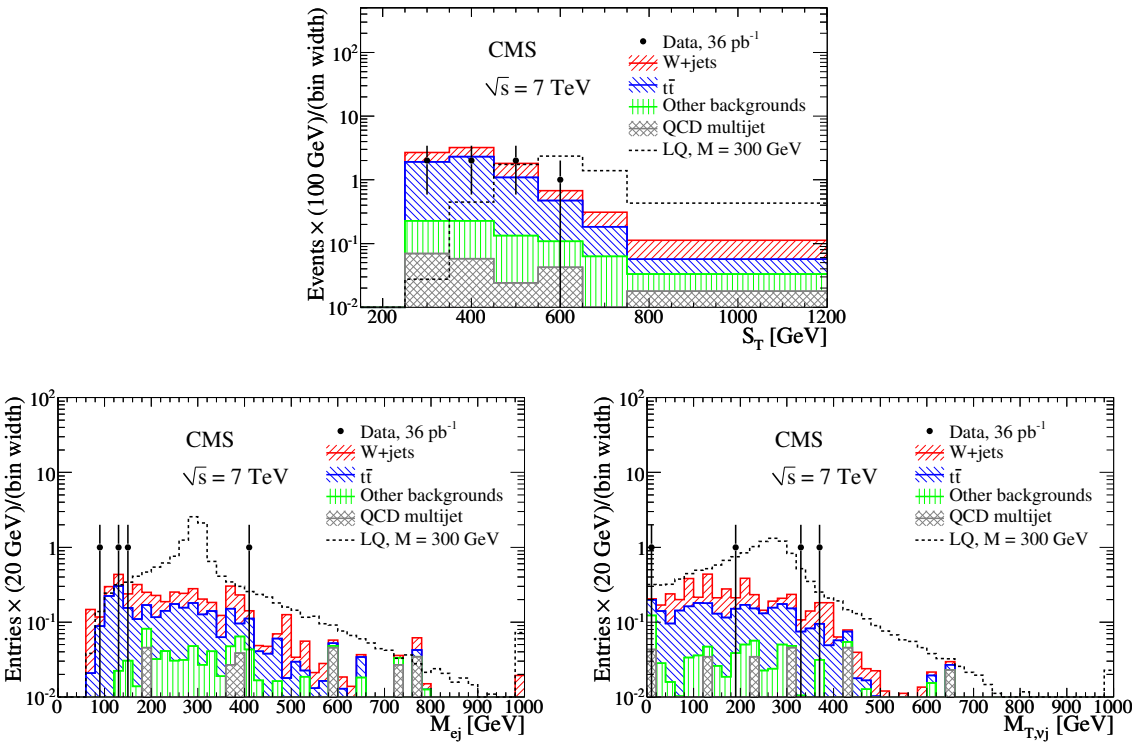

Figure 5.13: The S_{T} distribution (top) for events passing the final selection excluding the optimized S_{T} cut itself (the preselection $S_{\mathrm{T}} > 250$ GeV cut is applied), and the distributions of M_{ej} (bottom left) and $M_{\mathrm{T},\nu j}$ (bottom right) for events passing the final selection optimized for $M_{\mathrm{LQ}} = 300$ GeV ($S_{\mathrm{T}} > 490$ GeV). The distribution for the signal with $M_{\mathrm{LQ}} = 300$ GeV and the contributing backgrounds are shown. The distribution labeled "Other backgrounds" includes Z/γ^*+jets, diboson, single top, b+jets, and γ+jets. A rescaling factor of 1.18 described in Section 5.5.3 is applied to the W+jets MC prediction. The black dots indicate data, with error bars representing the Poisson uncertainty on the bin content. The rightmost bin includes the overflow.

diboson, b+jets, and γ+jets backgrounds are taken from the corresponding MC samples (normalized to the corresponding theoretical cross sections, as described in Section 5.3). The QCD multijet background is estimated from data using the fake rate method described in Section 5.5.2. Finally, the shapes of the kinematic distributions for the W+jets background are taken from the corresponding MC samples, with the overall normalization determined from data at the preselection stage. The procedure used to normalize the W+jets background is described in Section 5.5.3.

5.5.1 $t\bar{t}$ Background

Since an approximate NNLO cross section for the $t\bar{t}$ production of 165 ± 10 pb calculated for a top quark mass of 173 GeV [116] is consistent with the CMS measurement of the $t\bar{t}$ production cross section of 168 ± 18 (stat.) $\pm$ 14 (syst.) $\pm$ 7 (lumi.) pb [123], no rescaling of the $t\bar{t}$ MC sample is performed. However, the overall uncertainty of 14% on the measured cross section is assigned as the normalization uncertainty on the $t\bar{t}$ background.

5.5.2 QCD Multijet Background

A jet has a small probability to be reconstructed as a good electron. Such electrons are called *fake electrons*. The fake electrons are mainly produced through the following processes: charged pions charge-exchanging upon entering into a detecting element and the resulting π^0 decaying to a pair of photons, superclusters

accidentally overlapping with a charged particle track, and photons converting to an electron-positron pair inside the tracker volume. In addition, all non-prompt real electrons originating from decays of hadrons are also considered fake electrons.

Although the probability for a jet to be reconstructed as a good electron is relatively small, the presence of several jets in the event and a large production cross section lead to a non-negligible background from QCD multijet events. The large production cross section and the underlying uncertainties on the MC modeling of the QCD multijet events and the processes leading to the production of fake electrons make the use of MC samples to estimate this background impractical and insufficiently reliable. The contribution to the background from QCD multijet events is therefore estimated from data using the fake rate method described below.

5.5.2.1 Fake Rate Method

To estimate the background from QCD multijet events, we select multijet events with kinematics similar to the signal and weight each event by the probability for a jet to fake an electron. To do this, we need two samples: one to evaluate the probability for a jet to pass the electron identification requirements and another containing events with kinematics similar to the signal. The latter sample is obtained by selecting events with exactly one isolated supercluster passing the isolation criteria listed in Table 5.7 and the "Swiss Cross" cut described in Section 5.4.1, at least two jets, and large $\not\!\!E_{\mathrm{T}}$, that satisfy the selection criteria of the analysis described in Sections 5.4.4 and 5.4.5, where the listed kinematic requirements on

electrons are instead applied to superclusters. Because of the isolation requirements (see Table 5.7) looser than those in the HEEP selection and lack of electron identification requirements applied to the superclusters, this sample, referred to as the $c\nu jj$ sample, is dominated by QCD multijet events. The number of QCD multijet events entering the sample with one good electron, at least two jets, and large $\not\!\!E_{\mathrm{T}}$, referred to as the $e\nu jj$ sample, is estimated at each stage of the event selection using the following formula:

$$N_{\mathrm{QCD}}^{e\nu jj} = \sum_{c\nu jj \text{ events in data}} P(e|c : E_{\mathrm{T}}, \eta), \tag{5.6}$$

where e is a reconstructed electron passing the HEEP selection criteria described in Appendix C, $N_{\mathrm{QCD}}^{e\nu jj}$ is the number of QCD multijet events entering the $e\nu jj$ sample, c is a isolated supercluster passing the appropriate isolation and "Swiss Cross" cuts, and $P(e|c)$ is the probability for a supercluster c to be reconstructed as a good electron e. This probability, or "fake rate" can in principle depend on the E_{T} and η of the supercluster, and is thus denoted $P(e|c : E_{\mathrm{T}}, \eta)$. The sum is performed over the $c\nu jj$ events in data passing the selection criteria at each considered stage of the event selection. Events in the $c\nu jj$ sample with a good reconstructed electron are rejected in order to reduce the contamination from W+jets events or any other processes with prompt electrons in the final state. It is important to realize that in multijet events with more than one isolated superclusters present, each supercluster has a probability to be reconstructed as a good electron. However, it was found that such events, if considered, would represent only a few percent of the total

$c\nu jj$ sample, and were found to have kinematic features similar to $c\nu jj$ events with exactly one isolated supercluster. Hence, to simplify the procedure of calculating $N_{\mathrm{QCD}}^{e\nu jj}$, multijet events with two or more isolated superclusters are not considered in Equation 5.6.

Table 5.7: Isolation criteria for superclusters employed in the estimation of the QCD multijet background. This selection has to be looser than the one applied in the HEEP selection for electrons. However, in the barrel (endcaps) this is strictly true only for superclusters with $E_{\mathrm{T}} < 200$ GeV ($E_{\mathrm{T}} < 225$ GeV). Since the fake rate calculation is dominated by the lower-E_{T} superclusters, this inconsistency has a negligible effect on the final fake rate.

Variable name	Barrel threshold	Endcap threshold
H/E	< 0.05	< 0.05
ECAL Isolation [GeV]	$< 6 + 0.01 \times E_{\mathrm{T}}$	if $E_{\mathrm{T}} < 50$ GeV: $< 6 + 0.01 \times E_{\mathrm{T}}$ if $E_{\mathrm{T}} > 50$ GeV: $< 6 + 0.01 \times (E_{\mathrm{T}} - 50)$

The EG and Photon datasets listed in Table 5.2 are used to estimate the QCD multijet background. The events in the $c\nu jj$ sample are collected by a combination of prescaled and unprescaled (depending on the run range) single-photon triggers with different E_{T} thresholds, given in Table 5.8. The E_{T} threshold of the lowest-E_{T} trigger used (HLT_Photon30_Cleaned_L1R) is 30 GeV; this value is 5 GeV below the electron p_{T} cut used in the event preselection, which is enough to avoid any trigger threshold bias. Each event passing the $c\nu jj$ selection criteria is properly reweighted in the sum of Equation 5.6 according to the p_{T} of the triggered photon, with the event weight equal to the prescale of the corresponding single-photon trigger (e.g., in the run range 148108–149294, events in which the p_{T} of the triggered photon is between 30 and 50 GeV are reweighted with an event weight equal to the prescale of the HLT_Photon30_Cleaned_L1R trigger. Similarly events in which the p_{T} of the

triggered photon is between 50 and 70 GeV are reweighted with an event weight equal to the prescale of the HLT_Photon50_Cleaned_L1R trigger).

Table 5.8: Single-photon triggers employed in the estimation of the QCD multijet background. The information on the trigger prescales is reported for different run ranges. Single-photon triggers with higher p_{T} thresholds were included in the HLT trigger menus for later runs with higher instantaneous luminosities.

Trigger name / Run range	136035–147145	147146–148107	148108–149294
HLT_Photon30_Cleaned_L1R	not prescaled	prescaled	prescaled
HLT_Photon50_Cleaned_L1R	N/A	not prescaled	prescaled
HLT_Photon70_Cleaned_L1R	N/A	N/A	not prescaled

5.5.2.2 Fake Rate Calculation

The fake rate, $P(e|c)$, is defined as the ratio between the number of electrons, N_e, and the number of superclusters, N_c, in a sample of QCD multijet events passing the following selection criteria:

- single-photon trigger, as described in Section 5.5.2.1;
- exactly one isolated supercluster c with $p_{\mathrm{T}} > 35$ GeV, passing the isolation criteria and the "Swiss Cross" cut;
- at least N jets with p_{T} greater than 30 GeV, with N equal to 1, 2, or 3. Superclusters reconstructed as jets are removed from the jet collection using the same technique described in Section 5.4.3 for the electron-jet overlap;
- $\Delta R(c, j) > 0.7$, where j is any of the jets with p_{T} greater than 30 GeV;
- $\not\!\!E_{\mathrm{T}} < 35$ GeV.

Due to the $\not\!\!E_{\rm T}$ cut, this sample is orthogonal to the $c\nu jj$ used in the estimation of the QCD multijet background. The requirements of exactly one isolated supercluster and $\not\!\!E_{\rm T}$ reduce the contamination from real electrons from $Z \to ee$ and $W \to e\nu$ events, respectively. The event selection criteria listed above select a sample enriched in QCD multijets events with an overall N_e contamination of about 25–30%, mainly coming from γ+jets, W+jets and Z/γ^*+jets processes, as estimated from MC. This contamination becomes close to 90–100% for very high-$p_{\rm T}$ electrons in the barrel, and is dominated by W+jets events. The contamination for N_c is negligible.

The fake rates are calculated for the barrel and separately for the two endcap regions ($|\eta| < 2.2$ and $|\eta| > 2.2$). In addition, each set of fake rates is obtained for three different jet multiplicity requirements, i.e., for $N_{\rm jets} \geq 1$, 2, and 3. The fake rate is not expected to depend strongly on the multiplicity of jets far away from the supercluster. Any residual dependence of the fake rate on the jet multiplicity can be assigned as a systematic uncertainty on the estimated amount of the QCD multijet background. The contamination of real electrons in the numerator of the fake rate is based on MC predictions, and is subtracted from the data as a function of the electron $p_{\rm T}$. The MC-corrected fake rate for the $N_{\rm jets} \geq 1$ case is shown in Figure 5.14 as a function of the supercluster $E_{\rm T}$, separately for the barrel and the two endcap regions. In the barrel, the fake rate is essentially flat as a function of the supercluster $E_{\rm T}$, while it grows linearly in both endcap regions (a similar trend is observed also for the other jet multiplicity requirements). A zero-degree (first-degree) polynomial fit is performed for the barrel (endcap) fake rates. The fit results are reported in Table 5.9 for the various jet multiplicities.

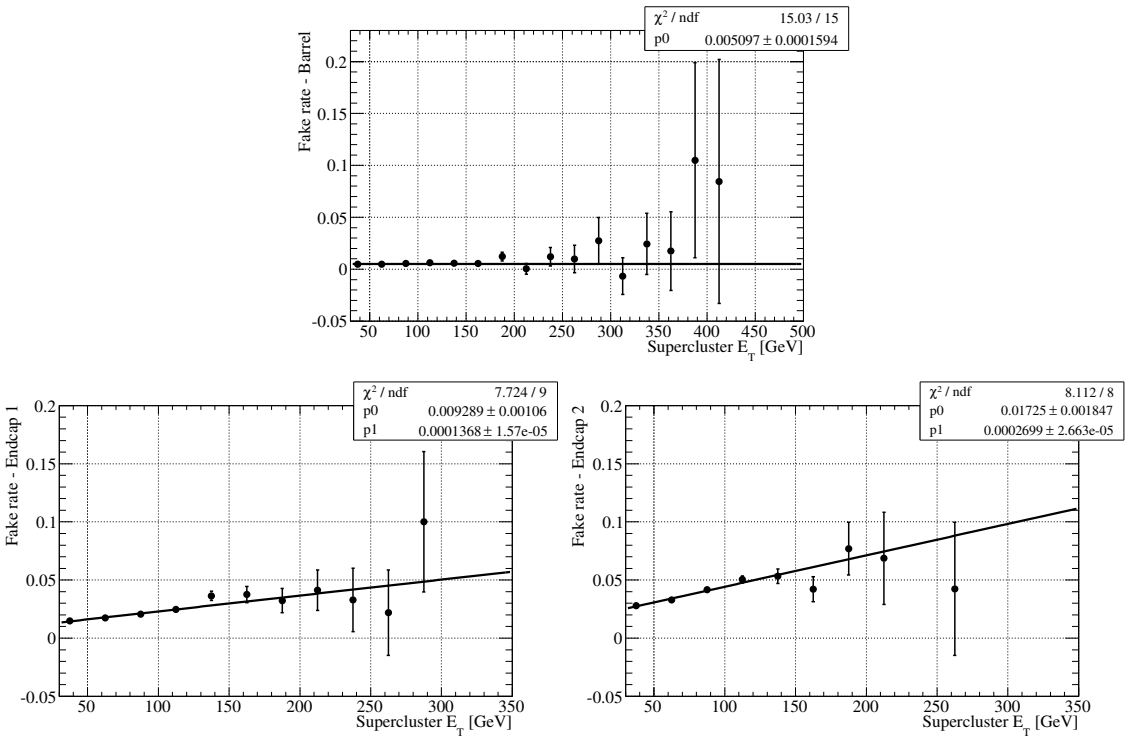

Figure 5.14: Probability $P(e|c)$ for an isolated supercluster c to be reconstructed as a HEEP electron e as a function of the supercluster E_{T} in the ECAL barrel (top) and two endcap regions, $|\eta| < 2.2$ (bottom left) and $|\eta| > 2.2$ (bottom right), calculated from data events with exactly one supercluster, at least one jet with $p_{\mathrm{T}} > 30$ GeV, and passing the other selection criteria described in Section 5.5.2.2. A MC-based p_{T}-dependent correction to remove the contribution from real electrons in the numerator of the fake rate is applied. The black line is the result of the zero-degree (first-degree) polynomial fit to the barrel (endcap) fake rate.

Table 5.9: MC-corrected fake rate functions, $P(e|c)$, for superclusters reconstructed in the ECAL barrel and endcaps for different jet multiplicity requirements (with jet $p_{\mathrm{T}} > 30$ GeV). Statistical uncertainties on the fit are shown. The last two columns show the estimate of the number of QCD multijet events (using Equation 5.6) in the $e\nu jj$ sample at the preselection stage (without the muon veto applied) and after the final selection (optimized for $M_{\mathrm{LQ}} = 300$ GeV) for different jet multiplicity requirements.

$P(e\|c) = A + B \times p_{\mathrm{T}}$	Barrel	Endcap 1 ($\|\eta\| < 2.2$)	Endcap 2 ($\|\eta\| > 2.2$)	$N_{\mathrm{QCD}}^{e\nu jj}$ presel.	$N_{\mathrm{QCD}}^{e\nu jj}$ final sel. ($M_{\mathrm{LQ}} = 300$ GeV)
$1\ c + N_{\mathrm{jets}} \geq 1$					
A	$(5.1 \pm 0.2) \times 10^{-3}$	$(9.3 \pm 1.1) \times 10^{-3}$	$(1.7 \pm 0.2) \times 10^{-2}$	16.8 ± 0.5	0.133 ± 0.041
B	-	$(1.4 \pm 0.2) \times 10^{-4}$	$(2.7 \pm 0.3) \times 10^{-4}$		
$1\ c + N_{\mathrm{jets}} \geq 2$					
A	$(4.0 \pm 0.2) \times 10^{-3}$	$(2.3 \pm 1.7) \times 10^{-3}$	$(1.1 \pm 0.3) \times 10^{-2}$	13.9 ± 0.4	0.135 ± 0.042
B	-	$(2.1 \pm 0.2) \times 10^{-4}$	$(2.8 \pm 0.4) \times 10^{-4}$		
$1\ c + N_{\mathrm{jets}} \geq 3$					
A	$(4.2 \pm 0.5) \times 10^{-3}$	$(2.9 \pm 3.6) \times 10^{-3}$	$(8.4 \pm 6.0) \times 10^{-3}$	13.6 ± 0.4	0.125 ± 0.038
B	-	$(1.8 \pm 0.4) \times 10^{-4}$	$(2.8 \pm 0.8) \times 10^{-4}$		

The QCD multijet events contributing to the $e\nu jj$ sample are events with at least three jets, with one of the jets reconstructed as a HEEP electron. Therefore, the sample used to estimate the fake rate for this analysis is the one labeled "1 $c + N_{\text{jets}} \geq 2$".

5.5.2.3 QCD Multijet Background Estimation

At each step of the event selection, the shape of the kinematic distributions and the normalization of the QCD multijet background are estimated using the method described in Section 5.5.2.1. Table 5.5 reports the contribution of the QCD multijet background at different stages of the event selection using the "1 $c + N_{\text{jets}} \geq 2$" fake rates. After the final selection, the contribution of the QCD multijet background varies from $\approx 3\%$ (for $M_{\text{LQ}} = 200$ GeV) to $\approx 10\%$ (for $M_{\text{LQ}} = 500$ GeV) of the total background, as reported in Table 5.6. The kinematic distributions for QCD multijet events are included in all the figures shown in Chapter 5.

The estimated of the QCD multijet background is repeated using the fake rates for different jet multiplicities. The results are reported in the last two columns of Table 5.9. A variation of $\approx 25\%$ among the different estimates at the preselection stage, calculated as

$$|N_{\text{QCD}}^{e\nu jj}(\text{"1 } c + N_{\text{jets}} \geq 1\text{"}) - N_{\text{QCD}}^{e\nu jj}(\text{"1 } c + N_{\text{jets}} \geq 3\text{"})|/N_{\text{QCD}}^{e\nu jj}(\text{"1 } c + N_{\text{jets}} \geq 2\text{"}),$$

is taken as a systematic uncertainty on the estimated amount of the QCD multijet background, since the statistical error on the prediction for this sample is still

relatively small.

5.5.3 W+jets Background

As described in Section 5.3, the W+jets MC samples are initially normalized to the NNLO production cross section assuming a constant k-factor for all bins of the boson p_{T} and additional parton multiplicity. Since higher order corrections can be different in different regions of the phase space, this assumption is not necessarily correct. Hence, the W+jets samples are normalized to data in a background-dominated region in order to reduce dependence on the theoretical modeling of the W+jets background. This normalization can only be done once all the other backgrounds have been determined.

After applying the event preselection described in Section 5.4.4, and requiring that the transverse mass $M_{\mathrm{T},e\nu}$ of the electron-neutrino pair is between 50 and 110 GeV, i.e., close to the W Jacobian peak, the event sample is dominated by W+jets events (see Figure 5.10), with a contamination of approximately 35% from other SM backgrounds and less than 1% from LQ signal with $M_{\mathrm{LQ}} \gtrsim 250$ GeV. The number of events in data is compared to the predicted background yields, and a data/MC rescaling factor for the W+jets background at the preselection stage is computed:

$$R_W = \frac{N_{\mathrm{data}} - (N_{t\bar{t}} + N_{\mathrm{QCD}} + N_{\mathrm{other}})}{N_W} = 1.18 \pm 0.12, \tag{5.7}$$

where N_{data} is the number of events in data, $N_{t\bar{t}}$ is the predicted number of $t\bar{t}$ events,

N_{QCD} is the predicted number of QCD multijet events, N_{other} is the predicted number of events from the other MC samples (Z/γ^*+jets, diboson, single top, b+jets, and γ+jets), and N_W is the number of W+jets events before any rescaling. This factor is included in all the W+jets MC predictions shown in tables and figures of this dissertation. The uncertainty on R_W is calculated by combining in quadrature the statistical uncertainty on the data and MC events and the systematic uncertainties on the "non-W+jets" backgrounds discussed in Section 5.6. The 10% uncertainty on R_W is the systematics uncertainty on the normalization of the W+jets background.

5.6 Systematic Uncertainties

Systematic uncertainties on the number of selected signal and background events are estimated using both MC-based and data-driven techniques. The following sources of systematic uncertainties are considered: data-driven normalization, $t\bar{t}$ and W+jets background shape, jet/$\not\!\!E_{\mathrm{T}}$ and electron energy scale, integrated luminosity, MC statistical uncertainty, and the electron trigger, reconstruction, identification and isolation efficiency.

As described in Section 5.5.1, an overall uncertainty on the CMS measurement of the $t\bar{t}$ production cross section of 14% [123] is assigned as a data-driven systematic uncertainty on the normalization of the $t\bar{t}$ background. The W+jets background is normalized to data at the preselection stage using events in the W Jacobian peak of the $M_{\mathrm{T},e\nu}$ distribution, as described in Section 5.5.3. An uncertainty on the rescaling factor R_W of 10% is assigned as a data-driven systematic uncertainty

on the normalization of the W+jets background. The data-driven normalization uncertainties for the $t\bar{t}$ and W+jets backgrounds are conservatively assumed to be fully correlated. A data-driven normalization uncertainty on the QCD multijet background consists of a 25% systematic uncertainty on the estimated amount of the QCD multijet background, described in Section 5.5.2.3, summed in quadrature with the statistical uncertainty on the estimated amount of the QCD multijet background reported in Table 5.6. An overall data-driven normalization uncertainty is obtained by first linearly adding $t\bar{t}$ and W+jets uncertainties, and then adding the result in quadrature with the QCD multijet uncertainty, taking into account the relative contributions of each of these backgrounds to the total background.

A systematic uncertainty due to the modeling of the shape of the $M_{\mathrm{T},e\nu}$ and S_{T} distribution of the dominant $t\bar{t}$ and W+jets backgrounds is estimated using MadGraph samples produced with renormalization/factorization scales and jet matching thresholds that are a factor of two higher and lower than the nominal values. In addition, for the study of the $t\bar{t}$ background shape, an inclusive $t\bar{t}$ sample generated using the mc@nlo [124] event generator is used. The largest deviation in the number of $t\bar{t}$ (W+jets) events passing the event preselection and the final $M_{\mathrm{T},e\nu}$ or S_{T} (for $M_{\mathrm{LQ}} = 300$ GeV) cut between these MC samples and the default MC sample is used to assign a 28% (49%) systematic uncertainty on the $t\bar{t}$ (W+jets) background shape, as described in Appendix E. The background shape uncertainties for the $t\bar{t}$ and W+jets backgrounds are conservatively assumed to be fully correlated, and are therefore added linearly, taking into account the relative contributions of each of these backgrounds to the total background.

The uncertainty on the electron energy scale in the ECAL barrel (endcaps) is estimated using π^0 and η meson decays to be 1% (3%) [80]. The uncertainty on the jet energy scale was estimated as a function of η and p_{T} of the reconstructed jets [122]. However, a conservative 5% uncertainty on the jet energy scale is used for the entire η and p_{T} range of the reconstructed jets. In order to estimate the effect of these uncertainties, the event selection is repeated after rescaling the jet and electron energies by a factor of $1 \pm \delta$, where δ is the relative uncertainty on their energy scales. Since $\not\!\!E_{\mathrm{T}}$ is a composite object, its scale depends on both the exact topology and the types of particles present in the final state. For the final state considered in this analysis, the uncertainty on the $\not\!\!E_{\mathrm{T}}$ scale is primarily affected by the uncertainty on the jet energy scale. Therefore, while varying the jet energy scale, a new $\not\!\!E_{\mathrm{T}}$ vector is computed event by event

$$\vec{\not\!\!E}_{\mathrm{T}}{}' = \vec{\not\!\!E}_{\mathrm{T}} + \sum_{\mathrm{jets}} (\vec{p}_{\mathrm{T}} - \vec{p}_{\mathrm{T}}{}'), \tag{5.8}$$

where $\vec{p}_{\mathrm{T}}$ is the transverse momentum vector of the original jet, $\vec{p}_{\mathrm{T}}{}'$ is the transverse momentum vector of the jet with modified energy scale, and the sum is performed over all reconstructed jets with $p_{\mathrm{T}} > 10$ GeV. The event selection is then repeated using $\vec{p}_{\mathrm{T}}{}'$ for the jets and $\not\!\!E_{\mathrm{T}}{}'$ for the missing transverse energy. The maximum change in the total number of signal and background events due to the variation of the jet/$\not\!\!E_{\mathrm{T}}$ and electron energy scales is used to estimate the size of this systematic uncertainty. Given that the data-driven uncertainties for the W+jets background are determined at the event preselection stage, the variation in number of W+jets

events is computed relative to that stage of the selection in order to avoid overestimation of the jet/$\not\!\!E_{\mathrm{T}}$ and electron energy scale uncertainties. The same procedure is applied for the $t\bar{t}$ background but without applying the $\min \Delta R(e, j)$, $\Delta\phi(e, \not\!\!E_{\mathrm{T}})$, $\Delta\phi(j1, \not\!\!E_{\mathrm{T}})$, N_{μ}, and S_{T} cuts from the event preselection, since in this case the data-driven uncertainties are derived from the CMS $t\bar{t}$ cross section measurement. This uncertainty is not derived for the QCD multijet background, since this background is estimated directly from data. The size of this systematic uncertainty for signal and background events is reported in Table 5.10. This systematic uncertainty is conservatively assumed to be fully correlated among individual background components, and is therefore combined by linearly adding individual uncertainties, taking into account the relative contributions of different background components to the total background.

The uncertainty on the absolute normalization of the integrated luminosity of the data sample used in this analysis is estimated to be 4% [125]. This uncertainty is taken into account for the signal samples and those background samples that do not have a data-driven normalization.

The trigger menu was evolving during the data taking to adapt to the steady increase in the instantaneous luminosity delivered by the LHC. About 80% of the data used in this analysis was collected towards the end of the 2010 run by single-electron unprescaled triggers with an efficiency of about 97% for HEEP electrons. This trigger efficiency is measured using a sample of $Z \to ee$ events from data that have both electrons passing the HEEP selection. The efficiency is measured using the *tag-and-probe method* [126]. The tag electron is required to have passed

a single-electron trigger, giving an unbiased sample of probe electrons to measure the trigger efficiencies. The main source of inefficiency for these triggers is that the HLT requires a track with a greater number of hits than the offline reconstruction. The same trigger menu that was used to collect the data is not available in the simulated samples. Hence, no HLT requirement was applied to MC samples. For this reason, a 3% uncertainty is assigned to the electron selection efficiency due to the electron trigger requirements. Similarly, the electron reconstruction, identification and isolation efficiency is estimated using a sample of $Z \to ee$ events from data. The uncertainty on the reco/ID/isolation efficiency is found to be 0.5% (0.9%) in the ECAL barrel (endcaps), and the efficiency itself in the ECAL barrel (endcaps) is found to be about 2% (1%) lower in data than in MC simulation [121]. Furthermore, MC studies indicate that this efficiency decreases with the presence of additional jets in the event. Hence, a conservative 5% uncertainty is assigned on the electron reco/ID/isolation efficiency. The trigger and reco/ID/isolation uncertainties are added in quadrature, giving an overall 6% uncertainty on the electron selection efficiency. This uncertainty is not applicable to the background samples that have data-driven normalization, since these effects are already included in the normalization uncertainty.

The statistical uncertainty on the number of MC signal and background events passing the final event selection is reported in Table 5.6 and summarized in Table 5.10 for the signal hypothesis with a leptoquark mass of 300 GeV.

Additional uncertainties on the signal efficiency due to the choice of PDFs (estimated using an event reweighting technique that makes use of the LHAPDF

package [127]), the presence of additional hadronic jets produced as a result of QCD radiation in the initial and final states, and the presence of additional inelastic pp collisions were all found to be negligible ($\lesssim 1\%$).

The size and the estimated effect of the main sources of systematic uncertainties are summarized in Table 5.10. In order to obtain the total systematic uncertainty, the individual sources are assumed to be uncorrelated, and their contributions are added in quadrature. The systematic uncertainties for the background are dominated by the $t\bar{t}$ and W+jets background shape uncertainty. The systematic uncertainties on the signal efficiency are dominated by the uncertainty on the jet/$\not\!\!E_{\mathrm{T}}$ energy scale and the electron selection efficiency.

Table 5.10: Summary of the systematic uncertainties on the number of signal and background events passing the final event selection for the signal hypothesis with a leptoquark mass of 300 GeV.

Source	Systematic uncertainty [%]	Effect on N_{signal} [%]	Effect on $N_{t\bar{t}}$ [%]	Effect on $N_{W+\text{jets}}$ [%]	Effect on N_{QCD} [%]	Effect on N_{Other} [%]	Effect on N_{AllBkg} [%]
Data-driven normalization	[Section 5.6]	-	14	10	40	-	10
$t\bar{t}$ (W+jets) background shape	28 (49)	-	28	49	-	-	32
Jet/$\not\!\!E_{\text{T}}$ energy scale	5	5	9	6	-	9	7
Electron energy scale EB (EE)	1 (3)	1	4	2	-	1	3
Integrated luminosity	4	4	-	-	-	4	0.4
MC statistics	[Table 5.6]	0.4	6	20	-	19	9
Electron trigger/reco/ID/isolation	6	6	-	-	-	6	0.7
Total		9	33	54	40	22	35

Chapter 6

Results

The last two columns of Table 5.6 show that the number of observed events in data passing the final event selections is in good agreement with the predictions for SM processes only. Hence, in the absence of an observed LQ signal, an upper limit on the LQ pair-production cross section times branching ratio $2\beta(1-\beta)$ is set. The limit is calculated using a Bayesian method described in Appendix F that uses a flat prior for the signal, and log-normal priors for nuisance parameters to integrate over the systematic uncertainties. Figure 6.1 and Table 6.1 show the observed and expected 95% CL upper limits on the LQ pair-production cross section times $2\beta(1-\beta)$ as a function of LQ mass. The systematic uncertainties reported in Table 5.10 are included in the calculation of the limits. The upper limits are compared to the NLO prediction of the LQ pair-production cross section in Figure 2.3 in order to set a lower limit on the LQ mass as a function of branching ratio β. Figure 6.1 shows $\sigma_{\mathrm{NLO}} \times 2\beta(1-\beta)$ as a function of LQ mass assuming β of 0.5. The theoretical uncertainties on σ_{NLO} reported in Table 5.3 are represented as a band around the central value. The intersection of the theoretical cross-section and the observed upper limit curve at $M_{\mathrm{LQ}} = 320$ GeV indicates the observed 95% CL lower limit on the LQ mass for β of 0.5. If the observed upper limit is compared with the lower boundary of the uncertainty band for the theoretical cross section, the observed

lower limit on the LQ mass for β of 0.5 becomes 309 GeV.

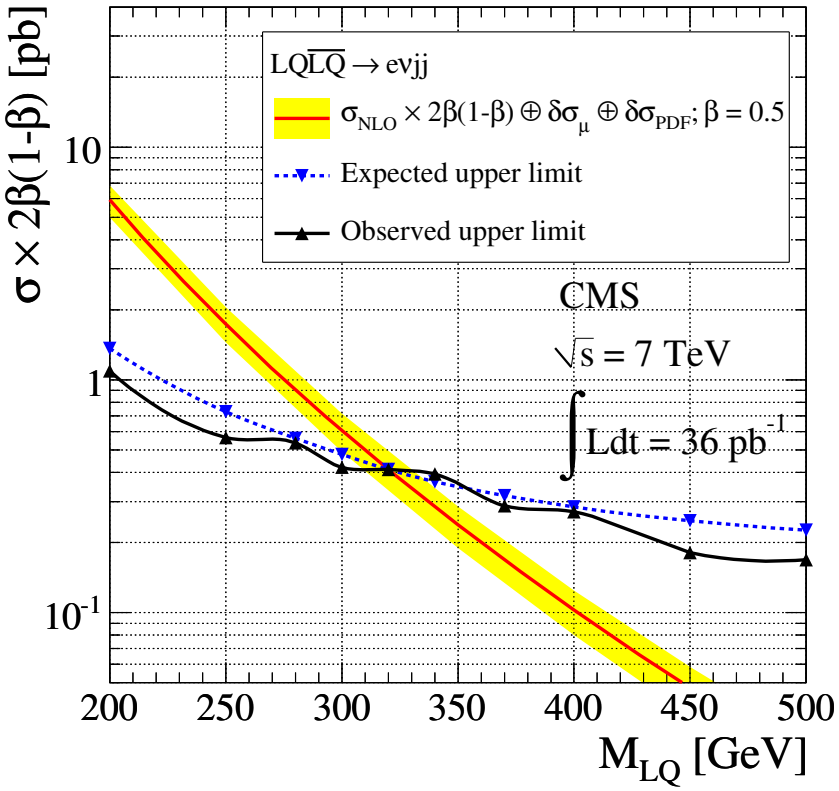

Figure 6.1: Observed and expected 95% CL upper limits on the LQ pair-production cross section times $2\beta(1-\beta)$ as a function of LQ mass. A NLO prediction of the LQ pair-production cross section times $2\beta(1-\beta)$ as a function of LQ mass, assuming $\beta = 0.5$, is also shown. The theoretical uncertainties on σ_{NLO} due to the definition of the renormalization/factorization scale and the choice of PDFs are represented as a band around the central value.

If a value of β different from 0.5 is assumed, the intersection of the theoretical cross section and the upper limit curve will change, resulting in a different lower limit on the LQ mass. Figure 6.2 shows the observed and expected 95% CL lower limits on the LQ mass as a function of β for the $e\nu jj$ channel, with the band around the observed limit corresponding to the uncertainty band for the theoretical cross section. The region to the left of the observed limit curve is excluded. As expected from the branching ratio for the $e\nu jj$ channels, the highest mass limit is obtained

Table 6.1: Observed and expected 95% CL upper limits on the LQ pair-production cross section times $2\beta(1-\beta)$ as a function of LQ mass.

M_{LQ} [GeV]	95% CL upper limit on $\sigma \times 2\beta(1-\beta)$ [pb]	
	Observed	Expected
200	1.092	1.363
250	0.565	0.729
280	0.536	0.560
300	0.421	0.479
320	0.412	0.411
340	0.394	0.365
370	0.287	0.318
400	0.271	0.284
450	0.181	0.248
500	0.169	0.226

for β of 0.5.

The results of this analysis are combined with the existing CMS results in the $eejj$ channel [56], thereby improving the reach of the LQ search in the intermediate β range. The same Bayesian method used to set the individual limits is used to set the combined limit. The likelihoods built for the individual $eejj$ and $e\nu jj$ channels are multiplied following the procedure described in Appendix F. While integrating over nuisance parameters, the systematic uncertainties on the signal and the background are assumed to be fully correlated, and conservatively the larger uncertainty between the two channels is used for both channels.

Figure 6.3 shows the observed 95% CL limits on the LQ mass as a function of β, obtained using the nominal value of the signal cross section ($\mu = M_{\mathrm{LQ}}$), for the individual $eejj$ and $e\nu jj$ channels, and their combination. The combined observed and expected lower limits on the LQ mass are reported in Table 6.2 for β values of 0.1, 0.5, and 1.

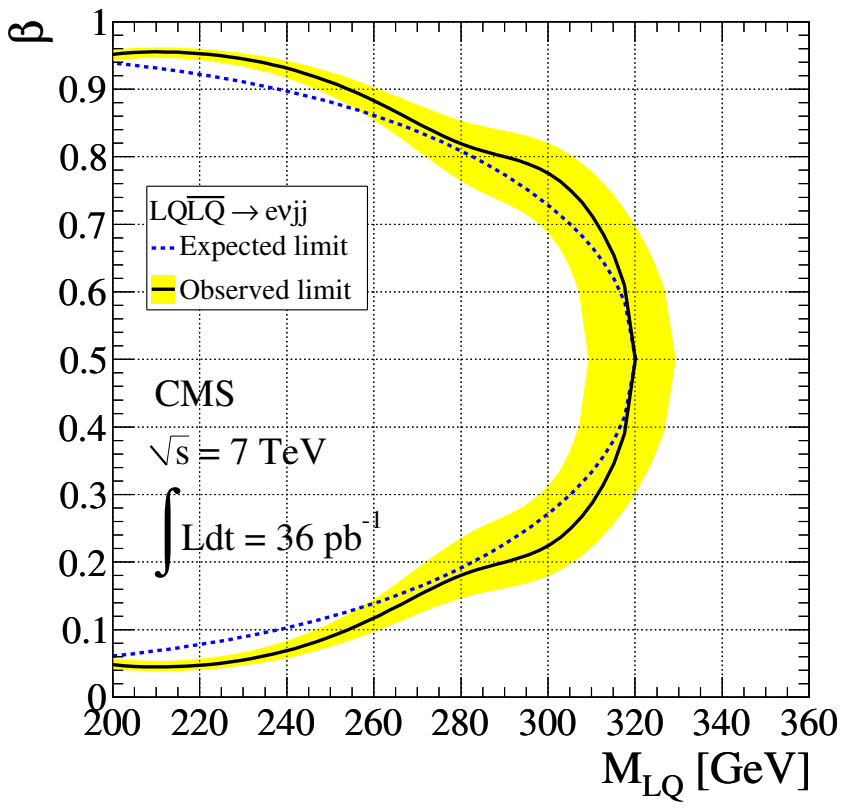

Figure 6.2: Observed and expected 95% CL lower limits on the LQ mass as a function of β for the $e\nu jj$ channel. The region to the left of the observed limit curve is excluded. The band around the observed limit corresponds to the uncertainty band for the theoretical cross section shown in Figure 6.1.

Table 6.2: Observed and expected 95% CL lower limits on the LQ mass for β values of 0.1, 0.5, and 1, obtained by combining the $eejj$ and $e\nu jj$ channels and using the nominal value of the signal cross section ($\mu = M_{\mathrm{LQ}}$).

β	Combined 95% CL lower limits on M_{LQ} [GeV]	
	Observed	Expected
1	384	391
0.5	339	344
0.1	254	236

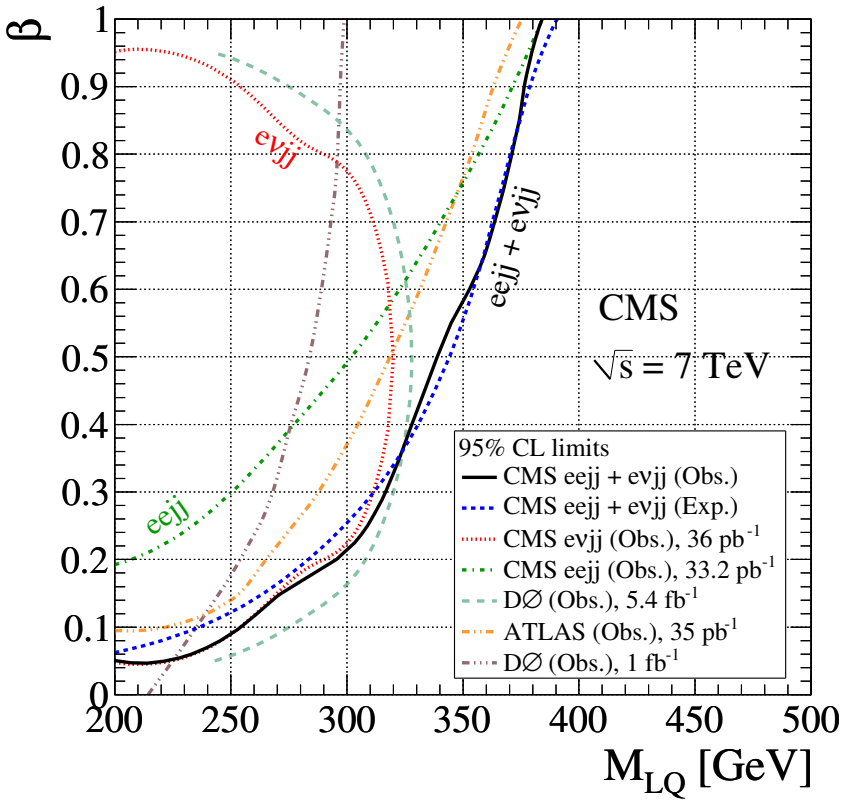

Figure 6.3: Observed 95% CL lower limits on the LQ mass as a function of β, obtained using the nominal value of the signal cross section ($\mu = M_{\mathrm{LQ}}$), for the individual $eejj$ and $e\nu jj$ channels, and their combination. The combined expected limit is also shown. The regions to the left of the observed limit curves are excluded. For comparison, D0 [53, 55] and ATLAS [54] limits are also shown.

Chapter 7

Conclusions and Prospects

Results of a search for pair production of first-generation scalar leptoquarks in a final state containing an electron, a neutrino, and at least two jets have been presented. The search was performed using the 2010 data sample of proton-proton collisions at $\sqrt{s} = 7$ TeV collected by the CMS detector at the CERN LHC, corresponding to an integrated luminosity of 36 pb^{-1}. The number of observed events in data passing the final event selection is in good agreement with the predicted yield for Standard Model processes for all leptoquark masses considered. A 95%-confidence-level upper limit on the pair-production cross section for first-generation scalar leptoquarks is set and compared to a NLO cross-section prediction, resulting in a 95%-confidence-level lower limit on the leptoquark mass of 320 GeV assuming β of 0.5. This limit is lower than the corresponding D0 limit at 326 GeV [55] obtained by analyzing 5.4 fb^{-1} of proton-antiproton collision data. Due to the higher center-of-mass energy at the LHC, the CMS results are competitive with those from D0 even with a small amount of integrated luminosity.

Prior results from CMS in the dielectron channel are combined with the results of this electron+neutrino search. A combined 95%-confidence-level lower limit is set on the mass of a first-generation scalar leptoquark as a function of β, resulting in a lower limit of 254, 339, and 384 GeV for β values of 0.1, 0.5, and 1, respec-

tively. These results represent the most stringent direct limits to date for values of β greater than 0.35. The result presented in this dissertation have been submitted for publication [57].

With the LHC still increasing the instantaneous luminosity in 2011 and delivering more data in one day than in the 2010, significant improvements in the mass reach of leptoquark searches with the full 2011 data sample can be expected. The inclusion of results from the $\nu\nu jj$ channel will help improve the sensitivity for low values of β. It is foreseen that the LHC will continues running at $\sqrt{s} = 7$ TeV until the end of 2012, with a total integrated luminosity at that point in excess of 10 fb^{-1}. In addition to adding more data to the analysis, additional improvements in the mass reach of leptoquark searches could follow from employing more sophisticated analysis techniques. Further improvements will follow with the increased center-of-mass energy after the next long maintenance shutdown scheduled to start at the end of 2012 and expected to finish in the first half of 2014.

Appendix A

Trigger Tables for Primary Datasets

Table A.1: Trigger table for EG primary dataset in run range 136035–137028.

Trigger name	Prescale factor	L1 seed
HLT_DoubleEle5_SW_L1R	1	L1_DoubleEG5
HLT_DoublePhoton10_L1R	1	L1_DoubleEG5
HLT_DoublePhoton4_Jpsi_L1R	1	L1_DoubleEG2
HLT_DoublePhoton4_Upsilon_L1R	1	L1_DoubleEG2
HLT_DoublePhoton4_eeRes_L1R	1	L1_DoubleEG2
HLT_DoublePhoton5_Jpsi_L1R	1	L1_SingleEG8 OR L1_DoubleEG5
HLT_DoublePhoton5_L1R	1	L1_DoubleEG5
HLT_DoublePhoton5_Upsilon_L1R	1	L1_SingleEG8 OR L1_DoubleEG5
HLT_Ele10_LW_EleId_L1R	1	L1_SingleEG5
HLT_Ele10_LW_L1R	1	L1_SingleEG5
HLT_Ele15_LW_L1R	1	L1_SingleEG8
HLT_Ele15_SC10_LW_L1R	1	L1_SingleEG8
HLT_Ele15_SiStrip_L1R	1	L1_SingleEG8
HLT_Ele20_LW_L1R	1	L1_SingleEG8
HLT_Photon10_L1R	1	L1_SingleEG5
HLT_Photon15_L1R	1	L1_SingleEG8
HLT_Photon15_LooseEcalIso_L1R	1	L1_SingleEG8
HLT_Photon15_TrackIso_L1R	1	L1_SingleEG8
HLT_Photon20_L1R	1	L1_SingleEG8
HLT_Photon30_L1R_8E29	1	L1_SingleEG8

Table A.2: Trigger table for EG primary dataset in run range 138560–138747.

Trigger name	Prescale factor			L1 seed
	$\mathcal{L}$ [$\mathrm{cm}^{-2}\mathrm{s}^{-1}$]	4×10^{29}	2×10^{29}	1×10^{29}	
HLT_DoubleEle5_SW_L1R		1	1	1	L1_DoubleEG5
HLT_DoublePhoton10_L1R		1	1	1	L1_DoubleEG5
HLT_DoublePhoton4_Jpsi_L1R		1	1	1	L1_DoubleEG2
HLT_DoublePhoton4_Upsilon_L1R		1	1	1	L1_DoubleEG2
HLT_DoublePhoton4_eeRes_L1R		1	1	1	L1_DoubleEG2
HLT_DoublePhoton5_Jpsi_L1R		1	1	1	L1_SingleEG8 OR L1_DoubleEG5
HLT_DoublePhoton5_L1R		1	1	1	L1_DoubleEG5
HLT_DoublePhoton5_Upsilon_L1R		1	1	1	L1_SingleEG8 OR L1_DoubleEG5
HLT_Ele10_LW_EleId_L1R		1	1	1	L1_SingleEG5
HLT_Ele10_LW_L1R		1	1	1	L1_SingleEG5
HLT_Ele15_LW_L1R		1	1	1	L1_SingleEG5
HLT_Ele15_SC10_LW_L1R		1	1	1	L1_SingleEG5
HLT_Ele15_SiStrip_L1R		1	1	1	L1_SingleEG5
HLT_Ele20_LW_L1R		1	1	1	L1_SingleEG8
HLT_Photon10_Cleaned_L1R		1	1	1	L1_SingleEG5
HLT_Photon15_Cleaned_L1R		1	1	1	L1_SingleEG5
HLT_Photon15_L1R		1	1	1	L1_SingleEG5
HLT_Photon15_LooseEcalIso_L1R		1	1	1	L1_SingleEG5
HLT_Photon15_TrackIso_L1R		1	1	1	L1_SingleEG5
HLT_Photon20_Cleaned_L1R		1	1	1	L1_SingleEG8
HLT_Photon20_L1R		1	1	1	L1_SingleEG8
HLT_Photon30_L1R_8E29		1	1	1	L1_SingleEG5

Table A.3: Trigger table for EG primary dataset in run range 138749–139103.

Trigger name	Prescale factor			L1 seed
	$\mathcal{L}$ [$\mathrm{cm}^{-2}\mathrm{s}^{-1}$]	4×10^{29}	2×10^{29}	1×10^{29}	
HLT_DoubleEle5_SW_L1R		1	1	1	L1_DoubleEG5
HLT_DoublePhoton10_L1R		1	1	1	L1_DoubleEG5
HLT_DoublePhoton4_Jpsi_L1R		1	1	1	L1_DoubleEG2
HLT_DoublePhoton4_Upsilon_L1R		1	1	1	L1_DoubleEG2
HLT_DoublePhoton4_eeRes_L1R		1	1	1	L1_DoubleEG2
HLT_DoublePhoton5_Jpsi_L1R		1	1	1	L1_SingleEG8 OR L1_DoubleEG5
HLT_DoublePhoton5_L1R		1	1	1	L1_DoubleEG5
HLT_DoublePhoton5_Upsilon_L1R		1	1	1	L1_SingleEG8 OR L1_DoubleEG5
HLT_Ele10_LW_EleId_L1R		1	1	1	L1_SingleEG5
HLT_Ele10_LW_L1R		1	1	1	L1_SingleEG5
HLT_Ele15_LW_L1R		1	1	1	L1_SingleEG5
HLT_Ele15_SC10_LW_L1R		1	1	1	L1_SingleEG5
HLT_Ele15_SiStrip_L1R		1	1	1	L1_SingleEG5
HLT_Ele20_LW_L1R		1	1	1	L1_SingleEG8
HLT_Photon10_Cleaned_L1R		10	1	1	L1_SingleEG5
HLT_Photon15_Cleaned_L1R		1	1	1	L1_SingleEG5
HLT_Photon15_L1R		1	1	1	L1_SingleEG5
HLT_Photon15_LooseEcalIso_L1R		1	1	1	L1_SingleEG5
HLT_Photon15_TrackIso_L1R		1	1	1	L1_SingleEG5
HLT_Photon20_Cleaned_L1R		1	1	1	L1_SingleEG8
HLT_Photon20_L1R		1	1	1	L1_SingleEG8
HLT_Photon30_L1R_8E29		1	1	1	L1_SingleEG5

Table A.4: Trigger table for EG primary dataset in run range 139195–139980.

Trigger name	Prescale factor			L1 seed
	$\mathcal{L}$ [$\mathrm{cm}^{-2}\mathrm{s}^{-1}$]	8×10^{29}	4×10^{29}	2×10^{29}	
HLT_DoubleEle5_SW_L1R		1	1	1	L1_DoubleEG5
HLT_DoublePhoton10_L1R		1	1	1	L1_DoubleEG5
HLT_DoublePhoton4_Jpsi_L1R		1	1	1	L1_DoubleEG2
HLT_DoublePhoton4_Upsilon_L1R		1	1	1	L1_DoubleEG2
HLT_DoublePhoton4_eeRes_L1R		10	5	2	L1_DoubleEG2
HLT_DoublePhoton5_Jpsi_L1R		1	1	1	L1_SingleEG8 OR L1_DoubleEG5
HLT_DoublePhoton5_L1R		1	1	1	L1_DoubleEG5
HLT_DoublePhoton5_Upsilon_L1R		1	1	1	L1_SingleEG8 OR L1_DoubleEG5
HLT_Ele10_LW_EleId_L1R		1	1	1	L1_SingleEG5
HLT_Ele10_LW_L1R		1	1	1	L1_SingleEG5
HLT_Ele10_SW_L1R		1	1	1	L1_SingleEG5
HLT_Ele15_LW_L1R		1	1	1	L1_SingleEG5
HLT_Ele15_SC10_LW_L1R		1	1	1	L1_SingleEG5
HLT_Ele15_SiStrip_L1R		1	1	1	L1_SingleEG5
HLT_Ele20_LW_L1R		1	1	1	L1_SingleEG8
HLT_Photon10_Cleaned_L1R		20	10	5	L1_SingleEG5
HLT_Photon15_Cleaned_L1R		1	1	1	L1_SingleEG5
HLT_Photon15_L1R		1	1	1	L1_SingleEG5
HLT_Photon15_LooseEcalIso_L1R		1	1	1	L1_SingleEG5
HLT_Photon15_TrackIso_L1R		1	1	1	L1_SingleEG5
HLT_Photon20_Cleaned_L1R		1	1	1	L1_SingleEG8
HLT_Photon20_L1R		1	1	1	L1_SingleEG8
HLT_Photon30_L1R_8E29		1	1	1	L1_SingleEG5

Table A.5: Trigger table for EG primary dataset in run range 140058–140076.

Trigger name	Prescale factor				L1 seed
	$\mathcal{L}$ [$cm^{-2}s^{-1}$]	1.6×10^{30}	8×10^{29}	4×10^{29}	2×10^{29}	
HLT_DoubleEle5_SW_L1R		1	1	1	1	L1_DoubleEG5
HLT_DoublePhoton10_L1R		1	1	1	1	L1_DoubleEG5
HLT_DoublePhoton4_Jpsi_L1R		20	10	5	2	L1_DoubleEG2
HLT_DoublePhoton4_Upsilon_L1R		20	10	5	2	L1_DoubleEG2
HLT_DoublePhoton4_eeRes_L1R		100	50	20	10	L1_DoubleEG2
HLT_DoublePhoton5_Jpsi_L1R		20	10	5	2	L1_SingleEG8 OR L1_DoubleEG5
HLT_DoublePhoton5_L1R		20	10	5	2	L1_DoubleEG5
HLT_DoublePhoton5_Upsilon_L1R		20	10	5	2	L1_SingleEG8 OR L1_DoubleEG5
HLT_Ele10_LW_EleId_L1R		1	1	1	1	L1_SingleEG5
HLT_Ele10_LW_L1R		20	10	5	2	L1_SingleEG5
HLT_Ele10_SW_L1R		20	10	5	2	L1_SingleEG5
HLT_Ele15_LW_L1R		1	1	1	1	L1_SingleEG5
HLT_Ele15_SC10_LW_L1R		1	1	1	1	L1_SingleEG5
HLT_Ele15_SW_L1R		1	1	1	1	L1_SingleEG5
HLT_Ele15_SiStrip_L1R		1	1	1	1	L1_SingleEG5
HLT_Ele20_LW_L1R		1	1	1	1	L1_SingleEG8
HLT_Ele20_SW_L1R		1	1	1	1	L1_SingleEG8
HLT_Photon10_Cleaned_L1R		80	40	20	10	L1_SingleEG5
HLT_Photon15_Cleaned_L1R		1	1	1	1	L1_SingleEG5
HLT_Photon15_LooseEcalIso_Cleaned_L1R		1	1	1	1	L1_SingleEG5
HLT_Photon15_TrackIso_Cleaned_L1R		1	1	1	1	L1_SingleEG5
HLT_Photon20_Cleaned_L1R		1	1	1	1	L1_SingleEG8
HLT_Photon30_L1R_8E29		1	1	1	1	L1_SingleEG5

Table A.6: Trigger table for EG primary dataset in run range 140116–140401.

Trigger name	Prescale factor				L1 seed
	$\mathcal{L}$ [$\mathrm{cm}^{-2}\mathrm{s}^{-1}$]	1.6×10^{30}	8×10^{29}	4×10^{29}	2×10^{29}	
HLT_DoubleEle5_SW_L1R		1	1	1	1	L1_DoubleEG5
HLT_DoublePhoton10_L1R		1	1	1	1	L1_DoubleEG5
HLT_DoublePhoton4_Jpsi_L1R		20	10	5	2	L1_DoubleEG2
HLT_DoublePhoton4_Upsilon_L1R		20	10	5	2	L1_DoubleEG2
HLT_DoublePhoton4_eeRes_L1R		100	50	20	10	L1_DoubleEG2
HLT_DoublePhoton5_CEP_L1R		1	1	1	1	L1_DoubleEG5
HLT_DoublePhoton5_Jpsi_L1R		20	10	5	2	L1_SingleEG8 OR L1_DoubleEG5
HLT_DoublePhoton5_L1R		20	10	5	2	L1_DoubleEG5
HLT_DoublePhoton5_Upsilon_L1R		20	10	5	2	L1_SingleEG8 OR L1_DoubleEG5
HLT_Ele10_LW_EleId_L1R		1	1	1	1	L1_SingleEG5
HLT_Ele10_LW_L1R		20	10	5	2	L1_SingleEG5
HLT_Ele10_SW_L1R		20	10	5	2	L1_SingleEG5
HLT_Ele15_LW_L1R		1	1	1	1	L1_SingleEG5
HLT_Ele15_SC10_LW_L1R		1	1	1	1	L1_SingleEG5
HLT_Ele15_SW_L1R		1	1	1	1	L1_SingleEG5
HLT_Ele15_SiStrip_L1R		1	1	1	1	L1_SingleEG5
HLT_Ele20_LW_L1R		1	1	1	1	L1_SingleEG8
HLT_Ele20_SW_L1R		1	1	1	1	L1_SingleEG8
HLT_Photon10_Cleaned_L1R		80	40	20	10	L1_SingleEG5
HLT_Photon15_Cleaned_L1R		1	1	1	1	L1_SingleEG5
HLT_Photon15_LooseEcalIso_Cleaned_L1R		1	1	1	1	L1_SingleEG5
HLT_Photon15_TrackIso_Cleaned_L1R		1	1	1	1	L1_SingleEG5
HLT_Photon20_Cleaned_L1R		1	1	1	1	L1_SingleEG8
HLT_Photon30_L1R		1	1	1	1	L1_SingleEG8

Table A.7: Trigger table for EG primary dataset in run range 141956–142936.

Trigger name	Prescale factor					L1 seed
	$\mathcal{L}$ [$\mathrm{cm}^{-2}\mathrm{s}^{-1}$]	3.5×10^{30}	3.2×10^{30}	2.3×10^{30}	1.6×10^{30}	EG	
HLT_DoubleEle10_SW_L1R		1	1	1	1	1	L1_DoubleEG5
HLT_DoubleEle4_SW_eeRes_L1R		1	1	1	1	1	L1_DoubleEG2
HLT_DoublePhoton15_L1R		1	1	1	1	1	L1_DoubleEG5
HLT_DoublePhoton20_L1R		1	1	1	1	1	L1_DoubleEG5
HLT_DoublePhoton5_CEP_L1R		1	1	1	1	1	L1_DoubleEG5
HLT_DoublePhoton5_Jpsi_L1R		20	18	13	9	20	L1_SingleEG8 OR L1_DoubleEG5
HLT_DoublePhoton5_Upsilon_L1R		20	18	13	9	20	L1_SingleEG8 OR L1_DoubleEG5
HLT_Ele10_SW_EleId_L1R		1	1	1	1	1	L1_SingleEG8
HLT_Ele15_SW_CaloEleId_L1R		1	1	1	1	1	L1_SingleEG5
HLT_Ele15_SW_EleId_L1R		1	1	1	1	1	L1_SingleEG5
HLT_Ele15_SW_L1R		1	1	1	1	2	L1_SingleEG5
HLT_Ele20_SW_L1R		1	1	1	1	1	L1_SingleEG8
HLT_Ele25_SW_L1R		1	1	1	1	1	L1_SingleEG8
HLT_Photon20_Cleaned_L1R		1	1	1	1	2	L1_SingleEG8
HLT_Photon30_Cleaned_L1R		1	1	1	1	1	L1_SingleEG8
HLT_Photon50_Cleaned_L1R		1	1	1	1	1	L1_SingleEG8
HLT_Photon50_L1R		1	1	1	1	1	L1_SingleEG8

Table A.8: Trigger table for EG primary dataset in run range 143318–143962.

Trigger name	Prescale factor				L1 seed
	$\mathcal{L}$ [$\mathrm{cm^{-2}s^{-1}}$]	9×10^{30}	6.4×10^{30}	4.5×10^{30}	3.2×10^{30}	
HLT_DoubleEle10_SW_L1R		1	1	1	1	L1_DoubleEG5
HLT_DoubleEle4_SW_eeRes_L1R		1	1	1	1	L1_DoubleEG2
HLT_DoublePhoton15_L1R		1	1	1	1	L1_DoubleEG5
HLT_DoublePhoton20_L1R		1	1	1	1	L1_DoubleEG5
HLT_DoublePhoton5_CEP_L1R		1	1	1	1	L1_DoubleEG5
HLT_DoublePhoton5_Jpsi_L1R		50	35	25	18	L1_SingleEG8 OR L1_DoubleEG5
HLT_DoublePhoton5_Upsilon_L1R		50	35	25	18	L1_SingleEG8 OR L1_DoubleEG5
HLT_Ele10_SW_EleId_L1R		1	1	1	1	L1_SingleEG8
HLT_Ele15_SW_CaloEleId_L1R		1	1	1	1	L1_SingleEG5
HLT_Ele15_SW_EleId_L1R		1	1	1	1	L1_SingleEG5
HLT_Ele15_SW_L1R		1	1	1	1	L1_SingleEG5
HLT_Ele20_SW_L1R		1	1	1	1	L1_SingleEG8
HLT_Ele25_SW_L1R		1	1	1	1	L1_SingleEG8
HLT_Photon20_Cleaned_L1R		1	1	1	1	L1_SingleEG8
HLT_Photon30_Cleaned_L1R		1	1	1	1	L1_SingleEG8
HLT_Photon50_Cleaned_L1R		1	1	1	1	L1_SingleEG8
HLT_Photon50_L1R		1	1	1	1	L1_SingleEG8

Table A.9: Trigger table for EG primary dataset in run range 144010–144011.

Trigger name	Prescale factor				L1 seed
	$\mathcal{L}$ [$\mathrm{cm^{-2}s^{-1}}$]	9×10^{30}	6.4×10^{30}	4.5×10^{30}	3.2×10^{30}	
HLT_DoubleEle10_SW_L1R		1	1	1	1	L1_DoubleEG5
HLT_DoubleEle4_SW_eeRes_L1R		1	1	1	1	L1_DoubleEG2
HLT_DoublePhoton15_L1R		1	1	1	1	L1_DoubleEG5
HLT_DoublePhoton20_L1R		1	1	1	1	L1_DoubleEG5
HLT_DoublePhoton5_CEP_L1R		1	1	1	1	L1_DoubleEG5
HLT_DoublePhoton5_Jpsi_L1R		50	35	25	18	L1_SingleEG8 OR L1_DoubleEG5
HLT_DoublePhoton5_Upsilon_L1R		50	35	25	18	L1_SingleEG8 OR L1_DoubleEG5
HLT_Ele15_SW_CaloEleId_L1R		1	1	1	1	L1_SingleEG5
HLT_Ele15_SW_EleId_L1R		1	1	1	1	L1_SingleEG5
HLT_Ele15_SW_L1R		40	28	20	14	L1_SingleEG5
HLT_Ele20_SW_L1R		1	1	1	1	L1_SingleEG8
HLT_Ele25_SW_L1R		1	1	1	1	L1_SingleEG8
HLT_Photon20_Cleaned_L1R		5	4	3	2	L1_SingleEG8
HLT_Photon25_Cleaned_L1R		1	1	1	1	L1_SingleEG8
HLT_Photon30_Cleaned_L1R		1	1	1	1	L1_SingleEG8
HLT_Photon50_Cleaned_L1R		1	1	1	1	L1_SingleEG8
HLT_Photon50_L1R		1	1	1	1	L1_SingleEG8

Table A.10: Trigger table for EG primary dataset in run range 144083–144114.

Trigger name	Prescale factor				L1 seed
	$\mathcal{L}$ [$\mathrm{cm}^{-2}\mathrm{s}^{-1}$]	9×10^{30}	6.4×10^{30}	4.5×10^{30}	3.2×10^{30}	
HLT_DoubleEle10_SW_L1R		1	1	1	1	L1_DoubleEG5
HLT_DoubleEle4_SW_eeRes_L1R		1	1	1	1	L1_DoubleEG2
HLT_DoublePhoton15_L1R		1	1	1	1	L1_DoubleEG5
HLT_DoublePhoton20_L1R		1	1	1	1	L1_DoubleEG5
HLT_DoublePhoton5_CEP_L1R		1	1	1	1	L1_DoubleEG5
HLT_DoublePhoton5_Jpsi_L1R		50	35	25	18	L1_SingleEG8 OR L1_DoubleEG5
HLT_DoublePhoton5_Upsilon_L1R		50	35	25	18	L1_SingleEG8 OR L1_DoubleEG5
HLT_Ele10_SW_EleId_L1R		1	1	1	1	L1_SingleEG5
HLT_Ele15_SW_CaloEleId_L1R		1	1	1	1	L1_SingleEG5
HLT_Ele15_SW_EleId_L1R		1	1	1	1	L1_SingleEG5
HLT_Ele15_SW_L1R		40	28	20	14	L1_SingleEG5
HLT_Ele20_SW_L1R		1	1	1	1	L1_SingleEG8
HLT_Ele25_SW_L1R		1	1	1	1	L1_SingleEG8
HLT_Photon20_Cleaned_L1R		5	4	3	2	L1_SingleEG8
HLT_Photon25_Cleaned_L1R		1	1	1	1	L1_SingleEG8
HLT_Photon30_Cleaned_L1R		1	1	1	1	L1_SingleEG8
HLT_Photon50_Cleaned_L1R		1	1	1	1	L1_SingleEG8
HLT_Photon50_L1R		1	1	1	1	L1_SingleEG8

Table A.11: Trigger table for Electron primary dataset in run range 146428–146644.

Trigger name	Prescale factor				L1 seed
	$\mathcal{L}$ [$cm^{-2}s^{-1}$]	2.8×10^{31}	2×10^{31}	1.4×10^{31}	1×10^{31}	
HLT_DoubleEle10_SW_L1R		1	1	1	1	L1_DoubleEG5
HLT_Ele12_SW_TightEleIdIsol_L1R		1	1	1	1	L1_SingleEG8
HLT_Ele12_SW_TightEleIdIsol_NoDEtaInEE_L1R		1	1	1	1	L1_SingleEG8
HLT_Ele17_SW_CaloEleId_L1R		1	1	1	1	L1_SingleEG8
HLT_Ele17_SW_EleId_L1R		1	1	1	1	L1_SingleEG8
HLT_Ele17_SW_LooseEleId_L1R		1	1	1	1	L1_SingleEG8
HLT_Ele22_SW_CaloEleId_L1R		1	1	1	1	L1_SingleEG8
HLT_Ele40_SW_L1R		1	1	1	1	L1_SingleEG8

Table A.12: Trigger table for Electron primary dataset in run range 146698–147116.

Trigger name	Prescale factor						L1 seed
	$\mathcal{L}$ [$cm^{-2}s^{-1}$]	6×10^{31}	4×10^{31}	2.8×10^{31}	2×10^{31}	1.4×10^{31}	1×10^{31}	
HLT_DoubleEle10_SW_L1R		1	1	1	1	1	1	L1_DoubleEG5
HLT_Ele12_SW_TightEleIdIsol_L1R		1	1	1	1	1	1	L1_SingleEG8
HLT_Ele12_SW_TightEleIdIsol_NoDEtaInEE_L1R		1	1	1	1	1	1	L1_SingleEG8
HLT_Ele17_SW_CaloEleId_L1R		1	1	1	1	1	1	L1_SingleEG8
HLT_Ele17_SW_EleId_L1R		1	1	1	1	1	1	L1_SingleEG8
HLT_Ele17_SW_LooseEleId_L1R		1	1	1	1	1	1	L1_SingleEG8
HLT_Ele17_SW_TightEleIdIsol_L1R		1	1	1	1	1	1	L1_SingleEG8
HLT_Ele17_SW_TightEleId_L1R		1	1	1	1	1	1	L1_SingleEG8
HLT_Ele22_SW_CaloEleId_L1R		1	1	1	1	1	1	L1_SingleEG8
HLT_Ele40_SW_L1R		1	1	1	1	1	1	L1_SingleEG8

Table A.13: Trigger table for Electron primary dataset in run range 147196–147284.

Trigger name	Prescale factor					L1 seed
	$\mathcal{L}$ [$\mathrm{cm}^{-2}\mathrm{s}^{-1}$]	1×10^{32}	8×10^{31}	6×10^{31}	4×10^{31}	2×10^{31}	
HLT_DoubleEle15_SW_L1R_v1		1	1	1	1	1	L1_DoubleEG5
HLT_Ele10_MET45_v1		1	1	1	1	1	L1_ETM20
HLT_Ele12_SW_TighterEleIdIsol_L1R_v1		1	1	1	1	1	L1_SingleEG8
HLT_Ele17_SW_TightCaloEleId_SC8HE_L1R_v1		1	1	1	1	1	L1_SingleEG8
HLT_Ele17_SW_TightEleIdIsol_L1R_v1		1	1	1	1	1	L1_SingleEG8
HLT_Ele17_SW_TightEleId_L1R		1	1	1	1	1	L1_SingleEG8
HLT_Ele17_SW_TighterEleIdIsol_L1R_v1		1	1	1	1	1	L1_SingleEG8
HLT_Ele17_SW_TighterEleId_L1R_v1		1	1	1	1	1	L1_SingleEG8
HLT_Ele27_SW_TightCaloEleIdTrack_L1R_v1		1	1	1	1	1	L1_SingleEG8
HLT_Ele32_SW_TightCaloEleIdTrack_L1R_v1		1	1	1	1	1	L1_SingleEG8

Table A.14: Trigger table for Electron primary dataset in run range 147390–148058.

Trigger name	Prescale factor					L1 seed
	$\mathcal{L}$ [$\mathrm{cm}^{-2}\mathrm{s}^{-1}$]	1×10^{32}	8×10^{31}	6×10^{31}	4×10^{31}	2×10^{31}	
HLT_DoubleEle15_SW_L1R_v1		1	1	1	1	1	L1_DoubleEG5
HLT_Ele10_MET45_v1		1	1	1	1	1	L1_ETM20
HLT_Ele12_SW_TighterEleIdIsol_L1R_v1		1	1	1	1	1	L1_SingleEG8
HLT_Ele17_SW_TightCaloEleId_Ele8HE_L1R_v1		1	1	1	1	1	L1_SingleEG8
HLT_Ele17_SW_TightCaloEleId_SC8HE_L1R_v1		1	1	1	1	1	L1_SingleEG8
HLT_Ele17_SW_TightEleIdIsol_L1R_v1		1	1	1	1	1	L1_SingleEG8
HLT_Ele17_SW_TightEleId_L1R		1	1	1	1	1	L1_SingleEG8
HLT_Ele17_SW_TighterEleIdIsol_L1R_v1		1	1	1	1	1	L1_SingleEG8
HLT_Ele17_SW_TighterEleId_L1R_v1		1	1	1	1	1	L1_SingleEG8
HLT_Ele27_SW_TightCaloEleIdTrack_L1R_v1		1	1	1	1	1	L1_SingleEG8
HLT_Ele32_SW_TightCaloEleIdTrack_L1R_v1		1	1	1	1	1	L1_SingleEG8

Table A.15: Trigger table for Electron primary dataset in run range 148819–149064.

Trigger name	Prescale factor						L1 seed
	$\mathcal{L}$ [$\mathrm{cm}^{-2}\mathrm{s}^{-1}$]	4×10^{32}	2×10^{32}	1.7×10^{32}	1.4×10^{32}	1.1×10^{32}	0.8×10^{32}	
HLT_DoubleEle17_SW_L1R_v1		1	1	1	1	1	1	L1_DoubleEG5
HLT_DoubleEle8_SW_HT70U_L1R_v1		1	1	1	1	1	1	L1_DoubleEG5
HLT_Ele10_SW_EleId_HT70U_L1R_v1		1	1	1	1	1	1	L1_SingleEG8
HLT_Ele10_SW_HT100U_L1R_v1		1	1	1	1	1	1	L1_SingleEG8
HLT_Ele10_SW_HT70U_L1R_v1		1	1	1	1	1	1	L1_SingleEG8
HLT_Ele17_SW_TightCaloEleId_Ele8HE_L1R_v1		1	1	1	1	1	1	L1_SingleEG8
HLT_Ele17_SW_TighterEleIdIsol_L1R_v2		1	1	1	1	1	1	L1_SingleEG8
HLT_Ele22_SW_TighterCaloIdIsol_L1R_v1		1	1	1	1	1	1	L1_SingleEG8
HLT_Ele22_SW_TighterEleId_L1R_v2		1	1	1	1	1	1	L1_SingleEG8
HLT_Ele32_SW_TighterEleId_L1R_v2		1	1	1	1	1	1	L1_SingleEG8
HLT_IsoEle12_PFTau15_v1		1	1	1	1	1	1	L1_SingleEG8

Table A.16: Trigger table for Electron primary dataset in run range 149181–149182.

Trigger name	Prescale factor						L1 seed
	$\mathcal{L}$ [$\mathrm{cm}^{-2}\mathrm{s}^{-1}$]	4×10^{32}	2×10^{32}	1.7×10^{32}	1.4×10^{32}	1.1×10^{32}	0.8×10^{32}	
HLT_DoubleEle17_SW_L1R_v1		1	1	1	1	1	1	L1_DoubleEG5
HLT_DoubleEle8_SW_HT70U_L1R_v1		1	1	1	1	1	1	L1_DoubleEG5
HLT_Ele10_SW_EleId_HT70U_L1R_v2		1	1	1	1	1	1	L1_SingleEG8
HLT_Ele10_SW_HT100U_L1R_v2		1	1	1	1	1	1	L1_SingleEG8
HLT_Ele10_SW_HT70U_L1R_v2		1	1	1	1	1	1	L1_SingleEG8
HLT_Ele17_SW_TightCaloEleId_Ele8HE_L1R_v2		1	1	1	1	1	1	L1_SingleEG8
HLT_Ele17_SW_TighterEleIdIsol_L1R_v3		1	1	1	1	1	1	L1_SingleEG8
HLT_Ele22_SW_TighterCaloIdIsol_L1R_v2		1	1	1	1	1	1	L1_SingleEG8
HLT_Ele22_SW_TighterEleId_L1R_v3		1	1	1	1	1	1	L1_SingleEG8
HLT_Ele32_SW_TighterEleId_L1R_v2		1	1	1	1	1	1	L1_SingleEG8
HLT_IsoEle12_PFTau15_v2		1	1	1	1	1	1	L1_SingleEG8

Table A.17: Trigger table for Electron primary dataset in run range 149291–149294.

Trigger name	Prescale factor						L1 seed
	$\mathcal{L}$ [$\mathrm{cm}^{-2}\mathrm{s}^{-1}$]	4×10^{32}	2×10^{32}	1.7×10^{32}	1.4×10^{32}	1.1×10^{32}	0.8×10^{32}	
HLT_DoubleEle17_SW_L1R_v1		1	1	1	1	1	1	L1_DoubleEG5
HLT_DoubleEle8_SW_HT70U_L1R_v1		1	1	1	1	1	1	L1_DoubleEG5
HLT_Ele10_SW_EleId_HT70U_L1R_v2		1	1	1	1	1	1	L1_SingleEG8
HLT_Ele10_SW_HT100U_L1R_v2		1	1	1	1	1	1	L1_SingleEG8
HLT_Ele10_SW_HT70U_L1R_v2		1	1	1	1	1	1	L1_SingleEG8
HLT_Ele17_SW_TightCaloEleId_Ele8HE_L1R_v2		1	1	1	1	1	1	L1_SingleEG8
HLT_Ele17_SW_TighterEleIdIsol_L1R_v3		1	1	1	1	1	1	L1_SingleEG8
HLT_Ele22_SW_TighterCaloIdIsol_L1R_v2		1	1	1	1	1	1	L1_SingleEG8
HLT_Ele22_SW_TighterEleId_L1R_v3		1	1	1	1	1	1	L1_SingleEG8
HLT_Ele32_SW_TighterEleId_L1R_v2		1	1	1	1	1	1	L1_SingleEG8
HLT_IsoEle12_PFTau15_v3		1	1	1	1	1	1	L1_SingleEG8

Table A.18: Trigger table for Photon primary dataset in run range 146428–146589.

Trigger name	Prescale factor					L1 seed
	$\mathcal{L}$ [$\mathrm{cm}^{-2}\mathrm{s}^{-1}$]	2.8×10^{31}	2×10^{31}	1.4×10^{31}	1×10^{31}	
HLT_DoublePhoton17_L1R		1	1	1	1	L1_DoubleEG5
HLT_DoublePhoton5_CEP_L1R		1	1	1	1	L1_DoubleEG5
HLT_Photon20_Cleaned_L1R		20	14	10	7	L1_SingleEG8
HLT_Photon30_Cleaned_L1R		1	1	1	1	L1_SingleEG8
HLT_Photon50_NoHE_Cleaned_L1R		1	1	1	1	L1_SingleEG8

Table A.19: Trigger table for Photon primary dataset in run range 146644–147116.

Trigger name	Prescale factor							L1 seed
	$\mathcal{L}$ [$\mathrm{cm}^{-2}\mathrm{s}^{-1}$]	6×10^{31}	4×10^{31}	2.8×10^{31}	2×10^{31}	1.4×10^{31}	1×10^{31}	
HLT_DoublePhoton17_L1R		1	1	1	1	1	1	L1_DoubleEG5
HLT_DoublePhoton5_CEP_L1R		1	1	1	1	1	1	L1_DoubleEG5
HLT_Photon20_Cleaned_L1R		40	28	20	14	10	7	L1_SingleEG8
HLT_Photon30_Cleaned_L1R		1	1	1	1	1	1	L1_SingleEG8
HLT_Photon50_NoHE_Cleaned_L1R		1	1	1	1	1	1	L1_SingleEG8

Table A.20: Trigger table for Photon primary dataset in run range 147196–147757.

Trigger name	Prescale factor					L1 seed
	$\mathcal{L}$ [$\mathrm{cm}^{-2}\mathrm{s}^{-1}$]	1×10^{32}	8×10^{31}	6×10^{31}	4×10^{31}	2×10^{31}	
HLT_DoublePhoton17_L1R		1	1	1	1	1	L1_DoubleEG5
HLT_DoublePhoton5_CEP_L1R		1	1	1	1	1	L1_DoubleEG5
HLT_Photon100_NoHE_Cleaned_L1R_v1		1	1	1	1	1	L1_SingleEG8
HLT_Photon17_SC17HE_L1R_v1		1	1	1	1	1	L1_SingleEG8
HLT_Photon20_Cleaned_L1R		125	100	70	50	25	L1_SingleEG8
HLT_Photon30_Cleaned_L1R		25	20	15	10	5	L1_SingleEG8
HLT_Photon30_Isol_EBOnly_Cleaned_L1R_v1		1	1	1	1	1	L1_SingleEG8
HLT_Photon35_Isol_Cleaned_L1R_v1		1	1	1	1	1	L1_SingleEG8
HLT_Photon50_Cleaned_L1R_v1		1	1	1	1	1	L1_SingleEG8
HLT_Photon70_NoHE_Cleaned_L1R_v1		1	1	1	1	1	L1_SingleEG8

Table A.21: Trigger table for Photon primary dataset in run range 147926–148058.

Trigger name	Prescale factor							L1 seed
	$\mathcal{L}$ [$\mathrm{cm}^{-2}\mathrm{s}^{-1}$]	1.4×10^{32}	1.2×10^{32}	1×10^{32}	8×10^{31}	6×10^{31}	4×10^{31}	2×10^{31}	
HLT_DoublePhoton17_L1R		1	1	1	1	1	1	1	L1_DoubleEG5
HLT_DoublePhoton5_CEP_L1R		1	1	1	1	1	1	1	L1_DoubleEG5
HLT_Photon100_NoHE_Cleaned_L1R_v1		1	1	1	1	1	1	1	L1_SingleEG8
HLT_Photon17_SC17HE_L1R_v1		1	1	1	1	1	1	1	L1_SingleEG8
HLT_Photon20_Cleaned_L1R		175	150	125	100	70	50	25	L1_SingleEG8
HLT_Photon30_Cleaned_L1R		35	30	25	20	15	10	5	L1_SingleEG8
HLT_Photon30_Isol_EBOnly_Cleaned_L1R_v1		1	1	1	1	1	1	1	L1_SingleEG8
HLT_Photon35_Isol_Cleaned_L1R_v1		1	1	1	1	1	1	1	L1_SingleEG8
HLT_Photon50_Cleaned_L1R_v1		1	1	1	1	1	1	1	L1_SingleEG8
HLT_Photon70_NoHE_Cleaned_L1R_v1		1	1	1	1	1	1	1	L1_SingleEG8

Table A.22: Trigger table for Photon primary dataset in run range 148819–149294.

Trigger name	Prescale factor						L1 seed
	$\mathcal{L}$ [$\mathrm{cm^{-2}s^{-1}}$]	4×10^{32}	2×10^{32}	1.7×10^{32}	1.4×10^{32}	1.1×10^{32}	0.8×10^{32}	
HLT_DoublePhoton17_SingleIsol_L1R_v1		1	1	1	1	1	1	L1_DoubleEG5
HLT_DoublePhoton22_L1R_v1		1	1	1	1	1	1	L1_DoubleEG5
HLT_DoublePhoton5_CEP_L1R_v3		1	1	1	1	1	1	L1_DoubleEG5
HLT_Photon110_NoHE_Cleaned_L1R_v1		1	1	1	1	1	1	L1_SingleEG8
HLT_Photon17_Isol_SC17HE_L1R_v1		1	1	1	1	1	1	L1_SingleEG8
HLT_Photon20_Cleaned_L1R		400	400	340	280	220	160	L1_SingleEG8
HLT_Photon22_SC22HE_L1R_v1		1	1	1	1	1	1	L1_SingleEG8
HLT_Photon30_Cleaned_L1R		90	90	77	63	50	36	L1_SingleEG8
HLT_Photon40_CaloId_Cleaned_L1R_v1		1	1	1	1	1	1	L1_SingleEG8
HLT_Photon40_Isol_Cleaned_L1R_v1		1	1	1	1	1	1	L1_SingleEG8
HLT_Photon50_Cleaned_L1R_v1		15	15	13	11	8	6	L1_SingleEG8
HLT_Photon70_Cleaned_L1R_v1		1	1	1	1	1	1	L1_SingleEG8

Appendix B

Monte Carlo Datasets

Dataset names and corresponding theoretical cross sections, before any data-driven rescaling, for the signal and background MC samples used in the analysis are reported in Table B.1.

Table B.1: Dataset names and corresponding theoretical cross sections, before any data-driven rescaling, for the signal and background MC samples used in the analysis. For the LQ signal samples, $\sigma_{\mathrm{NLO}} \times 2\beta(1-\beta)$, with $\beta = 0.5$, is reported. None of the samples listed below have pile-up simulated. GEN-SIM refers to the event generation and detector simulation stage of the sample production, while RECO refers to the event reconstruction stage of the sample production.

Dataset name	CMSSW version GEN-SIM/RECO	σ [pb]
/LQToUE_ENuJJFilter_M-200_7TeV-pythia6/Spring10-START3X_V26-v1/GEN-SIM-RECO	3_5_6/3_5_6	5.95
/LQToUE_ENuJJFilter_M-250_7TeV-pythia6/Spring10-START3X_V26-v1/GEN-SIM-RECO	3_5_6/3_5_6	1.735
/LQToUE_ENuJJFilter_M-280_7TeV-pythia6/Spring10-START3X_V26-v1/GEN-SIM-RECO	3_5_6/3_5_6	0.91
/LQToUE_ENuJJFilter_M-300_7TeV-pythia6/Spring10-START3X_V26-v1/GEN-SIM-RECO	3_5_6/3_5_6	0.605
/LQToUE_ENuJJFilter_M-320_7TeV-pythia6/Spring10-START3X_V26-v1/GEN-SIM-RECO	3_5_6/3_5_6	0.412
/LQToUE_ENuJJFilter_M-340_7TeV-pythia6/Spring10-START3X_V26-v1/GEN-SIM-RECO	3_5_6/3_5_6	0.285
/LQToUE_ENuJJFilter_M-370_7TeV-pythia6/Spring10-START3X_V26-v1/GEN-SIM-RECO	3_5_6/3_5_6	0.1685
/LQToUE_ENuJJFilter_M-400_7TeV-pythia6/Spring10-START3X_V26-v1/GEN-SIM-RECO	3_5_6/3_5_6	0.1025
/LQToUE_ENuJJFilter_M-450_7TeV-pythia6/Spring10-START3X_V26-v1/GEN-SIM-RECO	3_5_6/3_5_6	0.04745
/LQToUE_ENuJJFilter_M-500_7TeV-pythia6/Spring10-START3X_V26-v1/GEN-SIM-RECO	3_5_6/3_5_6	0.02315
/TTbarJets-madgraph/Spring10-START3X_V26_S09-v1/GEN-SIM-RECO	3_1_6/3_5_6	165
/SingleTop_sChannel-madgraph/Spring10-START3X_V26_S09-v1/GEN-SIM-RECO	3_1_6/3_5_6	4.6
/SingleTop_tChannel-madgraph/Spring10-START3X_V26_S09-v1/GEN-SIM-RECO	3_1_6/3_5_6	64.6
/SingleTop_tWChannel-madgraph/Spring10-START3X_V26_S09-v1/GEN-SIM-RECO	3_1_6/3_5_6	10.6
/Z0Jets_Pt0to100-alpgen/Spring10-START3X_V26_S09-v1/GEN-SIM-RECO	3_1_6/3_5_6	2472.42
/Z1Jets_Pt0to100-alpgen/Spring10-START3X_V26_S09-v1/GEN-SIM-RECO	3_1_6/3_5_6	479.654
/Z1Jets_Pt100to300-alpgen/Spring10-START3X_V26_S09-v1/GEN-SIM-RECO	3_1_6/3_5_6	11.9976

Continued on next page

Dataset name	CMSSW version GEN-SIM/RECO	σ [pb]
/Z1Jets_Pt300to800-alpgen/Spring10-START3X_V26_S09-v1/GEN-SIM-RECO	3_1_6/3_5_6	0.0981206
/Z1Jets_Pt800to1600-alpgen/Spring10-START3X_V26_S09-v1/GEN-SIM-RECO	3_1_6/3_5_6	0.000173233
/Z2Jets_Pt0to100-alpgen/Spring10-START3X_V26_S09-v1/GEN-SIM-RECO	3_1_6/3_5_6	119.749
/Z2Jets_Pt100to300-alpgen/Spring10-START3X_V26_S09-v1/GEN-SIM-RECO	3_1_6/3_5_6	10.4901
/Z2Jets_Pt300to800-alpgen/Spring10-START3X_V26_S09-v1/GEN-SIM-RECO	3_1_6/3_5_6	0.137534
/Z2Jets_Pt800to1600-alpgen/Spring10-START3X_V26_S09-v1/GEN-SIM-RECO	3_1_6/3_5_6	0.000330505
/Z3Jets_Pt0to100-alpgen/Spring10-START3X_V26_S09-v1/GEN-SIM-RECO	3_1_6/3_5_6	27.1099
/Z3Jets_Pt100to300-alpgen/Spring10-START3X_V26_S09-v1/GEN-SIM-RECO	3_1_6/3_5_6	4.73227
/Z3Jets_Pt300to800-alpgen/Spring10-START3X_V26_S09-v1/GEN-SIM-RECO	3_1_6/3_5_6	0.0929121
/Z3Jets_Pt800to1600-alpgen/Spring10-START3X_V26_S09-v1/GEN-SIM-RECO	3_1_6/3_5_6	0.000279339
/Z4Jets_Pt0to100-alpgen/Spring10-START3X_V26_S09-v1/GEN-SIM-RECO	3_1_6/3_5_6	5.33915
/Z4Jets_Pt100to300-alpgen/Spring10-START3X_V26_S09-v1/GEN-SIM-RECO	3_1_6/3_5_6	1.51771
/Z4Jets_Pt300to800-alpgen/Spring10-START3X_V26_S09-v1/GEN-SIM-RECO	3_1_6/3_5_6	0.0409194
/Z4Jets_Pt800to1600-alpgen/Spring10-START3X_V26_S09-v1/GEN-SIM-RECO	3_1_6/3_5_6	0.000143811
/Z5Jets_Pt0to100-alpgen/Spring10-START3X_V26_S09-v1/GEN-SIM-RECO	3_1_6/3_5_6	1.24635
/Z5Jets_Pt100to300-alpgen/Spring10-START3X_V26_S09-v1/GEN-SIM-RECO	3_1_6/3_5_6	0.521178
/Z5Jets_Pt300to800-alpgen/Spring10-START3X_V26_S09-v1/GEN-SIM-RECO	3_1_6/3_5_6	0.020835
/Z5Jets_Pt800to1600-alpgen/Spring10-START3X_V26_S09-v1/GEN-SIM-RECO	3_1_6/3_5_6	0.0000790519
/W0Jets_Pt0to100-alpgen/Spring10-START3X_V26_S09-v1/GEN-SIM-RECO	3_1_6/3_5_6	25059.9
/W1Jets_Pt0to100-alpgen/Spring10-START3X_V26_S09-v1/GEN-SIM-RECO	3_1_6/3_5_6	4582.28
/W1Jets_Pt100to300-alpgen/Spring10-START3X_V26_S09-v1/GEN-SIM-RECO	3_1_6/3_5_6	96.6582
/W1Jets_Pt300to800-alpgen/Spring10-START3X_V26_S09-v1/GEN-SIM-RECO	3_1_6/3_5_6	0.736145

Continued on next page

Dataset name	CMSSW version GEN-SIM/RECO	σ [pb]
/W1Jets_Pt800to1600-alpgen/Spring10-START3X_V26_S09-v1/GEN-SIM-RECO	3_1_6/3_5_6	0.0013139
/W2Jets_Pt0to100-alpgen/Spring10-START3X_V26_S09-v1/GEN-SIM-RECO	3_1_6/3_5_6	1125.56
/W2Jets_Pt100to300-alpgen/Spring10-START3X_V26_S09-v1/GEN-SIM-RECO	3_1_6/3_5_6	83.2536
/W2Jets_Pt300to800-alpgen/Spring10-START3X_V26_S09-v1/GEN-SIM-RECO	3_1_6/3_5_6	0.994012
/W2Jets_Pt800to1600-alpgen/Spring10-START3X_V26_S09-v1/GEN-SIM-RECO	3_1_6/3_5_6	0.00240563
/W3Jets_Pt0to100-alpgen/Spring10-START3X_V26_S09-v1/GEN-SIM-RECO	3_1_6/3_5_6	247.987
/W3Jets_Pt100to300-alpgen/Spring10-START3X_V26_S09-v1/GEN-SIM-RECO	3_1_6/3_5_6	38.7347
/W3Jets_Pt300to800-alpgen/Spring10-START3X_V26_S09-v1/GEN-SIM-RECO	3_1_6/3_5_6	0.690596
/W3Jets_Pt800to1600-alpgen/Spring10-START3X_V26_S09-v1/GEN-SIM-RECO	3_1_6/3_5_6	0.0020476
/W4Jets_Pt0to100-alpgen/Spring10-START3X_V26_S09-v1/GEN-SIM-RECO	3_1_6/3_5_6	48.7455
/W4Jets_Pt100to300-alpgen/Spring10-START3X_V26_S09-v1/GEN-SIM-RECO	3_1_6/3_5_6	11.8495
/W4Jets_Pt300to800-alpgen/Spring10-START3X_V26_S09-v1/GEN-SIM-RECO	3_1_6/3_5_6	0.313564
/W4Jets_Pt800to1600-alpgen/Spring10-START3X_V26_S09-v1/GEN-SIM-RECO	3_1_6/3_5_6	0.00103905
/W5Jets_Pt0to100-alpgen/Spring10-START3X_V26_S09-v1/GEN-SIM-RECO	3_1_6/3_5_6	11.7044
/W5Jets_Pt100to300-alpgen/Spring10-START3X_V26_S09-v1/GEN-SIM-RECO	3_1_6/3_5_6	3.94102
/W5Jets_Pt300to800-alpgen/Spring10-START3X_V26_S09-v1/GEN-SIM-RECO	3_1_6/3_5_6	0.166601
/W5Jets_Pt800to1600-alpgen/Spring10-START3X_V26_S09-v1/GEN-SIM-RECO	3_1_6/3_5_6	0.000694727
/WW/Spring10-START3X_V26_S09-v1/GEN-SIM-RECO	3_1_2/3_5_6	43
/ZZ/Spring10-START3X_V26_S09-v1/GEN-SIM-RECO	3_1_2/3_5_6	5.9
/WZ/Spring10-START3X_V26_S09-v1/GEN-SIM-RECO	3_1_2/3_5_6	18.2
/BJets_HT-100To250_TuneD6T_7TeV-madgraph/Fall10-START38_V12-v1/GEN-SIM-RECO	3_8_5/3_8_5	197000
/BJets_HT-250To500_TuneD6T_7TeV-madgraph/Fall10-START38_V12-v1/GEN-SIM-RECO	3_8_5/3_8_5	6213

Continued on next page

Dataset name	CMSSW version GEN-SIM/RECO	σ [pb]
/BJets_HT-500To1000_TuneD6T_7TeV-madgraph/Fall10-START38_V12-v1/GEN-SIM-RECO	3_8_5/3_8_5	161.7
/BJets_HT-1000_TuneD6T_7TeV-madgraph/Fall10-START38_V12-v1/GEN-SIM-RECO	3_8_5/3_8_5	2.281
/GJets_TuneD6T_HT-40To100_7TeV-madgraph/Fall10-START38_V12-v1/GEN-SIM-RECO	3_8_5/3_8_5	23620
/GJets_TuneD6T_HT-100To200_7TeV-madgraph/Fall10-START38_V12-v1/GEN-SIM-RECO	3_8_5/3_8_5	3476
/GJets_TuneD6T_HT-200_7TeV-madgraph/Fall10-START38_V12-v1/GEN-SIM-RECO	3_8_5/3_8_5	485

Appendix C

HEEP[1] Electron Identification and Isolation

The major difference between HEEP electrons and the standard GSF electrons is in the energy measurement. By default, the energy of the GSF electrons is an uncertainty weighted combination of the tracker and calorimeter measurements. This gives better performance at low energies ($\lesssim 15$ GeV) but for energies $\gtrsim 25$ GeV, it is entirely dominated by the calorimeter measurement. Under certain situations, however, a GSF electron can discard the calorimeter energy completely (most likely in the crack region, $1.442 < |\eta_{\rm sc}| < 1.56$) and just use the track momentum. There is, however, a possibility that the track is badly reconstructed and a momentum of > 500 GeV is measured. This has the effect of making a low energy electron or jet look like a high energy electron, and therefore adds an additional background. To get around this problem, the energy of the supercluster is taken as the energy of the HEEP electron, and the η and ϕ of the track are used to set the direction of the electron four-momentum. To further gain in efficiency, electrons in intermodule gaps are not rejected. However, electrons in the barrel-endcap gap ($1.442 < |\eta_{\rm sc}| < 1.56$) are rejected.

All of the variables and corresponding cut values used in the HEEP selection are reported in Table C.1. The HEEP selection is very similar to most other selections used at CMS [126]. The main difference is that the HEEP isolation cut is of

[1]High Energy Electron Pairs

the form $A + B \times E_{\mathrm{T}}$ which scales the isolation with E_{T} in a way related to the leakage of the electrons energy into the isolation cone in order to maintain efficiency without completely relaxing the isolation criteria at high energy. The second difference is that it exploits the depth segmentation of the endcaps which gives better performance at high energy. Finally, in the barrel it replaces the shower-shape variable $\sigma_{i\eta i\eta}$ with the variables $E^{2\times5}/E^{5\times5}$ and $E^{1\times5}/E^{5\times5}$. In the η-ϕ geometry of the barrel, these variables are logically identical to $\sigma_{i\eta i\eta}$ but they are simpler and easier to understand. The HEEP selection variables are described in more detail below.

Table C.1: HEEP v3.0 selection cuts.

Variable	Barrel	Endcap
E_{T}	> 25 GeV	> 25 GeV
$\lvert\eta_{\mathrm{sc}}\rvert$	< 1.442	$1.560 < \lvert\eta_{\mathrm{sc}}\rvert < 2.5$
isEcalDriven	$= 1$	$= 1$
$\lvert\Delta\eta_{\mathrm{in}}\rvert$	< 0.005	< 0.007
$\lvert\Delta\phi_{\mathrm{in}}\rvert$	< 0.09	< 0.09
H/E	< 0.05	< 0.05
$\sigma_{i\eta i\eta}$	N/A	< 0.03
$E^{2\times5}/E^{5\times5}$	> 0.94 OR $E^{1\times5}/E^{5\times5} > 0.83$	N/A
ECAL + Had Depth 1 Isolation	$< 2 + 0.03 \times E_{\mathrm{T}}$	< 2.5 for $E_{\mathrm{T}} < 50$ else $< 2.5 + 0.03 \times (E_{\mathrm{T}} - 50)$
Had Depth 2 Isolation	N/A	< 0.5
Track p_{T} Isolation	< 7.5	< 15

HEEP selection variable definition:

- $\boldsymbol{E}_{\mathrm{T}}$: Defined as the product of the supercluster energy and $\sin(\theta_{\mathrm{trk}})$, where θ_{trk} is the polar angle of the electrons track measured at the inner layer of the

tracker and then extrapolated to the interaction vertex.

- $\boldsymbol{\eta_{\mathrm{sc}}}$: Defined as the pseudorapidity of the supercluster with respect to the point $(0, 0, 0)$ so its use is for fiducial cuts due to detector effects and is not used to calculate four-momenta used in physics results.

- $\boldsymbol{\eta}$: Defined as the pseudo rapidity of the electron track measured at the inner layer of the tracker and then extrapolated to the interaction vertex. This definition of pseudorapidity is used for calculating the electrons four-momentum and for all physics results but is not used for detector fiducial cuts.

- **isEcalDriven**: Electrons can be ECAL driven (found using standard electron reconstruction techniques) or tracker driven (found using particle-flow techniques). While useful for low energy non-isolated electrons, particle-flow has been less validated for high energy electrons. Hence, HEEP electrons are required to be ECAL driven (it can and often will be tracker driven as well as it can be found by both reconstruction algorithms).

- $\boldsymbol{\Delta\eta_{\mathrm{in}}}$: The difference in η between the track position as measured in the inner layer, extrapolated to the interaction vertex and then extrapolated to the calorimeter, and the η of the supercluster.

- $\boldsymbol{\Delta\phi_{\mathrm{in}}}$: The difference in ϕ between the track position as measured in the inner layer, extrapolated to the interaction vertex and then extrapolated to the calorimeter, and the ϕ of the supercluster.

- $\boldsymbol{H/E}$: The ratio of the hadronic energy of the HCAL towers in a cone of

radius 0.15 centered on the position of the electron in the calorimeter to the electromagnetic energy of the electron's supercluster.

- $\boldsymbol{\sigma_{i\eta i\eta}}$: A measure of the spread in η in units of crystals of the electron energy in the 5×5 block of crystals centered on the seed crystal.

- $\boldsymbol{E^{5\times5}}$: Defined as the energy inside the 5×5 block of crystals surrounding the seed crystal.

- $\boldsymbol{E^{1\times5}}$: Defined as the energy inside the 1×5 block of crystals centered on the seed crystal.

- $\boldsymbol{E^{2\times5}}$: Defined as the energy inside the 2×5 block of crystals centered on the seed crystal, Maximum between the two possible sums is taken.

- **ECAL Isolation**: Defined as the transverse energy of all ECAL crystals with $|E| > 0.08$ GeV ($|E_{\mathrm{T}}| > 0.1$ GeV in endcaps) in a cone of radius 0.3 centered on the position of the electron in the calorimeter excluding those in an inner cone of radius 3 crystals and eta strip of total width of 3 crystals. This variable is used only in a sum with the Hadronic Depth 1 Isolation defined below.

- **Hadronic Depth 1 Isolation**: Defined as the transverse Depth 1 hadronic energy of all the HCAL towers in a hollow cone of internal (external) radius 0.15 (0.3) centered on the position of the electron in the calorimeter. Depth 1 is defined as all depths for towers 1-17, depth 1 for towers 18-29, and depth 2 for towers 27-29. This variable is always used summed with the ECAL isolation.

- **Hadronic Depth 1 Isolation**: Defined as the transverse Depth 2 hadronic energy of all the HCAL towers in a hollow cone of internal (external) radius 0.15 (0.3) centered on the position of the electron in the calorimeter. Depth 2 is defined as depth 2 for towers 18-26, and depth 3 for towers 27-29.

- **Track p_{T} Isolation**: Defined as the sum of the p_{T} of the tracks in a hollow cone of internal (external) radius 0.04 0.3 with $p_{\mathrm{T}} > 0.7$ GeV and $z0$ within ± 0.2 cm of the $z0$ of the electron GSF track and $d0 < 9999$ cm. The variable $z0$ is the minimum distance in z from the point $(0, 0, 0)$. The variable $d0$ is the minimum distance in the x-y plane from the beam spot.

Appendix D

Event Displays for Three Highest-S_{T} Events

Run: 148029 **Lumi section:** 53 **Event:** 9851751

$p_{\mathrm{T},e} = 107.286$ GeV, $\eta_e = 1.24111$
$\not{E}_{\mathrm{T}} = 243.173$ GeV
$p_{\mathrm{T},j1} = 131.181$ GeV, $\eta_{j1} = 1.96904$
$p_{\mathrm{T},j2} = 60.5791$ GeV, $\eta_{j2} = 1.30021$
$M_{\mathrm{T},e\nu} = 322.581$ GeV, $M_{jj} = 160.877$ GeV
$S_{\mathrm{T}} = 542.219$ GeV
$M_{ej}(1^{\mathrm{st}}\ \mathrm{pair}) = 126.881$ GeV, $M_{ej}(2^{\mathrm{nd}}\ \mathrm{pair}) = 90.4843$ GeV
$M_{\mathrm{T},\nu j}(1^{\mathrm{st}}\ \mathrm{pair}) = 336.667$ GeV, $M_{\mathrm{T},\nu j}(2^{\mathrm{nd}}\ \mathrm{pair}) = 193.488$ GeV
$\Delta\phi(e, \not{E}_{\mathrm{T}}) = 3.03468$, $\Delta\phi(j1, \not{E}_{\mathrm{T}}) = 2.46001$, $\Delta\phi(j2, \not{E}_{\mathrm{T}}) = 1.84491$
$\min \Delta R(e, j) = 1.07313$

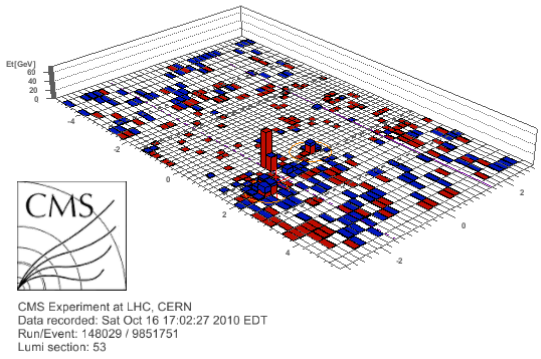

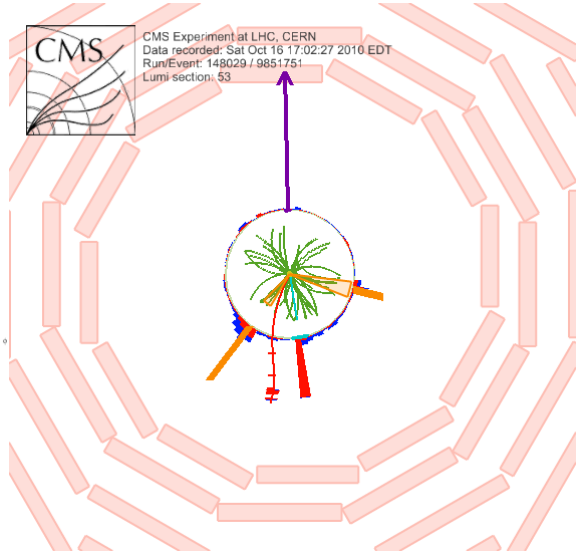

Run: 148029 **Lumi section:** 233 **Event:** 174059244

$p_{\mathrm{T},e} = 180.114$ GeV, $\eta_e = -0.238254$
$\not{E}_{\mathrm{T}} = 162.811$ GeV
$p_{\mathrm{T},j1} = 259.791$ GeV, $\eta_{j1} = 0.0745285$
$p_{\mathrm{T},j2} = 30.185$ GeV, $\eta_{j2} = 1.07262$
$M_{\mathrm{T},e\nu} = 250.075$ GeV, $M_{jj} = 178.992$ GeV
$S_{\mathrm{T}} = 632.901$ GeV
$M_{ej}(1^{\mathrm{st}}\ \mathrm{pair}) = 404.473$ GeV, $M_{ej}(2^{\mathrm{nd}}\ \mathrm{pair}) = 156.67$ GeV
$M_{\mathrm{T},\nu j}(1^{\mathrm{st}}\ \mathrm{pair}) = 375.566$ GeV, $M_{\mathrm{T},\nu j}(2^{\mathrm{nd}}\ \mathrm{pair}) = 14.3354$ GeV
$\Delta\phi(e,\not{E}_{\mathrm{T}}) = 1.63715$, $\Delta\phi(j1,\not{E}_{\mathrm{T}}) = 2.30148$, $\Delta\phi(j2,\not{E}_{\mathrm{T}}) = 0.204848$
$\min \Delta R(e,j) = 2.26082$

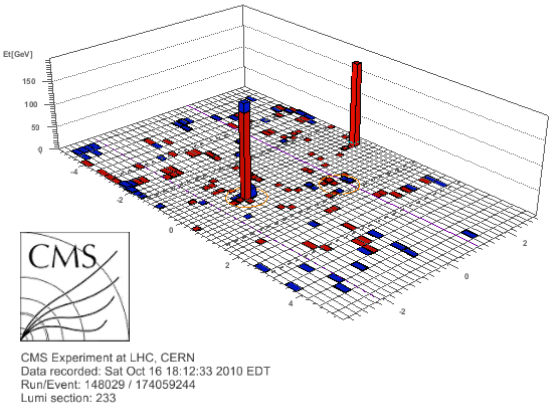

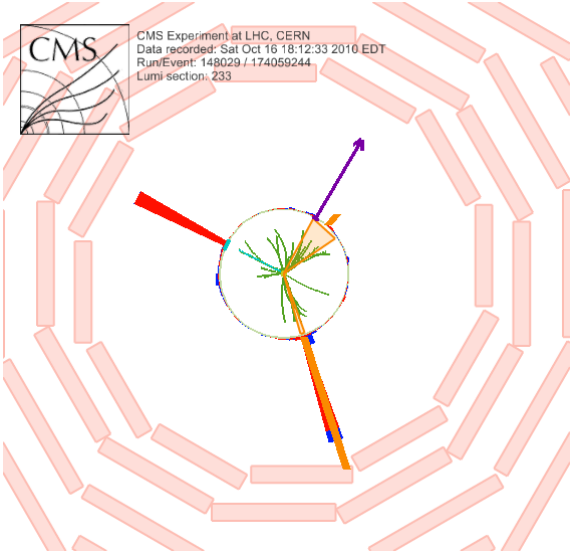

Run: 149003 **Lumi section:** 237 **Event:** 257672228

$p_{\mathrm{T},e} = 113.644$ GeV, $\eta_e = 1.06233$
$\not{E}_{\mathrm{T}} = 97.7588$ GeV
$p_{\mathrm{T},j1} = 147.614$ GeV, $\eta_{j1} = 2.01154$
$p_{\mathrm{T},j2} = 103.701$ GeV, $\eta_{j2} = 0.24734$
$M_{\mathrm{T},e\nu} = 163.753$ GeV, $M_{jj} = 333.063$ GeV
$S_{\mathrm{T}} = 462.718$ GeV
$M_{ej}(1^{\mathrm{st}}\ \mathrm{pair}) = 256.953$ GeV, $M_{ej}(2^{\mathrm{nd}}\ \mathrm{pair}) = 202.503$ GeV
$M_{\mathrm{T},\nu j}(1^{\mathrm{st}}\ \mathrm{pair}) = 225.195$ GeV, $M_{\mathrm{T},\nu j}(2^{\mathrm{nd}}\ \mathrm{pair}) = 19.2138$ GeV
$\Delta\phi(e,\not{E}_{\mathrm{T}}) = 1.77913$, $\Delta\phi(j1,\not{E}_{\mathrm{T}}) = 2.42971$, $\Delta\phi(j2,\not{E}_{\mathrm{T}}) = 0.19112$
$\min \Delta R(e,j) = 2.13216$

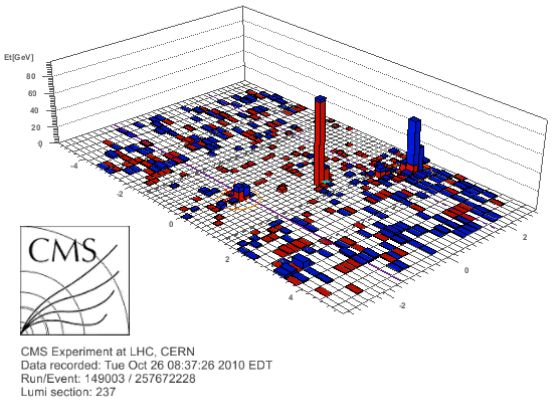

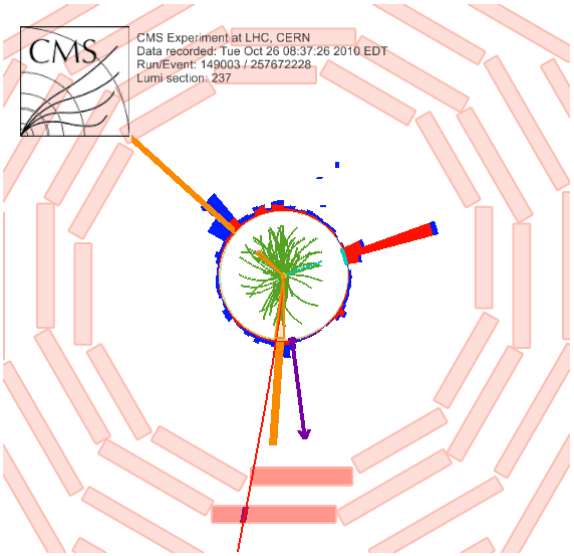

Appendix E

Background Shape Uncertainty

E.1 W+jets Background Shape Uncertainty

A systematic uncertainty due to the modeling of the shape of the $M_{\mathrm{T},e\nu}$ and S_{T} distribution for the W+jets background is estimated by repeating the full analysis chain, including the W+jets rescaling described in Section 5.5.3, using the MC datasets listed in Table E.1. The W+jets rescaling factors derived in this way are reported in the second column of Table E.2. The number of W+jets events passing the event preselection and the final $M_{\mathrm{T},e\nu}$ cut ($M_{\mathrm{T},e\nu} > 125$ GeV) is reported in the third column of Table E.2. The number of W+jets events passing the event preselection and the final S_{T} cut for $M_{\mathrm{LQ}} = 300$ GeV ($S_{\mathrm{T}} > 490$ GeV) is reported in the fourth column of Table E.2.

For a consistent evaluation of the shape uncertainties, only the MadGraph numbers are used. The largest deviation with respect to the default MadGraph sample corresponds to the "scaleup" sample for both the $M_{\mathrm{T},e\nu}$ shape:

$$\Delta_{M_{\mathrm{T}}}(\text{“scaleup” } - \text{ “default”}) = 2.96 \pm 2.51 \rightarrow 2.96/12.57 = 24\%,$$

and the S_{T} shape:

$$\Delta_{S_{\mathrm{T}}}(\text{“scaleup” } - \text{ “default”}) = 4.59 \pm 3.03 \rightarrow 4.59/18.05 = 25\%.$$

Table E.1: MC datasets and corresponding theoretical cross sections, before any data-driven rescaling, used in the estimation of the shape uncertainty for the W+jets background. The datasets are generated using MadGraph (v4.4.13), with matrix elements corresponding to up to four additional partons, and subsequently processed with pythia (v6.4.22), with tau decays handled by tauola [128] (v27.121.5). None of the datasets have pile-up simulated. GEN-SIM refers to the event generation and detector simulation stage of the sample production, while RECO refers to the event reconstruction stage of the sample production.

Dataset name	CMSSW version GEN-SIM/RECO	σ [pb]
/WJetsToLNu_TuneD6T_7TeV-madgraph-tauola/Fall10-START38_V12-v1/GEN-SIM-RECO	3_8_5/3_8_5	31314
/WJets_TuneD6T_scaledown_7TeV-madgraph-tauola/Fall10-START38_V12-v1/GEN-SIM-RECO	3_8_7/3_8_7	31314
/WJets_TuneD6T_scaleup_7TeV-madgraph-tauola/Fall10-START38_V12-v1/GEN-SIM-RECO	3_8_7/3_8_7	31314
/WJets_TuneD6T_matchingdown_7TeV-madgraph-tauola/Fall10-START38_V12-v1/GEN-SIM-RECO	3_8_7/3_8_7	31314
/WJets_TuneD6T_matchingup_7TeV-madgraph-tauola/Fall10-START38_V12-v1/GEN-SIM-RECO	3_8_7/3_8_7	31314

Table E.2: W+jets rescaling factors, the number of events passing the event preselection and the final $M_{\mathrm{T},e\nu}$ cut ($M_{\mathrm{T},e\nu} > 125$ GeV), and the number of events passing the event preselection and the final S_{T} cut for $M_{\mathrm{LQ}} = 300$ GeV ($S_{\mathrm{T}} > 490$ GeV) for datasets listed in Table E.1. For reference, the corresponding values for the ALPGEN samples used in the main analysis are also included.

Dataset	R_W	Presel. + $M_{\mathrm{T},e\nu}$	Presel. + S_{T}
W+jets (MADGRAPH, default)	1.27 ± 0.12	12.57 ± 1.13	18.05 ± 1.35
W+jets (MADGRAPH, scaledown)	0.70 ± 0.07	11.95 ± 1.35	19.92 ± 1.75
W+jets (MADGRAPH, scaleup)	1.81 ± 0.19	15.53 ± 2.24	22.64 ± 2.71
W+jets (MADGRAPH, matchingdown)	1.45 ± 0.16	14.60 ± 2.98	21.29 ± 3.60
W+jets (MADGRAPH, matchingup)	1.14 ± 0.11	10.43 ± 1.13	19.14 ± 1.53
W+jets (ALPGEN)	1.18 ± 0.12	14.20 ± 0.77	22.86 ± 0.91

The overall shape uncertainty for the W+jets background, assuming conservatively that the $M_{\mathrm{T},e\nu}$ and S_{T} shape uncertainties are fully correlated, is 49%.

E.2 $t\bar{t}$ Background Shape Uncertainty

A systematic uncertainty due to the modeling of the shape of the $M_{\mathrm{T},e\nu}$ and S_{T} distribution for the $t\bar{t}$ background is estimated by comparing the number of $t\bar{t}$ events passing the event preselection and the final $M_{\mathrm{T},e\nu}$ or S_{T} (for $M_{\mathrm{LQ}} = 300$ GeV) cut using the MC datasets listed in Table E.3. The number of $t\bar{t}$ events passing the event preselection and the final $M_{\mathrm{T},e\nu}$ cut ($M_{\mathrm{T},e\nu} > 125$ GeV) is reported in the second column of Table E.4, and the number of $t\bar{t}$ events passing the event preselection and the final S_{T} cut for $M_{\mathrm{LQ}} = 300$ GeV ($S_{\mathrm{T}} > 490$ GeV) is reported in the third column of Table E.4.

For a consistent evaluation of the shape uncertainties, only the "Fall10" numbers are used. The largest deviation with respect to the default MADGRAPH sample

Table E.3: MC datasets and corresponding theoretical cross sections used in the estimation of the shape uncertainty for the $t\bar{t}$ background. The datasets are generated using the MadGraph (v4.4.12) event generator, with matrix elements corresponding to up to three additional partons, and subsequently processed with pythia (v6.4.22), with tau decays handled by tauola [128] (v27.121.5); and using the mc@nlo [124, 129] (v3.4) event generator and subsequently processed with herwig [107, 130] (v6.510.3). None of the datasets have pile-up simulated. GEN-SIM refers to the event generation and detector simulation stage of the sample production, while RECO refers to the event reconstruction stage of the sample production.

Dataset name	CMSSW version GEN-SIM/RECO	σ [pb]
/TTJets_TuneD6T_7TeV-madgraph-tauola/Fall10-START38_V12-v2/GEN-SIM-RECO	3_8_5/3_8_5	165
/TTJets_TuneD6T_scaledown_7TeV-madgraph-tauola/Fall10-START38_V12-v1/GEN-SIM-RECO	3_8_5/3_8_5	165
/TTJets_TuneD6T_scaleup_7TeV-madgraph-tauola/Fall10-START38_V12-v1/GEN-SIM-RECO	3_8_5/3_8_5	165
/TTJets_TuneD6T_matchingdown_7TeV-madgraph-tauola/Fall10-START38_V12-v2/GEN-SIM-RECO	3_8_5/3_8_5	165
/TTJets_TuneD6T_matchingup_7TeV-madgraph-tauola/Fall10-START38_V12-v1/GEN-SIM-RECO	3_8_5/3_8_5	165
/TT_7TeV-mcatnlo/Fall10-START38_V12-v1/GEN-SIM-RECO	3_8_5/3_8_5	165

Table E.4: The number of events passing the event preselection and the final $M_{\mathrm{T},e\nu}$ cut ($M_{\mathrm{T},e\nu} > 125$ GeV), and the number of events passing the event preselection and the final S_{T} cut for $M_{\mathrm{LQ}} = 300$ GeV ($S_{\mathrm{T}} > 490$ GeV) for datasets listed in Table E.3. For reference, the corresponding values for the "Spring10" MadGraph sample used in the main analysis are also included.

Dataset	Presel. + $M_{\mathrm{T},e\nu}$	Presel. + S_{T}
$t\bar{t}$ (MadGraph, Fall10 default)	22.53 ± 0.31	7.62 ± 0.18
$t\bar{t}$ (MadGraph, Fall10 scaledown)	23.32 ± 0.35	8.95 ± 0.22
$t\bar{t}$ (MadGraph, Fall10 scaleup)	22.23 ± 0.34	7.18 ± 0.19
$t\bar{t}$ (MadGraph, Fall10 matchingdown)	22.47 ± 0.38	7.80 ± 0.22
$t\bar{t}$ (MadGraph, Fall10 matchingup)	22.49 ± 0.36	7.93 ± 0.21
$t\bar{t}$ (mc@nlo, Fall10)	21.77 ± 0.36	9.47 ± 0.24
$t\bar{t}$ (MadGraph, Spring10)	22.74 ± 0.30	8.07 ± 0.18

corresponds to the "scaledown" sample for the $M_{\mathrm{T},e\nu}$ shape:

$$\Delta_{M_{\mathrm{T}}}(\text{"scaledown"} - \text{"default"}) = 0.79 \pm 0.47 \rightarrow 0.79/22.53 = 3.5\%,$$

and to the mc@nlo sample for the S_{T} shape:

$$\Delta_{S_{\mathrm{T}}}(\text{"mc@nlo"} - \text{"default"}) = 1.85 \pm 0.30 \rightarrow 1.85/7.62 = 24\%.$$

The overall shape uncertainty for the $t\bar{t}$ background, assuming conservatively that the $M_{\mathrm{T},e\nu}$ and S_{T} shape uncertainties are fully correlated, is 28%.

Appendix F

Bayesian Method for Calculating Upper Limits

F.1 Upper Limit Calculation

To set an upper limit on the signal cross section, the standard Bayesian approach [4, 131] is used. This approach is well suited for counting experiments in the Poisson regime with low expected signal and background yields. As a starting point, a Poisson probability to observe n event within the counting window in the presence of both the signal and the background is constructed:

$$P(n|\sigma,\varepsilon,L,b) = \frac{(\sigma\varepsilon L+b)^n}{n!}e^{-(\sigma\varepsilon L+b)}, \tag{F.1}$$

where σ is the signal cross section, ε is the signal efficiency (that includes the signal acceptance), L is the integrated luminosity, and b is the expected number of background events for the integrated luminosity L. Using Bayes' theorem and the Poisson probability in Equation F.1, a posterior likelihood function for the signal cross section is defined:

$$L(\sigma|n,\varepsilon,L,b) = \frac{P(n|\sigma,\varepsilon,L,b)\pi(\sigma)}{\int_{-\infty}^{+\infty} P(n|\sigma,\varepsilon,L,b)\pi(\sigma)d\sigma}, \tag{F.2}$$

where $\pi(\sigma)$ is the signal prior. The posterior likelihood function $L(\sigma|n, \varepsilon, L, b)$ in Equation F.2 represents the degree of belief for σ to take on values in a certain range given n, ε, L, and b. The denominator in Equation F.2 serves to normalize the posterior likelihood function to unity.

The existence of the signal prior $\pi(\sigma)$ is a feature specific to the Bayesian statistics, and there is no unique rule for defining it. The signal prior reflects the experimenter's subjective degree of belief (or state of knowledge) about σ before the measurement was carried out. In this analysis, as is often the case, a flat signal prior, defined as

$$\pi(\sigma) = \begin{cases} 0 & \sigma < 0 \\ 1 & \sigma \geq 0 \end{cases}, \tag{F.3}$$

is used, reflecting the fact that the signal cross section is a positive-definite quantity.

The *observed* 95%-confidence-level upper limit on the signal cross section given n observed event, $\sigma^{95}(n)$, is obtained by solving the following integral equation:

$$\int_0^{\sigma^{95}(n)} L(\sigma|n, \varepsilon, L, b) d\sigma = 0.95. \tag{F.4}$$

Hence, for n observed events in data, the signal efficiency ε, the integrated luminosity L, and b expected background events, signal cross sections greater than $\sigma^{95}(n)$ are excluded at 95% confidence level (CL). Even if there is no signal present, it is not possible to know *a priori* how many events are going to be observed because of statistical fluctuations. As a consequence, the *expected* 95% CL upper limit on the

signal cross section assuming background-only hypothesis is defined as follows:

$$\langle \sigma^{95} \rangle = \sum_{n=0}^{+\infty} \sigma^{95}(n) \frac{b^n}{n!} e^{-b}, \tag{F.5}$$

i.e., it is equal to a weighted average of individual upper limits $\sigma^{95}(n)$ over all possible values of n, with the weight equal to the Poisson probability to observe n events in the background-only hypothesis.

In practice, the values of measured parameters are known only up to some uncertainty. It is therefore necessary to incorporate these uncertainties in the final result. Bayesian statistics provides a framework for incorporating statistical uncertainties in the calculation of upper limits. This is achieved by convoluting the Poisson likelihood function in Equation F.1 with priors for ε, L, and b, resulting in a modified Poisson likelihood function:

$$P'(n|\sigma) = \int_0^\infty d\varepsilon \, f(\varepsilon) \int_0^\infty dL \, g(L) \int_0^\infty db \, h(b) \, P(n|\sigma, \varepsilon, L, b), \tag{F.6}$$

where $f(\varepsilon)$, $g(L)$, and $h(b)$ are priors for ε, L, and b, respectively. Because the interest here is in σ, the parameters that are integrated out (ε, L, b) are often called *nuisance parameters*.

In this analysis, log-normal priors for nuisance parameters are used, per recommendations of the CMS Statistics Committee [132]. For positive-definite quantities, a log-normal distribution is a more meaningful way to describe systematic uncertainties than a truncated Gaussian. In its standard form, a log-normal distribution

of a random variable x is defined as

$$F(x, \mu, \sigma) = \frac{1}{x\sigma\sqrt{2\pi}} \exp\left[-\frac{(\ln x - \mu)^2}{2\sigma^2}\right]. \tag{F.7}$$

With the following substitutions:

$$\begin{aligned} \mu &= \ln m, \\ \sigma &= \ln \kappa, \end{aligned} \tag{F.8}$$

an equivalent form of a log-normal distribution is

$$F(x, m, \kappa) = \frac{1}{x(\ln \kappa)\sqrt{2\pi}} \exp\left[-\frac{(\ln (x/m))^2}{2(\ln \kappa)^2}\right], \tag{F.9}$$

where m is the median of the distribution, which can be identified with the physicist's best estimate of x, and $\kappa > 1$ encodes the spread of the distribution, with $(\kappa - 1)$ corresponding roughly to a physicist's relative uncertainty on x, i.e.,

$$\kappa - 1 = \delta x/x = r. \tag{F.10}$$

Therefore, for a quantity with a measured value ν and a relative systematic uncertainty $r_\nu = \delta\nu/\nu$, the log-normal distribution used in the calculation of upper limits is given by

$$F(x, \nu, r_\nu) = \frac{1}{x\left[\ln\left(1 + r_\nu\right)\sqrt{2\pi}\right.} \exp\left\{-\frac{(\ln (x/\nu))^2}{2\left[\ln\left(1 + r_\nu\right)\right]^2}\right\}. \tag{F.11}$$

F.2 Combination with the $eejj$ Channel

The $eejj$ and $e\nu jj$ channel analyses are combined using the same Bayesian approach used to set the individual limits. As a first step in the combination, individual Poisson likelihood functions, like the one in Equation F.1, are constructed for the two channels:

$$P_1(n_1|\sigma,\varepsilon_1,L_1,b_1) = \frac{(\sigma\beta^2\varepsilon_1 L_1 + b_1)^{n_1}}{n_1!}e^{-(\sigma\beta^2\varepsilon_1 L_1+b_1)}, \tag{F.12}$$

$$P_2(n_2|\sigma,\varepsilon_2,L_2,b_2) = \frac{(\sigma 2\beta(1-\beta)\varepsilon_2 L_2 + b_2)^{n_2}}{n_2!}e^{-(\sigma 2\beta(1-\beta)\varepsilon_2 L_2+b_2)}, \tag{F.13}$$

where σ is the signal cross section, and n_i, ε_i, L_i, and b_i are the number of observed events, the signal efficiency, the integrated luminosity, and the expected number of background events, respectively, with index $i = 1$ referring to the $eejj$ channel and $i = 2$ to the $e\nu jj$ channel. The combined likelihood is defined as the product of the individual likelihood functions:

$$P(n_1,n_2|\sigma,\varepsilon_1,L_1,b_1,\varepsilon_2,L_2,b_2) = P_1(n_1|\sigma,\varepsilon_1,L_1,b_1)\times P_2(n_2|\sigma,\varepsilon_2,L_2,b_2). \tag{F.14}$$

As before, using Bayes' theorem and the combined likelihood function in Equation F.14, a combined posterior likelihood function for the signal cross section is defined:

$$L(\sigma|n_1,n_2,\varepsilon_1,L_1,b_1,\varepsilon_2,L_2,b_2) = \frac{P(n_1,n_2|\sigma,\varepsilon_1,L_1,b_1,\varepsilon_2,L_2,b_2)\pi(\sigma)}{\int_{-\infty}^{+\infty} P(n_1,n_2|\sigma,\varepsilon_1,L_1,b_1,\varepsilon_2,L_2,b_2)\pi(\sigma)d\sigma}. \tag{F.15}$$

The combined observed 95% CL upper limit on the signal cross section given n_1 and n_2, $\sigma^{95}(n_1, n_2)$, is obtained by solving the following integral equation:

$$\int_0^{\sigma^{95}(n_1,n_2)} L(\sigma|n_1, n_2, \varepsilon_1, L_1, b_1, \varepsilon_2, L_2, b_2)d\sigma = 0.95. \tag{F.16}$$

The combined expected 95% CL upper limit on the signal cross section assuming background-only hypothesis is defined as follows:

$$\langle\sigma^{95}\rangle = \sum_{i=0}^{+\infty}\sum_{j=0}^{+\infty}\sigma^{95}(i,j)\frac{b_1^i}{i!}e^{-b_1}\frac{b_2^j}{j!}e^{-b_2}. \tag{F.17}$$

Both of these limits are a straightforward generalization of the single-channel case.

The $eejj$ and $e\nu jj$ channel have many of the sources of systematic uncertainties in common, and thus systematic uncertainties that are to a large extent correlated between the two channels. However, to simplify the inclusion of the systematic uncertainties in the combined posterior likelihood in Equation F.15, it is assumed that the systematic uncertainties are fully correlated between the two channels, and conservatively the larger uncertainty between the two channels is used for both, i.e.,

$$\begin{aligned} P'(n_1, n_2|\sigma) = \int_0^\infty d\varepsilon'\, F(\varepsilon', 1, r_\varepsilon) \int_0^\infty dL'\, F(L', 1, r_L) \int_0^\infty db'\, F(b', 1, r_b) \\ \cdot P(n_1, n_2|\sigma, \varepsilon'\varepsilon_1, L'L_1, b'b_1, \varepsilon'\varepsilon_2, L'L_2, b'b_2), \end{aligned} \tag{F.18}$$

where $F(\varepsilon', 1, r_\varepsilon)$, $F(L', 1, r_L)$, and $F(b', 1, r_b)$ are the log-normal priors for integration over the nuisance parameters ε', L', and b', respectively, and r_ε, r_L, and r_b are

the larger relative uncertainty between the two channels for ε, L, and b, respectively.

Appendix G

The CMS Collaboration[1]

Yerevan Physics Institute, Yerevan, Armenia
S. Chatrchyan, V. Khachatryan, A.M. Sirunyan, A. Tumasyan

Institut für Hochenergiephysik der OeAW, Wien, Austria
W. Adam, T. Bergauer, M. Dragicevic, J. Erö, C. Fabjan, M. Friedl, R. Frühwirth, V.M. Ghete, J. Hammer[1], S. Hänsel, M. Hoch, N. Hörmann, J. Hrubec, M. Jeitler, W. Kiesenhofer, M. Krammer, D. Liko, I. Mikulec, M. Pernicka, H. Rohringer, R. Schöfbeck, J. Strauss, A. Taurok, F. Teischinger, P. Wagner, W. Waltenberger, G. Walzel, E. Widl, C.-E. Wulz

National Centre for Particle and High Energy Physics, Minsk, Belarus
V. Mossolov, N. Shumeiko, J. Suarez Gonzalez

Universiteit Antwerpen, Antwerpen, Belgium
S. Bansal, L. Benucci, E.A. De Wolf, X. Janssen, J. Maes, T. Maes, L. Mucibello, S. Ochesanu, B. Roland, R. Rougny, M. Selvaggi, H. Van Haevermaet, P. Van Mechelen, N. Van Remortel

Vrije Universiteit Brussel, Brussel, Belgium
F. Blekman, S. Blyweert, J. D'Hondt, O. Devroede, R. Gonzalez Suarez, A. Kalogeropoulos, M. Maes, W. Van Doninck, P. Van Mulders, G.P. Van Onsem, I. Villella

Université Libre de Bruxelles, Bruxelles, Belgium
O. Charaf, B. Clerbaux, G. De Lentdecker, V. Dero, A.P.R. Gay, G.H. Hammad, T. Hreus, P.E. Marage, L. Thomas, C. Vander Velde, P. Vanlaer

Ghent University, Ghent, Belgium
V. Adler, A. Cimmino, S. Costantini, M. Grunewald, B. Klein, J. Lellouch, A. Marinov, J. Mccartin, D. Ryckbosch, F. Thyssen, M. Tytgat, L. Vanelderen, P. Verwilligen, S. Walsh, N. Zaganidis

Université Catholique de Louvain, Louvain-la-Neuve, Belgium
S. Basegmez, G. Bruno, J. Caudron, L. Ceard, E. Cortina Gil, J. De Favereau De Jeneret, C. Delaere[1], D. Favart, A. Giammanco, G. Grégoire, J. Hollar, V. Lemaitre, J. Liao, O. Militaru, S. Ovyn, D. Pagano, A. Pin, K. Piotrzkowski, N. Schul

[1] As of May 26, 2011

Université de Mons, Mons, Belgium
N. Beliy, T. Caebergs, E. Daubie

Centro Brasileiro de Pesquisas Fisicas, Rio de Janeiro, Brazil
G.A. Alves, D. De Jesus Damiao, M.E. Pol, M.H.G. Souza

Universidade do Estado do Rio de Janeiro, Rio de Janeiro, Brazil
W. Carvalho, E.M. Da Costa, C. De Oliveira Martins, S. Fonseca De Souza, L. Mundim, H. Nogima, V. Oguri, W.L. Prado Da Silva, A. Santoro, S.M. Silva Do Amaral, A. Sznajder

Instituto de Fisica Teorica, Universidade Estadual Paulista, Sao Paulo, Brazil
C.A. Bernardes[2], F.A. Dias, T.R. Fernandez Perez Tomei, E. M. Gregores[2], C. Lagana, F. Marinho, P.G. Mercadante[2], S.F. Novaes, Sandra S. Padula

Institute for Nuclear Research and Nuclear Energy, Sofia, Bulgaria
N. Darmenov[1], V. Genchev[1], P. Iaydjiev[1], S. Piperov, M. Rodozov, S. Stoykova, G. Sultanov, V. Tcholakov, R. Trayanov

University of Sofia, Sofia, Bulgaria
A. Dimitrov, R. Hadjiiska, A. Karadzhinova, V. Kozhuharov, L. Litov, M. Mateev, B. Pavlov, P. Petkov

Institute of High Energy Physics, Beijing, China
J.G. Bian, G.M. Chen, H.S. Chen, C.H. Jiang, D. Liang, S. Liang, X. Meng, J. Tao, J. Wang, J. Wang, X. Wang, Z. Wang, H. Xiao, M. Xu, J. Zang, Z. Zhang

State Key Lab. of Nucl. Phys. and Tech., Peking University, Beijing, China
Y. Ban, S. Guo, Y. Guo, W. Li, Y. Mao, S.J. Qian, H. Teng, B. Zhu, W. Zou

Universidad de Los Andes, Bogota, Colombia
A. Cabrera, B. Gomez Moreno, A.A. Ocampo Rios, A.F. Osorio Oliveros, J.C. Sanabria

Technical University of Split, Split, Croatia
N. Godinovic, D. Lelas, K. Lelas, R. Plestina[3], D. Polic, I. Puljak

University of Split, Split, Croatia
Z. Antunovic, M. Dzelalija

Institute Rudjer Boskovic, Zagreb, Croatia
V. Brigljevic, S. Duric, K. Kadija, S. Morovic

University of Cyprus, Nicosia, Cyprus
A. Attikis, M. Galanti, J. Mousa, C. Nicolaou, F. Ptochos, P.A. Razis

Charles University, Prague, Czech Republic
M. Finger, M. Finger Jr.

Academy of Scientific Research and Technology of the Arab Republic of Egypt, Egyptian Network of High Energy Physics, Cairo, Egypt
A. Aly, A. Ellithi Kamel, S. Khalil[4]

National Institute of Chemical Physics and Biophysics, Tallinn, Estonia
A. Hektor, M. Kadastik, M. Müntel, M. Raidal, L. Rebane

Department of Physics, University of Helsinki, Helsinki, Finland
V. Azzolini, P. Eerola, G. Fedi

Helsinki Institute of Physics, Helsinki, Finland
S. Czellar, J. Härkönen, A. Heikkinen, V. Karimäki, R. Kinnunen, M.J. Kortelainen, T. Lampén, K. Lassila-Perini, S. Lehti, T. Lindén, P. Luukka, T. Mäenpää, E. Tuominen, J. Tuominiemi, E. Tuovinen, D. Ungaro, L. Wendland

Lappeenranta University of Technology, Lappeenranta, Finland
K. Banzuzi, A. Korpela, T. Tuuva

Laboratoire d'Annecy-le-Vieux de Physique des Particules, IN2P3-CNRS, Annecy-le-Vieux, France
D. Sillou

DSM/IRFU, CEA/Saclay, Gif-sur-Yvette, France
M. Besancon, S. Choudhury, M. Dejardin, D. Denegri, B. Fabbro, J.L. Faure, F. Ferri, S. Ganjour, F.X. Gentit, A. Givernaud, P. Gras, G. Hamel de Monchenault, P. Jarry, E. Locci, J. Malcles, M. Marionneau, L. Millischer, J. Rander, A. Rosowsky, I. Shreyber, M. Titov, P. Verrecchia

Laboratoire Leprince-Ringuet, Ecole Polytechnique, IN2P3-CNRS, Palaiseau, France
S. Baffioni, F. Beaudette, L. Benhabib, L. Bianchini, M. Bluj[5], C. Broutin, P. Busson, C. Charlot, T. Dahms, L. Dobrzynski, S. Elgammal, R. Granier de Cassagnac, M. Haguenauer, P. Miné, C. Mironov, C. Ochando, P. Paganini, D. Sabes, R. Salerno, Y. Sirois, C. Thiebaux, B. Wyslouch[6], A. Zabi

Institut Pluridisciplinaire Hubert Curien, Université de Strasbourg, Université de Haute Alsace Mulhouse, CNRS/IN2P3, Strasbourg, France

J.-L. Agram[7], J. Andrea, D. Bloch, D. Bodin, J.-M. Brom, M. Cardaci, E.C. Chabert, C. Collard, E. Conte[7], F. Drouhin[7], C. Ferro, J.-C. Fontaine[7], D. Gelé, U. Goerlach, S. Greder, P. Juillot, M. Karim[7], A.-C. Le Bihan, Y. Mikami, P. Van Hove

Centre de Calcul de l'Institut National de Physique Nucleaire et de Physique des Particules (IN2P3), Villeurbanne, France
F. Fassi, D. Mercier

Université de Lyon, Université Claude Bernard Lyon 1, CNRS-IN2P3, Institut de Physique Nucléaire de Lyon, Villeurbanne, France
C. Baty, S. Beauceron, N. Beaupere, M. Bedjidian, O. Bondu, G. Boudoul, D. Boumediene, H. Brun, J. Chasserat, R. Chierici, D. Contardo, P. Depasse, H. El Mamouni, J. Fay, S. Gascon, B. Ille, T. Kurca, T. Le Grand, M. Lethuillier, L. Mirabito, S. Perries, V. Sordini, S. Tosi, Y. Tschudi, P. Verdier

Institute of High Energy Physics and Informatization, Tbilisi State University, Tbilisi, Georgia
D. Lomidze

RWTH Aachen University, I. Physikalisches Institut, Aachen, Germany
G. Anagnostou, M. Edelhoff, L. Feld, N. Heracleous, O. Hindrichs, R. Jussen, K. Klein, J. Merz, N. Mohr, A. Ostapchuk, A. Perieanu, F. Raupach, J. Sammet, S. Schael, D. Sprenger, H. Weber, M. Weber, B. Wittmer

RWTH Aachen University, III. Physikalisches Institut A, Aachen, Germany
M. Ata, W. Bender, E. Dietz-Laursonn, M. Erdmann, J. Frangenheim, T. Hebbeker, A. Hinzmann, K. Hoepfner, T. Klimkovich, D. Klingebiel, P. Kreuzer, D. Lanske[†], C. Magass, M. Merschmeyer, A. Meyer, P. Papacz, H. Pieta, H. Reithler, S.A. Schmitz, L. Sonnenschein, J. Steggemann, D. Teyssier

RWTH Aachen University, III. Physikalisches Institut B, Aachen, Germany
M. Bontenackels, M. Davids, M. Duda, G. Flügge, H. Geenen, M. Giffels, W. Haj Ahmad, D. Heydhausen, T. Kress, Y. Kuessel, A. Linn, A. Nowack, L. Perchalla, O. Pooth, J. Rennefeld, P. Sauerland, A. Stahl, M. Thomas, D. Tornier, M.H. Zoeller

Deutsches Elektronen-Synchrotron, Hamburg, Germany
M. Aldaya Martin, W. Behrenhoff, U. Behrens, M. Bergholz[8], A. Bethani, K. Borras, A. Cakir, A. Campbell, E. Castro, D. Dammann, G. Eckerlin, D. Eckstein, A. Flossdorf, G. Flucke, A. Geiser, J. Hauk, H. Jung[1], M. Kasemann, I. Katkov[9], P. Katsas, C. Kleinwort, H. Kluge, A. Knutsson, M. Krämer, D. Krücker, E. Kuznetsova, W. Lange, W. Lohmann[8], R. Mankel, M. Marienfeld, I.-A. Melzer-Pellmann, A.B. Meyer, J. Mnich, A. Mussgiller, J. Olzem, A. Petrukhin, D. Pitzl, A. Raspereza, A. Raval, M. Rosin, R. Schmidt[8], T. Schoerner-Sadenius, N. Sen, A. Spiridonov,

M. Stein, J. Tomaszewska, R. Walsh, C. Wissing

University of Hamburg, Hamburg, Germany
C. Autermann, V. Blobel, S. Bobrovskyi, J. Draeger, H. Enderle, U. Gebbert, M. Görner, K. Kaschube, G. Kaussen, H. Kirschenmann, R. Klanner, J. Lange, B. Mura, S. Naumann-Emme, F. Nowak, N. Pietsch, C. Sander, H. Schettler, P. Schleper, E. Schlieckau, M. Schröder, T. Schum, J. Schwandt, H. Stadie, G. Steinbrück, J. Thomsen

Institut für Experimentelle Kernphysik, Karlsruhe, Germany
C. Barth, J. Bauer, J. Berger, V. Buege, T. Chwalek, W. De Boer, A. Dierlamm, G. Dirkes, M. Feindt, J. Gruschke, C. Hackstein, F. Hartmann, M. Heinrich, H. Held, K.H. Hoffmann, S. Honc, J.R. Komaragiri, T. Kuhr, D. Martschei, S. Mueller, Th. Müller, M. Niegel, O. Oberst, A. Oehler, J. Ott, T. Peiffer, G. Quast, K. Rabbertz, F. Ratnikov, N. Ratnikova, M. Renz, C. Saout, A. Scheurer, P. Schieferdecker, F.-P. Schilling, G. Schott, H.J. Simonis, F.M. Stober, D. Troendle, J. Wagner-Kuhr, T. Weiler, M. Zeise, V. Zhukov[9], E.B. Ziebarth

Institute of Nuclear Physics "Demokritos", Aghia Paraskevi, Greece
G. Daskalakis, T. Geralis, S. Kesisoglou, A. Kyriakis, D. Loukas, I. Manolakos, A. Markou, C. Markou, C. Mavrommatis, E. Ntomari, E. Petrakou

University of Athens, Athens, Greece
L. Gouskos, T.J. Mertzimekis, A. Panagiotou, E. Stiliaris

University of Ioánnina, Ioánnina, Greece
I. Evangelou, C. Foudas, P. Kokkas, N. Manthos, I. Papadopoulos, V. Patras, F.A. Triantis

KFKI Research Institute for Particle and Nuclear Physics, Budapest, Hungary
A. Aranyi, G. Bencze, L. Boldizsar, C. Hajdu[1], P. Hidas, D. Horvath[10], A. Kapusi, K. Krajczar[11], F. Sikler[1], G.I. Veres[11], G. Vesztergombi[11]

Institute of Nuclear Research ATOMKI, Debrecen, Hungary
N. Beni, J. Molnar, J. Palinkas, Z. Szillasi, V. Veszpremi

University of Debrecen, Debrecen, Hungary
P. Raics, Z.L. Trocsanyi, B. Ujvari

Panjab University, Chandigarh, India
S.B. Beri, V. Bhatnagar, N. Dhingra, R. Gupta, M. Jindal, M. Kaur, J.M. Kohli, M.Z. Mehta, N. Nishu, L.K. Saini, A. Sharma, A.P. Singh, J. Singh, S.P. Singh

University of Delhi, Delhi, India

S. Ahuja, S. Bhattacharya, B.C. Choudhary, B. Gomber, P. Gupta, S. Jain, S. Jain, R. Khurana, A. Kumar, M. Naimuddin, K. Ranjan, R.K. Shivpuri

Saha Institute of Nuclear Physics, Kolkata, India
S. Dutta, S. Sarkar

Bhabha Atomic Research Centre, Mumbai, India
R.K. Choudhury, D. Dutta, S. Kailas, V. Kumar, P. Mehta, A.K. Mohanty[1], L.M. Pant, P. Shukla

Tata Institute of Fundamental Research - EHEP, Mumbai, India
T. Aziz, M. Guchait[12], A. Gurtu, M. Maity[13], D. Majumder, G. Majumder, K. Mazumdar, G.B. Mohanty, A. Saha, K. Sudhakar, N. Wickramage

Tata Institute of Fundamental Research - HECR, Mumbai, India
S. Banerjee, S. Dugad, N.K. Mondal

Institute for Research and Fundamental Sciences (IPM), Tehran, Iran
H. Arfaei, H. Bakhshiansohi[14], S.M. Etesami, A. Fahim[14], M. Hashemi, A. Jafari[14], M. Khakzad, A. Mohammadi[15], M. Mohammadi Najafabadi, S. Paktinat Mehdiabadi, B. Safarzadeh, M. Zeinali[16]

INFN Sezione di Bari [a], Università di Bari [b], Politecnico di Bari [c], Bari, Italy
M. Abbrescia[a,b], L. Barbone[a,b], C. Calabria[a,b], A. Colaleo[a], D. Creanza[a,c], N. De Filippis[a,c,1], M. De Palma[a,b], L. Fiore[a], G. Iaselli[a,c], L. Lusito[a,b], G. Maggi[a,c], M. Maggi[a], N. Manna[a,b], B. Marangelli[a,b], S. My[a,c], S. Nuzzo[a,b], N. Pacifico[a,b], G.A. Pierro[a], A. Pompili[a,b], G. Pugliese[a,c], F. Romano[a,c], G. Roselli[a,b], G. Selvaggi[a,b], L. Silvestris[a], R. Trentadue[a], S. Tupputi[a,b], G. Zito[a]

INFN Sezione di Bologna [a], Università di Bologna [b], Bologna, Italy
G. Abbiendi[a], A.C. Benvenuti[a], D. Bonacorsi[a], S. Braibant-Giacomelli[a,b], L. Brigliadori[a], P. Capiluppi[a,b], A. Castro[a,b], F.R. Cavallo[a], M. Cuffiani[a,b], G.M. Dallavalle[a], F. Fab-bri[a], A. Fanfani[a,b], D. Fasanella[a], P. Giacomelli[a], M. Giunta[a], C. Grandi[a], S. Marcellini[a], G. Masetti[b], M. Meneghelli[a,b], A. Montanari[a], F.L. Navarria[a,b], F. Odorici[a], A. Per-rotta[a], F. Primavera[a], A.M. Rossi[a,b], T. Rovelli[a,b], G. Siroli[a,b], R. Travaglini[a,b]

INFN Sezione di Catania [a], Università di Catania [b], Catania, Italy
S. Albergo[a,b], G. Cappello[a,b], M. Chiorboli[a,b,1], S. Costa[a,b], A. Tricomi[a,b], C. Tuve[a,b]

INFN Sezione di Firenze [a], Università di Firenze [b], Firenze, Italy
G. Barbagli[a], V. Ciulli[a,b], C. Civinini[a], R. D'Alessandro[a,b], E. Focardi[a,b], S. Frosali[a,b], E. Gallo[a], S. Gonzi[a,b], P. Lenzi[a,b], M. Meschini[a], S. Paoletti[a], G. Sguazzoni[a], A. Tropiano[a,1]

INFN Laboratori Nazionali di Frascati, Frascati, Italy
L. Benussi, S. Bianco, S. Colafranceschi[17], F. Fabbri, D. Piccolo

INFN Sezione di Genova, Genova, Italy
P. Fabbricatore, R. Musenich

INFN Sezione di Milano-Biccoca [a], Università di Milano-Bicocca [b], Milano, Italy
A. Benaglia[a,b], F. De Guio[a,b,1], L. Di Matteo[a,b], S. Gennai[1], A. Ghezzi[a,b], S. Malvezzi[a], A. Martelli[a,b], A. Massironi[a,b], D. Menasce[a], L. Moroni[a], M. Paganoni[a,b], D. Pedrini[a], S. Ragazzi[a,b], N. Redaelli[a], S. Sala[a], T. Tabarelli de Fatis[a,b]

INFN Sezione di Napoli [a], Università di Napoli "Federico II" [b], Napoli, Italy
S. Buontempo[a], C.A. Carrillo Montoya[a,1], N. Cavallo[a,18], A. De Cosa[a,b], F. Fabozzi[a,18], A.O.M. Iorio[a,1], L. Lista[a], M. Merola[a,b], P. Paolucci[a]

INFN Sezione di Padova [a], Università di Padova [b], Università di Trento (Trento) [c], Padova, Italy
P. Azzi[a], N. Bacchetta[a], P. Bellan[a,b], D. Bisello[a,b], A. Branca[a], R. Carlin[a,b], P. Checchia[a], M. De Mattia[a,b], T. Dorigo[a], U. Dosselli[a], F. Fanzago[a], F. Gasparini[a,b], U. Gasparini[a,b], A. Gozzelino, S. Lacaprara[a,19], I. Lazzizzera[a,c], M. Margoni[a,b], M. Mazzucato[a], A.T. Meneguzzo[a,b], M. Nespolo[a,1], L. Perrozzi[a,1], N. Pozzobon[a,b], P. Ronchese[a,b], F. Simonetto[a,b], E. Torassa[a], M. Tosi[a,b], S. Vanini[a,b], P. Zotto[a,b], G. Zumerle[a,b]

INFN Sezione di Pavia [a], Università di Pavia [b], Pavia, Italy
P. Baesso[a,b], U. Berzano[a], S.P. Ratti[a,b], C. Riccardi[a,b], P. Torre[a,b], P. Vitulo[a,b], C. Viviani[a,b]

INFN Sezione di Perugia [a], Università di Perugia [b], Perugia, Italy
M. Biasini[a,b], G.M. Bilei[a], B. Caponeri[a,b], L. Fanò[a,b], P. Lariccia[a,b], A. Lucaroni[a,b,1], G. Mantovani[a,b], M. Menichelli[a], A. Nappi[a,b], F. Romeo[a,b], A. Santocchia[a,b], S. Taroni[a,b,1], M. Valdata[a,b]

INFN Sezione di Pisa [a], Università di Pisa [b], Scuola Normale Superiore di Pisa [c], Pisa, Italy
P. Azzurri[a,c], G. Bagliesi[a], J. Bernardini[a,b], T. Boccali[a,1], G. Broccolo[a,c], R. Castaldi[a], R.T. D'Agnolo[a,c], R. Dell'Orso[a], F. Fiori[a,b], L. Foà[a,c], A. Giassi[a], A. Kraan[a], F. Ligabue[a,c], T. Lomtadze[a], L. Martini[a,20], A. Messineo[a,b], F. Palla[a], G. Segneri[a], A.T. Serban[a], P. Spagnolo[a], R. Tenchini[a], G. Tonelli[a,b,1], A. Venturi[a,1], P.G. Verdini[a]

INFN Sezione di Roma [a], Università di Roma "La Sapienza" [b], Roma, Italy

L. Barone[a,b], F. Cavallari[a], D. Del Re[a,b], E. Di Marco[a,b], M. Diemoz[a], D. Franci[a,b], M. Grassi[a,1], E. Longo[a,b], P. Meridiani, S. Nourbakhsh[a], G. Organtini[a,b], F. Pandolfi[a,b,1], R. Paramatti[a], S. Rahatlou[a,b], C. Rovelli[1]

INFN Sezione di Torino [a], Università di Torino [b], Università del Piemonte Orientale (Novara) [c], Torino, Italy
N. Amapane[a,b], R. Arcidiacono[a,c], S. Argiro[a,b], M. Arneodo[a,c], C. Biino[a], C. Botta[a,b,1], N. Cartiglia[a], R. Castello[a,b], M. Costa[a,b], N. Demaria[a], A. Graziano[a,b,1], C. Mariotti[a], M. Marone[a,b], S. Maselli[a], E. Migliore[a,b], G. Mila[a,b], V. Monaco[a,b], M. Musich[a,b], M.M. Obertino[a,c], N. Pastrone[a], M. Pelliccioni[a,b], A. Romero[a,b], M. Ruspa[a,c], R. Sacchi[a,b], V. Sola[a,b], A. Solano[a,b], A. Staiano[a], A. Vilela Pereira[a]

INFN Sezione di Trieste [a], Università di Trieste [b], Trieste, Italy
S. Belforte[a], F. Cossutti[a], G. Della Ricca[a,b], B. Gobbo[a], D. Montanino[a,b], A. Penzo[a]

Kangwon National University, Chunchon, Korea
S.G. Heo, S.K. Nam

Kyungpook National University, Daegu, Korea
S. Chang, J. Chung, D.H. Kim, G.N. Kim, J.E. Kim, D.J. Kong, H. Park, S.R. Ro, D. Son, D.C. Son, T. Son

Chonnam National University, Institute for Universe and Elementary Particles, Kwangju, Korea
Zero Kim, J.Y. Kim, S. Song

Korea University, Seoul, Korea
S. Choi, B. Hong, M. Jo, H. Kim, J.H. Kim, T.J. Kim, K.S. Lee, D.H. Moon, S.K. Park, H.B. Rhee, E. Seo, K.S. Sim

University of Seoul, Seoul, Korea
M. Choi, S. Kang, H. Kim, C. Park, I.C. Park, S. Park, G. Ryu

Sungkyunkwan University, Suwon, Korea
Y. Choi, Y.K. Choi, J. Goh, M.S. Kim, E. Kwon, J. Lee, S. Lee, H. Seo, I. Yu

Vilnius University, Vilnius, Lithuania
M.J. Bilinskas, I. Grigelionis, M. Janulis, D. Martisiute, P. Petrov, T. Sabonis

Centro de Investigacion y de Estudios Avanzados del IPN, Mexico City, Mexico
H. Castilla-Valdez, E. De La Cruz-Burelo, I. Heredia-de La Cruz, R. Lopez-Fernandez, R. Magaña Villalba, A. Sánchez-Hernández, L.M. Villasenor-Cendejas

Universidad Iberoamericana, Mexico City, Mexico

S. Carrillo Moreno, F. Vazquez Valencia

Benemerita Universidad Autonoma de Puebla, Puebla, Mexico
H.A. Salazar Ibarguen

Universidad Autónoma de San Luis Potosí, San Luis Potosí, Mexico
E. Casimiro Linares, A. Morelos Pineda, M.A. Reyes-Santos

University of Auckland, Auckland, New Zealand
D. Krofcheck, J. Tam

University of Canterbury, Christchurch, New Zealand
P.H. Butler, R. Doesburg, H. Silverwood

National Centre for Physics, Quaid-I-Azam University, Islamabad, Pakistan
M. Ahmad, I. Ahmed, M.I. Asghar, H.R. Hoorani, W.A. Khan, T. Khurshid, S. Qazi

Institute of Experimental Physics, Faculty of Physics, University of Warsaw, Warsaw, Poland
G. Brona, M. Cwiok, W. Dominik, K. Doroba, A. Kalinowski, M. Konecki, J. Krolikowski

Soltan Institute for Nuclear Studies, Warsaw, Poland
T. Frueboes, R. Gokieli, M. Górski, M. Kazana, K. Nawrocki, K. Romanowska-Rybinska, M. Szleper, G. Wrochna, P. Zalewski

Laboratório de Instrumentação e Física Experimental de Partículas, Lisboa, Portugal
N. Almeida, P. Bargassa, A. David, P. Faccioli, P.G. Ferreira Parracho, M. Gallinaro, P. Musella, A. Nayak, P.Q. Ribeiro, J. Seixas, J. Varela

Joint Institute for Nuclear Research, Dubna, Russia
S. Afanasiev, P. Bunin, I. Golutvin, A. Kamenev, V. Karjavin, G. Kozlov, A. Lanev, P. Moisenz, V. Palichik, V. Perelygin, M. Savina, S. Shmatov, V. Smirnov, A. Volodko, A. Zarubin

Petersburg Nuclear Physics Institute, Gatchina (St Petersburg), Russia
V. Golovtsov, Y. Ivanov, V. Kim, P. Levchenko, V. Murzin, V. Oreshkin, I. Smirnov, V. Sulimov, L. Uvarov, S. Vavilov, A. Vorobyev, An. Vorobyev

Institute for Nuclear Research, Moscow, Russia
Yu. Andreev, A. Dermenev, S. Gninenko, N. Golubev, M. Kirsanov, N. Krasnikov, V. Matveev, A. Pashenkov, A. Toropin, S. Troitsky

Institute for Theoretical and Experimental Physics, Moscow, Russia
V. Epshteyn, V. Gavrilov, V. Kaftanov†, M. Kossov[1], A. Krokhotin, N. Lychkovskaya, V. Popov, G. Safronov, S. Semenov, V. Stolin, E. Vlasov, A. Zhokin

Moscow State University, Moscow, Russia
E. Boos, M. Dubinin[21], L. Dudko, A. Ershov, A. Gribushin, O. Kodolova, I. Lokhtin, A. Markina, S. Obraztsov, M. Perfilov, S. Petrushanko, L. Sarycheva, V. Savrin, A. Snigirev

P.N. Lebedev Physical Institute, Moscow, Russia
V. Andreev, M. Azarkin, I. Dremin, M. Kirakosyan, A. Leonidov, S.V. Rusakov, A. Vinogradov

State Research Center of Russian Federation, Institute for High Energy Physics, Protvino, Russia
I. Azhgirey, S. Bitioukov, V. Grishin[1], V. Kachanov, D. Konstantinov, A. Korablev, V. Krychkine, V. Petrov, R. Ryutin, S. Slabospitsky, A. Sobol, L. Tourtchanovitch, S. Troshin, N. Tyurin, A. Uzunian, A. Volkov

University of Belgrade, Faculty of Physics and Vinca Institute of Nuclear Sciences, Belgrade, Serbia
P. Adzic[22], M. Djordjevic, D. Krpic[22], J. Milosevic

Centro de Investigaciones Energéticas Medioambientales y Tecnológicas (CIEMAT), Madrid, Spain
M. Aguilar-Benitez, J. Alcaraz Maestre, P. Arce, C. Battilana, E. Calvo, M. Cepeda, M. Cerrada, M. Chamizo Llatas, N. Colino, B. De La Cruz, A. Delgado Peris, C. Diez Pardos, D. Domínguez Vázquez, C. Fernandez Bedoya, J.P. Fernández Ramos, A. Ferrando, J. Flix, M.C. Fouz, P. Garcia-Abia, O. Gonzalez Lopez, S. Goy Lopez, J.M. Hernandez, M.I. Josa, G. Merino, J. Puerta Pelayo, I. Redondo, L. Romero, J. Santaolalla, M.S. Soares, C. Willmott

Universidad Autónoma de Madrid, Madrid, Spain
C. Albajar, G. Codispoti, J.F. de Trocóniz

Universidad de Oviedo, Oviedo, Spain
J. Cuevas, J. Fernandez Menendez, S. Folgueras, I. Gonzalez Caballero, L. Lloret Iglesias, J.M. Vizan Garcia

Instituto de Física de Cantabria (IFCA), CSIC-Universidad de Cantabria, Santander, Spain
J.A. Brochero Cifuentes, I.J. Cabrillo, A. Calderon, S.H. Chuang, J. Duarte Campderros, M. Felcini[23], M. Fernandez, G. Gomez, J. Gonzalez Sanchez, C. Jorda, P. Lobelle Pardo, A. Lopez Virto, J. Marco, R. Marco, C. Martinez Rivero, F. Matorras, F.J. Munoz Sanchez, J. Piedra Gomez[24], T. Rodrigo, A.Y. Rodríguez-Marrero,

A. Ruiz-Jimeno, L. Scodellaro, M. Sobron Sanudo, I. Vila, R. Vilar Cortabitarte

CERN, European Organization for Nuclear Research, Geneva, Switzerland
D. Abbaneo, E. Auffray, G. Auzinger, P. Baillon, A.H. Ball, D. Barney, A.J. Bell[25], D. Benedetti, C. Bernet[3], W. Bialas, P. Bloch, A. Bocci, S. Bolognesi, M. Bona, H. Breuker, K. Bunkowski, T. Camporesi, G. Cerminara, J.A. Coarasa Perez, B. Curé, D. D'Enterria, A. De Roeck, S. Di Guida, N. Dupont-Sagorin, A. Elliott-Peisert, B. Frisch, W. Funk, A. Gaddi, G. Georgiou, H. Gerwig, D. Gigi, K. Gill, D. Giordano, F. Glege, R. Gomez-Reino Garrido, M. Gouzevitch, P. Govoni, S. Gowdy, L. Guiducci, M. Hansen, C. Hartl, J. Harvey, J. Hegeman, B. Hegner, H.F. Hoffmann, A. Honma, V. Innocente, P. Janot, K. Kaadze, E. Karavakis, P. Lecoq, C. Lourenço, T. Mäki, M. Malberti, L. Malgeri, M. Mannelli, L. Masetti, A. Maurisset, F. Meijers, S. Mersi, E. Meschi, R. Moser, M.U. Mozer, M. Mulders, E. Nesvold[1], M. Nguyen, T. Orimoto, L. Orsini, E. Perez, A. Petrilli, A. Pfeiffer, M. Pierini, M. Pimiä, D. Piparo, G. Polese, A. Racz, J. Rodrigues Antunes, G. Rolandi[26], T. Rommerskirchen, M. Rovere, H. Sakulin, C. Schäfer, C. Schwick, I. Segoni, A. Sharma, P. Siegrist, M. Simon, P. Sphicas[27], M. Spiropulu[21], M. Stoye, P. Tropea, A. Tsirou, P. Vichoudis, M. Voutilainen, W.D. Zeuner

Paul Scherrer Institut, Villigen, Switzerland
W. Bertl, K. Deiters, W. Erdmann, K. Gabathuler, R. Horisberger, Q. Ingram, H.C. Kaestli, S. König, D. Kotlinski, U. Langenegger, F. Meier, D. Renker, T. Rohe, J. Sibille[28], A. Starodumov[29]

Institute for Particle Physics, ETH Zurich, Zurich, Switzerland
L. Bäni, P. Bortignon, L. Caminada[30], N. Chanon, Z. Chen, S. Cittolin, G. Dissertori, M. Dittmar, J. Eugster, K. Freudenreich, C. Grab, W. Hintz, P. Lecomte, W. Lustermann, C. Marchica[30], P. Martinez Ruiz del Arbol, P. Milenovic[31], F. Moortgat, C. Nägeli[30], P. Nef, F. Nessi-Tedaldi, L. Pape, F. Pauss, T. Punz, A. Rizzi, F.J. Ronga, M. Rossini, L. Sala, A.K. Sanchez, M.-C. Sawley, B. Stieger, L. Tauscher†, A. Thea, K. Theofilatos, D. Treille, C. Urscheler, R. Wallny, M. Weber, L. Wehrli, J. Weng

Universität Zürich, Zurich, Switzerland
E. Aguilo, C. Amsler, V. Chiochia, S. De Visscher, C. Favaro, M. Ivova Rikova, B. Millan Mejias, P. Otiougova, C. Regenfus, P. Robmann, A. Schmidt, H. Snoek

National Central University, Chung-Li, Taiwan
Y.H. Chang, K.H. Chen, C.M. Kuo, S.W. Li, W. Lin, Z.K. Liu, Y.J. Lu, D. Mekterovic, R. Volpe, J.H. Wu, S.S. Yu

National Taiwan University (NTU), Taipei, Taiwan
P. Bartalini, P. Chang, Y.H. Chang, Y.W. Chang, Y. Chao, K.F. Chen, W.-S. Hou, Y. Hsiung, K.Y. Kao, Y.J. Lei, R.-S. Lu, J.G. Shiu, Y.M. Tzeng, M. Wang

Cukurova University, Adana, Turkey
A. Adiguzel, M.N. Bakirci[32], S. Cerci[33], C. Dozen, I. Dumanoglu, E. Eskut, S. Girgis, G. Gokbulut, I. Hos, E.E. Kangal, A. Kayis Topaksu, G. Onengut, K. Ozdemir, S. Ozturk[34], A. Polatoz, K. Sogut[35], D. Sunar Cerci[33], B. Tali[33], H. Topakli[32], D. Uzun, L.N. Vergili, M. Vergili

Middle East Technical University, Physics Department, Ankara, Turkey
I.V. Akin, T. Aliev, B. Bilin, S. Bilmis, M. Deniz, H. Gamsizkan, A.M. Guler, K. Ocalan, A. Ozpineci, M. Serin, R. Sever, U.E. Surat, E. Yildirim, M. Zeyrek

Bogazici University, Istanbul, Turkey
M. Deliomeroglu, D. Demir[36], E. Gülmez, B. Isildak, M. Kaya[37], O. Kaya[37], M. Özbek, S. Ozkorucuklu[38], N. Sonmez[39]

National Scientific Center, Kharkov Institute of Physics and Technology, Kharkov, Ukraine
L. Levchuk

University of Bristol, Bristol, United Kingdom
F. Bostock, J.J. Brooke, T.L. Cheng, E. Clement, D. Cussans, R. Frazier, J. Goldstein, M. Grimes, M. Hansen, D. Hartley, G.P. Heath, H.F. Heath, L. Kreczko, S. Metson, D.M. Newbold[40], K. Nirunpong, A. Poll, S. Senkin, V.J. Smith, S. Ward

Rutherford Appleton Laboratory, Didcot, United Kingdom
L. Basso[41], K.W. Bell, A. Belyaev[41], C. Brew, R.M. Brown, B. Camanzi, D.J.A. Cockerill, J.A. Coughlan, K. Harder, S. Harper, J. Jackson, B.W. Kennedy, E. Olaiya, D. Petyt, B.C. Radburn-Smith, C.H. Shepherd-Themistocleous, I.R. Tomalin, W.J. Womersley, S.D. Worm

Imperial College, London, United Kingdom
R. Bainbridge, G. Ball, J. Ballin, R. Beuselinck, O. Buchmuller, D. Colling, N. Cripps, M. Cutajar, G. Davies, M. Della Negra, W. Ferguson, J. Fulcher, D. Futyan, A. Gilbert, A. Guneratne Bryer, G. Hall, Z. Hatherell, J. Hays, G. Iles, M. Jarvis, G. Karapostoli, L. Lyons, B.C. MacEvoy, A.-M. Magnan, J. Marrouche, B. Mathias, R. Nandi, J. Nash, A. Nikitenko[29], A. Papageorgiou, M. Pesaresi, K. Petridis, M. Pioppi[42], D.M. Raymond, S. Rogerson, N. Rompotis, A. Rose, M.J. Ryan, C. Seez, P. Sharp, A. Sparrow, A. Tapper, S. Tourneur, M. Vazquez Acosta, T. Virdee, S. Wakefield, N. Wardle, D. Wardrope, T. Whyntie

Brunel University, Uxbridge, United Kingdom
M. Barrett, M. Chadwick, J.E. Cole, P.R. Hobson, A. Khan, P. Kyberd, D. Leslie, W. Martin, I.D. Reid, L. Teodorescu

Baylor University, Waco, USA

K. Hatakeyama, H. Liu

The University of Alabama, Tuscaloosa, USA
C. Henderson

Boston University, Boston, USA
T. Bose, E. Carrera Jarrin, C. Fantasia, A. Heister, J. St. John, P. Lawson, D. Lazic, J. Rohlf, D. Sperka, L. Sulak

Brown University, Providence, USA
A. Avetisyan, S. Bhattacharya, J.P. Chou, D. Cutts, A. Ferapontov, U. Heintz, S. Jabeen, G. Kukartsev, G. Landsberg, M. Luk, M. Narain, D. Nguyen, M. Segala, T. Sinthuprasith, T. Speer, K.V. Tsang

University of California, Davis, Davis, USA
R. Breedon, M. Calderon De La Barca Sanchez, S. Chauhan, M. Chertok, J. Conway, P.T. Cox, J. Dolen, R. Erbacher, E. Friis, W. Ko, A. Kopecky, R. Lander, H. Liu, S. Maruyama, T. Miceli, M. Nikolic, D. Pellett, J. Robles, S. Salur, T. Schwarz, M. Searle, J. Smith, M. Squires, M. Tripathi, R. Vasquez Sierra, C. Veelken

University of California, Los Angeles, Los Angeles, USA
V. Andreev, K. Arisaka, D. Cline, R. Cousins, A. Deisher, J. Duris, S. Erhan, C. Farrell, J. Hauser, M. Ignatenko, C. Jarvis, C. Plager, G. Rakness, P. Schlein†, J. Tucker, V. Valuev

University of California, Riverside, Riverside, USA
J. Babb, A. Chandra, R. Clare, J. Ellison, J.W. Gary, F. Giordano, G. Hanson, G.Y. Jeng, S.C. Kao, F. Liu, H. Liu, O.R. Long, A. Luthra, H. Nguyen, B.C. Shen†, R. Stringer, J. Sturdy, S. Sumowidagdo, R. Wilken, S. Wimpenny

University of California, San Diego, La Jolla, USA
W. Andrews, J.G. Branson, G.B. Cerati, D. Evans, F. Golf, A. Holzner, R. Kelley, M. Lebourgeois, J. Letts, B. Mangano, S. Padhi, C. Palmer, G. Petrucciani, H. Pi, M. Pieri, R. Ranieri, M. Sani, V. Sharma, S. Simon, E. Sudano, M. Tadel, Y. Tu, A. Vartak, S. Wasserbaech[43], F. Würthwein, A. Yagil, J. Yoo

University of California, Santa Barbara, Santa Barbara, USA
D. Barge, R. Bellan, C. Campagnari, M. D'Alfonso, T. Danielson, K. Flowers, P. Geffert, J. Incandela, C. Justus, P. Kalavase, S.A. Koay, D. Kovalskyi, V. Krutelyov, S. Lowette, N. Mccoll, V. Pavlunin, F. Rebassoo, J. Ribnik, J. Richman, R. Rossin, D. Stuart, W. To, J.R. Vlimant

California Institute of Technology, Pasadena, USA
A. Apresyan, A. Bornheim, J. Bunn, Y. Chen, M. Gataullin, Y. Ma, A. Mott, H.B. Newman, C. Rogan, K. Shin, V. Timciuc, P. Traczyk, J. Veverka, R. Wilkin-

son, Y. Yang, R.Y. Zhu

Carnegie Mellon University, Pittsburgh, USA
B. Akgun, R. Carroll, T. Ferguson, Y. Iiyama, D.W. Jang, S.Y. Jun, Y.F. Liu, M. Paulini, J. Russ, H. Vogel, I. Vorobiev

University of Colorado at Boulder, Boulder, USA
J.P. Cumalat, M.E. Dinardo, B.R. Drell, C.J. Edelmaier, W.T. Ford, A. Gaz, B. Heyburn, E. Luiggi Lopez, U. Nauenberg, J.G. Smith, K. Stenson, K.A. Ulmer, S.R. Wagner, S.L. Zang

Cornell University, Ithaca, USA
L. Agostino, J. Alexander, D. Cassel, A. Chatterjee, S. Das, N. Eggert, L.K. Gibbons, B. Heltsley, W. Hopkins, A. Khukhunaishvili, B. Kreis, G. Nicolas Kaufman, J.R. Patterson, D. Puigh, A. Ryd, E. Salvati, X. Shi, W. Sun, W.D. Teo, J. Thom, J. Thompson, J. Vaughan, Y. Weng, L. Winstrom, P. Wittich

Fairfield University, Fairfield, USA
A. Biselli, G. Cirino, D. Winn

Fermi National Accelerator Laboratory, Batavia, USA
S. Abdullin, M. Albrow, J. Anderson, G. Apollinari, M. Atac, J.A. Bakken, S. Banerjee, L.A.T. Bauerdick, A. Beretvas, J. Berryhill, P.C. Bhat, I. Bloch, F. Borcherding, K. Burkett, J.N. Butler, V. Chetluru, H.W.K. Cheung, F. Chlebana, S. Cihangir, W. Cooper, D.P. Eartly, V.D. Elvira, S. Esen, I. Fisk, J. Freeman, Y. Gao, E. Gottschalk, D. Green, K. Gunthoti, O. Gutsche, J. Hanlon, R.M. Harris, J. Hirschauer, B. Hooberman, H. Jensen, M. Johnson, U. Joshi, R. Khatiwada, B. Klima, K. Kou-souris, S. Kunori, S. Kwan, C. Leonidopoulos, P. Limon, D. Lincoln, R. Lipton, J. Lykken, K. Maeshima, J.M. Marraffino, D. Mason, P. McBride, T. Miao, K. Mishra, S. Mrenna, Y. Musienko[44], C. Newman-Holmes, V. O'Dell, R. Pordes, O. Prokofyev, N. Saoulidou, E. Sexton-Kennedy, S. Sharma, W.J. Spalding, L. Spiegel, P. Tan, L. Taylor, S. Tkaczyk, L. Uplegger, E.W. Vaandering, R. Vidal, J. Whitmore, W. Wu, F. Yang, F. Yumiceva, J.C. Yun

University of Florida, Gainesville, USA
D. Acosta, P. Avery, D. Bourilkov, M. Chen, M. De Gruttola, G.P. Di Giovanni, D. Dobur, A. Drozdetskiy, R.D. Field, M. Fisher, Y. Fu, I.K. Furic, J. Gartner, B. Kim, J. Konigsberg, A. Korytov, A. Kropivnitskaya, T. Kypreos, K. Matchev, G. Mitselmakher, L. Muniz, C. Prescott, R. Remington, M. Schmitt, B. Scurlock, P. Sellers, N. Skhirtladze, M. Snowball, D. Wang, J. Yelton, M. Zakaria

Florida International University, Miami, USA
C. Ceron, V. Gaultney, L. Kramer, L.M. Lebolo, S. Linn, P. Markowitz, G. Martinez, D. Mesa, J.L. Rodriguez

Florida State University, Tallahassee, USA
T. Adams, A. Askew, J. Bochenek, J. Chen, B. Diamond, S.V. Gleyzer, J. Haas, S. Hagopian, V. Hagopian, M. Jenkins, K.F. Johnson, H. Prosper, L. Quertenmont, S. Sekmen, V. Veeraraghavan

Florida Institute of Technology, Melbourne, USA
M.M. Baarmand, B. Dorney, S. Guragain, M. Hohlmann, H. Kalakhety, R. Ralich, I. Vodopiyanov

University of Illinois at Chicago (UIC), Chicago, USA
M.R. Adams, I.M. Anghel, L. Apanasevich, Y. Bai, V.E. Bazterra, R.R. Betts, J. Callner, R. Cavanaugh, C. Dragoiu, L. Gauthier, C.E. Gerber, S. Hamdan, D.J. Hofman, S. Khalatyan, G.J. Kunde[45], F. Lacroix, M. Malek, C. O'Brien, C. Silvestre, A. Smoron, D. Strom, N. Varelas

The University of Iowa, Iowa City, USA
U. Akgun, E.A. Albayrak, B. Bilki, W. Clarida, F. Duru, C.K. Lae, E. McCliment, J.-P. Merlo, H. Mermerkaya[46], A. Mestvirishvili, A. Moeller, J. Nachtman, C.R. Newsom, E. Norbeck, J. Olson, Y. Onel, F. Ozok, S. Sen, J. Wetzel, T. Yetkin, K. Yi

Johns Hopkins University, Baltimore, USA
B.A. Barnett, B. Blumenfeld, A. Bonato, C. Eskew, D. Fehling, G. Giurgiu, A.V. Gritsan, Z.J. Guo, G. Hu, P. Maksimovic, S. Rappoccio, M. Swartz, N.V. Tran, A. Whitbeck

The University of Kansas, Lawrence, USA
P. Baringer, A. Bean, G. Benelli, O. Grachov, R.P. Kenny Iii, M. Murray, D. Noonan, S. Sanders, J.S. Wood, V. Zhukova

Kansas State University, Manhattan, USA
A.F. Barfuss, T. Bolton, I. Chakaberia, A. Ivanov, S. Khalil, M. Makouski, Y. Maravin, S. Shrestha, I. Svintradze, Z. Wan

Lawrence Livermore National Laboratory, Livermore, USA
J. Gronberg, D. Lange, D. Wright

University of Maryland, College Park, USA
A. Baden, M. Boutemeur, S.C. Eno, D. Ferencek, J.A. Gomez, N.J. Hadley, R.G. Kellogg, M. Kirn, Y. Lu, A.C. Mignerey, K. Rossato, P. Rumerio, F. Santanastasio, A. Skuja, J. Temple, M.B. Tonjes, S.C. Tonwar, E. Twedt

Massachusetts Institute of Technology, Cambridge, USA
B. Alver, G. Bauer, J. Bendavid, W. Busza, E. Butz, I.A. Cali, M. Chan, V. Dutta, P. Everaerts, G. Gomez Ceballos, M. Goncharov, K.A. Hahn, P. Harris, Y. Kim,

M. Klute, Y.-J. Lee, W. Li, C. Loizides, P.D. Luckey, T. Ma, S. Nahn, C. Paus, D. Ralph, C. Roland, G. Roland, M. Rudolph, G.S.F. Stephans, F. Stöckli, K. Sumorok, K. Sung, E.A. Wenger, S. Xie, M. Yang, Y. Yilmaz, A.S. Yoon, M. Zanetti

University of Minnesota, Minneapolis, USA
S.I. Cooper, P. Cushman, B. Dahmes, A. De Benedetti, P.R. Dudero, G. Franzoni, J. Haupt, K. Klapoetke, Y. Kubota, J. Mans, V. Rekovic, R. Rusack, M. Sasseville, A. Singovsky, N. Tambe

University of Mississippi, University, USA
L.M. Cremaldi, R. Godang, R. Kroeger, L. Perera, R. Rahmat, D.A. Sanders, D. Summers

University of Nebraska-Lincoln, Lincoln, USA
K. Bloom, S. Bose, J. Butt, D.R. Claes, A. Dominguez, M. Eads, J. Keller, T. Kelly, I. Kravchenko, J. Lazo-Flores, H. Malbouisson, S. Malik, G.R. Snow

State University of New York at Buffalo, Buffalo, USA
U. Baur, A. Godshalk, I. Iashvili, S. Jain, A. Kharchilava, A. Kumar, S.P. Shipkowski, K. Smith

Northeastern University, Boston, USA
G. Alverson, E. Barberis, D. Baumgartel, O. Boeriu, M. Chasco, S. Reucroft, J. Swain, D. Trocino, D. Wood, J. Zhang

Northwestern University, Evanston, USA
A. Anastassov, A. Kubik, N. Odell, R.A. Ofierzynski, B. Pollack, A. Pozdnyakov, M. Schmitt, S. Stoynev, M. Velasco, S. Won

University of Notre Dame, Notre Dame, USA
L. Antonelli, D. Berry, A. Brinkerhoff, M. Hildreth, C. Jessop, D.J. Karmgard, J. Kolb, T. Kolberg, K. Lannon, W. Luo, S. Lynch, N. Marinelli, D.M. Morse, T. Pearson, R. Ruchti, J. Slaunwhite, N. Valls, M. Wayne, J. Ziegler

The Ohio State University, Columbus, USA
B. Bylsma, L.S. Durkin, J. Gu, C. Hill, P. Killewald, K. Kotov, T.Y. Ling, M. Rodenburg, G. Williams

Princeton University, Princeton, USA
N. Adam, E. Berry, P. Elmer, D. Gerbaudo, V. Halyo, P. Hebda, A. Hunt, J. Jones, E. Laird, D. Lopes Pegna, D. Marlow, T. Medvedeva, M. Mooney, J. Olsen, P. Piroué, X. Quan, H. Saka, D. Stickland, C. Tully, J.S. Werner, A. Zuranski

University of Puerto Rico, Mayaguez, USA
J.G. Acosta, X.T. Huang, A. Lopez, H. Mendez, S. Oliveros, J.E. Ramirez Vargas,

A. Zatserklyaniy

Purdue University, West Lafayette, USA
E. Alagoz, V.E. Barnes, G. Bolla, L. Borrello, D. Bortoletto, A. Everett, A.F. Garfinkel, L. Gutay, Z. Hu, M. Jones, O. Koybasi, M. Kress, A.T. Laasanen, N. Leonardo, C. Liu, V. Maroussov, P. Merkel, D.H. Miller, N. Neumeister, I. Shipsey, D. Silvers, A. Svyatkovskiy, H.D. Yoo, J. Zablocki, Y. Zheng

Purdue University Calumet, Hammond, USA
P. Jindal, N. Parashar

Rice University, Houston, USA
C. Boulahouache, V. Cuplov, K.M. Ecklund, F.J.M. Geurts, B.P. Padley, R. Redjimi, J. Roberts, J. Zabel

University of Rochester, Rochester, USA
B. Betchart, A. Bodek, Y.S. Chung, R. Covarelli, P. de Barbaro, R. Demina, Y. Eshaq, H. Flacher, A. Garcia-Bellido, P. Goldenzweig, Y. Gotra, J. Han, A. Harel, D.C. Miner, D. Orbaker, G. Petrillo, D. Vishnevskiy, M. Zielinski

The Rockefeller University, New York, USA
A. Bhatti, R. Ciesielski, L. Demortier, K. Goulianos, G. Lungu, S. Malik, C. Mesropian, M. Yan

Rutgers, the State University of New Jersey, Piscataway, USA
O. Atramentov, A. Barker, D. Duggan, Y. Gershtein, R. Gray, E. Halkiadakis, D. Hidas, D. Hits, A. Lath, S. Panwalkar, R. Patel, A. Richards, K. Rose, S. Schnetzer, S. Somalwar, R. Stone, S. Thomas

University of Tennessee, Knoxville, USA
G. Cerizza, M. Hollingsworth, S. Spanier, Z.C. Yang, A. York

Texas A&M University, College Station, USA
R. Eusebi, W. Flanagan, J. Gilmore, A. Gurrola, T. Kamon, V. Khotilovich, R. Montalvo, I. Osipenkov, Y. Pakhotin, J. Pivarski, A. Safonov, S. Sengupta, A. Tatarinov, D. Toback, M. Weinberger

Texas Tech University, Lubbock, USA
N. Akchurin, C. Bardak, J. Damgov, C. Jeong, K. Kovitanggoon, S.W. Lee, P. Mane, Y. Roh, A. Sill, I. Volobouev, R. Wigmans, E. Yazgan

Vanderbilt University, Nashville, USA
E. Appelt, E. Brownson, D. Engh, C. Florez, W. Gabella, M. Issah, W. Johns, P. Kurt, C. Maguire, A. Melo, P. Sheldon, B. Snook, S. Tuo, J. Velkovska

University of Virginia, Charlottesville, USA
M.W. Arenton, M. Balazs, S. Boutle, B. Cox, B. Francis, R. Hirosky, A. Ledovskoy, C. Lin, C. Neu, R. Yohay

Wayne State University, Detroit, USA
S. Gollapinni, R. Harr, P.E. Karchin, P. Lamichhane, M. Mattson, C. Milstène, A. Sakharov

University of Wisconsin, Madison, USA
M. Anderson, M. Bachtis, J.N. Bellinger, D. Carlsmith, S. Dasu, J. Efron, K. Flood, L. Gray, K.S. Grogg, M. Grothe, R. Hall-Wilton, M. Herndon, A. Hervé, P. Klabbers, J. Klukas, A. Lanaro, C. Lazaridis, J. Leonard, R. Loveless, A. Mohapatra, F. Palmonari, D. Reeder, I. Ross, A. Savin, W.H. Smith, J. Swanson, M. Weinberg

†: Deceased
1: Also at CERN, European Organization for Nuclear Research, Geneva, Switzerland
2: Also at Universidade Federal do ABC, Santo Andre, Brazil
3: Also at Laboratoire Leprince-Ringuet, Ecole Polytechnique, IN2P3-CNRS, Palaiseau, France
4: Also at British University, Cairo, Egypt
5: Also at Soltan Institute for Nuclear Studies, Warsaw, Poland
6: Also at Massachusetts Institute of Technology, Cambridge, USA
7: Also at Université de Haute-Alsace, Mulhouse, France
8: Also at Brandenburg University of Technology, Cottbus, Germany
9: Also at Moscow State University, Moscow, Russia
10: Also at Institute of Nuclear Research ATOMKI, Debrecen, Hungary
11: Also at Eötvös Loránd University, Budapest, Hungary
12: Also at Tata Institute of Fundamental Research - HECR, Mumbai, India
13: Also at University of Visva-Bharati, Santiniketan, India
14: Also at Sharif University of Technology, Tehran, Iran
15: Also at Shiraz University, Shiraz, Iran
16: Also at Isfahan University of Technology, Isfahan, Iran
17: Also at Facoltà Ingegneria Università di Roma "La Sapienza", Roma, Italy
18: Also at Università della Basilicata, Potenza, Italy
19: Also at Laboratori Nazionali di Legnaro dell' INFN, Legnaro, Italy
20: Also at Università degli studi di Siena, Siena, Italy
21: Also at California Institute of Technology, Pasadena, USA
22: Also at Faculty of Physics of University of Belgrade, Belgrade, Serbia
23: Also at University of California, Los Angeles, Los Angeles, USA
24: Also at University of Florida, Gainesville, USA
25: Also at Université de Genève, Geneva, Switzerland
26: Also at Scuola Normale e Sezione dell' INFN, Pisa, Italy
27: Also at University of Athens, Athens, Greece
28: Also at The University of Kansas, Lawrence, USA

29: Also at Institute for Theoretical and Experimental Physics, Moscow, Russia
30: Also at Paul Scherrer Institut, Villigen, Switzerland
31: Also at University of Belgrade, Faculty of Physics and Vinca Institute of Nuclear Sciences, Belgrade, Serbia
32: Also at Gaziosmanpasa University, Tokat, Turkey
33: Also at Adiyaman University, Adiyaman, Turkey
34: Also at The University of Iowa, Iowa City, USA
35: Also at Mersin University, Mersin, Turkey
36: Also at Izmir Institute of Technology, Izmir, Turkey
37: Also at Kafkas University, Kars, Turkey
38: Also at Suleyman Demirel University, Isparta, Turkey
39: Also at Ege University, Izmir, Turkey
40: Also at Rutherford Appleton Laboratory, Didcot, United Kingdom
41: Also at School of Physics and Astronomy, University of Southampton, Southampton, United Kingdom
42: Also at INFN Sezione di Perugia; Università di Perugia, Perugia, Italy
43: Also at Utah Valley University, Orem, USA
44: Also at Institute for Nuclear Research, Moscow, Russia
45: Also at Los Alamos National Laboratory, Los Alamos, USA
46: Also at Erzincan University, Erzincan, Turkey

Bibliography

[1] David Griffiths, "Introduction to Elementary Particles". Wiley-VCH, 2008. 3

[2] Francis Halzen and Alan D. Martin, "Quarks and Leptons: An Introductory Course in Modern Particle Physics". Wiley, 1984.

[3] Gordon Kane, "Modern Elementary Particle Physics: The Fundamental Particles and Forces?". Perseus, 1993. 3

[4] Particle Data Group, K. Nakamura et al., "Review of particle physics," *J.Phys.* **G37** (2010) 075021. and references therein. doi:10.1088/0954-3899/37/7A/075021. 8, 24, 87, 178

[5] Michael E. Peskin and Dan V. Schroeder, "An Introduction To Quantum Field Theory". Westview Press, 1995. 12

[6] H. Georgi and S. L. Glashow, "Unity of All Elementary-Particle Forces," *Phys. Rev. Lett.* **32** (1974) 438–441. doi:10.1103/PhysRevLett.32.438. 12 "Unified theory of elementary-particle forces," *Phys. Today* **33N9** (1980) 30–39.

[7] H. Murayama and T. Yanagida, "A viable SU(5) GUT with light leptoquark bosons," *Mod.Phys.Lett.* **A7** (1992) 147–152. doi:10.1142/S0217732392000070. 12, 17

[8] H. Fritzsch and P. Minkowski, "Unified Interactions of Leptons and Hadrons," *Annals Phys.* **93** (1975) 193–266. doi:10.1016/0003-4916(75)90211-0. 12

[9] G. Senjanović and A. Šokorac, "Light leptoquarks in SO(10)," *Z.Phys.* **C20** (1983) 255. doi:10.1007/BF01574858. 12

[10] J. C. Pati and A. Salam, "Unified Lepton-Hadron Symmetry and a Gauge Theory of the Basic Interactions," *Phys.Rev.* **D8** (1973) 1240–1251. doi:10.1103/PhysRevD.8.1240. 12, 17

[11] J. C. Pati and A. Salam, "Lepton number as the fourth "color"," *Phys.Rev.* **D10** (1974) 275–289. doi:10.1103/PhysRevD.10.275. 12, 17 "Erratum," *Phys.Rev.* **D11** (1975), no. 3, 703. doi:10.1103/PhysRevD.11.703.2.

[12] P. H. Frampton and B.-H. Lee, "SU(15) Grand Unification," *Phys.Rev.Lett.* **64** (1990) 619. doi:10.1103/PhysRevLett.64.619. 12, 17

[13] P. H. Frampton and T. W. Kephart, "Higgs sector and proton decay in SU(15) grand unification," *Phys.Rev.* **D42** (1990) 3892–3894. doi:10.1103/PhysRevD.42.3892. 12, 17

[14] J. L. Hewett and T. G. Rizzo, "Low-Energy Phenomenology of Superstring Inspired E(6) Models," *Phys.Rept.* **183** (1989) 193. doi:10.1016/0370-1573(89)90071-9. 12, 17

[15] E. Farhi and L. Susskind, "Technicolor," *Phys.Rept.* **74** (1981) 277. doi:10.1016/0370-1573(81)90173-3. 13

[16] E. Eichten, I. Hinchliffe, K. Lane, and C. Quigg, "Signatures for Technicolor," *Phys.Rev.* **D34** (1986) 1547. doi:10.1103/PhysRevD.34.1547.

[17] K. D. Lane and M. Ramana, "Walking technicolor signatures at hadron colliders," *Phys.Rev.* **D44** (1991) 2678–2700. doi:10.1103/PhysRevD.44.2678. 13

[18] B. Schrempp and F. Schrempp, "Light leptoquarks," *Phys.Lett.* **B153** (1985) 101. doi:10.1016/0370-2693(85)91450-9. 13

[19] J. Wudka, "Composite leptoquarks," *Phys.Lett.* **B167** (1986) 337. doi:10.1016/0370-2693(86)90356-4. 13

[20] S. Pakvasa, "Signatures for horizontal symmetries and some other exotica at hadron colliders," *Int.J.Mod.Phys.* **A2** (1987) 1317. doi:10.1142/S0217751X87000685. 13

[21] L. Abbott and E. Farhi, "Are the Weak Interactions Strong?," *Phys.Lett.* **B101** (1981) 69. doi:10.1016/0370-2693(81)90492-5. 13
"A Confining Model of the Weak Interactions," *Nucl.Phys.* **B189** (1981) 547–556. doi:10.1016/0550-3213(81)90580-0.

[22] D. Choudhury and S. Raychaudhuri, "R-parity violation at HERA?," *Phys.Lett.* **B401** (1997) 54–61, arXiv:hep-ph/9702392. doi:10.1016/S0370-2693(97)00391-2. 13

[23] H. K. Dreiner, "An introduction to explicit R-parity violation," *Pramana* **51** (1998) 123–133. doi:10.1007/BF02827485. 13

[24] W. Buchmüller, R. Rückl, and D. Wyler, "Leptoquarks in lepton-quark collisions," *Phys.Lett.* **B191** (1987) 442–448. doi:10.1016/0370-2693(87)90637-X. 13, 14, 21
"Erratum," *Phys.Lett.* **B448** (1999), no. 3-4, 320 – 320. doi:10.1016/S0370-2693(99)00014-3.

[25] A. Djouadi, T. Kohler, M. Spira, and J. Tutas, "(eb), (et) type leptoquark at ep colliders," *Z.Phys.* **C46** (1990) 679–686. doi:10.1007/BF01560270. 14

[26] S. Davidson, D. C. Bailey, and B. A. Campbell, "Model independent constraints on leptoquarks from rare processes," *Z.Phys.* **C61** (1994) 613–644, arXiv:hep-ph/9309310. doi:10.1007/BF01552629. 15, 24

[27] J. L. Hewett and T. G. Rizzo, "Much ado about leptoquarks: A Comprehensive analysis," *Phys.Rev.* **D56** (1997) 5709–5724, arXiv:hep-ph/9703337. doi:10.1103/PhysRevD.56.5709. 15, 16, 24

[28] M. Kuze and Y. Sirois, "Search for Particles and Forces Beyond the Standard Model in High Energy Lepton-Hadron and Hadron-Hadron Collisions," *Prog.Part.Nucl.Phys.* **50** (2003) 1–62, arXiv:hep-ex/0211048. doi:10.1016/S0146-6410(02)00176-X. 16, 18, 24
"Erratum," *Prog.Part.Nucl.Phys.* **53** (2004), no. 2, 679 – 679. doi:10.1016/j.ppnp.2004.03.001.

[29] J. Blümlein and R. Rückl, "Production of scalar and vector leptoquarks in e^+e^- annihilation," *Phys.Lett.* **B304** (1993) 337–346. doi:10.1016/0370-2693(93)90306-3. 17

[30] J. Blümlein, E. Boos, and A. Kryukov, "Vector leptoquark pair production in e^+e^- annihilation," *Phys.Lett.* **B392** (1997) 150–154, arXiv:hep-ph/9610506. doi:10.1016/S0370-2693(96)01531-6.

[31] J. Blümlein, E. Boos, and A. Kryukov, "Leptoquark pair production in hadronic interactions," *Z.Phys.* **C76** (1997) 137–153, arXiv:hep-ph/9610408. doi:10.1007/s002880050538. 17, 18

[32] D. Acosta and S. K. Blessing, "Leptoquark searches at HERA and the Tevatron," *Ann.Rev.Nucl.Part.Sci.* **49** (1999) 389–434. doi:10.1146/annurev.nucl.49.1.389. 18

[33] A. Belyaev, C. Leroy, R. Mehdiyev, and A. Pukhov, "Leptoquark single and pair production at LHC with CalcHEP/CompHEP in the complete model," *JHEP* **0509** (2005) 005, arXiv:hep-ph/0502067. doi:10.1088/1126-6708/2005/09/005. 18, 21

[34] M. Krämer, T. Plehn, M. Spira, and P. Zerwas, "Pair production of scalar leptoquarks at the CERN LHC," *Phys.Rev.* **D71** (2005) 057503, arXiv:hep-ph/0411038. and private communication. doi:10.1103/PhysRevD.71.057503. viii, xii, 18, 20, 92, 93

[35] J. Pumplin, D. Stump, J. Huston, H. Lai, P. M. Nadolsky, et al., "New generation of parton distributions with uncertainties from global QCD analysis," *JHEP* **0207** (2002) 012, arXiv:hep-ph/0201195. xii, 20, 90

[36] P. M. Nadolsky, H.-L. Lai, Q.-H. Cao, J. Huston, J. Pumplin, et al., "Implications of CTEQ global analysis for collider observables," *Phys.Rev.* **D78** (2008) 013004, arXiv:0802.0007. doi:10.1103/PhysRevD.78.013004. xii, 20, 92

[37] T. Plehn, H. Spiesberger, M. Spira, and P. Zerwas, "Formation and decay of scalar leptoquarks/squarks in *ep* collisions," *Z.Phys.* **C74** (1997) 611–614, arXiv:hep-ph/9703433. doi:10.1007/s002880050426. 21

[38] K. Babu, C. F. Kolda, and J. March-Russell, "Implications of a charged current anomaly at HERA," *Phys.Lett.* **B408** (1997) 261–267, arXiv:hep-ph/9705414. doi:10.1016/S0370-2693(97)00766-1. 21

[39] G. Altarelli, G. Giudice, and M. L. Mangano, "What if charged current events at large Q^2 are observed at HERA?," *Nucl.Phys.* **B506** (1997) 29–47, arXiv:hep-ph/9705287. doi:10.1016/S0550-3213(97)00534-8.

[40] J. L. Hewett and T. G. Rizzo, "Don't stop thinking about leptoquarks: Constructing new models," *Phys.Rev.* **D58** (1998) 055005, arXiv:hep-ph/9708419. doi:10.1103/PhysRevD.58.055005. 21

[41] W. Buchmüller and D. Wyler, "Constraints on SU(5) Type Leptoquarks," *Phys.Lett.* **B177** (1986) 377. doi:10.1016/0370-2693(86)90771-9. 24

[42] M. Leurer, "A comprehensive study of leptoquark bounds," *Phys.Rev.* **D49** (1994) 333–342, arXiv:hep-ph/9309266. doi:10.1103/PhysRevD.49.333. "Bounds on vector leptoquarks," *Phys.Rev.* **D50** (1994) 536–541, arXiv:hep-ph/9312341. doi:10.1103/PhysRevD.50.536.

[43] A. F. Żarnecki, "Leptoquark signal from global analysis," *Eur.Phys.J.* **C17** (2000) 695–706, arXiv:hep-ph/0003271. doi:10.1007/s100520000511. 24

[44] ALEPH Collaboration, D. Decamp et al., "Searches for new particles in Z decays using the ALEPH detector," *Phys.Rept.* **216** (1992) 253–340. doi:10.1016/0370-1573(92)90177-2. 24

[45] L3 Collaboration, O. Adriani et al., "Results from the L3 experiment at LEP," *Phys.Rept.* **236** (1993) 1–146. doi:10.1016/0370-1573(93)90027-B.

[46] DELPHI Collaboration, P. Abreu et al., "Limits on the production of scalar leptoquarks from Z^0 decays at LEP," *Phys.Lett.* **B316** (1993) 620–630. doi:10.1016/0370-2693(93)91053-P.

[47] DELPHI Collaboration, P. Abreu et al., "Search for Leptoquarks and FCNC in e^+e^- annihilations at $\sqrt{s} = 183$ GeV," *Phys.Lett.* **B446** (1999) 62–74, arXiv:hep-ex/9903072. doi:10.1016/S0370-2693(98)01525-1.

[48] OPAL Collaboration, G. Abbiendi et al., "Search for leptoquarks in electron photon scattering at $\sqrt{s_{ee}}$ up to 209 GeV at LEP," *Phys.Lett.* **B526** (2002) 233–246, arXiv:hep-ex/0112024. doi:10.1016/S0370-2693(01)01485-X.

[49] OPAL Collaboration, G. Abbiendi et al., "Search for pair produced leptoquarks in e^+e^- interactions at $\sqrt{s} \simeq$189–209 GeV," *Eur.Phys.J.* **C31** (2003) 281–305, arXiv:hep-ex/0305053. doi:10.1140/epjc/s2003-01325-y. 24

[50] ZEUS Collaboration, S. Chekanov et al., "A Search for resonance decays to lepton + jet at HERA and limits on leptoquarks," *Phys.Rev.* **D68** (2003) 052004, arXiv:hep-ex/0304008. doi:10.1103/PhysRevD.68.052004. 24

[51] H1 Collaboration, A. Aktas et al., "Search for leptoquark bosons in ep collisions at HERA," *Phys.Lett.* **B629** (2005) 9–19, arXiv:hep-ex/0506044. doi:10.1016/j.physletb.2005.09.048.

[52] H1 Collaboration, "Search for First Generation Leptoquarks in ep Collisions at HERA," arXiv:1107.3716. (*submitted to Phys. Lett.* ***B***). 24

[53] D0 Collaboration, V. Abazov et al., "Search for pair production of first-generation leptoquarks in $p\bar{p}$ collisions at $\sqrt{s} = 1.96$ TeV," *Phys.Lett.* **B681** (2009) 224–232, arXiv:0907.1048. doi:10.1016/j.physletb.2009.10.016. xii, xvi, 25, 26, 27, 28, 137

[54] ATLAS Collaboration, "Search for pair production of first or second generation leptoquarks in proton-proton collisions at $\sqrt{s} = 7$ TeV using the ATLAS detector at the LHC," arXiv:1104.4481. (*submitted to Phys. Rev.* ***D***). xii, xvi, 25, 27, 28, 137

[55] D0 Collaboration, V. M. Abazov et al., "Search for first generation leptoquark pair production in the electron + missing energy + jets final state," arXiv:1107.1849. (*submitted to Phys. Rev.* ***D***). xii, xvi, 25, 28, 137, 138

[56] CMS Collaboration, "Search for Pair Production of First-Generation Scalar Leptoquarks in pp Collisions at $\sqrt{s} = 7$ TeV," *Phys.Rev.Lett.* **106** (2011) 201802, arXiv:1012.4031. doi:10.1103/PhysRevLett.106.201802. xii, 27, 28, 135

[57] CMS Collaboration, "Search for First Generation Scalar Leptoquarks in the $e\nu jj$ Channel in pp Collisions at $\sqrt{s} = 7$ TeV," arXiv:1105.5237. (*accepted by Phys. Lett.* ***B***). xii, 28, 139

[58] G. Bachy, A. Hofmann, S. Myers, E. Picasso, and G. Plass, "The LEP collider: construction, project status and outlook," *Part.Accel.* **26** (1990) 19–32. CERN-LEP-DI-IM-RF-89-44. 29

[59] L. Evans and P. Bryant, "LHC Machine," *JINST* **3** (2008) S08001. doi:10.1088/1748-0221/3/08/S08001. 29

[60] O. S. Brüning, P. Collier, P. Lebrun, S. Myers, R. Ostojic, J. Poole, and P. Proudlock, "LHC Design Report, Vol. I: The LHC Main Ring". CERN, Geneva, 2004. CERN-2004-003-V-1.

[61] O. S. Brüning, P. Collier, P. Lebrun, S. Myers, R. Ostojic, J. Poole, and P. Proudlock, "LHC Design Report, Vol. II: The LHC Infrastructure and General Services". CERN, Geneva, 2004. CERN-2004-003-V-2.

[62] M. Benedikt, P. Collier, V. Mertens, J. Poole, and K. Schindl, "LHC Design Report, Vol. III: The LHC Injector Chain". CERN, Geneva, 2004. CERN-2004-003-V-3. 29

[63] CERN Document Server, http://cdsweb.cern.ch. xii, 30, 31, 33

[64] ATLAS Collaboration, "The ATLAS Experiment at the CERN Large Hadron Collider," *JINST* **3** (2008) S08003. doi:10.1088/1748-0221/3/08/S08003. 30

[65] CMS Collaboration, "The CMS Experiment at the CERN LHC," *JINST* **3** (2008) S08004. doi:10.1088/1748-0221/3/08/S08004. 30, 41, 70, 100

[66] ALICE Collaboration, "The ALICE Experiment at the CERN LHC," *JINST* **3** (2008) S08002. doi:10.1088/1748-0221/3/08/S08002. 30

[67] LHCb Collaboration, "The LHCb Detector at the LHC," *JINST* **3** (2008) S08005. doi:10.1088/1748-0221/3/08/S08005. 30

[68] CERN Press Office, "CERN announces new start-up schedule for world's most powerful particle accelerator." http://press.web.cern.ch/press/PressReleases/Releases2007/PR06.07E.html, Jun. 22, 2007. 37

[69] CERN Press Office, "First beam in the LHC - accelerating science." http://press.web.cern.ch/press/PressReleases/Releases2008/PR08.08E.html, Sep. 10, 2008. 37

[70] CERN Press Office, "Incident in LHC sector 3-4." http://press.web.cern.ch/press/PressReleases/Releases2008/PR09.08E.html, Sep. 19, 2008. 37

[71] CERN Press Office, "CERN releases analysis of LHC incident." http://press.web.cern.ch/press/PressReleases/Releases2008/PR14.08E.html, Oct. 16, 2008. 37

[72] CERN Press Office, "LHC to run at 3.5 TeV for early part of 2009-2010 run rising later." http://press.web.cern.ch/press/PressReleases/Releases2009/PR13.09E.html, Aug. 6, 2009. 37

[73] CERN Press Office, "The LHC is back." http://press.web.cern.ch/press/PressReleases/Releases2009/PR16.09E.html, Nov. 20, 2009. 37

[74] CERN Press Office, "Two circulating beams bring first collisions in the LHC." http://press.web.cern.ch/press/PressReleases/Releases2009/PR17.09E.html, Nov. 23, 2009. 37

[75] CERN Press Office, "LHC sets new record – accelerates beam to 3.5 TeV." http://press.web.cern.ch/press/PressReleases/Releases2010/PR05.10E.html, Mar. 19, 2010. 37

[76] CERN Press Office, "LHC research programme gets underway." http://press.web.cern.ch/press/PressReleases/Releases2010/PR07.10E.html, Mar. 30, 2010. 37

[77] CERN Press Office, "The LHC enters a new phase." http://press.web.cern.ch/press/PressReleases/Releases2010/PR20.10E.html, Nov. 4, 2010. 37

[78] CERN Press Office, "CERN announces LHC to run in 2012." http://press.web.cern.ch/press/PressReleases/Releases2011/PR01.11E.html, Jan. 31, 2011. 37

[79] CMS Collaboration, "CMS Physics Technical Design Report, Vol. I: Detector Performance and Software". CERN, Geneva, 2006. CERN-LHCC-2006-001, CMS-TDR-008-1. 41, 70, 83

[80] CMS Collaboration, "Electromagnetic calorimeter calibration with 7 TeV data," *CMS Physics Analysis Summary* **EGM-10-003** (2010). 52, 53, 128

[81] CMS Collaboration, "Electromagnetic calorimeter commissioning and first results with 7 TeV data," *CMS Note* **2010/012** (2010). 53, 97

[82] CMS Collaboration, "Missing Transverse Energy Performance of the CMS Detector," (2011) arXiv:1106.5048. (*accepted by the Journal of Instrumentation*). 53, 60, 78

[83] CMS Collaboration, "Identification and Filtering of Uncharacteristic Noise in the CMS Hadron Calorimeter," *JINST* **5** (2010) T03014, arXiv:0911.4881. doi:10.1088/1748-0221/5/03/T03014. 60

[84] G. Wrochna, "CMS Level-1 Trigger," *Nucl.Instrum.Meth.* **A384** (1996) 143–146. doi:10.1016/S0168-9002(96)01068-6. 61

[85] R. Brun and F. Rademakers, "ROOT: An object oriented data analysis framework," *Nucl.Instrum.Meth.* **A389** (1997) 81–86. doi:10.1016/S0168-9002(97)00048-X. 69

[86] I. Antcheva, M. Ballintijn, B. Bellenot, M. Biskup, R. Brun, et al., "ROOT: A C++ framework for petabyte data storage, statistical analysis and visualization," *Comput.Phys.Commun.* **180** (2009) 2499–2512. doi:10.1016/j.cpc.2009.08.005.

[87] I. Antcheva, M. Ballintijn, B. Bellenot, M. Biskup, R. Brun, et al., "ROOT: A C++ framework for petabyte data storage, statistical analysis and visualization," *Comput.Phys.Commun.* **182** (2011) 1384–1385. doi:10.1016/j.cpc.2011.02.008. 69

[88] W. Adam et al., "Track Reconstruction in the CMS Tracker," *CMS Note* **2006/041** (2006). 70

[89] CMS Collaboration, "Tracking and Vertexing Results from First Collisions," *CMS Physics Analysis Summary* **TRK-10-001** (2010). 71

[90] CMS Collaboration, "CMS Tracking Performance Results from Early LHC Operation," *Eur.Phys.J.* **C70** (2010) 1165–1192, arXiv:1007.1988. doi:10.1140/epjc/s10052-010-1491-3. 70

[91] T. Speer et al., "Vertex Fitting in the CMS Tracker," *CMS Note* **2006/032** (2006). 72

[92] CMS Collaboration, "Tracking and Primary Vertex Results in First 7 TeV Collisions," *CMS Physics Analysis Summary* **TRK-10-005** (2010). 72

[93] R. Frühwirth et al., "Adaptive Vertex Fitting," *CMS Note* **2007/008** (2007). 72

[94] S. Baffioni et al., "Electron Reconstruction in CMS," *Eur.Phys.J.* **C49** (2007) 1099–1116. doi:10.1140/epjc/s10052-006-0175-5. 73

[95] CMS Collaboration, "Electromagnetic Physics Objects Commissioning with First LHC Data," *CMS Physics Analysis Summary* **EGM-10-001** (2010).

[96] CMS Collaboration, "Electron Reconstruction and Identification at $\sqrt{s} = 7$ TeV," *CMS Physics Analysis Summary* **EGM-10-004** (2010). 73

[97] W. Adam et al., "Reconstruction of Electrons with the Gaussian-Sum Filter in the CMS Tracker at the LHC," *J.Phys* **G31** (2005) N9. doi:10.1088/0954-3899/31/9/N01. 74

[98] CMS Collaboration, "Commissioning of the Particle-flow Event Reconstruction with the First LHC Collisions Recorded in the CMS Detector," *CMS Physics Analysis Summary* **PFT-10-001** (2010). 74, 77

[99] CMS Collaboration, "Performance of Muon Identification in *pp* Collisions at $\sqrt{s} = 7$ TeV," *CMS Physics Analysis Summary* **MUO-10-002** (2010). 74

[100] CMS Collaboration, "Particle-Flow Event Reconstruction in CMS and Performance for Jets, Taus, and MET," *CMS Physics Analysis Summary* **PFT-09-001** (2010). 76

[101] CMS Collaboration, "Commissioning of the Particle-Flow Reconstruction in Minimum-Bias and Jet Events from *pp* Collisions at 7 TeV," *CMS Physics Analysis Summary* **PFT-10-002** (2010). 77

[102] G. P. Salam, "Towards Jetography," *Eur.Phys.J.* **C67** (2010) 637–686, arXiv:0906.1833. doi:10.1140/epjc/s10052-010-1314-6. 77

[103] M. Cacciari, G. P. Salam, and G. Soyez, "The Anti-k_{T} Jet Clustering Algorithm," *JHEP* **0804** (2008) 063, arXiv:0802.1189. doi:10.1088/1126-6708/2008/04/063. 77, 78

[104] CMS Collaboration, "Jet Performance in pp Collisions at $\sqrt{s} = 7$ TeV," *CMS Physics Analysis Summary* **JME-10-003** (2010). 77

[105] J. M. Campbell, J. Huston, and W. Stirling, "Hard Interactions of Quarks and Gluons: A Primer for LHC Physics," *Rept.Prog.Phys.* **70** (2007) 89, arXiv:hep-ph/0611148. doi:10.1088/0034-4885/70/1/R02. xiii, 80, 81, 82, 83

[106] T. Sjöstrand, S. Mrenna, and P. Z. Skands, "PYTHIA 6.4 Physics and Manual," *JHEP* **0605** (2006) 026, arXiv:hep-ph/0603175. doi:10.1088/1126-6708/2006/05/026. 82, 92

[107] G. Corcella, I. Knowles, G. Marchesini, S. Moretti, K. Odagiri, et al., "HERWIG 6: an event generator for Hadron Emission Reactions With Interfering Gluons (including supersymmetric processes)," *JHEP* **0101** (2001) 010, arXiv:hep-ph/0011363. xi, 82, 176

[108] F. Maltoni and T. Stelzer, "MadEvent: Automatic event generation with MadGraph," *JHEP* **0302** (2003) 027, arXiv:hep-ph/0208156. 83, 92

[109] M. L. Mangano, M. Moretti, F. Piccinini, R. Pittau, and A. D. Polosa, "ALPGEN, a generator for hard multiparton processes in hadronic collisions," *JHEP* **0307** (2003) 001, arXiv:hep-ph/0206293. 83, 94

[110] GEANT4 Collaboration, S. Agostinelli et al., "GEANT4: A Simulation Toolkit," *Nucl.Instrum.Meth.* **A506** (2003) 250–303. doi:10.1016/S0168-9002(03)01368-8. 83

[111] GEANT4 Collaboration, J. Allison et al., "GEANT4 Developments and Applications," *IEEE Trans.Nucl.Sci.* **53** (2006) 270. doi:10.1109/TNS.2006.869826. 83

[112] A. R. Baden, "Jets and Kinematics in Hadronic Collisions," *Int.J.Mod.Phys.* **A13** (1998) 1817–1845. doi:10.1142/S0217751X98000809. 87

[113] R. Field, "Early LHC Underlying Event Data - Findings and Surprises," (2010) arXiv:1010.3558. 90

[114] P. Z. Skands, B. Allanach, H. Baer, C. Balazs, G. Belanger, et al., "SUSY Les Houches accord: Interfacing SUSY spectrum calculators, decay packages, and event generators," *JHEP* **0407** (2004) 036, arXiv:hep-ph/0311123. doi:10.1088/1126-6708/2004/07/036. 92

[115] J. Alwall et al., "MadGraph/MadEvent v4: The New Web Generation," *JHEP* **0709** (2007) 028, arXiv:0706.2334. doi:10.1088/1126-6708/2007/09/028. 92

[116] N. Kidonakis, "Higher-order corrections to top-antitop pair and single top quark production," (2009) arXiv:0909.0037. 94, 116

[117] N. Kidonakis, "Next-to-next-to-leading soft-gluon corrections for the top quark cross section and transverse momentum distribution," *Phys.Rev.* **D82** (2010) 114030, arXiv:1009.4935. doi:10.1103/PhysRevD.82.114030. 94

[118] K. Melnikov and F. Petriello, "Electroweak gauge boson production at hadron colliders through $\mathcal{O}(\alpha_s^2)$," *Phys.Rev.* **D74** (2006) 114017, arXiv:hep-ph/0609070. doi:10.1103/PhysRevD.74.114017. 94

[119] N. Kidonakis, "NNLL resummation for s-channel single top quark production," *Phys.Rev.* **D81** (2010) 054028, arXiv:1001.5034. doi:10.1103/PhysRevD.81.054028. 95

[120] J. M. Campbell and R. K. Ellis, "MCFM home page,". http://mcfm.fnal.gov. 95

[121] CMS Collaboration, "Search for Resonances in the Dilepton Mass Distribution in pp Collisions at $\sqrt{s} = 7$ TeV," *JHEP* **1105** (2011) 093, arXiv:1103.0981. doi:10.1007/JHEP05(2011)093. 97, 130

[122] CMS Collaboration, "Determination of the Jet Energy Scale in CMS with pp Collisions at $\sqrt{s} = 7$ TeV," *CMS Physics Analysis Summary* **JME-10-010** (2010). 99, 128

[123] CMS Collaboration, "Measurement of the $t\bar{t}$ production cross section and the top quark mass in the dilepton channel in pp collisions at $\sqrt{s} = 7$ TeV," *JHEP* **1107** (2011) 049, arXiv:1105.5661. doi:10.1007/JHEP07(2011)049. 116, 126

[124] S. Frixione and B. R. Webber, "Matching NLO QCD Computations and Parton Shower Simulations," *JHEP* **0206** (2002) 029, arXiv:hep-ph/0204244. xi, 127, 176

[125] CMS Collaboration, "Absolute luminosity normalization," *CMS Detector Performance Summary* **2011-002** (2011). 129

[126] CMS Collaboration, "Measurements of Inclusive W and Z Cross Sections in pp Collisions at $\sqrt{s} = 7$ TeV," *JHEP* **1101** (2011) 080, arXiv:1012.2466. doi:10.1007/JHEP01(2011)080. 129, 165

[127] D. Bourilkov, R. C. Group, and M. R. Whalley, "LHAPDF: PDF use from the Tevatron to the LHC," (2006) arXiv:hep-ph/0605240. 131

[128] N. Davidson, G. Nanava, T. Przedzinski, E. Richter-Was, and Z. Was, "Universal Interface of TAUOLA Technical and Physics Documentation," (2010) arXiv:1002.0543. x, xi, 174, 176

[129] S. Frixione and B. R. Webber, "The MC@NLO 3.4 Event Generator," (2008) arXiv:0812.0770. xi, 176

[130] G. Corcella, I. Knowles, G. Marchesini, S. Moretti, K. Odagiri, et al., "HERWIG 6.5 Release Note," (2002) arXiv:hep-ph/0210213. xi, 176

[131] D0 Collaboration, I. Bertram et al., "A Recipe for the construction of confidence limits," *FERMILAB-TM* **2104** (2000). 178

[132] CMS Statistics Committee, "Probability Density Functions for Positive Nuisance Parameters." http://www.physics.ucla.edu/~cousins/stats/cousins_lognormal_prior.pdf (2010). 180